Neutron Detection and Imaging

Development of Lithium Indium Diselenide for Applications in Solid-State Devices

A Dissertation Presented for the

Doctor of Philosophy

Degree

The University of Tennessee, Knoxville

Elan Hunter Herrera

August 2018

Copyright © 2018 by Elan Hunter Herrera
All rights reserved.

Dedication

This work has been rightfully dedicated to **Lise Meitner (1878-1968)** for her contribution in the study of radioactivity and nuclear physics. We have colloquially named this sensor **LISe**, in posthumous honor of her lifetime achievements.



"You must not blame us scientists for the use which war technicians have put our discoveries."

- Lise Meitner

Acknowledgments

To my family:

Thank you to my grandparents, *Lilia and Faustino Herrera*, for pushing me to achieve my goals and more. You have been my unfaltering support and inspiration through the entirety of my academic career. I love you both very much. Thank you to my father, *Eduardo Herrera* for supporting and encouraging my academic pursuits. Thank you to my aunt and uncle, *Jaime and Pamela Herrera*, for opening your home and supporting my completion of graduate school.

To my colleagues:

Thank you to my close friend *Jae-Ho Song*. You have been an unconditional ally in the pursuit of scientific and engineering excellence, providing invaluable collaboration on numerous projects.

Thank you to my colleagues at the Univeristy of Tennessee: *Dustin Giltnane, Dr. Daniel S. Hamm, Robert W. Milburn, C. Ryan Priest, M. Dylan Richardson, Mikah R. Rust, and Dr. Thomas G. Wulz.*

Thank you to my colleagues at The Univeristy of Texas at Austin: *Austin Davis, Hunter Fuentes, Jason Guidry, Jacob Navar, Johnathan Sims, Sigmund Søgnesand, and Nick Wynne* .

Thank you to all the collaborators on the LISe Project from Fisk University, Oak Ridge National Lab, University of Tennessee, Vanderbilt University, and Y-12 National Security Complex.

To the McNair Scholars Program:

Thank you to all the faculty and staff from The University of Texas at Austin and especially *Dr. James Brown* for your guidance and support.

To my academic mentors:

Thank you to my Senior Reactor Operator and Supervisor, Michael Krause, for teaching me to operate the TRIGA nuclear reactor and instilling an appreciation for the nuclear security culture.

Thank you to my undergraduate faculty mentor, *Dr. Sheldon Landsberger*, for overseeing my undergraduate research and senior design project, introducing me to the field of nuclear engineering.

Thank you to my graduate advisor, *Dr. Eric D. Lukosi*, for allowing me to work on the LISe Project.

This work is supported through subcontract number 4300090406 from CNS Y-12 National Security Complex and this material is based upon work supported under a Department of Energy Nuclear Energy University Programs Graduate Fellowship. A portion of this research at ORNL's High Flux Isotope Reactor was sponsored by the Scientific User Facilities Division, Office of Basic Energy Sciences, U.S. Department of Energy.

A special thank you to all the members of my Doctoral Committee, for your advisement and support.



Eric D. Lukosi



Jason P. Hayward



Jamie B. Coble



Mongi A. Abidi



Hassina Z. Bilheux

Quotes

"You cannot teach a man anything; you can only help him discover it in himself."

- Galileo Galilei

"An experiment is a question which science poses to Nature, and a measurement is the recording of Nature's answer."

- Max Planck

"Nothing in life is to be feared, it is only to be understood. Now is the time to understand more, so that we may fear less."

- Marie Curie

Abstract

This work demonstrates the neutron sensitivity of single crystal lithium indium diselenide ($LiInSe_2$ or LISe [lithium indium diselenide]). The study aimed to design and characterize a neutron imaging system capable of achieving spatial resolution less than 50 µm [micrometer], operating as a first of its kind direct conversion semiconductor neutron detector. Early detection experiments utilized lithium-6 indium diselenide, enriched to 95% in ^{6}Li [lithium-6], following the experimental investigation of enriched chalcopyrites for semiconductor detection. In this work, lithium indium diselenide (LISe) interchangeably refers to its isotopically enriched complement ($^6LiInSe_2$ or ^{6}LISe [lithium-6 indium diselenide]). The primary detection mechanism follows the $^6\mathrm{Li}(n,\alpha)^3\mathrm{H}$ [lithium-6, neutron, alpha, hydrogen-3] reaction, with a Q-value of 4.78 MeV. The proof-of-concept detector consisted of a single LISe crystal patterned with thin film gold contacts on opposite surfaces. After showing a semiconductor response to both alpha particles (α's) and mixed neutron spectrum, the technology was extended to a 4×4 pixel detector using square pixels of 500 µm size and 550 µm pitch. Using the super-sampling technique, this system successfully resolved features of 300 µm, roughly half the pixel pitch, in a cold neutron beam. Concurrently in the study, higher optical quality LISe sensors demonstrated a scintillation response to neutron exposure. An array of scintillating LISe sensors achieved a resolution of 34 µm, calculated via modulation transfer function (MTF), and were used to reconstruct a neutron computed tomography (nCT) of a small biological sample. Bolstering these results, a semiconducting LISe sensor was patterned with the 55 µm pitch pattern, derived from the 256×256 channel Timepix. The Timepix coupled LISe imager (LISePix) completed the groundwork for the detector as a high-resolution neutron imager, surpassing the design goal with a published spatial resolution limit of 34 µm (full width at half maximum (FWHM) of 111 µm) for LISe. This project has demonstrated the first application of direct conversion semiconductors for neutron detection and imaging, while qualifying a viable neutron detection material for solid-state devices. The LISePix imaging technology offers a low-cost, low-power, compact neutron detection platform comparable to state-of-the-art neutron imaging technologies.

Table of Contents

1 Introduction **1**

1.1 Motivation . . . 1

1.2 Aims and Objectives . . . 6

1.3 Overview . . . 6

1.4 Disclaimer . . . 7

2 Literature Review **8**

2.1 Radiation Detection . . . 8

2.1.1 Types of Radiation . . . 8

2.1.2 Neutron Interactions . . . 10

2.1.3 Neutron Sensitive Isotopes . . . 14

2.1.4 Radiography . . . 18

2.2 Scintillator Detectors . . . 21

2.2.1 Glasses . . . 21

2.2.2 Plastics . . . 22

2.2.3 Ceramics . . . 24

2.3 Semiconductor Detectors . . . 27

2.3.1 Properties of Semiconductors . . . 28

2.3.2 Pulse Formation . . . 28

2.3.3 Charge Collection . . . 32

2.3.4 Diamond . . . 33

2.3.5 Boron Compounds . . . 35

2.4 Lithium Indium Diselenide . . . 36

2.4.1 Material Growth . . . 37

2.4.2 Crystal Structure . . . 38

2.4.3 Material Properties . . . 41

2.5 Advanced Detectors . . . 42

2.5.1 Medipix / Timepix Coupled Systems . . . 45
2.5.2 Microchannel Plates . . . 45
2.5.3 Neutron Microscope . . . 46

3 Materials and Methods 48
3.1 Sensor Fabrication . . . 48
3.1.1 Sensor Preparation . . . 48
3.1.2 Photolithography and Patterning . . . 49
3.1.3 Packaging and Electronic Coupling . . . 50
3.2 Early Detector Designs . . . 51
3.2.1 Basic Readout System . . . 51
3.2.2 Single Channel Counting Detector . . . 53
3.2.3 Prototyping LISe Semiconductor Neutron Imager . . . 55
3.3 Pixelated 16-Channel Detection System . . . 55
3.3.1 Electronic Readout System . . . 55
3.3.2 Sensor Board Design . . . 58
3.3.3 Sensor Design . . . 60
3.3.4 LISe Pixel Detector Assembly . . . 63
3.4 Timepix Coupled Neutron Imaging System . . . 64
3.4.1 LISePix Sensor . . . 64
3.4.2 Timepix ASIC . . . 66
3.4.3 LISePix Imaging Module . . . 66
3.5 HFIR CG-1D Beamline Testing . . . 67
3.5.1 Beamline Overview . . . 67
3.5.2 Scintillator Operation . . . 69
3.5.3 Semiconductor Operation . . . 72
3.5.4 Timepix Operation . . . 73
3.5.5 Imaging Targets . . . 73
3.6 Imaging Techniques . . . 78
3.6.1 Super-Sampling . . . 78
3.6.2 Contrast . . . 79
3.6.3 Modulation Transfer Function Resolution Calculation . . . 80
3.6.4 Full Width at Half Maximum Resolution Calculation . . . 82
3.6.5 Simulation . . . 82
3.6.6 Computational Tomography w/ Scintillator . . . 84

4 Results and Discussion **87**

4.1 Scintillator: Single Sensor . . . 87

4.1.1 Open Beam . . . 87

4.1.2 Power-T Target . . . 88

4.1.3 CNS-Y12 Target . . . 89

4.1.4 PSI Siemens Star . . . 89

4.2 Scintillator: Sensor Array . . . 91

4.2.1 Open Beam . . . 91

4.2.2 Resolution Calculations . . . 93

4.2.3 Computed Tomography . . . 94

4.3 Semiconductor Response and Sensitivity . . . 96

4.3.1 Fast Neutron Detection . . . 100

4.4 Semiconductor: 16 Channel Imager . . . 101

4.4.1 LISe Pixel Detector v1 . . . 102

4.4.2 LISe Pixel Detector v2 . . . 102

4.5 Semiconductor: Timepix Imager . . . 105

4.5.1 Plutonium / Beryllium Source . . . 105

4.5.2 Open Beam . . . 106

4.5.3 Resolution Calculation . . . 106

4.5.4 Feature Detection . . . 110

5 Conclusion **112**

5.1 Project Outcomes . . . 112

5.1.1 Fabrication Techniques . . . 112

5.1.2 Operational Modes . . . 113

5.1.3 Resolution Limits . . . 113

5.2 Moving Forward . . . 114

5.2.1 LISe Timepix Device Improvements . . . 115

5.2.2 Coplanar Device . . . 115

5.2.3 Time of Flight Measurements . . . 115

5.3 Closing Remarks . . . 117

References **118**

Appendix **131**

A General Chemistry **132**

A.1 Sensor Etching 132

A.2 PCB Etching 135

B Thin Film Processing **140**

B.1 Plasma Sputtering 141

B.2 Negative Photolithography 142

B.3 Positive Photolithography 148

B.4 Wire Bonding 150

B.5 Bump Bonding 153

C Image Processing **155**

C.1 Neutron Image Pre-Processing 155

C.2 Mosaic Stitching 158

C.3 Super-Sampling 159

C.4 Modulation Transfer Function 164

C.4.1 Analytical Methods 164

C.4.2 MTF Calculator 173

D Nuclear Cross Sections **176**

D.1 Neutron Sensitive Isotopes for Detection and Imaging 176

D.2 Lithium Indium Diselenide 180

D.3 Engineering Materials 185

E Glossary **190**

Vita **198**

List of Tables

2.1 Bulk material properties for LISe . . . 37
2.2 Crystal lattice parameters for LISe . . . 40
2.3 Bandgap for LISe . . . 42
2.4 Optoelectronic properties for LISe . . . 43
2.5 Thermomechanical properties of LISe . . . 44

3.1 LISe scintillator sample identification, thickness, and measured surface roughness . . . 71

4.1 LISe scintillator neutron absorption efficiency and light yield . . . 93
4.2 LISe scintillator spatial resolution measurements using FWHM and MTF . . . 94

5.1 Estimated cost for hypothetical LISePix (4×) high-resolution neutron imaging system . . . 114

A.1 Sensor BrMeOH etching chemicals . . . 133
A.2 LISe sensor BrMeOH etching process . . . 134
A.3 PCB wet etching chemicals . . . 136
A.4 PCB wet etching process . . . 139

B.1 Photolithography negative process chemicals . . . 143
B.2 Spin coater negative resist recipe . . . 145
B.3 Photolithography with negative photoresist for sensor fabrication . . . 147
B.4 Photolithography positive process chemicals . . . 148
B.5 Photolithography with positive photoresist for PCB manufacturing . . . 151
B.6 Calibrated base settings for the K&S wire bonder . . . 152

List of Figures

2.1 The $^{6}\mathrm{Li}(n,\alpha)^{3}\mathrm{H}$ reaction 16
2.2 Complementary transmission radiographs captured using X-ray and neutron radiation 20
2.3 SRIM simulations of secondary particle trajectories in LISe 30
2.4 Neutron detection in LISe semiconductor: neutron absorption 31
2.5 Neutron detection in LISe semiconductor: carrier generation 31
2.6 Neutron detection in LISe semiconductor: charge formation 32
2.7 Relative position-dependent charge collection for electron and hole transport 34
2.8 LISe crystal growth ampule being loaded into vertical growth furnace at Y-12 38
2.9 LISe cube of sensor grade material 39
2.10 LISe crystal lattice structure 39
2.11 Pair of LISe sensors used for scintillator and semiconductor devices 41

3.1 Cremat CR-110 chip pinout and circuit diagram 52
3.2 Cremat CR-150 schematic diagram 52
3.3 Original single channel LISe prototype using TO header 53
3.4 Test enclosure for TO header package 54
3.5 Prototype single channel pre-amp PCB 56
3.6 Prototype single channel pre-amp 57
3.7 LISe PD CAD model 57
3.8 LISe PD pre-amp assembly 59
3.9 Neutron readout PCB for LISe PD 59
3.10 Layer diagram of LISe PD for PCB manufacturing 61
3.11 Assembled LISe PD sensor readout board 61
3.12 Photo of LISe PD sensor (v1) after photolithography process 62
3.13 LISe PD electronically coupled using 25 µm gold wire bonds 62
3.14 LISe PD with open lid to expose internal circuitry 63
3.15 Micrograph analysis of exposed photoresist pattern on LISePix sensor 64
3.16 Micrograph analysis of gold contacts on metalized LISePix sensor 65

3.17 Microscopy of LISePix pattern . . . 65
3.18 LISePix sensor layering design . . . 66
3.19 LISe high-resolution sensor mounted to Timepix . . . 67
3.20 Timepix coupled LISe imager imaging system . . . 68
3.21 The High-Flux Isotope Reactor cold neutron guide hall . . . 68
3.22 Generalized beamline geometry for neutron imaging . . . 69
3.23 Scintillator experimental setup at CG-1D . . . 70
3.24 LISe scintillator arrays . . . 71
3.25 LISe PD running bolt super-sampling experiment . . . 72
3.26 LISe PD installed at the HFIR CG-1D beamline . . . 73
3.27 LISePix installed at HFIR CG-1D beamline . . . 75
3.28 Small PSI Siemens star imaging mask . . . 75
3.29 Large PSI Siemens star imaging mask . . . 76
3.30 *CNS-Y12* neutron imaging target . . . 76
3.31 *Power-T* neutron imaging targets . . . 77
3.32 *Halyomorpha halys*: biological neutron imaging target . . . 78
3.33 Determining the ESF from a line pair mask . . . 81
3.34 Photo of Siemens Star compared with simulated imaging experiment . . . 83
3.35 MCNP simulation of Siemens Star neutron image using LISe PD . . . 84
3.36 Example of object projection used for nCT . . . 86

4.1 Open beam image of single LISe scintillator . . . 88
4.2 Scintillator performance comparison of *Power-T* transmission neutron imaging target . . . 89
4.3 Scintillator performance comparison of *CNS-Y12* neutron imaging target . . . 90
4.4 Radiograph comparison of Siemens Star using LiF/ZnS and LISe scintillators . . . 90
4.5 Open beam image of LISe scintillator array (v2) . . . 92
4.6 NCT slice comparing raw LISe scintillator neutron radiographs . . . 95
4.7 NCT slice comparing cleaned and filtered LISe scintillator neutron radiographs . . . 95
4.8 Neutron computed tomography using ^{6}LiF/ZnS screen and LISe scintillator . . . 96
4.9 Bias polarity effects on LISe response to ^{234}U alpha source . . . 97
4.10 Neutron spectra at the Cold Guide 1D Instrument (CG-1D) from channel 15 of LISe PD . . . 100
4.11 LISe fast neutron testing enclosure . . . 101
4.12 Neutron radiograph of stainless steel bolt comparison using LISe PD and scintillator screen . 103
4.13 Reconstructed image of the Siemens Star using the LISe PD . . . 104
4.14 LISePix neutron response to Pu/Be source . . . 107
4.15 LISePix neutron response image of HFIR CG-1D open beam . . . 107

4.16 LISePix neutron image of Siemens Star . . . 108
4.17 LISePix neutron image of knife edge slit . . . 109
4.18 MTF method to calculate edge resolution . . . 109
4.19 Centered LSF with Gaussian fit and FWHM . . . 110
4.20 LISePix neutron image of 3D printed *Power-T* . . . 111

5.1 WidePIX: a 10×10 Timepix array . . . 116
5.2 Coplanar strip detector design and fabricated LISe prototype . . . 116

A.1 Printed circuit board etching station . . . 135
A.2 Pre-amp PCB etching process . . . 138

B.1 Micro-Processing Research Facility clean room . . . 140
B.2 Photolithography process using negative resist for pixelated LISe semiconductor sensor fabrication . . . 144
B.3 Silicon test wafer patterned with coplanar, circular, and rectangular broadface contacts . . . 147
B.4 Photolithography process using positive resist for PCB manufacturing . . . 149
B.5 Ultra-sonic wedge bonding process . . . 151
B.6 LISe PDs under K&S wire bonder . . . 153
B.7 Indium bump deposition processes followed by reflow and flip chip operation . . . 154

C.1 Example of mosaic stitching technique using LISe scintillator . . . 158
C.2 Normalized component neutron images used to create the composite *Power-T* neutron image 160
C.3 Super-sampling mosaic . . . 161
C.4 Composite image of Siemens Star using super-sampling technique . . . 163
C.5 Raw image after dark field subtraction and open beam normalization . . . 164
C.6 Raw image with ROI overlay . . . 165
C.7 ROI image crop and oversampling perpendicular to edge . . . 166
C.8 Canny edge detector applied to the interpolated ROI image . . . 166
C.9 Hough transform applied to binary edge profile to extract line angle . . . 167
C.10 ESF for each vector showing raw position . . . 168
C.11 ESF after edge angle correction using value calculated with Hough transform . . . 169
C.12 Averaged ESF . . . 169
C.13 ESF centered about inflection point . . . 169
C.14 Raw LSF after numerical differentiation of the ESF . . . 169
C.15 LSF normalized to edge spread peak with location found from Gaussian fit . . . 170
C.16 LSF centered about inflection point . . . 170
C.17 Tukey window application . . . 171

C.18 LSF after applying Tukey window . . . 172
C.19 MTF curve with evaluated resolution marked by 10% cutoff limit . . . 173

D.1 Total neutron cross section for ^{3}He . . . 176
D.2 Total neutron cross section for ^{6}Li . . . 177
D.3 Total neutron cross section for ^{10}B . . . 177
D.4 Total neutron cross section for ^{113}Cd . . . 178
D.5 Total neutron cross section for ^{155}Gd . . . 178
D.6 Total neutron cross section for ^{157}Gd . . . 179
D.7 Selected neutron cross sections for ^{6}Li . . . 180
D.8 Selected neutron cross sections for ^{7}Li . . . 180
D.9 Selected neutron cross sections for ^{113}In . . . 181
D.10 Selected neutron cross sections for ^{115}In . . . 181
D.11 Selected neutron cross sections for ^{76}Se . . . 182
D.12 Selected neutron cross sections for ^{77}Se . . . 182
D.13 Selected neutron cross sections for ^{78}Se . . . 183
D.14 Selected neutron cross sections for ^{80}Se . . . 183
D.15 Selected neutron cross sections for ^{82}Se . . . 184
D.16 Selected neutron cross sections for LISe compound . . . 184
D.17 Total neutron cross section for H . . . 185
D.18 Total neutron cross section for C . . . 185
D.19 Total neutron cross section for N . . . 186
D.20 Total neutron cross section for O . . . 186
D.21 Total neutron cross section for Al . . . 187
D.22 Total neutron cross section for Si . . . 187
D.23 Total neutron cross section for Fe . . . 188
D.24 Total neutron cross section for Cu . . . 188
D.25 Total neutron cross section for Au . . . 189

List of Attachments

The following attachments are available online as a companion to the digital manuscript. The attached supplemental files are freely open to downloaded for reference. Any usage or reproduction must follow all guidelines set forth by the The University of Tennessee.

1 "Timepix-layer-diagram.pdf" : CAD model of LISePix layering 66
2 "LISe-Timepix-imager-module.pdf" : CAD model of LISePix imaging module 66
3 "Neutron-imaging-target-stand.pdf" : CAD model of target stand and neutron imaging targets 77
4 "CT-scan-raw.gif" : Raw neutron computed tomography 94
5 "CT-scan-cleaned.gif" : Cleaned neutron computed tomography 94
6 "CT-scan-filtered.gif" : Filtered neutron computed tomography 94
7 "Timepix-image-preprocessor.zip" : Python class file and processing script for large image sets 155
8 "MTF-calculator.zip" : MATLAB based MTF calculator script 173

List of Terminology

Symbols

(2D) 2-dimensional
(3D) 3-dimensional

A

(ABS) acrylonitrile butadiene styrene
(AC) alternating current
(ADC) analog-to-digital converter
(α) alpha particle
(AM) additive manufacturing
(ASIC) application specific integrated circuit
(ATI) Atominstitut
(ATLAS) A Toroidal LHC ApparatuS

B

(B_2Pin_2) bis(pinacolato)diboron
(β) beta particle
(β^-) beta minus particle
(β^+) beta plus particle
(BGO) bismuth germanate
(BNC) Bayonet Neill-Concelmann
($^{10}B(n,\alpha)^7Li$) boron-10 (n,a) reaction
(BrMeOH) bromine/methanol

C

(CAD) computer-aided design
($^{113}Cd(n,\gamma)^{114}Cd$) cadmium-113 (n,g) reaction
(CAM) computer-aided manufacturing
(CANS) compact accelerator-driven neutron source
($^{12}C(n,\alpha)^9Be$) carbon-12 (n,a) reaction
(CCD) charge-coupled device
(CERN) European Organization for Nuclear Research
(CFT) continuous Fourier transform
(CG-1) Cold Guide 1 Beamline
(CG-1A) Cold Guide 1A Instrument
(CG-1D) Cold Guide 1D Instrument
($^{35}Cl(n,p)^{35}S$) chlorine-35 (n,p) reaction
(CMOS) complementary metal-oxide semiconductor
(CSP) charge sensitive preamplifier
(CT) computed tomography
(CVD) chemical vapor deposition

D

(DAQ) data acquisition
(DC) direct current
(δ-ray) delta-ray
(DFT) discrete Fourier transform
(DHS) Department of Homeland Security
(DOE) Department of Energy
(DPP-PHA) digital pulse processing and pulse height analysis

E

(EAGLE) Easily Applicable Graphical Layout Editor
(eCT) electron computed tomography
(EDA) electronic design automation
(EMI) electromagnetic interference
(ENDF) Evaluated Nuclear Data File
(ε-ray) epsilon-ray
(ESF) edge spread function

F

(FCC) Federal Communications Commission
(FDM) fused deposition modeling
(FET) field effect transistor
(FFT) fast Fourier transform
(FIB) focused ion beam
(FOV) field of view
(FR-4) Flame Retardant 4
(FWHM) full width at half maximum

G

(G-M) Geiger-Müller
($^{155}Gd(n,\gamma)^{156}Gd$) gadolinium-155 (n,g) reaction
($^{157}Gd(n,\gamma)^{158}Gd$) gadolinium-157 (n,g) reaction
(Gadox) gadolinium oxysulfide
(γ-ray) gamma-ray
(GA) General Atomics

H

(HDR) high dynamic range
(^{3}He$(n,p)^3$H) helium-3 (n,p) reaction
(HFIR) High-Flux Isotope Reactor
(HZB) Helmholtz-Zentrum Berlin

I

(IPA) isopropyl alcohol
(IV) current-voltage

J

(JSI) Jožef Stefan Institute

K

(Karl Süss) Süss MicroTec
(K&S) Kulicke and Soffa

L

(LabVIEW) Lab Virtual Instrument Engineering Workshop
(LCD) liquid crystal display
(LEMO 00) LEMO 00 coaxial connector
(LHC) Large Hadron Collider
(LIB) Li-ion battery
(^{6}LiF) lithium-6 fluoride
(LiF/ZnS) lithium fluoride, zinc sulfide
(LiF/ZnS screen) ^{6}LiF/ZnS:(Cu) (1:2) scintillator screen
(LiME) lithium methacrylate
(LiPSA) lithium phenylsalicylate
(LiSal) lithium salicylate
(LISe) lithium indium diselenide
(^{6}LISe) lithium-6 indium diselenide
(LISe PD) LISe 16-channel pixel detector
(LISePix) Timepix coupled LISe imager
(^{6}Li$(n,\alpha)^3$H) lithium-6 (n,a) reaction
(LM) light microscope
(LSF) line spread function
(LY) light yield

M

(MATLAB) Matrix Laboratory
(MBB) monoborylated benzene
(MCA) multi-channel analyzer
(MCNP) Monte Carlo N-Particle
(MCP) microchannel plate
(μCT) micro computed tomography
(MCX) micro coaxial connector
(MEMS) microelectromechanical systems
(MeOH) methanol
(MFP) mean free path
(mid-IR) mid infra-red
(MPRF) Micro-Processing Research Facility
(MRI) magnetic resonance imaging
(MTF) modulation transfer function

N

(NAA) neutron activation analysis
(nCT) neutron computed tomography
(NDT) non-destructive testing
(negative photoresist) NR9-1000PY
(NI) National Instruments
(NIH) National Institute of Health
(NIM) nuclear instrumentation module
(NIP) neutron imaging plate
(NIST) National Institute of Standards and Technology
(NLO) non-linear optics
(NORM) naturally occurring radioactive material
(NRC) Nuclear Regulatory Commission

O

(ORNL) Oak Ridge National Lab

P

(PBN) pyrolitic boron nitride
(PC) personal computer
(PCB) printed circuit board
(PCI) peripheral component interconnect
(PCIe) peripheral component interconnect express
(PE) polyethylene
(PECVD) plasma-enhanced CVD
(PEFC) polymer electrolytic fuel cell
(phoswich) photon sandwich
(PLA) polylactic acid
(PMMA) poly(methyl methacrylate)
(PMT) photomultiplier tube
(PNG) portable network graphic
(positive photoresist) PR1-1000A
(PP) polypropylene
(PPE) personal protective equipment
(PPO) poly(p-phenylene oxide)
(pre-amp) preamplifier
(PS) polystyrene
(PSD) pulse shape discrimination
(PSI) Paul Scherrer Institute
(Pu/Be) plutonium/beryllium
(PVT) polyvinyl toluene

R

(R&D) research and development
(redox) reduction-oxidation
(RF) radio frequency
(RIE) reactive ion etching
(RMD) Radiation Monitoring Devices
(RMS) root mean square

(RPM) radiation portal monitor

S

(sCMOS) scientific complementary metal-oxide semiconductor
(SDS) Safety Data Sheets
(SHV) safe high-voltage connector
(SiPM) silicon photomultiplier
(SLA) stereolithography
(SNM) special nuclear material
(SNS) Spallation Neutron Source
(SCS) Specialty Coating Systems
(SRIM) Stopping and Range of Ions in Matter

T

(TC) ternary chalcogenide
(TCT) transient-current technique
(TIFF) tagged image file format
(TO) transistor outline
(TOF) time-of-flight
(*T*) triton

U

(UCN) ultra-cold neutron
(UHV) ultra-high vacuum
(UT) The University of Texas at Austin
(UTK) University of Tennessee
(US) ultra-sonic
(USB) universal serial bus
(UV) ultraviolet

V

(VENUS) Versatile Neutron Imaging Instrument
(VI) virtual instrument
(VME) Versa Module Europa communication bus

W

(WLS) wavelength-shifting

X

(XDL) cross delay line anode
(XEOL) X-ray excited optical luminescence

Y

(Y-12) CNS Y-12

Z

(ZC) zero-crossing

Chapter 1

Introduction

Digital images have become commonplace in everyday life, with mobile devices including smartphones, tablets, digital cameras, and laptops able to capture and display these images with unprecedented clarity and definition. The human visual system is tuned to light in the aptly named visible spectrum, or electromagnetic waves ranging from around 390 nm to 700 nm. While the visible world consists of vibrant colors, forming a plethora of information stockpiled in digital images, there exists even more secrets invisible to the naked eye. Outside of the visual spectrum, the broader electromagnetic spectrum and various forms of particle radiation illuminate the hidden world. Neutron imaging grants a unique view into a variety of natural and man-made systems.

1.1 Motivation

Anderson *et al.* gives a general overview of neutrons, neutron imaging and nCT, neutron generation facilities, various detectors, and applications of the science [1]. Brenizer reviewed the prior two decades of neutron imaging as a non-destructive testing (NDT) and the historical milestones achieved along the broader history of neutron sciences. Most importantly, the number of facilities directly supporting neutron imaging has increased, seeking improvements in beam quality (producing colder neutrons at higher fluxes) as well as increasing the timing, spatial and energy resolutions of detection systems [2]. Summarizing the current state of neutron imaging sciences available globally, Anderson *et al.* presents an overview of compact accelerator-driven neutron source (CANS) and their potential for supplementing current reactor or spallation based facilities. The small size and lower overhead cost of infrastructure would boost the availability of such neutron beams for a wide variety of research, including neutron imaging. A number of facilities and their respective experimental setups are described in detail, looking to decouple neutron based sciences from nuclear reactor facilities and expand their applications [3]. In support of neutron imaging sciences, Taylor *et al.* reported on an electronic neutron generator using a deutirium target for neutron production. Specifically

designed around neutron imaging applications, this technology opens the door for a broader range of scientists to utilize neutron imaging techniques. While the flux is significantly lower than reactor based sources, an electronic neutron source would permit many universities and scientific institutions to conduct experiments without petitioning for low-availability beam time. The study successfully generated neutron images using scintillation screens, while performance with a microchannel plate (MCP) was deemed inconclusive and warrants further experimentation [4].

Lehmann *et al.* presents an up-to-date overview of neutron imaging methodologies and the history of the science. While the best feature resolution presently measured is sub 10 µm, most neutron imaging facilities operate in the 20 µm to 100 µm resolution range to balance exposure time requirements [6]. They also noted the successes in imaging lighter elements with high contrast, unavailable via X-ray, as well as imaging thicker metallic samples while avoiding the beam hardening effects seen in X-rays [5]. As suggested by Lehmann *et al.*, the following studies implement neutron imaging experiments across a variety of material and engineering investigations. In developing more sophisticated imaging systems and techniques, the practical applications of neutron detection and imaging will expand to new fields while providing more detailed NDT methods. These experiments provide a strong justification for the continued advancement of neutron sources, detectors and high-resolution imaging platforms.

Hydrogen and Water

Hydrogen in its most common terrestrial form, water, is used to moderate nuclear reactors because of its sizable interaction cross section. In neutron imaging, hydrogenous compounds, including water, create significant contrast through beam attenuation. Lehmann *et al.* tested a series of practical scenarios where hydrogen concentration varied throughout a dynamic system including: moisture in clay, water entrainment in soil, methanol distribution in a fuel cell, and isotopic mixing between light and heavy water [7]. At CG-1D, Kang *et al.* imaged an adjustable, water saturated sand column to evaluate the attenuation coefficient of water [8]. Time resolved imaging offered insight into the drainage of rain water in porous asphalt as studied by Poulikakos *et al.* The complex geometry of the paving mixture resulted in unusual water retention and associated drying, revealing the hydrological mechanisms in porous asphalt responsible for enhancing motorist safety [9]. Perfect *et al.* measured the drying of water saturated sand columns, permeation of water into clay and siliceous bricks, saturation of polymer electrolytic fuel cells (PEFCs), and phase changes in heat pipes [10].

Fuel Cells

Boillat *et al.* observed water distribution in PEFCs using the neutron radiography facilities at the Paul Scherrer Institute (PSI). An experimental correlation was established showing a voltage drop in the fuel cell in accordance with water concentration near the cathode [11]. Santamaria *et al.* mated a 3-dimensional (3D) printed plastic manifold to an aluminum flow-field to measure the water saturation across individual cell

channels [12].

Engines

Schillinger *et al.* captured a short neutron video, at PSI, of an operational BMW engine driven by an electric motor at 1,000 RPM. Covering a $24 \times 24\,\mathrm{cm}^2$ field of view (FOV), the lithium fluoride, zinc sulfide (LiF/ZnS) based scintillator was coupled to a MCP detection system, showing the internal dispersion of oil under the piston while it lubricated the connecting rod [13]. Likewise, Kardjilov *et al.* used a LiF/ZnS scintillator at the Helmholtz-Zentrum Berlin for Materials and Energy (HZB) to record a model air-craft engine operating at 1,110 RPM. The large flux at HZB ($10^9\,\mathrm{n/cm}^2 \cdot \mathrm{s}$) across the $30 \times 50\,\mathrm{cm}^2$ FOV provided the high speed imaging capabilities needed for stroboscopic neutron imaging [14]. Later, Butler *et al.* demonstrated the edge enhancement effect in a diesel fuel injector. The abrupt transition at the air-to-steel interface created increased contrast, potentially useful in future applications for detection of internal cracks and voids, following the development of a suitable high-resolution imager [15].

Alloys

Beyer *et al.* investigated hydrogen effusion in austenitic stainless steel, a common engineering material. They were able to measure hydrogen concentrations down to 20 ppm reducing the detection limit from the previously tested 100 ppm [16]. In the same year, Grosse *et al.* reported on hydrogen and oxygen ratios in zirconium alloys, favored by the nuclear industry for their low thermal neutron cross sections and desirable mechanical properties. The zirconium based nuclear fuel cladding alloys demonstrated rapid hydrogen uptake on the bare metal with decreased rates in the presence of a surface oxidation layer [17].

Batteries

Mobile electronics rely heavily on Li-ion batteries (LIBs) to supply the power consuming processors, sensors and displays. The rechargeable batteries operate by creating a voltage potential across the electrolytic cell, containing lithium ions. In attempts to better understand the electrochemical dynamics in LIBs, Butler *et al.* used neutron imaging and nCT to observe the changes in an operational cell. The visible effects of charging and discharging were revealed through changes in LiC_6 concentration, with increased LiC_6 providing larger beam attenuation, darkening the region. While the computed tomography (CT) was successful, the results left much to be desired and the author made provisions for future experiments [18]. In the follow-up experiment, Butler *et al.* used neutron imaging to reveal cell degradation in the LIB over multiple charging and discharging cycles. They noted an increase in salt-and-pepper noise along with linear structures following the electrode fold structure. With a refined set of experiments, the study provided a basis for monitoring the dynamics of an actively performing LIB, suggesting further benefits by increasing the energy and spatial resolutions as well as time-of-flight (TOF) techniques [19].

Biology

Offering an *in situ* view of active biology, neutron imaging has been implemented to study the growth of plants. Because living organisms are comprised mostly of water, neutron imaging provides a means of capturing the uptake and flow of hydrogenous compounds within the living system. Anderson *et al.* investigated the internal morphological development of plants grown in a thin aluminum planter. Imaging a soybean plan root after 8 d and 15 d showed extensive root penetration into the soil, a process that would have otherwise been interrupted by invasive techniques. Furthermore, the reuse of the original, unadulterated sample provided significant benefit over invasive measurements when studying root response to variations in soil composition. Neutron images of the same root system reduced systematic errors, showing progression of the root profile towards water-rich regions of soil, impossible to duplicate between samples due to the semi-random, dendritic growth of plant root structures. Similarly, imaging Japanese tree trunk cross sections illustrated the differing mechanisms of water uptake between species. While some trees maintained a significant portion of moisture in the outer rings or sapwood, others presereved their moisture in the core or heartwood of the tree, creating difficulties in drying the lumber and future warping issues when used as a structural material [1].

Archaeology

Broadening the application of neutron imaging, archaeological studies benefit from the NDT techniques offered through radiographic imaging. Because the artifacts being studied may be hundreds or thousands of years old, they are often delicate and irreplaceable, requiring minimal handling. Like photography, X-ray and more recently neutron imaging offer complementary methods of capturing the details and structure of artifacts without direct taction. Deschler-erb *et al.* used these methods, at PSI, to illuminate the structure of Iron Age and Roman era weaponry and garments. A combination of metals, organics, animal hides and fabrics, these artifacts exhibited striking contrast between each imaging technique. Comparing X-ray and neutron images, archaeologists were able to better document the construction methods and metalurgical technology available during the respective periods of human history [20]. Similarly, Rant *et al.* discussed the trend in archaeology to utilize neutron radiography facilities across Europe, conducting their investigations at the Jožef Stefan Institute (JSI) using their TRIGA nuclear reactor (TRIGA). They were able to distinguish the lead shot, gunpowder, and internal mechanisms of a 16^{th} century iron wheel lock pistol. Furthermore, the team captured organic internal fragments in an iron cross reliquary using neutron radiographs, not visible in the X-ray images [21].

As an engineering design tool, Hameed *et al.* used neutron imaging to analyze the penetration and distribution of stone strengtheners to be used in historic building restoration. In particular, the solid bodies created with nCT measured the ingress of actual consolidants into material samples of the time wethered edifice stones, prescribing a more effective concentration of consolidant for each application. The measurements

were conducted at the Atominstitut (ATI) with the ANATARES neutron imaging facility (ANTARES) [22, 23]. Using the imaging facilities at PSI, Lehmann *et al.* investigated bronze Tibetan Buddha statues from the 14^{th}, 15^{th} and 17^{th} centuries. A comparison between X-ray and neutron imaging techniques is shown in Figure 2.2, as described in Section 2.1.4. To avoid desecrating the religious and cultural artifacts, radiographic imaging provided an ideal method for exploring the internal components [24]. Similarly, Ryzewski *et al.* conducted neutron imaging experiments at CG-1D, imaging a Late Roman bronze lamp and dog statue. The team successfully verified the structural integrity of the metal body while also illuminating the existance of internal organic residue from burnt material [25].

Helium-3 and National Security

The detection and regulation of special nuclear materials (SNMs) presents a unique problem for law enforcement, noted Anderson *et al.*, due to the physics of the system. Because these materials may be hidden in large shipping containers, masked by other non-regulated materials, SNMs require significant effort to detect. Chemical and radiographic techniques, commonly employed to detect conventional weapons and hazardous materials, are much less effective in application to SNM. New systems are being investigated that utilize neutron imaging, or a complementary approach including X-rays, to create a picture of the hidden materials inside cargo, identifying not only their density, but chemical composition. Using car-wash style portal checkpoints for shipping trucks, many of the technologies propose scanning the containers with neutron beams, detecting the secondary radiation produced from the cargo to establish an idea of what materials are present. Rapid and accurate verification that SNM is not present is paramount to a successful system [1].

As the official steward of the U.S. nuclear stockpile and materials, the U.S. Department of Energy (DOE) is also responsible for production of helium-3. This particular isotope, while used in nuclear weapons, has played a critical role in radiation detection, particularly as a neutron sensitive isotope. Used in a wide variety of national security applications and sciences, ^{3}He was consumed at a rate of 70,000 L/yr. In the past decade, fears of dwindling ^{3}He reserves have led the DOE to seek alternatives where possible, reducing the annual consumption by an estimated 90 % and mitigating a premature shortage [26]. Used in large radiation portal monitors (RPMs), ^{3}He filled tubes account for a majority of the national consumption, as noted by Kouzes *et al.* Both the DOE and U.S. Department of Homeland Security (DHS) have stringent requirements for minimizing false radiation detection alarms, requiring heavily verified technologies.

Other direct alternatives, such as BF_3, pose a health risk and regulations limit the transport and utilization of the hazardous gas. Boron-10 lined proportional counters do not exhibit the same neutron detection efficiency as ^{3}He, while ^{6}Li loaded glass fibers do not meet the criterion for gamma-ray (γ-ray) insensitivity [28, 29]. Kouzes *et al.* revisited the issue in a follow-up report, documenting the continuing trend of ^{3}He consumption reduction and new developments in wide area neutron detection for national security. In this article, he expands the possibilities to scintillators and semiconductors, having improved in overall efficiency while becoming more available through improvements in fabrication and processing. He concludes that as

of 2015, "... there appears to be no existing alternative that combines all the capabilities of ^{3}He for neutron detection efficiency, gamma-neutron separation, commercial availability, and robustness for deployment" [27].

1.2 Aims and Objectives

The overall aim of the project was the following: design and build a functional, high-resolution neutron imager using a direct conversion semiconductor, exhibiting spatial resolution on par or better than current state-of-the-art technologies while operating under similar experimental conditions. This achievement introduces a new category of solid-state neutron detector, overcoming the cost and complexity restrictions of previous systems while offering a new platform for expanding the capabilities of neutron detection and imaging sciences. In evaluation of this promising neutron sensitive material, a set of objective criteria was established to confirm the success or failure of the investigation. The preliminary task required validating the neutron sensitivity of the material, demonstrating its basic functionality as a neutron detector. A single-channel counter was fabricated to capture neutron spectra, yielding information regarding spectroscopic capabilities, along with experiments using α's and γ-rays to study charge collection and the possibility of neutron/γ discrimination, respectively. Because the material had not been studied in the context of neutron detection in the past, fabrication techniques were developed to accommodate the material specific requirements for detector construction. Expanding on the success of a functional counter, a few-channel pixel detector was designed to serve as a proof of concept verifying the usage of LISe for neutron imaging. The dual-nature of the material was examined through scintillator experiments to evaluate performance metrics between both operational modes and potential energy loss mechanisms, producing inefficiencies within the material. In producing a scintillation response, the performance as a semiconductor may be degraded or sub-optimal in comparison to theoretical expectations. Encompassing the aim of this research, a final imaging system was constructed, integrating a high-resolution application specific integrated circuit (ASIC) to evaluate the material's performance in a direct comparison with other current neutron imaging platforms. The anticipated spatial resolution aimed to reach values less than the 55 µm pixel size of the Timepix v2 ASIC (Timepix).

1.3 Overview

This work documents the design, development and experimental evaluation of a novel neutron detection material. A literature review is presented in Chapter 2, beginning with an summary of radiation types, their interactions with matter and the fundamentals of neutron detection. The subsequent sections survey neutron detection and imaging technologies including scintillator, semiconductor and advanced hybrid systems. The material under study has demonstrated both scintillator and semiconductor capabilities, requiring evaluation along both design avenues to determine the extent of the material's capabilities. Prior materials studies

were also included as a framework for understanding electronic behavior and fabrication requirements. The experimental process is described in Chapter 3, covering preparation, implementation and data analysis. The chapter begins with fabrication procedures, establishing a routine for device construction. In progression, the next sections report the designs for the single channel counter, the multi-channel pixel detector, and the high-resolution imager. The chapter concludes with an outline of the neutron imaging experiments and the postliminary data processing methods. Chapter 4 presents the results of the study, comparing the two modes of operation with other state-of-the-art technologies. The performance of the system is qualified and any shortcomings due to experimental methods or design have been described. Final conclusions are drawn in Chapter 5, validating the goals and success of the investigation. Suggestions for improvements on experimental methods are offered along with suggestions for moving forward in future studies. A series of appendices have also been included for more thorough explanation of technical processes and methods.

1.4 Disclaimer

This document was compiled using the LaTeX typesetting system [30, 31]. Two custom packages were developed to support this document; *ProjectX* offers a large document structuring system as the base package, while *DissertationX* is a thesis and dissertation package following the formatting requirements designated by the University of Tennessee. These packages have been made available as open source tools (via GitHub), free to use by other students and authors in accordance with the GNU General Public License. The manuscript and associated works remain the sole property of the author under copyright law, with express permission granted to the University of Tennessee for publication.

Chapter 2

Literature Review

This chapter comprises an overview of prior work on LISe, including material studies evaluating its electrical and detection properties. Radiation fundamentals pertaining to neutron imaging are described as a foundation for the physical processes integral to the technology. Applicable studies in semiconducting and scintillating neutron detectors are discussed leading to a comparison of state-of-the-art imaging systems.

2.1 Radiation Detection

Neutron imaging is a contemporary subscience within the broader study of radiation detection. More generally, radiological imaging requires a deep understanding of the interactions between the various types of radiation and the materials with which they interact. This section describes the types of radiation encountered in radiological imaging experiments along with their interaction mechanisms.

2.1.1 Types of Radiation

The U.S. Nuclear Regulatory Commission (NRC) defines *radiation* as "energy given off by matter in the form of rays or high-speed particles" [32]. In the context of this research, radiation can be broken down into two categories, electromagnetic radiation and particle radiation. Some of the more common types of radiation are discussed below.

Electromagnetic Radiation

Electromagnetic radiation can be explained as waves in the electromagnetic field, carrying energy through a space or medium. These waves are interchangeably described by their frequency, wavelength or energy. While visible light falls in the middle of the electromagnetic spectrum, electromagnetic radiation, as discussed in nuclear engineering, typically lies along the shorter wavelength (higher energy) end of the spectrum. Because electromagnetic radiation exhibits wave-particle duality, it becomes useful to quantize a unit of

electromagnetic radiation. The term photon is used to define an elementary particle of zero rest mass, with a velocity defined by the speed of light in a vacuum [33].

At the middle of the spectrum, visible light ranges from wavelengths of around 750 nm (red) to 380 nm (violet), corresponding to photon energies between 1.65 eV and 3.26 eV. The ultraviolet radiation threshold is crossed at a wavelength of 400 nm (3.1 eV) and increases in energy to a wavelength of 10 nm (124 eV). X-rays span the wavelengths between 10 nm down to 0.01 nm, possessing enough energy to ionize atoms (100 eV-100 keV), through interactions with orbital electrons. Higher energy photons (typically >100 keV) are conventionally termed γ-rays. The generally accepted trend defines the type of radiation based on generation source, with X-rays stemming from electron interactions and gammas from atomic nuclei interactions (thus higher energies) [34].

Alpha Particles

α's are a type of ionizing radiation, akin to a $^4_2$He nucleus stripped of its orbital electrons, consisting of two neutrons and two protons. Naturally occurring radioactive materials (NORMs) emit α's as a form of decay and include isotopes of uranium, thorium and radium. Because of their large size and +2 electronic charge, α's tend to travel the shortest distances. Alpha particles can generally be stopped by a normal sheet of paper, human skin (epidermis), or a few inches of atmospheric air [35].

Beta Particles

Beta particles (β's) are a type of ionizing radiation, corresponding to a high-speed, high-energy electrons (beta minus particles) or positrons (beta plus particles). This type of radiation is capable of increased penetration depths, maintaining a charge of ± 1 and a relative mass roughly 3 orders of magnitude smaller than a proton. While β radiation may penetrate human skin, this type of radiation typically requires only a thin layer of metal, plastic, or any other dense material to stop particles [35].

Neutrons

Free neutrons are short lived particles (half-life of 636.6 ± 9.6 s) emitted from atomic nuclear interactions, with a mass slightly larger than a proton [36]. Unlike the other forms of radiation, neutrons do not possess an electric charge, predominately interacting with the nucleus of target atoms or molecules. For this reason, they penetrate much deeper than other types of particle radiation, requiring multiple collisions to slow down and stop a neutron. Typically, hydrogenous materials are used to moderate, or slow down neutrons, reducing their kinetic energy [37].

Neutrons are often categorized into energy ranges, based on their interaction characteristics and source of generation. Fast neutrons are born from nuclear reactions with energies ranging from 1.0 MeV to 20.0 MeV [38]. These energies are characteristic of neutrons created during fission reactions in nuclear reactors. Between energies ranging from 1.0 eV to 1.0 MeV, multiple sub-ranges are defined, typically useful in reactor

engineering. In context of neutron imaging, cadmium neutrons are those with energies between 0.4 eV to 0.5 eV, and strongly absorbed by the isotope ^{113}Cd. Thermal neutrons have an energy ranging from 0.025 eV to 1.0 eV, with the thermal energy of 0.025 eV defined as the most probable energy along a Maxwellian distribution for a particle in equilibrium with an environment at 290 K [38].

As a neutron undergoes a series of collisions, it loses kinetic energy, finally arriving close to the thermal neutron energy. Typically, isotopes have an exponentially larger probability of interaction with thermal neutrons, leading to the neutron's removal from most systems once they reach thermal energy. Cold neutrons, those with energy less than 0.025 eV, are generated in specially engineered systems. To lower the neutron energy beyond the thermal energy, cold neutron sources utilize substances such as liquid deuterium at temperatures around 20 K, further scattering the neutrons without absorbing them [39–41]. The production of low energy cold neutrons accordingly maximizes the neutron wavelength, enhancing resolution in neutron imaging systems.

2.1.2 Neutron Interactions

Radiation detection is predicated on the interaction of radiation with engineering materials. When the target material absorbs or scatters the incident radiation, the reaction yields a characteristic energy signature. A well designed neutron detection system accounts for the various probabilistic reactions in a given radiation environment and utilizes these energy signatures to produce quantifiable radiation statistics.

Cross Sections

In the context of radiation interactions with materials, the term cross section describes the probability that a given type of radiation, will interact with a target particle. Furthermore, nuclear cross sections, $\sigma(E)$, are given as an area, indicating the relative size of a target nucleus to a radiation particle with an energy, E. The cross section value may be given in standard metric units of cm^2 or in the the colloquial unit of barns used in nuclear engineering, with 1 b $= 10^{-24}$ cm^2, representing a significantly large cross section. The total cross section, σ_{tot}, is the summation of the scattering, σ_{scat}, and absorption, σ_{abs}, cross sections, shown in eq. (1).

$$\sigma_{tot} = \sigma_{scat} + \sigma_{abs} \tag{1}$$

In a scattering interaction, eq. (2), the incident radiation is emitted as a byproduct at the same energy for elastic scattering, σ_e, or at a lower energy for inelastic scattering, σ_i.

$$\sigma_{scat} = \sigma_e + \sigma_i \tag{2}$$

Inelastic collisions will impart some of the energy from the incident particle to the target nucleus, leaving it in an excited state. The nucleus may release radiation directly or through nuclear decay as it drops back to

its lower energy ground state. The absorption cross section, σ_{abs}, consists of more terms, varying with the target nucleus as described in eq. (3).

$$\sigma_{abs} = \sigma_\gamma + \sigma_f + \sigma_p + \sigma_\alpha + \dots \tag{3}$$

Radiative capture, σ_γ, occurs when the incident particle is absorbed by the target nucleus, emitting one or more photons, typically in the gamma energy range. In fissionable isotopes, the fission cross section, σ_f, describes events where the incident particle is absorbed, producing one or more neutron emissions following the decay of the target nucleus. Particle emission cross sections are designated by their daughter particle such as the proton emission cross section, σ_p, and the alpha particle emission cross section, σ_α. When all the cross sections are considered, the total cross section for a given isotope may be expressed by its constituents as shown in eq. (4).

$$\sigma_{tot} = \sigma_e + \sigma_i + \sigma_\gamma + \sigma_f + \sigma_p + \sigma_\alpha + \dots \tag{4}$$

The microscopic cross sections, σ, are useful in describing the probability of interaction with a single target nucleus. When describing bulk materials, the macroscopic cross section, Σ, is used to evaluate the probability per unit path length a reaction will occur. For a pure, uniform material of microscopic cross section, σ_{tot}, and atomic number density, N, the total macroscopic cross section, Σ_{tot}, will be given by eq. (5).

$$\Sigma_{tot} = N\sigma_{tot} \tag{5}$$

For mixed materials, the macroscopic cross section will account for stoichiometric variations, using the molecular number density and the appropriate microscopic cross sections for the included isotopes.

Attenuation

A radiation source flux describes the number of particles passing through a unit surface area per unit time. Neutron flux is often designated as, ϕ, given in units of $(\mathrm{n/cm^2 \cdot s})$, and includes neutrons passing through the area in all directions. For neutron beams of approximately monodirectional source flux, the intensity, $I(x)$, quantifies the neutron flux along the beam axis. As the neutron beam front passes through an interacting material of differential thickness, dx, the intensity will attenuate, or gradually decrease, proportional to the total macroscopic interaction cross section, Σ_{tot}, as given by eq. (6).

$$-dI(x) = \Sigma_{tot} I(x) dx \tag{6}$$

With the change in intensity given by, $dI(x)$, this equation captures the neutron removal rate at any linear position, x, in the uniform attenuating material. For a thin, absorbing material, with a small target area, neutrons are assumed to either pass straight through, or interact corresponding to one of the cross sections,

removing them from the incident beam, I_0. Using the material thickness as the path distance, x, the total beam attenuation can be found by integrating eq. (6). The resulting intensity of the exiting beam is given as, $I(x)$, and the transmission fraction, I/I_0, is given by eq. (7).

$$I(x) = I_0 \cdot \exp\left(-\Sigma_{tot} \cdot x\right)$$

$$\frac{I}{I_0} = \exp\left(-\Sigma_{tot} \cdot x\right) \tag{7}$$

Furthermore, the transmission fraction indicates the probability that a neutron will pass through an attenuating material of thickness, x. Along the same lines, the total macroscopic cross section also dictates the mean free path, λ, of the neutron, shown in eq. (8).

$$\lambda = \frac{1}{\Sigma_{tot}} \tag{8}$$

The mean free path (MFP) represents the average linear distance a neutron may travel through the attenuating material before a collision removes the neutron. This parameter is useful when designing detection systems, specifying a required thickness of material to capture the anticipated radiation source. More generally, radiation cross sections are a function of the incident radiation energy, creating energy dependent forms of the equations derived in this section. For practical analysis, cross sections are often averaged across a range of energies, mentioned in Section 2.1.1, binning together particles of approximately equivalent behavior in the system.

Reaction Q-Value

Nuclear reactions are defined in a similar manner as their chemical analogs. Each reaction is characterized by a set of parent species, and their resulting daughter products. In a nuclear reaction, the reacting species include the two nuclei or nucleons, one being the target nucleus, a, and the other being the incident radiation particle, b. Ternary reactions occur with such low probability, due to the speed at which reactions occur, and are only considered in special applications. The resulting daughter products include a combination of two or more nuclei, nucleons or photons, denoted c and d. The shorthand for a nuclear reaction is written as $a(b,d)c$ where the corresponding full reaction is shown in eq. (9) [42].

$$a + b \rightarrow c + d \tag{9}$$

Nuclear reactions abide by a set of physical conservation laws summarized by the following: conservation of nucleons, conservation of charge, conservation of momentum, and conservation of energy. Conservation of nucleons requires the total number of protons and neutrons be the same before and after the reaction, although the number of each nucleon type, protons or neutrons, may change. Conservation of charge requires

the total charge from positive and negative carries to be maintained across the reaction, typically balanced at zero, or neutral charge. The conservation of momentum and conservation of energy are implemented to develop an expression for the nuclear reaction Q-value as it relates to the kinetic energy of the daughter products. The momentum of a non-zero mass particle can be described in terms of wavelength, λ, and Planck's constant, h. Alternatively, the momentum may be represented using the mass of the particle, m, and its speed, v, with both forms shown in eq. (10).

$$\frac{h}{\lambda} = p = mv \tag{10}$$

Using a frame of reference where the target, a, is stationary, and assuming the incident particle, b, has negligible kinetic energy, the total momentum before the reaction is approximately zero. Conservation of momentum requires that the total momentum after the reaction also be approximately zero, indicated by eq. (11).

$$p_a + p_b = 0 = p_c + p_d \tag{11}$$

When the two non-zero mass products are generated at the reaction site, they are emitted in opposite directions with velocities inversely proportional to their mass, following eq. (12b), to fulfill the conservation of momentum law.

$$p_c = p_d \tag{12a}$$

$$m_c v_c = m_d v_d \tag{12b}$$

The next step rewrites the conservation of momentum in terms of particle energy. The energy, E, of a particle is related to its mass, m, using the speed of light, c, as given by the eq. (13a). For a non-relativistic particle, the energy is given by eq. (13b), using the rest mass, m_0, and speed, v, where, $v \ll c$.

$$E = mc^2 \tag{13a}$$

$$E = \frac{1}{2} m_0 v^2 \tag{13b}$$

Combing eq. (10) and eq. (13b), the non-relativistic momentum of each daughter product can be written in terms of kinetic energy, shown in eq. (14).

$$v = \sqrt{\frac{2E}{m_0}}$$

$$p = \sqrt{2m_0 E} \tag{14}$$

Following the momentum balance given in eq. (12a), the final conservation of momentum equation can be written in terms of kinetic energy in eq. (15).

$$\sqrt{2m_cE_c} = \sqrt{2m_dE_d} \tag{15}$$

The conservation of energy relationship, given by eq. (16), dictates the total kinetic energy imparted to the daughter products is equivalent to the Q-value for the reaction.

$$E_c + E_d = Q \tag{16}$$

Simultaneously solving eq. (15) and eq. (16) will yield the kinetic energies of the emitted daughter products in the nuclear reaction. The Q-value for the reaction comes from the mass balance between the parent and daughter species. Using the rest mass energy from eq. (13a), the total energy conservation equation for the reaction can be written as eq. (17).

$$E_a + m_ac^2 + E_b + m_bc^2 = E_c + m_cc^2 + E_d + m_dc^2 \tag{17}$$

Rewriting the equation, the change in kinetic energy is produced from the change in rest mass, illustrated in eq. (18).

$$(E_c + E_d) - (E_a + E_b) = [(m_c + m_d) - (m_a + m_b)]c^2 \tag{18}$$

The mass of an isotope is slightly less than the sum of the mass of its individual constituent nucleons, known as the mass defect. When these individual nucleons bind into larger nuclei, a portion of the mass is converted into binding energy, providing the force that holds the nucleus together. The mass defect, or binding energy, accounts for the change in total mass between the parent and daughter nuclei, defining for the Q-value for a particular nuclear reaction as in eq. (19).

$$Q = [(m_c + m_d) - (m_a + m_b)]c^2 \tag{19}$$

Using eq. (18) and eq. (19) it can be shown that eq. (16) will be the result when the parents are assumed stationary. These equations show the origin of the Q-value and its relation to the kinetic energy of daughter products in a nuclear reaction.

2.1.3 Neutron Sensitive Isotopes

Isotopes with large interaction cross sections are useful in neutron detection. Because neutrons do not interact with charge carriers directly, the incident radiation must first react with a nucleus before it can produce an observable signal. The resultant daughter products offer a means of sensing the neutron interactions,

generating directly observable photons or charge carriers. The following isotopes play an important role in neutron detection and/or imaging, each offering a range of benefits and restrictions based on intended application.

Helium-3

Helium is the second lightest element and non-reactive as a noble gas. The isotope ^{3}He has a very low natural abundance of 0.000134 %, as its low mass allows any free atoms to boil off in the atmosphere [43]. Aside from natural ^{3}He sources, terrestrial production primarily stems from beta minus particle (β^-) decay of stored tritium, produced for the nuclear weapons industry [44]. The ^{3}He neutron reaction, $^3\mathrm{He}(n,p)^3\mathrm{H}$, is shown below in eq. (20).

$$\begin{array}{cc} & \underline{Q\text{-value}} \\ {}^3_2\mathrm{He} + n \rightarrow {}^3_1\mathrm{H} + p & 0.764\,\mathrm{MeV} \end{array} \tag{20}$$

$$E_T = 0.191\,\mathrm{MeV} \qquad E_p = 0.573\,\mathrm{MeV}$$

The isotope's interaction probability follows an almost ideal $1/v$ trend, with the cross section following an inverse relationship with the particle velocity (see Figure D.1). With a large thermal cross section of 5,333 b, gaseous ^{3}He is commonly used as a neutron conversion gas in Geiger-Müller (G-M) tubes and proportional counters [45, 46]. This isotope is typically used in portal monitors where prior applications aimed to scale up the technology for national security, detecting the proliferated nuclear materials. With the decline of active tritium production and total stockpile, the availability of ^{3}He has been limited, requiring other isotopes as replacement for mass scale neutron detection [26, 27].

Lithium-6

Lithium is the lightest solid metal compound, readily available in natural and enriched forms. The isotope ^{6}Li only accounts for a small fraction of the natural lithium, 7.59 %, and was stockpiled in its enriched form by major nuclear powers across the globe for their nuclear defense industries [45]. This isotope may be converted to tritium through neutron bombardment, useful in general tritium production as well as in thermonuclear weapons to enhance the fusion process [47]. For the same reason, the 940 b thermal cross section of ^{6}Li serves a more benign utility in neutron detection [45]. Following a smooth $1/v$ curve, similar to ^{3}He, lithium is best suited to detect cold and thermal energy neutrons (see Figure D.2). Compared to the other isotopes, the neutron reaction produces a larger Q-value with the daughter nuclei proceeding along a single branch to the ground state, shown in eq. (21).

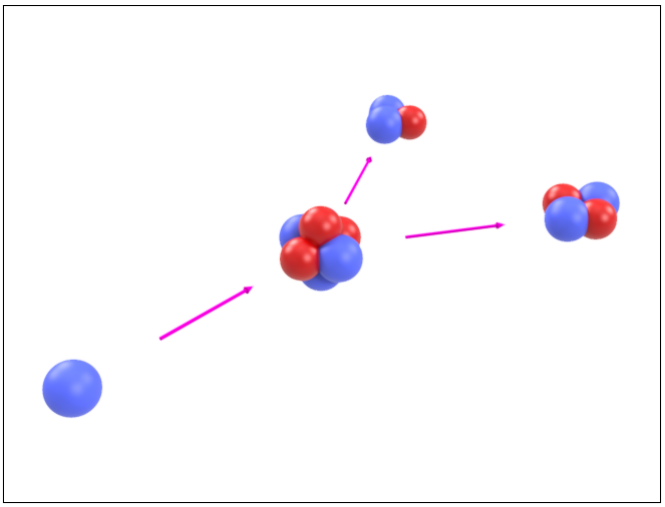


Figure 2.1. The $^{6}\mathrm{Li}(n,\alpha)^{3}\mathrm{H}$ reaction utilized in the LISe neutron detector.

$$\begin{array}{cc} & \underline{Q\text{-value}} \\ {}^{6}_{3}\mathrm{Li} + n \rightarrow {}^{3}_{1}\mathrm{H} + \alpha & 4.780\,\mathrm{MeV} \end{array} \tag{21}$$

$$E_T = 2.73\,\mathrm{MeV} \qquad E_\alpha = 2.05\,\mathrm{MeV}$$

These characteristics of the lithium reaction produce a large, fixed energy pulse when a neutron is intercepted. As the paramount neutron interaction in this research, the $^{6}\mathrm{Li}(n,\alpha)^{3}\mathrm{H}$ reaction has been graphically illustrated in Figure 2.1. The incident neutron (shown in blue) collides with the ^{6}Li nucleus consisting of 3 neutrons and 3 protons (shown in red). The neutron and ^{6}Li briefly form an unstable nucleus, then split into two daughter products, an α and a triton (T). Before this research, ^{6}Li was utilized in scintillator detectors or as a conversion layer in semiconductor neutron imaging systems. The isotope has been manufactured in plastic, crystal, glass and liquid scintillators. As a conversion layer, the isotope is mixed into a thin film coating, transmuted by the neutron into the α and T pair for detection in a subsequent charge particle detector.

Boron-10

The most common isotope for slow neutron absorption, ^{10}B is commonly integrated into nuclear reactor systems for neutron moderation. In solid form, borosillicate control rods are strategically placed throughout the core matrix, while boric acid is dissolved in reactor cooling water to control neutron flux. With a large thermal cross section of 3,840 b, and significant natural abbundance of 19.9 %, this isotope also makes an effective low energy neutron counter [45]. Following the $1/v$ trend (see Figure D.3), neutrons react with ^{10}B following one of two $^{10}\mathrm{B}(n,\alpha)^{7}\mathrm{Li}$ reactions, shown in eq. (22).

$$\begin{aligned} & & & Q\text{-value} & \\ {}^{10}_{5}\mathrm{B} + n &\rightarrow {}^{7}_{3}\mathrm{Li} + \alpha & & 2.792\,\mathrm{MeV} & \text{(22a)} \\ {}^{10}_{5}\mathrm{B} + n &\rightarrow {}^{7}_{3}\mathrm{Li}^{*} + \alpha & & 2.310\,\mathrm{MeV} & \text{(22b)} \\ {}^{7}_{3}\mathrm{Li}^{*} &\rightarrow {}^{7}_{3}\mathrm{Li} + \gamma(480\,\mathrm{keV}) & & (\mathrm{IT}) & \text{(22c)} \end{aligned}$$

$$E_{^{7}\mathrm{Li}} = 0.84\,\mathrm{MeV} \qquad E_{\alpha} = 1.47\,\mathrm{MeV}$$

Only about 6 % of reactions branch to the ground state, releasing the full Q-value for the reaction, while the remaining 94 % of neutrons produce an excited $^{7}\mathrm{Li}^{*}$ nucleus [35]. The smaller Q-value will generate the primary detection peak in proportional counters such as BF_3 gaseous detectors. The ^{10}B enriched gas offers a high molecular density of the neutron sensitive isotope while performing well as a proportional gas. Because the daughter products may travel around 1 cm in the proportional gas, there is a chance one or both of the particles may impact the wall, depositing only a portion of their energy in the gas. Termed the "wall effect", the resulting spectrum will contain two broad continuum across lower energies, with drop off energies corresponding to the kinetic energy of the daughter products. Furthermore, these detectors become susceptible to interference from γ-rays interacting with the tube wall. Gamma-rays scattering into the tube generate electrons which ionize the proportional gas, resulting in non-neutron energy counts. As the flux increases, the resulting counts increase in energy, potentially contaminating the neutron signature.

As with lithium, ^{10}B may be integrated into scintillating devices, offering enhanced signal response time. Used in neutron TOF measurements, conversion layers incorporating ^{10}B provide scintillation light in response to neutrons, but are limited in thickness, and thus overall efficiency, by self attenuation [35]. Plastic scintillators offer increased ^{10}B concentration and response time, but suffer from increased gamma sensitivity as the secondary electrons may overwhelm the response of the reaction products.

Cadmium-113

Cadmium is a heavy metal used in nuclear engineering for its large cross section in the thermal energy regions. The isotope ^{113}Cd is one of 8 naturally occurring isotopes, with a natural abundance of 12.22 % [45]. This isotope follows the $1/v$ trend until a dramatic drop off for energies exceeding ∼1.0 eV (see Figure D.4). Common with heavier elements, ^{113}Cd exhibits a resonance region featuring large, narrow peaks, with the principal resonance peak occurring at 0.178 eV. The $^{113}\mathrm{Cd}(n,\gamma)^{114}\mathrm{Cd}$ reaction produces an excited intermediate state, before deenergizing via γ-ray cascade, as shown in eq. (23) [48, 49].

$$\begin{aligned} & & Q\text{-value} & \\ {}^{113}_{48}\mathrm{Cd} + n \rightarrow {}^{114}_{48}\mathrm{Cd}^{*} \rightarrow {}^{114}_{48}\mathrm{Cd} + \gamma & & 9.043\,\mathrm{MeV} & \text{(23)} \end{aligned}$$

The large Q-value from the sum of γ-ray emissions makes this isotope an effective neutron detector for thermal neutrons. Because the initial reaction produces γ-rays instead of charged particles, more sophisticated detector designs are required. The γ-rays must be slowed through nuclear interactions, leading to the production of secondary electrons or scintillation light for detection.

Cadmium, a known carcinogen in humans, poses health risks targeting organs in the renal and cardiovascular systems. The metal may also lead to bone damage, weaken the immune system and increase the rate of reproductive complications [50]. The modern electronics industry has increased the use of cadmium in compounds such as CdSe and CdTe, which have the potential to increase the exposure rate to workers as well as the general public [51].

Gadolinium

Gadolinium, a heavy metal lanthanide, possesses the largest cross sections of any element. Out of the 6 stable isotopes of gadolinium, the isotopes ^{155}Gd and ^{157}Gd exhibit the largest neutron cross sections of 65,000 b and 255,000 b, respectively [45]. These two isotopes occur at 14.80 % and 15.65 % natural abundance, respectively. Similar to ^{113}Cd, these two isotopes of gadolinium also follow the $1/v$ trend with a large drop off between 0.1 eV to 1.0 eV preceding the resonance region (see Figures D.5 and D.6). As with many of the heavier elements, gadolinium favors γ-ray production in response to neutrons. The $^{155}\mathrm{Gd}(n,\gamma)^{156}\mathrm{Gd}$ reaction is shown in eq. (24), resulting in γ-ray production yielding a large Q-value.

$$\begin{array}{ll} & \underline{\quad Q\text{-value}\quad} \\ {}^{155}_{64}\mathrm{Gd} + n \rightarrow {}^{156}_{64}\mathrm{Gd} + \gamma & 8.5\,\mathrm{MeV} \end{array} \tag{24}$$

Having a larger neutron cross section, ^{157}Gd is commonly used in enriched material, interacting with neutrons following the $^{157}\mathrm{Gd}(n,\gamma)^{158}\mathrm{Gd}$ reaction shown in eq. (25).

$$\begin{array}{ll} & \underline{\quad Q\text{-value}\quad} \\ {}^{157}_{64}\mathrm{Gd} + n \rightarrow {}^{158}_{64}\mathrm{Gd} + \gamma & 7.9\,\mathrm{MeV} \end{array} \tag{25}$$

Gadolinium contrasting agents are utilized in magnetic resonance imaging (MRI), generally considered to be safe in small doses, and are a warranted risk compared to the underlying ailment. However, for patients recieving multiple MRIs, an increase in free Gd^{3+} ion concentration may lead to toxic effects in multiple biological systems [52, 53].

2.1.4 Radiography

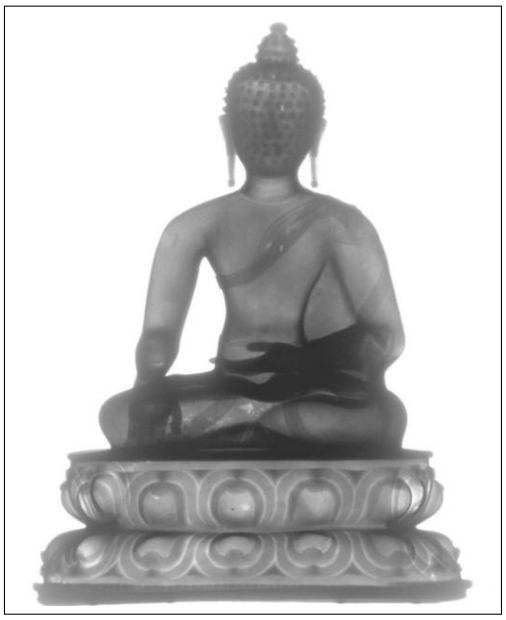
The NRC defines *radiography* as "The use of sealed sources of ionizing radiation for nondestructive examination of the structure of materials" [32]. The first radiographs were produced by the German physicist

Wilhelm Röntgen, on November 8, 1895 [38]. Röntgen was experimenting with a Crookes-Hittorf tube, a relatively new technology at the time, studying the fluorescent response produced by the energetic cathode rays. Unbeknownst to him, the electrons formed in the vacuum had enough energy to produce X-rays as they impinged on the glass surface. He discovered this phenomenon after observing a luminescent effect on a barium platinocyanide coated screen across the room from the opaque vacuum tube. Shortly after witnessing an image of his own skeleton on the screen during experimentation, he captured the first X-ray radiograph of his wife's hand; thus the field of radiography was formed [54].

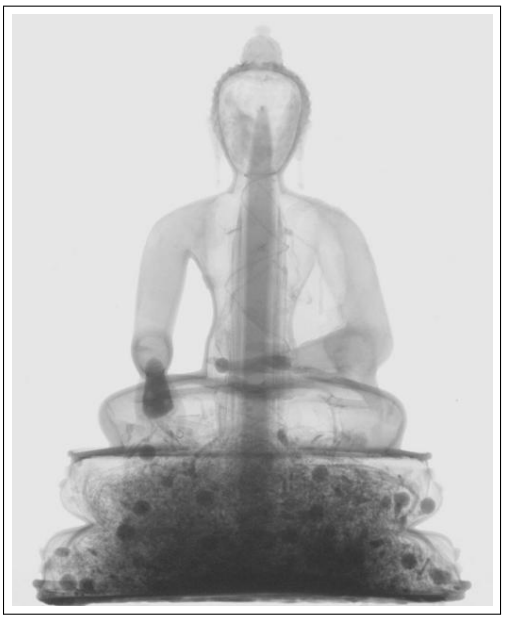
While modern radiography uses more advanced technology than Röntegn's experiments, the premise remains the same. A controlled source emits radiation on an absorbing material, the incident beam is attenuated and the transmitted beam is recorded via imaging detector. Originally developed for X-ray applications, radiography may be extended to other forms of radiation as a set of NDT techniques. It wasn't until the 1960's when the burgeoning nuclear industry prompted the advancement of neutron detection and radiography [55, 56].

Neutron and X-ray imaging are complementary techniques, revealing distinct internal material structures as shown in Figure 2.2. The absorption cross section for X-rays increases proportional to the atomic number, Z, of the target material, with low-Z elements appearing more transparent and high-Z elements more opaque [58]. Bone has a high calcium content, with a larger Z value than other components of the human body, thus X-rays are commonly used in medical imaging of skeletal systems. In contrast, neutron absorption cross sections vary across elements and even isotopes. The average energy lost by a neutron undergoing elastic scattering is maximized for low atomic weights. A neutron colliding with hydrogen will have an average energy loss of roughly 1/2 the incident kinetic energy. Biological samples tend to concentrate hydrogen, attributed to water content, making neutrons suitable for imaging biological samples. In engineering systems, neutron imaging may be used to detect hydrogen gas trapped in defect sites or contrast hydrocarbons from the surrounding mechanical structures.

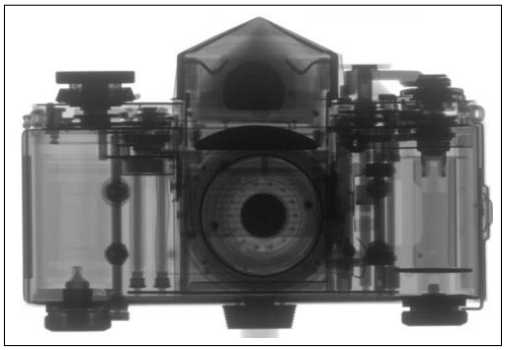
Significant contributions to the advancement of radiographic imaging have been accomplished at PSI [57]. The metallic Buddha statue offers a clear example of the different capabilities for each imaging technique. The X-ray image shown in Figure 2.2a captures the details corresponding to the metallic shell, consisting of heavy elements. The internal structure of the statue is revealed in the neutron image (Figure 2.2b), showing a wooden support beam in the center, surrounded by organic plant matter such as flowers and buds. As a ritualistic artifact, opening or adulterating the statue would defile the object, a restriction overcome using neutron imaging [24]. Similarly, the analog camera shown in Figure 2.2c, reveals metal pins, knobs and mechanical components in the lens focal stage. In the neutron image (Figure 2.2d), the photographic film, consisting of a plastic strip coated in gelatin emulsion is highly visible. Also visible are plastic components, such as the receiving film cartridge, and some glass components including the lens and viewing optics.



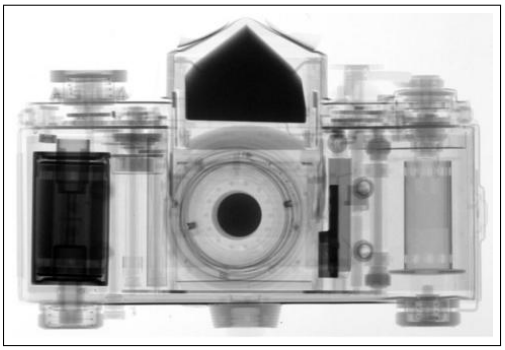
(a) metallic statue X-ray image



(b) metallic statue neutron image



(c) film camera X-ray image



(d) film camera neutron image

Figure 2.2. Complementary transmission radiographs captured using X-ray and neutron radiation (radiographs courtesy: Paul Scherrer Institut) [24, 57].

2.2 Scintillator Detectors

Scintillation materials for neutron detection have been studied since the discovery of the neutron. The physical phenomena of scintillation occurs in response to excitation from a radiation source (see Section 2.1.1), generating photons characteristic of the scintillation material. When light is promptly generated with respect to the excitation event (nanoseconds), the process is known as fluorescence, typically producing visible spectrum light. If the light output is delayed, the process is termed phosphorescence, yielding light with a longer wavelength and lower energy than fluorescent reactions. The phosphorescence in some materials may release absorbed radiation energy for hours after the initial exposure. A chemical compound responsible for fluorescence is termed a fluorophore, while the more general term, phosphor, includes compounds producing either form of luminescence. In the discussion of scintillation materials, highly luminous fluorescent materials are desirable, producing a large amount of light in rapid response to excitation from radiation. Phosphorescence should be minimized through the chemical makeup to limit the amount of delayed light output, effectively creating signal noise long after the radiation event transpired [35].

2.2.1 Glasses

Glass scintillators offered some of the earliest forms of neutron detection. Lithium and boron based silicate glasses utilize experience derived from centuries of usage, more readily available than many of the polymers today. Though manufacture requires high temperatures to melt and form the glass (>500 °C), the resulting material properties offer favorable characteristics for challenging environments. Often transparent, glasses allow scintillation light to pass through the bulk, in may cases with a quick response time (<100 ns).

In 1959, Bollinger *et al.* noted a lack of suitable thermal neutron detectors for TOF spectroscopy. Two glass scintillators containing boron were reported: the Type GL-55 with composition $Na_2O : B_2O_3 : Al_2O_3 : Ce_2O_3$ at a ratio of (1:3:1.3:0.1) and the Type GL-127 with composition $Na_2O : B_2O_3 : SiO_2 : Al_2O_3 : Ce_2O_3$ at a ratio of (1:1:1.5:1.3:0.1). The decay time constants for the glass were measured to be 0.045, 0.2 and 10 µs 1959. Firk *et al.* presented the results of $Li_2O : SiO_2 : Al_2O_3 : Ce_2O_3$ at a ratio of (0.355:0.075:0.02:0.55) enriched to 95 % ^{6}Li. The glass demonstrated excellent time resolution and better neutron/γ-ray sensitivity over boron-loaded glasses at the time [56].

Katagiri *et al.* tested a Ce^{3+} doped (1 mol %) scintillating glass consisting of $^6Li^{11}BP$ at a composition of 45, 20 and 35 wt.%. The $4 \times 5 \times 1\,mm^3$ sample demonstrated 63.3 % thermal neutron efficiency [59]. Mizukami *et al.* sought to expand the acquisition rate of lithium-loaded glass scintillators for high rate TOF spectroscopy. They coupled an array of 8×8 glass scintillators to a photomultiplier tube (PMT) operating with 64 discrete channels. In this way, the combined counts from each channel would be able to surpass the saturation limited count rate from a single larger scintillator. For this configuration, a total detector count rate of 15.4 Mcps (8.3 Mcps/cm^2) was achievable in a thermal neutron beam [60].

Ishii *et al.* synthesized 5 mixture ratios of B_2O_3/Li_2O glass (66 wt.% to 90 wt.% B_2O_3). To enhance

light output, 6 recipes for CeO_2 doping were used, maxing out at 12.8 mol %. While they reported a light yield (LY) of only 9.2 %, compared to Bicron GS20 lithium glass, they demonstrated a much fast decay constant of 45 ns [61]. Matsumoto *et al.* designed a miniature neutron detector using lithium-6 glass for active neutron field monitoring of inaccessible locations, such as inside a graphite pile. The inner ^{6}Li-glass scintillator, a cylinder of 1 mm diameter by 2 mm long is coupled to a 1 mm optical fiber, embedded in the end of the scintillator. To reduce the interference from γ-ray, the original system was wrapped in 40 µm of Al, and placed inside a hollowed CsI(Tl) scintillator. The outer shell of CsI(Tl) serves as a γ-ray detector, with the aluminum layer optically decoupling the shell from the inner ^{6}Li glass. The small unit is designed to accurately measure neutron dose, overcoming the extensive time requirements of other methods, such as foil activation and subsequent neutron activation analysis (NAA) [62]. Ban *et al.* used a lithium glass stack to increase the peak separation between ultra-cold neutrons (UCNs) and γ-rays. The top layer in the stack consisted of 100 µm GS3 glass (0.01 % ^{6}Li) while the bottom layer, also 100 µm thick, consisted of GS20 glass (95 % ^{6}Li). The resulting stack was senstive to UCNs with velocities as low as 4 m/s [63].

Park *et al.* tested a gadolinium and boron-loaded silicate glass, doped with Ce^{3+} to enhance luminescence. The glass was varied across compositions conforming to a $25\,Gd_2O_3 : 10\,CaO : 10\,SiO_2 : (B_2O_3)_{55-x} : (CeF_3)_x$ recipe with doping ranging from 0.05 mol % to 2.5 mol % Ce^{3+}. The absorption spectrum for the glass varied between 330 nm to 440 nm with Ce^{3+} concentration exhibiting an emission peak at 380 nm. The experimental decay time constant was evaluated at 36 ns at the 0.15 % mol Ce^{3+} [64].

2.2.2 Plastics

Plastic scintillation materials incorporate a broad range of polymers, loaded with neutron sensitive isotopes. The fluorescent component, also called a 'fluor' in historical convention, is embedded in the polymer matrix. By carefully selecting appropriate base polymers and additives, the compound may be engineered to produce a visibly transparent material, increasing LY. Plastic scintillators are also desirable for their rapid signal generation time (few nanoseconds) as well as malleability. Thermoplastics offer the widest variety of shapes and sizes in comparison to glasses and other ceramics. Some of the polymer bases most commonly used in scintillator complexes include: poly(methyl methacrylate) (PMMA), polyvinyl toluene (PVT) and polystyrene (PS).

Lithium-Loaded Plastics

Breukers *et al.* described a novel PS scintillator incorporating lithium methacrylate (LiME) for neutron detection, with poly(*p*-phenylene oxide) (PPO) as a wavelength-shifting (WLS) additive. Up to this study, ^{6}Li scintillators were primarily developed as glasses and ceramics (powders or crystals). The desire to combine the higher thermal neutron cross section for ^{6}Li and fast response time (3 ns as tested) of plastic scintillators motivated the project. Furthermore, a bulk plastic scintillator containing ^{6}Li offers a larger Q-value

(almost double) over comparable ^{10}B plastics, without the associated γ-ray produced in the more probable $^{10}B(n,\alpha)^{7}Li$ reaction branch. They were able to successfully incorporate 0.63 wt.% ^{6}Li in the scintillator [65]. Cherepy *et al.* tested two carboxylates for separate use in γ-ray detection and neutron detection, both having high solubility in PVT. The first material, bismuth pivalate measured a LY of 5,000 photons/MeV at 15 wt.% bismuth loading. The second material, lithium pivalate was able to maintain transparency with up to 1.9 wt.% lithium, with a 98 % thermal neutron capture efficiency at a thickness of 3.75 mm. Coating the bismuth pivalate plastic in 200 µm of LiF/ZnS produced a photon sandwich (phoswich) detector. The fast γ-ray detection (2 ns) and slower neutron detection (200 ns), allowed the use of a single PMT by implementing pulse shape discrimination (PSD) [66].

Mabe *et al.* provided a method for creating a transparent film containing 2.96 wt.% of ^{6}Li. The polymer VPPO was selected, integrating all components of the scintillator mixture directly in the matrix polymer chain, instead of additives commonly used in other mixtures. They reported a decrease in LY for charged particles while demonstrating improved neutron/γ-ray discrimination [67]. Mabe *et al.* later investigated two ^{6}Li-loaded non-aromatic monomers, using them to introduce the lithium component into aromatic polymers (PS or PVT) through copolymerization, adding the potential for PSD. Of the two chemicals, lithium salicylate (LiSal) was deemed the most favorable over the more difficult to synthesize lithium phenylsalicylate (LiPSA). Lithium-6 was introduced into the polymer chain as anhydrous ^{6}LiOH. The final result quantified the upper limit of 0.40 wt.% for ^{6}Li in LiSal, exhibiting a relative LY from 55(3) % to 70(4) % in comparison to a pure PS matrix. [68].

Boron-Loaded Plastics

Normand *et al.* presented a 5 wt.% boron-loaded PS scintillator for neutron detection. This proprietary mixture reduced the material cost by a factor of 4 compared to the Bicron BC454 plastic scintillator with similar boron content. Cylindrically shaped, the samples measured 15 cm long by 4 cm in diameter, with the proprietary material demonstrating equivalent or superior performance over the Bicron scintillator [69]. Pawełczak *et al.* presented a boron-loaded palstic scintillator using PSD to detect thermal neutrons. The scintillators were 2.5 cm diameter by 1 cm thickness, composed of PPO (28 %) in PVT or PS, with *m*--carborane supplying the boron component. The samples tested possessed 0.06, 0.11, 0.3 and 0.74 wt.% concentration of ^{10}B with the highest concentration simulated at 84 % detection efficiency using a thickness of 1 cm [70]. Mahl *et al.* fabricated a series of plastic scintillators using bis(pinacolato)diboron (B_2Pin_2) and PVT as the primary base with varying amounts of PPO to balance the mixture. As a source of ^{10}B, the B_2Pin_2 additive ($0.50/g) offered a lower cost solution for plastic scintillators. By overdoping the mixture with PPO, the scintillator exhibited PSD capabilities, detecting thermal neutrons with 1 wt.% boron content [71]. Mahl *et al.* later developed a synthesis process for boron-loaded PVT based scintillators using boric acid as a precursor. The low cost acid precursor ($1.74/g), enriched to >96 % ^{10}B, is processed into monoborylated benzene (MBB), soluble in PVT. For a ^{10}B concentration of 0.05 wt.% the light yield

measured 9,790 photons/MeV versus 5,940 photons/MeV for the 1.06 wt.% sample [72].

Gadolinium-Loaded Plastics

Gadolinium is typically used in scintillators to boost the neutron detection efficiency, possessing an exponentially larger cross section than the other common absorbers. Ovechkina *et al.* investigated a gadolinium-loaded scintillator in a PS base with PPO as a minor additive. Using transparent scintillator disks of 14 mm diameter and 3 mm length, they tested mixtures of with 0, 0.5, 1 and 3 wt.% gadolinium. At the 3 wt.% mixture, the relative LY was 1.08 (8,850 photons/MeV) compared to bismuth germanate (BGO) (8,200 photons/MeV), as tested [73]. Bedrik *et al.* enhanced the LY by 20 % for a PS incorporating gadolinium phenylpropionate using between 1.5 wt.% to 2 wt.% of the luminescent additive DMDPA [74]. Dumazert *et al.* proposed a new design concept for a gadolinium based replacement for the Bonner sphere type neutron detector. The system utilizes a gadolinium (metal) core inside a larger plastic sphere, similar to the ^{3}He filled proportional counters or ^{6}LiI scintillators operating inside Bonner spheres. Coupled to a PMT, the system further requires a method for γ-ray discrimination to avoid pulse pile up, along with optimization of the gadolinium core geometry, as the high cross section leads to interaction concentration at the surface of the sphere [75].

2.2.3 Ceramics

Ceramic scintillator detectors cover a range of inorganic materials existing in crystalline or power form. Applied as a coating, many of the powder forms are mixed with non-ceramic materials and binders to create a uniform thin film, generating light output in response to a neutron interaction within the matrix.

CLYC

Developed by Radiation Monitoring Devices (RMD), the scintillator CLYC aims to provide a suitable alternative to ^{3}He proportional counters. Enriched in ^{6}Li, the material is operated as a simultaneous γ-ray and neutron detector using PSD techniques. D'Olympia *et al.* demonstrated the sensitivity to thermal neutrons via the $^{6}\mathrm{Li}(n,\alpha)^{3}\mathrm{H}$ reaction. The material was also able to distinguish between fast neutrons, interacting via the $^{35}\mathrm{Cl}(n,p)^{35}\mathrm{S}$ reaction. The measured rise time for γ-rays, fast neutrons, and thermal neutrons were 16, 40 and 47 ns, respectively [76]. Glodo *et al.* documented the ten year anniversary by compiling achievements using the CLYC detector. In their work, the detector produced a γ-ray energy resolution of 3.6 % for a 1 in diameter sample and 4.1 % for a 2 in diameter sample, both 1 in long [77]. Smith *et al.* presented an analysis of CLYC coupled to silicon based devices, replacing the traditional PMT used in previous configurations. They concluded, as a first investigation, the performance of the silicon devices was insufficient to provide γ-ray energy resolution comparable to previous studies, attributed to the lower detection efficiency of the scintillation photons in the silicon devices [78].

Bourne *et al.* presented the results of ^{137}Cs and ^{252}Cf exposures along with MCNP (Monte Carlo N-Particle) simulations. They reported a value of 10 % for capture efficiency from intrinsic ^{6}Li, yielding a 5 times increase over a matched ^{3}He volume [79]. Machrafi *et al.* used MCNP to generate a set of response functions for CLYC. The thermal neutron energy peak from the $^{6}\mathrm{Li}(n,\alpha)^{3}\mathrm{H}$ reaction demonstrated a resolution of 3.3 % with a 1.55 MeV shift in the simulated spectrum, indicating 33 % conversion losses in the scintillator [80]. Whitney *et al.* showed the results of a CLYC based radiation camera developed by RMD. The camera system was able to image ^{252}Cf and ^{241}AmBe sources using PSD to isolate the γ-ray and neutron components [81]. Giaz *et al.* explored the difference between CLYC-6 and CLYC-7, using the ^{6}Li enriched compound to detect thermal neutrons and the ^{7}Li enriched version for fast neutrons, suppressing the thermal neutron response. The results illustrated a significant removal of the thermal neutron signal in CLYC-7, with an efficiency <0.3 % compared to the geometryically identical CLYC-6. In response to fast neutrons the CLYC-7 showed a peak for 2.5 MeV neutrons and a contiuum for 14.1 MeV neutrons [82].

Lithium Fluoride

Stedman briefly discussed a scintillator consisting of LiF/ZnS, enriched in ^{6}Li, mixed with a Lucite binder, a trade name for PMMA. In this complex, the lithium-6 fluoride (^{6}LiF) compound acts as the neutron absorber, and the ZnS acts as the fluorophore, producing scintillation light when excited by the daughter products from the $^{6}\mathrm{Li}(n,\alpha)^{3}\mathrm{H}$ reaction. Comparing the detection effeciency to a $^{10}\mathrm{BF}_3$ counter, the LiF/ZnS scintillator yielded 60 %, 50 % and 25 % efficiency at 0.005 eV, 0.025 eV and 0.2 eV neutron energies, repstively. Testing the scintillator with a ^{90}Sr-^{90}Y γ-ray source provided little response, utilizing a basic discrimination circuit to supply γ-ray rejection [83]. Helm tested a similar mixture of LiF/ZnS(Ag) and Lucite in a 2:1:1 ratio. Testing the use of corrugated surfaces and reflectors, he reported an efficiency of 28 % noting the presence of ^{6}Li accounted for the primary increase in performance [84].

Iikura *et al.* worked towards increasing the usable brightness from LiF/ZnS for applications in high frame rate imaging, such as motors and engines. They investigated two mixtures of LiF/ZnS(Ag), a previously tested Cl doped mixture and a newly developed Al doped scintillator. Using brightness enhancing films common in liquid crystal displays (LCDs) the light output saw a factor of 3 increase in intensity, while the spatial resolution calculated via MTF saw a 2 times performance drop. With the enhanced scintillator performance, they were able to continuously image an operating car engine at 2,000 RPM [85]. Kawaguchi *et al.* improved a Bridgman growth method to create lamellar structure in a $^{6}\mathrm{LiF/CaF}_2$:Eu eutectic. Using fluoride precursors LiF, CaF_2, and EuF_3, the material was grown varying the lamellae thickness by adjusting the pull rate, measuring from 3 µm to 7 µm thick. The largest count rate was observed for the thinnest layers (3 µm), producing a noticible peak in response to a ^{252}Cf neutron source [86]. Matsubayashi *et al.* used a 20 mm diameter by 3 mm thick crystal of ^{6}LiF, along with a neutron imaging plate (NIP), to conduct a sensitivity study for ^{6}LiF. At the time, the reported spatial resolution for NIPs was 58 µm, providing the capability to qualify the spatial resolution in ^{6}LiF. Viewing a neutron sensitivity indicator fabricated from

aluminum shims, the ^{6}LiF crystal was able to observe a 22 µm gap between shim stacks [87].

Yang *et al.* presented a modified compound composed of the fluorophore ZnS, typically used with ^{6}LiF, and polypropylene (PP) to be used as a fast neutron detector. The self opaque material yielded an optimum light output between 2 and 3 mm, optimizing for fast neutron by the exclusion of ^{6}LiF [88]. Santodonato *et al.* documented the current experimental capabilities of the ^{6}LiF/ZnS:(Cu) (1:2) scintillator screen (^{6}LiF/ZnS screen) installed at the CG-1D beamline, also discussed later as related to this research. A range of LiF/ZnS film thicknesses from 50 µm to 200 µm are currently available as commercial products [90]. At this beam line, the ^{6}LiF/ZnS screen offers a $7 \times 7\,\mathrm{cm}^2$ FOV at just below 80 µm spatial resolution under standard operating conditions [89]. To directly address the question of replacing large, ^{3}He base proportional counting systems, Stave *et al.* fabricated a prototype neutron multiplicity counter using LiF/ZnS. The system implemented 500 µm thick sheets of LiF/ZnS sandwiched between 7 mm thick layers of PMMA. As a viable design for ^{3}He proportional counter replacement, other problems must be solved first, including size reduction of the PMT, potentially using silicon photomultipliers (SiPMs) as well as a real time PSD algorithm [91]. Stoykov *et al.* demonstrated the construction of single-channel LiF/ZnS scintillator coupled to a SiPM. Withing the $2.4 \times 2.8 \times 50\,\mathrm{mm}^3$ LiF/ZnS module, 12 WLS fibers were embedded in the crystal, reducing the energy of the scintillation photons, while acting as a multiplier, conforming to the device sensitivity of the SiPM [92].

Lithium Chalcogenides

For around four decades, lithium containing ternary chalcogenides (TCs), including LISe, have been studied as a tunable bandwidth material for mid infra-red (mid-IR) non-linear optics, and more recently as semiconductor detectors. Studying TCs for neutron detection applications, Tupitsyn *et al.* refined the growth technique, producing higher quality sensor material than achievable with prior methods. In contrast to the red or grayish crystals synthesized by other groups, the bright yellow material exhibited optical transparency, with a room temperature absorption edge near 450 nm, at the spectral transition from blue to violet light [93]. While refining the growth mechanics, Tupitsyn *et al.* confirmed the absorption edge for the yellow material, noting an edge shift for the annealed yellow-red crystals to 525 nm and around 610 nm for red material [94].

Wiggins *et al.* encountered the scintillation mechanism while characterizing LISe for semiconductor detector performance. The light output from a BGO scintillator was used for reference, yielding ∼9,000 photons/MeV for γ-rays with a peak wavelength of 480 nm. In comparison, the LISe scintillator demonstrated a LY of 4,400 photons/MeV at a peak intensity of 512 nm. Absorbing the full Q-value from the $^{6}\mathrm{Li}(n,\alpha)^{3}\mathrm{H}$ would produce an estimated 21,000 photons/neutron (thermal energy). Furthermore, the study quantified the detection speed of LISe scintillators, revealing a fast decay constant of 31 ± 1 ns and a slow constant of 143 ± 9 ns 2015. Additional LY measurements were conducted as part of the neutron imaging experiments discussed in Section 4.2.1 [96, 97].

GadOx

Exhibiting some of the best recorded spatial resolutions to date, gadolinium oxysulfide (Gadox) scintillator screens are implemented nearly identical to LiF/ZnS screens. Tözke *et al.* reported the use of Gadox layers ranging from 5 µm to 30 µm, yielding spatial resolutions from 25 µm to 61 µm. For thermal neutrons, a 10 µm thick layer was able to absorb up to 90 % of the incident neutrons [98]. A popular manufacturer of neutron sensitive scintillator screens, RC TRITEC reports a 5 times decrease in LY for a Gadox screen compared to LiF/ZnS (50 µm thickness). In additon, the light output spectrum from LiF/ZnS exhibits a single broad peak, while the light output spectrum from Gadox screens feautures multiple sharp peaks, with a maximum intensity peak at 549 nm. Combining the two scintillator compounds has been shown to boost the overall LY without affecting the spatial resolution [90]. A key drawback when using a gadolinium based scintillator screen is the large amount of secondary radiation produced in the screen, particularly X-rays and γ-rays, requiring additional distance and shielding for experiments using this type of scintillator. Further progress in Gadox neutron imaging is discussed in Section 2.5.3, covering recent advancements in ultra high-resolution imaging.

Others

Yanagida *et al.* grew crystals of $LiCaAlF_6$, doped with Eu^{2+}, to evaluate the potential for neutron imaging. In a sample doped with 2 mol % Eu^{2+}, the measured LY came to 29,000(2900) photons/MeV. This material exhibited an emission peak at 375 nm with the smallest decay time for the 2 mol % sample at 1.15 µs. The sample was used for thermal neutron imaging with a sub-mm spatial resolution [99]. In addition to Eu^{2+} doping, Yanagida *et al.* later studied the effects of Ce^{3+} doping in $LiCaAlF_6$. The emission wavelength was again 370 ± 15 nm for Eu^{2+} and 290 ± 15 nm for Ce^{3+}. The Ce^{3+} exhibited a significantly improved decay time (40 ns) over that for Eu^{2+} (1.5 µs), agreeing with the previous study [100]. Wu *et al.* developed a new eutectic scintillator composed of $LiCl/BaCl_2:Eu^{2+}$. The eutectic demonstrated two emission peaks at wavelengths 406 and 526 nm, producing a 412 ns decay constant. The relative LY was determined to be comparable to the lithium glass scintillator, Nucsafe [101].

2.3 Semiconductor Detectors

Radiation sensitive materials may also be designed to operate as semiconductors. Unlike scintillators, a radiation semiconductor requires an active voltage bias through the bulk material for operation. The bias creates an internal electrical field, suitable for separating the charged particles created during radiation interactions. Capturing these charge carriers allows semiconductors to record information about the incident radiation including energy, position and source intensity.

2.3.1 Properties of Semiconductors

Semiconductors are a special class of non-metal solids, widely used in modern electronics for their specific material properties. Unlike true conductors (*i.e.* metals) or insulators (*e.g.* glass), semiconductors fall in the middle, with resistivities commonly ranging from $10^{-2}\,\Omega\cdot\text{cm}$ to $10^{8}\,\Omega\cdot\text{cm}$ [102]. Conduction arises as electrons move from atom to atom in a bulk material, carrying with them a negative charge while leaving a positively charge hole as they move. In metals, conduction is free to occur because the electron valence band and the conduction band overlap ($E_g < 0\,\text{eV}$), permitting the free exchange of electrons between atomic valence shells. Alternatively, insulators have such a wide bandgap, it becomes difficult or impossible to excite the valence electrons with enough energy to reach the conduction band. Exhibiting a bandgap, E_g, ranging from $0\,\text{eV}$ to $4\,\text{eV}$, semiconductors behave like insulators that will conduct once a threshold excitation event occurs. A key physical characteristic of semiconductors, the resistance decreases inversely with temperature, approaching conductive behavior at high temperatures and insulating behavior at cold, or even room temperature. For this reason, radiation detectors are often operated at liquid nitrogen temperatures ($77\,\text{K}$) to minimize free electrons, with room temperature operation limited to materials with larger band gaps. Typically, semiconductors exhibit a crystalline lattice structure, however thin films applications may utilize amorphous or even liquid compounds as well. Similar to temperature effects, the electronic behavior of the bulk material is highly sensitive to lattice defects, generally requiring single crystal sensing material.

2.3.2 Pulse Formation

Semiconductor detector designs have been developed for most radiation types. As the radiation particle or photon interacts with the sensing material, ionized particles are created, and the charge carriers are read as electrical pulses.

Photon Interactions

In photon sensitive detectors, the incident photon will lose energy as it traverses the material through a series of ionizing interactions. At higher photon energies ($E_\gamma > 1.022\,\text{MeV}$) γ-rays may interact with nuclei to convert their energy into an electron-positron pair, known as pair production. The anti-matter positron eventually combines with an electron in the bulk, annihilating to produce two new gamma photons of $0.511\,\text{MeV}$ each. Gamma-rays ranging from $0.1\,\text{MeV}$ to $10\,\text{MeV}$ are deenergized through Compton scattering. The incident photon is absorbed by the nucleus, with some of the energy used to eject an atomic electron, and the remainder of the energy imparted to a lower energy gamma ray emission [103]. At energies below $50\,\text{keV}$, both X-rays and γ-rays are subject to the photoelectric effect. This mechanism is similar to Compton scattering, resulting in an electron emission, however the photon is completely absorbed [38].

Charged Particle Interactions

Interactions involving charged particle radiation generally interact with the orbital electrons of a target atom, instead of the nucleus. Light charged particles include beta plus particles (β^+s), β^-s, delta-rays (δ-rays), and epsilon-rays (ε-ray), all possessing the rest mass of an electron. Heavy charge particles include species with a mass of a proton or greater. While this definition includes all heave ions, typically the larger variations are found in extraterrestrial or nuclear reactor environments. In neutron detection, smaller nuclei such as protons and α's are the most common forms of heavy charged particles.

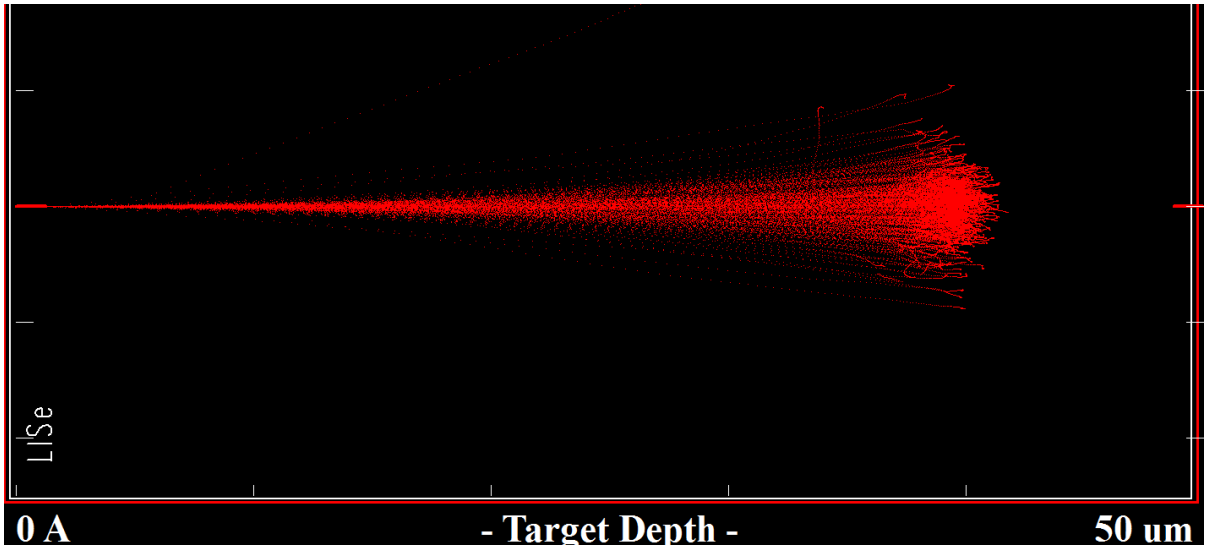
Heavier charged particles may be slowed through Coulombic interactions with the electrons in the target material, generally carrying a positive electronic charge. The charged particles exert an electromagnetic force on the outermost orbital electrons, potentially stripping them from the atom. If the atom is not ionized, it may still be excited, potentially leading to other emissions [104]. These particles will follow a linear trajectory, releasing a majority of their energy close to the end of travel as described by their Bragg curve. To determine the range of $\mathcal{T}$'s and α's in LISe, the SRIM (Stopping and Range of Ions in Matter) software package was used to simulate 500 ions of each type traveling through the sensor, shown in Figure 2.3 [105]. The simulated trajectory cloud offers a statistical average for the range of each ion, evaluating to 39.4 µm for a $\mathcal{T}$ and 7.44 µm for an α [106]. Light particles experience the following loss mechanisms: elastic scattering, inelastic scattering, bremsstrahlung emission (braking radiation), and positron annihilation. These particles, typically negative, scatter off orbital electrons, potentially ejecting them as δ-rays [38].

Neutron Interactions and Detection

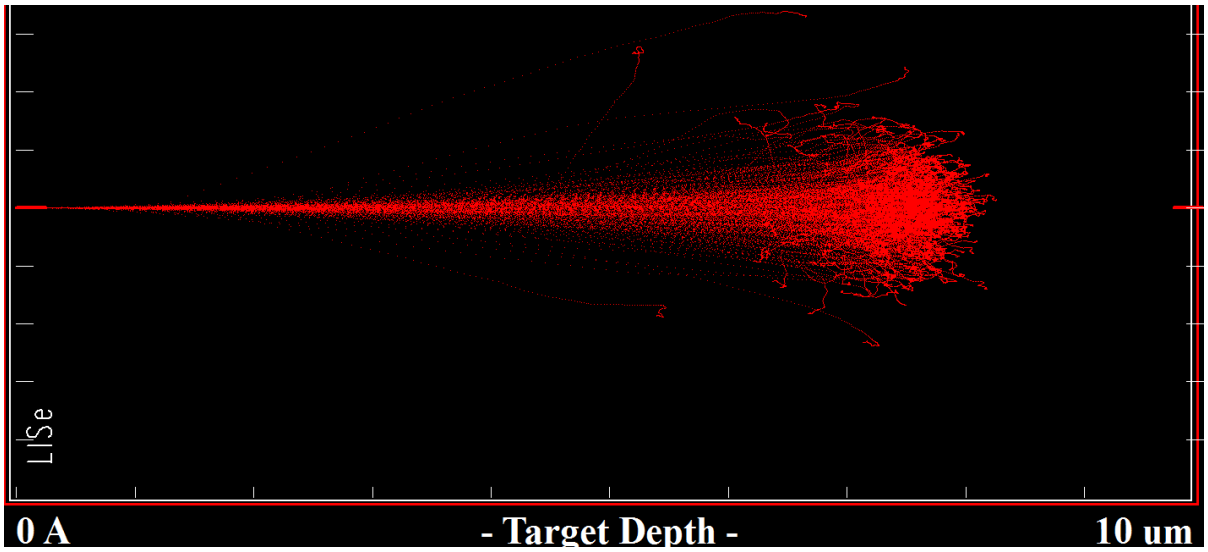
Neutrons, like γ-rays, are indirectly ionizing radiation, requiring a nuclear reaction to generate directly ionizing secondary particles. Following the neutron interaction mechanisms described in Section 2.1.2, an incident neutron will pass straight through the material until it encounters a nucleus. In a LISe detector, the neutron must find a ^{6}Li nucleus, shown in Figure 2.4, to induce the desirable $^6\mathrm{Li}(n,\alpha)^3\mathrm{H}$ reaction, described in Section 2.1.3. The reaction yields two daughter particles, a $\mathcal{T}$ and an α, traveling in opposite directions through the sensor. Following the previous description of charged particle interactions, these secondary particles will ionize atoms through the bulk. Along the ion trajectory, electron-hole pairs will be generated, shown in Figure 2.5. An analysis described by Klein relates the kinetic energy of an ionizing radiation particle to the anticipated number of resultant electron-hole pairs produced in a target material [108]. The quantum yield, Q, describing the number of electron-hole pairs per charged particle is proportional to the energy lost by the ionizing radiation particle, W, and the radiation-ionization energy, ϵ, shown in eq. (26).

$$Q \equiv W/\epsilon \tag{26}$$

For semiconductors with a bandgap, $E_g \gtrapprox 2\,\mathrm{eV}$, the radiation-ionization energy can be approximated using the bandgap, $\epsilon \approx 3E_g$. Assuming an ionizing radiation particle stops within the bulk sensor, depositing its



(a) triton ion trajectories



(b) alpha ion trajectories

Figure 2.3. SRIM simulations of secondary particle trajectories in LISe.

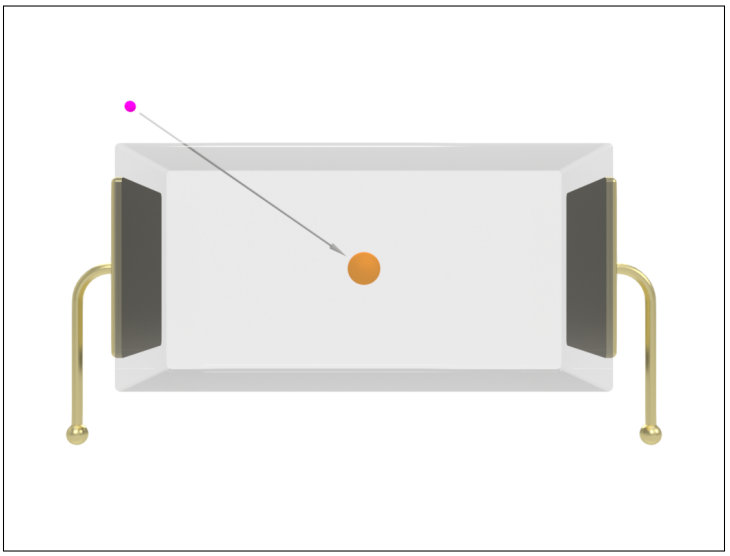


Figure 2.4. Incident neutron is absorbed by ^{6}Li in semiconductor bulk [107].

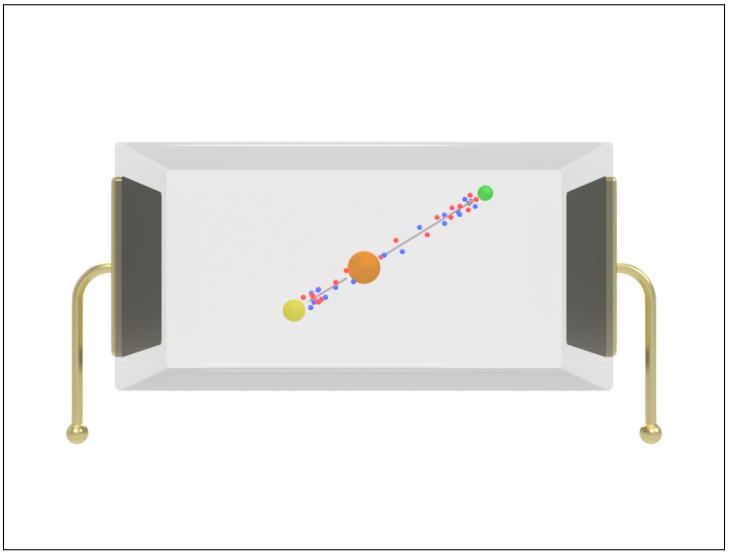


Figure 2.5. Emitted ^{3}H and α generate charged particle pairs [107].

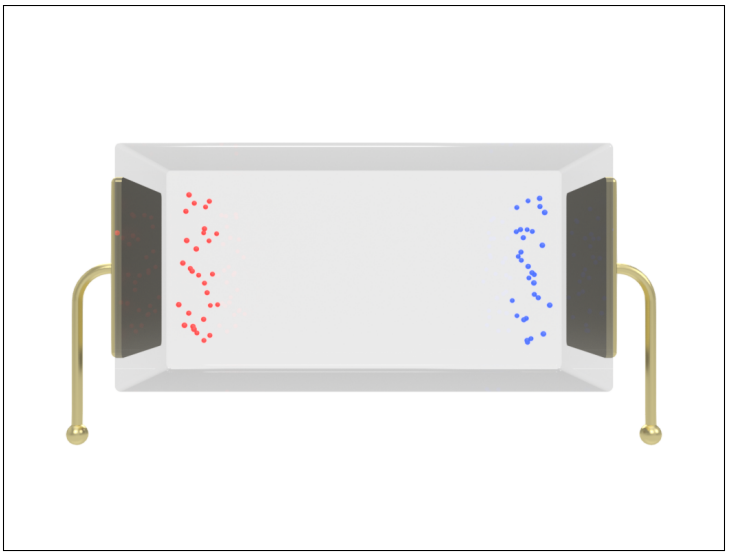


Figure 2.6. Charge carriers driven to opposing electrodes by applied internal electric field [107].

full kinetic energy, the total number of electron-hole pairs produced by the incident particle can be found from eq. (27).

$$Q = \frac{W}{3E_g} \tag{27}$$

Klein noted the specific type of radiation does not directly impact this estimation, relying solely on the incident particle's kinetic energy. Given the reaction Q-value of 4.780 MeV and a semiconductor band gap of, $E_g = 2.85\,\text{eV}$, an incident neutron will produce roughly 5.6×10^5 electron-hole pairs [93]. These charge carriers are driven to the metal electrodes by the internal electric field generated from the bias voltage, as seen in Figure 2.6. As the charge carriers approach the electrode of opposite polarity, an image charge is created on the thin metal film, generating the electrical pulse indicative of the neutron capture event. This charge pulse is collected by the coupling capacitor as it enters the electronic readout circuit.

2.3.3 Charge Collection

For a single set of parallel contacts, the Shockley-Ramo Theorem can be used to describe the induced charge, dQ, given a sensor material thickness, W, the number of electron-hole pairs generated by the nuclear interaction, N_0, and the charge of an electron, e [109]. The differential distances, dx, are written for electrons and holes respectively. The idealized relationship shown in eq. (28) neglects the real world losses seen in compound semiconductors.

$$dQ^* = \frac{-eN_0}{W}\left(dx\Big|_e + dx\Big|_h\right) \tag{28}$$

Once these electron-hole pairs reach the surface contacts, they create an image charge, collected by the front-end electronics. This charge will vary temporally as electrons generally exhibit better charge carrier transport properties compared to holes, arriving at their respective electrode first. The total charge on

the electrode is given by integrating eq. (28). Ideally, the charge is equal to the charge of a single carrier multiplied by the number of carriers produce in the radiation detection event. When the effects of charge trapping are introduced via Hecht's relation, the charge equation takes the following form in eq. (29) [35].

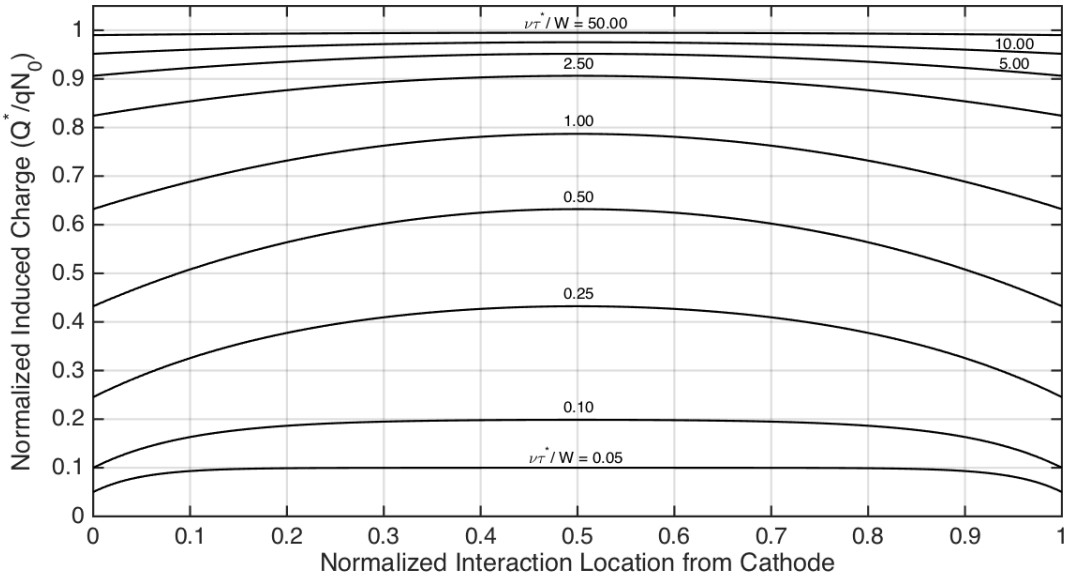
$$Q^* = eN_0 \left\{ \frac{v_h \tau_h^*}{W} \left(1 - \exp\left[\frac{-x_i}{v_h \tau_h^*} \right] \right) + \frac{v_e \tau_e^*}{W} \left(1 - \exp\left[\frac{(x_i - W)}{v_e \tau_e^*} \right] \right) \right\} \tag{29}$$

Here, the electron and hole components are separated since they have different carrier velocities, v, and carrier lifetimes, τ. The difference in electron and hole charge carrier properties alters the induced image charge based on the location of charge carrier generation. The effect of charge trapping is shown below in Figure 2.7, where the ideal case is represented in Figure 2.7a, and the real case is represented in Figure 2.7b. The real case accounts for the fact that electrons typically move faster through the lattice, resulting in decreased charge generated from the holes. As shown in Figure 2.7a, the maximum induced charge occurs when the interaction is located at the center. When centered, the combined effect of distance based charge trapping is minimized for the electron-hole pair. As the location is moved to the edge, the increased distance the electron, or hole, must travel causes non-linear trapping losses. Furthermore, the normalized induced charge increases inversely with the detector thickness because more of the charge carriers are able to reach the electrodes without being trapped in the substrate.

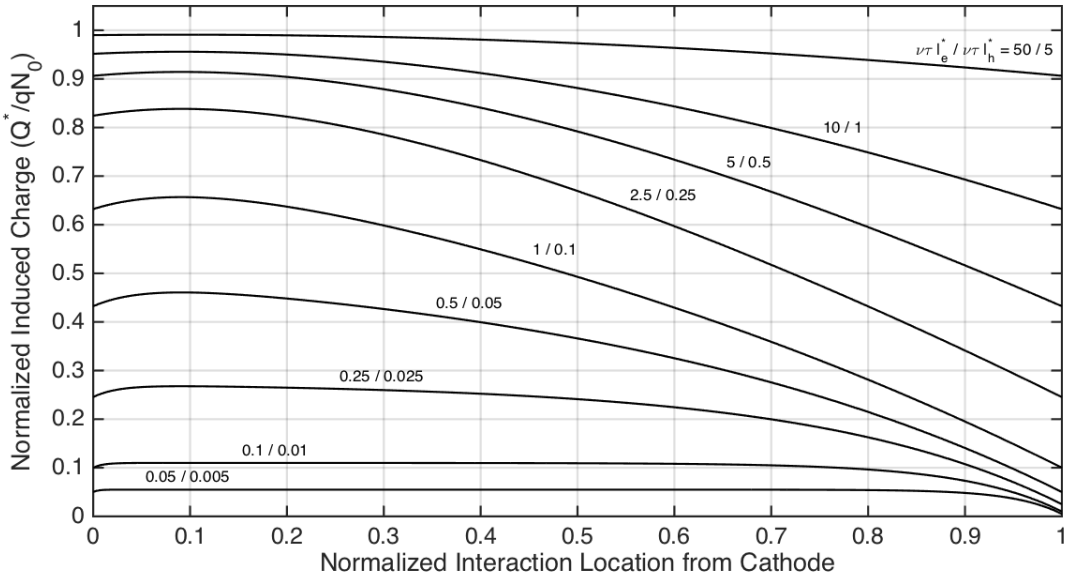
When the difference in charge carrier velocities is factored in the equation, the plot transforms to Figure 2.7b. It can be seen that for the range of electron to hole mobility ratios, the charge collection is degraded the further from the cathode the interaction occurs. This effect is worsened when a large number of trap states exist, either intrinsically or due to imperfections in the crystal after processing. For this reason, it was decided the cathode should face the neutron beam to maximize charge collection. Since the neutron interaction rate is maximum on the incident surface, the majority of the charge should be deposited near the cathode and follow an attenuation curve through the sensor towards the anode [35].

2.3.4 Diamond

Among its wide range of applications, diamond has demonstrated radiation detection capabilities. Early on, Kania *et al.* proposed the use of an undoped, intrinsic diamond as an ohmic semiconductor detector with a material resistivty over $10^{12}\,\Omega \cdot \mathrm{cm}$ [110]. As a generalized "solid ionization chamber", the diamond detector could theoretically convert any ionizing radiation that interacted with the lattice into a detectable signal. As the chemical vapor deposition (CVD) growth process became more reliable, the simple detector was fabricated by depositing thin film metal contacts on both faces of the crystal to form electrodes, tested by Behnke *et al.* They confirmed a larger resistivity, exceeding $10^{13}\,\Omega \cdot \mathrm{cm}$, noting the polarisation effect created from trapped charge carriers [111]. The high bandgap of diamond ($E_g = 5.5\,\mathrm{eV}$) eliminated the need for additional doping to suppress leakage current at room temperature. However, with a bandgap 5 times larger than silicon, more energy is required for each charge carrier pair, reducing material sensitivity.



(a) identical electron and hole transport



(b) electron transport 10× greater than holes

Figure 2.7. Relative position-dependent charge collection for electron and hole transport. Various values of $\nu\tau^*/W$ are assumed to show the dependence (recreated from Figure 13.24 in Knoll (2010) [35]).

A decade later, Pernegger *et al.* was able to successfully apply the transient-current technique (TCT) to diamonds under α radiation from a ^{241}Am source, characterizing charge carrier transport times. The tests were conducted with a sample measuring $4 \times 4\,\mathrm{mm}^2$, with an electrical field of $1\,\mathrm{V/\mu m}$ applied across the 470 µm thick sensor [112]. Pomorski *et al.* confirmed the high speed operation of the diamond, demonstrating the materials nanosecond pulse response, unintuitively favoring hole drift over electron drift [113]. They also studied the signal degradation apparent after high flux charged particle bombardment. While the radiation hard diamond did not see an increase in leakage current or drift velocity, the sensor required annealing to respond with the same pre-irradiation signal amplitude [114]. Because of its radiation hardness, Wallny of the RD42 Diamond Detector Collaboration proposed diamond strip and pixel detectors for beam monitoring in the high radiation environment seen in the A Toroidal LHC ApparatuS (ATLAS) experiment at the Large Hadron Collider (LHC) [115].

Being one of the hardest materials known, diamond can be polished down and maintain an extremely smooth surface ($R_a \sim 5\,\mathrm{nm}$), eliminating electronic trapping sites. However, the smooth surface creates difficulties in the contact metal adhesion process. Galbiati *et al.* demonstrated the use of a diamond-like carbon as a tunneling junction to effectively coupled the Pt and Au metal contacts [116].

Diamond has been proposed as a potential fast neutron detector for its radiation hardness and high energy resolution. Pillon *et al.* studied fast neutron detection through the $^{12}\mathrm{C}(n,\alpha)^{9}\mathrm{Be}$ reaction as demonstrated in eq. (30) [117].

$$\begin{array}{ll} & \underline{Q\text{-value}} \\ {}^{12}_{6}\mathrm{C} + n \rightarrow {}^{9}_{4}\mathrm{Be} + \alpha & -5.701\,\mathrm{MeV} \end{array} \tag{30}$$

They also explored the possibility of broad spectrum neutron detection by applying a ^{6}LiF converter layer (0.5 µm–4.0 µm) to the surface of the diamond. The $^{6}\mathrm{Li}(n,\alpha)^{3}\mathrm{H}$ reaction converts a neutron to an alpha particle, escaping the thin conversion layer and depositing in the diamond for secondary detection. While limited by size, the system resolved neutron interactions across a broad energy range and demonstrated utility as a dose monitor [118]. Recently shown by Wulz *et al.*, deep channels were etched into the surface of electronics grade diamonds [119]. The vias measured 30 µm diameter and penetrated the full 150 µm thick diamond sensor. Electroplating was used to fill each channel with chromium, creating a conductive wire through the sensor bulk. The 3D diamond detector prototype successfully demonstrated a response to a plutonium/beryllium (Pu/Be) neutron source [120].

2.3.5 Boron Compounds

The boron semiconductor concept functions as an analog of the lithium based LISe detector. By embedding one of the light-weight isotopes (^{6}Li or ^{10}B) into a semiconductor compound, the number density largely exceeds what is possible in a proportional gas. The increased reaction density would result in higher neutron

stopping power and detection efficiency while reducing the required size of the device.

Citing earlier studies by Kumashiro *et al.*, using ^{10}BP, and Bykovskii *et al.*, using lithium doped B_4C semiconductors, Robertson *et al.* investigated the application of B_4C grown on silicon substrates for neutron detection [121–123]. In the study, a 276 ± 5 nm thick boron carbide layer formed the neutron sensitive film, utilizing natural ^{10}B enrichment. The detector was able to sense reactor neutrons coming from a TRIGA neutron beam port, however, the exceedingly thin boron carbide film only achieved a reported 3.2×10^{-4} neutron detection efficiency. Deviating from the standard semiconductor design, Emin *et al.* proposed a detector made of two cells, one enriched in ^{10}B and the other in ^{11}B. He proposed the large Seebeck coefficient of boron carbide could be utilized to detect thermal excitation from neutron absorption in the ^{10}B side. Electronically coupling the two sides, a neutron interaction would produce a small amount of heating, creating a detectable electrical potential between the chemically identical compounds [124]. Building on prior works implementing boron carbide in heterojunctions, Caruso *et al.* proposed a heteroisomeric stack, using two distinct isomers of boron carbide to create the diode junction. The neutron pulse height spectrum differed from the conversion layer systems, favoring the reaction sum peak over the individual product peaks [125].

Conversion layer detectors suffer from conflicting design goals, limited in thickness by the range of secondary particles, creating a ceiling on the detection efficiency. Leaning on decades of research in the semiconductor industry, Li *et al.* presented a design for a hexagonal boron nitride (hBN) micro-strip detector. The 1 µm thick hBN detector exhibited a conversion efficiency of 80 % for absorbed neutrons [126]. A few years later, Doan *et al.* reported the team was able to resolve the individual particle peaks in the neutron pulse height spectrum. The refined design switched to an interdigitated micro-strip detector layout (6 µm spacing and width), across a 0.3 µm thick hBN substrate. They noted the probability of a sum peak response would remain low until the thickness was increased beyond 5 µm, exceeding the secondary particle ranges [127].

2.4 Lithium Indium Diselenide

Originally, the semiconductor LISe was investigated for visible and infrared spectrum optoelectronics [128]. In the past decade, the desire for a solid-state, direct conversion, neutron detector revived the investigation of lithium based semiconductors. In solid-state neutron detection, the isotopes ^{6}Li and ^{10}B offer the most viable options for semiconductor integration. As previously described in Section 2.3.5, multiple ^{10}B containing compounds have been the subject of semiconductor detector research, benefiting from developments in the microelectronics industry. Despite their well understood electronic behavior, boron semiconductor sensors have proven difficult to fabricate with an appreciably thickness, limiting the device detection efficiency and applicability in real world detection systems. Alternatively, lithium compounds have received less consideration, having a narrower application space, a smaller thermal cross section for ^{6}Li, and a lower

Table 2.1. Bulk material properties for $LiInSe_2$.

Material Property	**Symbol**	**Value**		**Source**	
Resistivity	ρ	2.67×10^{11}	$\Omega \cdot$ cm	Kamijoh *et al.*	(1980)
		3.00×10^{11}		Petrov *et al.*	(2010)
		6.50×10^{11}		Tupitsyn *et al.*	(2012)
		3.43×10^{10}		Vijayakumar *et al.*	(2014)
Relative Permativity	ε_r	9.40		Kamijoh *et al.*	(1980)
		8.45		Kamijoh *et al.*	(1982)
		9.8		Vijayakumar *et al.*	(2014)

natural isotopic abundance. Nonetheless, recent advances in lithium purification and precursor compound synthesis have promoted ^{6}Li to the forefront of semiconductor neutron detector technology [93].

2.4.1 Material Growth

In the early 1980's, Kamijoh *et al.* conducted initial studies on lithium indium diselenide in Tokyo, Japan at Hosei University [129]. The study focused on the development of lithium based TCs, including LISe, for optoelectronic applications. Their work documented the basic growth process beginning with $LiInS_2$, evolving into $LiInSe_2$ and $LiGaSe_2$ [130–132]. The raw precursor materials for LISe had lower purity, using Li (3 N), In (5 N) and Se (5 N), while the growth process itself has been maintained in current research. The final, as-grown boule measured 20 mm long by 10 mm diameter, exhibiting red coloration and a bandgap of 1.88 eV. Bulk material properties for LISe are listed below in Table 2.1.

The patented detector grade LISe material was prepared by the synthesis and growth team collaborating between CNS Y-12 National Security Complex (Y-12), Fisk University (Fisk) and Vanderbilt University (Vanderbilt) [93, 136]. Both Bridgman growth techniques, horizontal and vertical, were implemented in initial crystal growth processes, with later growth cycles relying on the vertical process (see Figure 2.8) [137, 138]. To enhance the sensitivity of LISe to thermal neutrons, the lithium precursor is enriched to a nominal 95 % in the ^{6}Li isotope. A custom vacuum distillation process, developed by Stowe *et al.* at Y-12, provides the ultra high purity (5 N) enriched lithium metal suitable for semiconductor applications [139]. The LISe synthesis begins with production of the binary alloy LiIn. Mixing the enriched lithium with commercially available 6 N purity indium, the metals are heated in a sealed, pyrolitic boron nitride (PBN) crucible to 800 °C. Afterwards, 5 N purity selenium is introduced to the alloy and heated at a temperature of 940 °C, to form the ternary compound. It was shown that 1 % excess Li produced the red sensor coloration while increasing to 3 % excess Li yielded the more desirable yellow sensors [94].



Figure 2.8. LISe crystal growth ampule being loaded into vertical growth furnace at Y-12.

The two zone growth furnace operated at a temperature of 940 °C on the hot side and 760 °C on the cold side, moving the boule at a linear rate of roughly 0.7 cm/d [95]. The extracted crystal boule measured roughly 50 mm long by 20 mm in diameter. Individual sensors were cut from the growth boule into 13 mm diameter wafers ranging in thickness from 1.0 mm to 2.0 mm [138]. Preliminary performance validation and material studies were conducted to determine if the raw sensor would yield a viable neutron detector.

2.4.2 Crystal Structure

Single crystal LISe, was one of many lithium containing TCs explored by the synthesis team for neutron imaging applications, shown in Figure 2.9. This ternary I-III-VI semiconductor was designed around the neutron sensitive ^{6}Li isotope. Following the molecular formula $A^{I}B^{III}C_2^{VI}$, the prospects included $^6LiBC_2$ (B = In or Ga, C = S, Se or Te) [94]. These compounds offer desirable characteristics for radiation detection, including structural and chemical stability, minimizing the use of heavy metals or radioactive compounds. Figure 2.10 depicts the orthorhombic unit cell for LISe, exhibiting a wurtzite crystal structure following the $Pna2_1$ space group [140]. The Li and In atoms form tetrahedral bonds, $LiSe_4$ and $InSe_4$, connected at shared Se atoms to form the larger crystalline structure. A summary of crystal lattice parameters have been tabulated in Table 2.2, capturing the historical changes in experimentally evaluated crystal structure and its correlation with crystal color. While the reported empirical values have varied, they remain within the calculated uncertainty, accommodating slight differences following composition and color. The consistency in lattice structure across decades of experimentation indicates the coloration and overall electrical performance

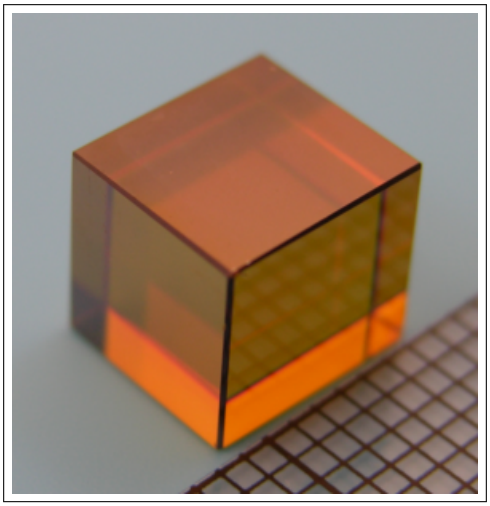


Figure 2.9. LISe cube of sensor grade material (0.7 cm side length).

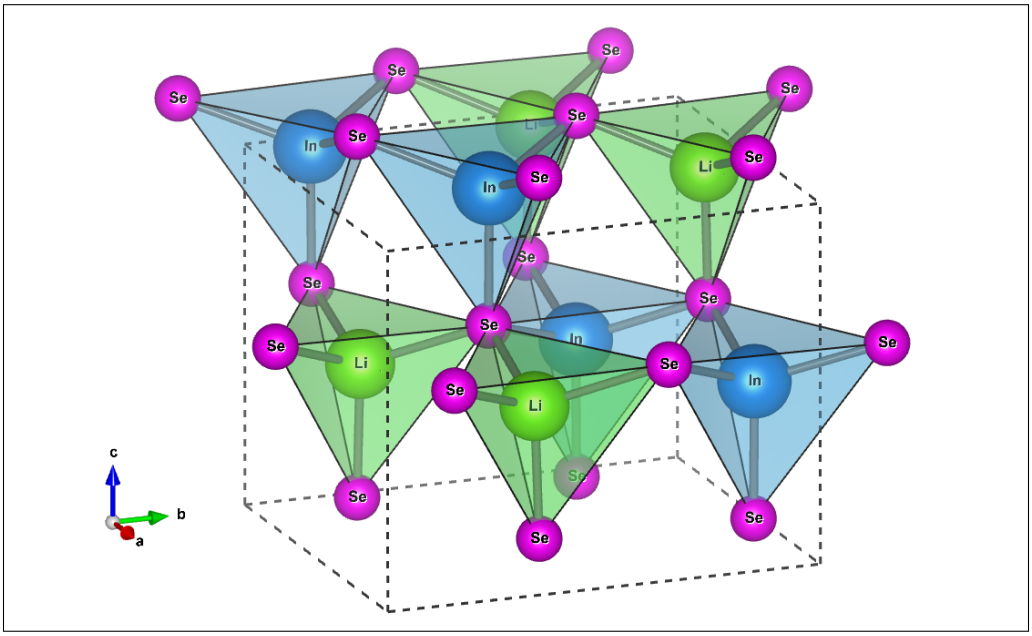


Figure 2.10. LISe crystal lattice structure, recreated from lattice parameters reported by Wiggins *et al.* (2016) [140].

Table 2.2. Crystal lattice parameters for $LiInSe_2$.

a	***b***	***c***	***V***		**Source**	
7.218	8.441	6.772	412.6	^{y}	Kamijoh *et al.*	(1981)
7.192	8.412	6.793	410.97	^{g}	Isaenko *et al.*	(2001)
7.1917(8)	8.4116(10)	6.7926(8)	410.90(8)	^{y}		
7.1939(8)	8.4163(10)	6.7926(8)	411.27(8)	^{r}		
7.1934(10)	8.4159(11)	6.7971(9)	411.49(9)	^{dr}		
7.162	8.543	6.769	414.2	^{y}	Tupitsyn *et al.*	(2012)
7.1976(13)	8.4159(15)	6.7986(12)	411.82(13)	^{y}	Wang *et al.*	(2014)
7.166(9)	8.398(10)	6.788(8)	408.5(9)		Vijayakumar *et al.*	(2014)
7.201(6)	8.420(6)	6.804(2)	412.62(9)	^{y}	Ma *et al.*	(2015)
7.202(3)	8.423(3)	6.801(6)	412.63(7)	^{r}		
7.201(1)	8.419(8)	6.803(1)	412.49(6)	^{dr}		
7.201(3)	8.422(7)	6.802(1)	412.58(2)	^{dr*}		
7.15	8.29	6.74	399.5	^{y}	Wiggins *et al.*	(2016)

Note: The standard units for a, b and c are Å. The units for V are $Å^3$.

^{r} light red / rose / ruby color

^{dr} dark / deep red color

^{dr*} dark red color after anneal

^{y} yellow color

^{g} greenish-yellow color



Figure 2.11. Pair of LISe sensors used for scintillator and semiconductor devices [145].

varies in response to other material characteristics.

2.4.3 Material Properties

At room temperature, the band gap for LISe ($E_g \leq 3\,\text{eV}$) offers ideal semiconductor operation suitable for radiation detection. The high grade single crystal is translucent, ranging in color from deep red ($E_g \approx 1.9\,\text{eV}$) as described by Kamijoh *et al.*, to a light yellow ($E_g \approx 2.8\,\text{eV}$) as studied by Isaenko *et al.*, shown in Figure 2.11 [131, 144]. As reported by Wiggins *et al.*, the synthesis team collaborating with this study attained a bright chartreuse or greenish yellow ($E_g \approx 3.0\,\text{eV}$) in some growths, exhibiting near ideal stoichiometry. The visible color is directly correlated to the band gap (see Table 2.3), indicating a shift from ideal stochiometric atomic ratios and electrical properties [146].

Through ongoing experimentation, the coloration was indicative of the Se/(Li+In) ratio, with Se depleted crystals (relative excess of Li and In) exhibiting a red hue, and stoichiometric crystals appearing more yellow [133, 143, 146]. Studying the phase diagram for the solid-state solution Li_2Se-In_2Se_3, Weise *et al.* noted the color change from yellow to red with increasing molar concentration of In_2Se_3. At an even mixture of the two compounds (50 mol % of In_2Se_3) the resultant crystal maintained a yellow coloration with the single ternary phase, $LiInSe_2$, present in the solution. The solution continued to show a single phase down to a 44 mol % concentration of In_2Se_3, after which the binary Li_2Se phase was present. In the other direction, increasing In_2Se_3 concentration past 52 mol % quickly introduced a new ternary phase, $LiIn_5Se_8$, shifting the coloration to a light red, then deep red [153]. During the growth process, the relatively large vapor pressures of lithium and selenium induce evaporation, reducing both Li/In and Se/In ratios. Furthermore, the preferential evaporation of selenium over lithium, also reduces the Se/Li ratio, shifting the stoichiometry and possibly introducing secondary phases.

Charge trapping in $LiInSe_2$ was evaluated by Cui *et al.* and later confirmed by Hamm *et al.*, identifying

Table 2.3. Bandgap for $LiInSe_2$.

E_g (eV)	Source	E_g (eV)	Source
1.88 [r]	Kamijoh *et al.* (1981)	2.63 [y]	Ma *et al.* (2009)
2.03 [r]	Beister *et al.* (1991)	2.86 [y]	Petrov *et al.* (2010)
2.90 [y]	Beister *et al.* (1991)	2.85	Tupitsyn *et al.* (2012)
2.83 [y]	Eifler *et al.* (2000)	2.03 [r]	Cui *et al.* (2013)
2.85	Weise *et al.* (1996)	2.85 [y]	Cui *et al.* (2013)
2.83 [y]	Isaenko *et al.* (2005)	2.99 [y]	Wiggins *et al.* (2016)

[r] red color crystal

[y] yellow color crystal

at least three electron and three hole trap states present in the single phase. Both In and Se vacancies exist, agreeing with a In_2Se_3 concentration <50 mol % for yellow crystals. Also present are two hole related defects at Li on In antisites as well as their correspond In on Li antisites corresponding to electrons [150, 154]. These point defects reduce the carrier lifetime and mobility (see Table 2.4), degrading the electronic performance in semiconductor mode of operation while also increasing self absorption and reducing the light output in scintillator mode [159, 160]. As a preliminary exclusion criterion, a yellow coloration indicates a sensor suitable for neutron detector fabrication, while red regions in the growth boule are suitable for material studies and fabrication process testing. Furthermore, only the highest quality samples were viable semiconductor candidates, while most yellow sensors showed some degree of scintillation in response to neutrons.

Investigated for applications in non-linear optics (NLO), single crystal LISe exhibited desirable characteristics for mid-IR spectrum devices [144, 161]. The material exhibits broad optical transparency across the visible spectrum, also beneficial for light yield in scintillators. The thermomechanical properties of $LiInSe_2$ were evaluated across multiple studies, compiled in Table 2.5. These parameters play a vital role in understanding the growth process and resulting phase formed in the crystal bulk.

2.5 Advanced Detectors

Advanced neutron detectors describe a category of hybrid devices, optimized to overcome the intrinsic limitations of the core imaging technologies described in the previous sections. These systems combine scintillator or semiconductor detectors with 3D structures, specialized readout ASICs and hardware based data processing. The Medipix platform has become a leader in the field of high-resolution radiological

Table 2.4. Optoelectronic properties for $LiInSe_2$.

Material Property	**Symbol**	**Value**		**Source**	
Absorption Coefficient	α	2.00×10^4	1/cm	Beister *et al.*	(1991)
		0.04		Isaenko *et al.*	(2006)
Photocurrent Peak	λ	445	nm	Tupitsyn *et al.*	(2012)
Transparency Range		0.60–12.0	µm	Isaenko *et al.*	(2001)
		0.63–10.0		Badikov *et al.*	(2003)
		0.60–13.0		Yelisseyev *et al.*	(2004)
		0.47–13.3		Isaenko *et al.*	(2005)
Charge Carrier Mobility	μ	122 ± 6^e	$cm^2/V\,s$	Hamm *et al.*	(2018)
Charge Carrier Lifetime	τ	45 ± 1^e	ns	Hamm *et al.*	(2018)
Mobility Lifetime Product	$\mu\tau$	$3 \times 10^{-6*}$	cm^2/V	Bell *et al.*	(2015)
		$5.5 \pm 1.2 \times 10^{-6e}$		Hamm *et al.*	(2018)

[*] average of both charge carriers

[e] negative charge carrier

Table 2.5. Thermomechanical properties of $LiInSe_2$.

Material Property	**Symbol**	**Value**		**Source**	
Microhardness	HK	1.75 ± 0.04	GPa	Petrov *et al.*	(2010)
Melting Point	T_m	904	°C	Kamijoh *et al.*	(1981)
		915 ± 5		Isaenko *et al.*	(2005)
		905		Isaenko *et al.*	(2008)
		915 ± 5		Petrov *et al.*	(2010)
		915		Tupitsyn *et al.*	(2012)
Thermal Conductivity	K_x	4.74 ± 0.25	W/m K	Petrov *et al.*	(2010)
	K_y	4.68 ± 0.25			
	K_z	5.46 ± 0.32			
	K_z	5.42 ± 0.27		Giltnane	(2016)
Heat Capacity	C_p	99.770	J/mol K	Kühn *et al.*	(1987)
		96.045		Gmelin *et al.*	(1995)
		98.1		Yelisseyev *et al.*	(2004)
		98.1		Petrov *et al.*	(2010)
Standard Enthalpy	ΔH	20.17	J/mol	Gmelin *et al.*	(1995)
Entropy	S	146.6	J/mol K	Gmelin *et al.*	(1995)

Note: Thermodynamic parameters reported were evaluated at room temperature.

imaging. Used in a variety of scientific and consumer optics applications, MCP technology is particularly well suited for high-resolution radiographic imaging.

2.5.1 Medipix / Timepix Coupled Systems

Jakubek *et al.* compared early high resolution neutron imaging systems, first utilizing the Medipix1 chip (Medipix1), followed by the Medipix2 ASIC (Medipix2), with a 300 µm thick silicon wafer coated in a neutron sensitive converter layers [167]. They conducted studies at PSI with multiple neutron sensitive materials, as described in Section 2.1.3, to determine which materials gave the best overall response with an ASIC based system. With the Medipix2, a ^{6}LiF powder conversion layer produced a spatial resolution of 107 µm, measured using the FWHM of the line spread function (LSF), captured with a 1 mm thick Cd knife edge mask. While the amorphous ^{10}B produced a more respectable resolution on par with the pixel pitch size, benefiting from the lower energy and transport range of secondary particles, the detection efficiency accordingly suffered. Because ^{113}Cd and Gd produce γ-rays and conversion electrons, they create long, weaker interacting paths. The experimental value reported for ^{113}Cd was 1.7 mm and simulations for Gd expected similar emprical results. Uher *et al.* followed with the resolution values of competing systems, reporting on the Medipix1 (370 µm), the Medipix2 (108 µm), a ^{6}Li based scintillator coupled to a charge-coupled device (CCD) (824 µm), and an imaging plate (124 µm) [166, 168–170].

In 2007, Jakubek proposed a set of sensor options for a Medipix2 based neutron imaging system. The active structure may be composed of (a) a sensor chip coated in a neutron sensitive converter layer (as previously mentioned), (b) a 3D sensor chip with a converter back fill, and (c) a sensor with embedded neutron sensitive isotopes (as seen with LISe). Experimenting with CdTe as an embedded sensor, the neutron images exhibited a spatial resolution of 450 µm with an 8 % detection efficiency, underperforming other materials used in the study [171].

In 2009, Uher *et al.* suggested the usage of the Timepix platform for fast neutron imaging by coupling the ASIC with a plastic scintillator. Based on MCNP simulations, they predicted an energy resolution of around 1 MeV for fast neutrons of 14 MeV energy [172]. Further design developments suggested a device featuring an EJ 204 plastic scintillator measuring $1 \times 1 \times 0.3\,\mathrm{cm}^3$, with spectroscopic capabilities for fast neutrons [173]. Recently, Krejci *et al.* demonstrated the 4×5 Timepix array, dubbed WidePIX, for neutron imaging. Spanning a $71 \times 57\,\mathrm{mm}^2$ area, a thin film of ^{6}LiF produced the expected 55 µm resolution, prescribed by the pixel, pitch while a spatial resolution around 10 µm was achievable in the event counting mode [174].

2.5.2 Microchannel Plates

One of the most common technologies implemented in high-resolution imaging, glass MCPs have been able to produce high spatial resolution, down to ∼10 µm. The typical MCP, as implemented by Tremsin *et al.*, utilizes the $^{10}\mathrm{B}(n,\alpha)^{7}\mathrm{Li}$ reaction by doping the glass channels with the neutron sensitive isotope. When a

neutron is absorbed by the ^{10}B in the channel wall, the resulting secondary products may either stop in the wall, or scatter into the pores, creating an electron avalanche. The electron avalanche is required to register a detection event, so the pore geometry has been driven by the desire to maximize secondary particle escape from the wall material. For this reason, the early design analysis indicated that a square pore design would minimize the "no-escape" zones (where an event goes undetected), followed by a hexagonal geometry and lastly a circular geometry [175].

In the following tests at the High-Flux Isotope Reactor (HFIR), Tremsin *et al.* used the hexagonal channel geometry, with a 6 µm to 10 µm channel diameter and a 2 µm to 3 µm wall thickness. Within the MCP glass, the reaction products have a range of 2 µm and 3.5 µm, for the α and ^{7}Li, respectively. Noting these values, the secondary products would only be capable of traveling a distance spanning a maximum of two channels. A performance comparison between the MCP and Medipix2 readouts traded resolution for acquisition bandwidth. The cross delay line anode (XDL) readout of the MCP achieved resolution ~30 µm at an acquisition rate of 0.5 MHz while the Medipix2 produced a pixel limited 55 µm resolution at over 100 MHz. Backing the MCP stack with a Timepix produced a hybrid system, capable of higher resolution in the MCP readout mode or higher counting rates with the Timepix detector. The system produced a minimum, sub-15 µm resolution, limited by the pore spacing parameter [176, 177].

The next year (2009), Tremsin *et al.* tested the MCP-Medipix2 system at PSI, capturing an image of the PSI Siemens star imaging mask (Siemens Star). Again, the imager demonstrated a sub-15 µm resolution with the 11 µm hexagonal pore pattern visible in the image [178, 179]. In 2011, Tremsin *et al.* revisited PSI to conduct nCTs of multiple samples. They were able to separate the lower density layering in a wood block and the individual gunpowder grains (~400 µm size) in a bullet using nCT, captured with 201 projections across 180° at 150 s exposures [180]. In a separate experiment, Tremsin *et al.* captured a nCT of a set of bolts at 8 s exposures, capable of distinguishing the individual bodies in the volume data [181]. Later experiments in 2015 used the MCP to capture hydrogen cracks in Zr alloy, edge effects from a TiN coating on Al, and magnetic field imaging using polarized neutrons [182].

2.5.3 Neutron Microscope

The concept of a neutron microscope stems from the goal of advancing neutron imaging spatial resolution to the 1 µm limit, commonly reached by X-ray analogs. The general approach to such a system varies, building off current technologies as a basis for extending present state-of-the-art capabilities. While a true "neutron microscope" stems from the application of cold neutron Wolter optics [183], other systems aim to achieve comparable results.

Trtik *et al.* explored the possibilities of a neutron microscope using an advanced optics stage coupled to a high-resolution CCD or scientific complementary metal-oxide semiconductor (sCMOS). Coupling the objective lens from a lithography instrument (0.8 µm resolving power) to a sCMOS of 6.5 µm pixel size, the effective image pixel size for the neutron microscope came to be 1.5 µm. With a thin Gd_2O_2S:Tb scintillation

screen, the system was able to resolve down to 7.6 µm while observing a focused ion beam (FIB) enhanced Siemens Star, milled to a 12 µm period [6]. Pursuing higher neutron detection efficiency, the 2.5 µm thick scintillator film was fabricated with ^{157}Gd enriched Gd_2O_2S:Tb, boosting the neutron sensitivity by over a factor of 3 [184]. In the subsequent iteration, Trtik *et al.* used the $^{157}Gd_2O_2S$:Tb scintillator screen with a custom designed, 13 lens objective. With a further enhanced Siemens Star (8 µm period), the system produced a spatial resolution of 5.4 µm using 33 frames captured with a 30 s exposure.

Hussey *et al.* described a similar approach underway at the National Institute of Standards and Technology (NIST), using a Gadox screen and centroiding of the output scintillation light. Using two Nikon lenses as the objective and ocular lenses, and a Hamamatsu MCP as an image intensifier, the effective pixel pitch measured 1.625 µm. Using event based neutron imaging detection, the system produced a spatial resolution of 2 µm. They proposed that advances in hardware setup, such as coupling to a Timepix for hardware based centroiding, could produce an even lower spatial resolution of 1 µm [186].

Chapter 3

Materials and Methods

This chapter discusses the design, implementation and post analysis methodology applied in this research. The progression of the LISe semiconductor technology spans the single channel sensor, followed by the LISe 16-channel pixel detector (LISe PD), and finally the LISePix. Following a synopsis of the instrument design, the beam line facilities and experimental setup are reported. Finally, the image processing techniques are outlined.

3.1 Sensor Fabrication

Radiation detection and imaging begins with the construction of the acquisition system. At the most basic level, a radiation detector requires a sensing apparatus, and signal processing hardware. In solid--state imaging, the sensing apparatus or material generally consists of a thin film, substrate or refined bulk crystalline material. Solids offer increased atomic packing, resulting in higher density and smaller form factor to achieve desirable detection efficiency. Detector grade LISe presents itself as a single crystal bulk material, destined for operation as either scintillator or semiconductor detector. The following section discusses the preparation of LISe sensors for integration with both operational modes. Particular focus is given to semiconductor detectors, due to inherent system complexity and novelty in the neutron imaging field.

3.1.1 Sensor Preparation

Independent of their future role, LISe scintillators and semiconductors are both prepared for radiological testing in identical fashion. After growth and sectioning of raw material, the LISe sensors have sharp edges and rough surfaces. An optically smooth surface offers benefits in both modes, decreasing photon scattering at the material interface as well as increasing thin film adhesion during contact deposition. Accordingly the first step in sensor preparation begins with etching and polishing.

The raw LISe crystal attains the geometric shape specified by the sensor design through rough polishing. Using a wet polish with 1.0 µm diamond particle polishing compound, the sensor is manually polished with a 1,200 grit, and then 2,400 grit silicon carbide polishing pad. This stage is used to flatten uneven edges and remove large lattice defects from the crystal. The addition of diamond polishing paste helps to smooth and grind any LISe shards that break free during bulk removal, preventing large streaking or potential cracks.

A subsequent mechanical wet polish further reduces surface roughness while also planing the two primary sensor surfaces. The crystal is mounted to the polishing chuck using crystal bonding wax, providing a soft layer between the sensor back face and stainless steel chuck. The lapping pads consist of 3 mil thick polyester disks coated with a diamond resin, ranging in diamond particle size from 30 µm to 0.1 µm. Again, the diamond paste containing 1 µm particle compound is used, transitioning to a 0.1 µm compound once the pad particle size drops below 1 µm. The weighted piston crystal chuck applies uniform pressure across the crystal surface, evenly polishing the sensor face along the abrasive wheel. Polishing speed is minimized to reduced vibrational shock in the relatively soft LISe crystal. After the first side is polished, the polishing chuck is heated on a hot plate, softening the wax so the crystal may be flipped to polish the back face.

After mechanical polishing, the sensor is removed from the crystal bonding wax and thoroughly cleaned in acetone to remove any remaining crystal bonding wax. The crystal bonding wax has reduced sensitivity to the subsequent chemical etch and may lead to uneven surfaces if residual wax coats the surface. A final methanol (MeOH) rise is used to remove acetone streaking and any surface deposits remaining from the mechanical etching process. It was beneficial to store the sensor in a small beaker of MeOH during the elapsed time between polishing and chemical etching. The MeOH helped prevent any further contamination or surface reaction, prepping the sensor for the chemical etching process. At this stage, the sensor was chemically etched using a bromine/methanol (BrMeOH) solution as described in Appendix A.1. The chemical etch provides a final clean before photolithographic processing, obtaining an optical finish and minimum surface roughness.

3.1.2 Photolithography and Patterning

Semiconductor detectors require electrical connections to couple the senor bulk to a voltage bias. Applying a voltage through the bulk creates an internal electrical field, used to drive radiation induced charge particles towards the electrical contacts. The contacts play a vital roll in signal charge generation, with well adhered metal providing a uniform electrical field. The metal contacts throughout this study were deposited using radio frequency (RF) plasma sputtering via the ATC-Orion 5 UHV Plasma Sputtering System (AJA sputterer).

Photolithography is a fabrication technique using precision optics to transfer a microscopic pattern to the surface of a thin film or bulk crystal material. Imaging detectors use photolithography to obtain the micron level features required for state-of-the-art resolution capabilities. The sensor is coated in a photosensitive resin, activated by the ultraviolet (UV) light, hardening the resin as described in Appendix B.2. Forming a

protective layer, the photoresist selectively blocks the metal sputtered by the plasma deposition process.

Multiple contact recipes were tested in experimentation, using the RF plasma deposition process [187]. Pure metals were tested including: aluminum, indium and gold. Ohmic contacts were successfully formed using indium and gold layers, suitable for reverse biased radiation detection. Having a low melting point and a stoichiometric component in the LISe crystal, indium served as an initial contact candidate. After refining the photolithography process and subsequent packaging sequence, the use of gold contacts became the standard practice.

3.1.3 Packaging and Electronic Coupling

The final step in fabricating the radiation detection system is coupling the sensor to the readout electronics. Electronic coupling takes many forms, including permanent and non-permanent mounting solutions. In the laboratory, crystal samples may be readily exchanged for testing using non-permanent, spring loaded contact systems. Generally the sensor is placed on a conducting pad, and held down by the very small compressive force from a helical or cantilever type spring. Because the sensor is removable, the sample may be cleaned and properly stored in between testing to preserve the material quality and sensitive surfaces. Some characterization systems have specialized substrate mounting to subject the sensor to low vacuum or a temperature gradient, also requiring a non-permanent coupling solution. Furthermore, probe stations with microscopic positioning are essential for testing individual channels in pixelated devices.

After a sensor demonstrates preliminary radiation sensitivity and favorable electronic behavior, the sensor is installed in a more permanent configuration. In single channel counters and few channel pixel detectors, wirebonding achieves a semi-permanent bond (see Appendix B.4). The sensor is first mounted to a substrate carrier or printed circuit board (PCB) using high purity silver paste if a bottom contact is present, or non-conductive crystal bonding wax if the device only utilizes the top surface. A micron scale metal wire is then bonded between each pixel on the detector and a corresponding bond pad on the substrate carrier or PCB, forming an electrical connection with the appropriate node in the readout system. The substrate carrier or PCB may be removed from the detection system, with minor soldering, when not actively in use to store the sensitive crystal. This method of coupling is considered semi-permanent because the wires may be carefully pulled from the crystal, and the bonding paste or wax may be chemically dissolved, returning the sensor with only cosmetic imperfections. Generally, wirebonding offers enhanced contact performance over compression methods, creating a consistent electrical junction that is more resistant to electromechanical vibrations and shock.

The most preferred method of coupling in refined imaging systems is flip-chip bump bonding (see Appendix B.5). This technique places the active sensor in proximal contact with the readout electronics, reducing signal line losses and undesirable electronic interference. Each pixel on the detector is directly bonded to its corresponding channel on the readout ASIC using a micron scale bead of metal, typically indium. This bonding scheme creates the most robust mechanical union, however, removing the bonded

sensor from the ASIC can be difficult to near impossible without significantly damaging both the ASIC and the sensor. The sensor/ASIC stack is mounted to a readout PCB and wirebonded to applicable signal bond pads similar to the previous coupling explanation. Using a combination of techniques, an imaging device with thousands of channels may be feasibly constructed with only tens of wirebonds, reducing the overall package form and simplifying the design.

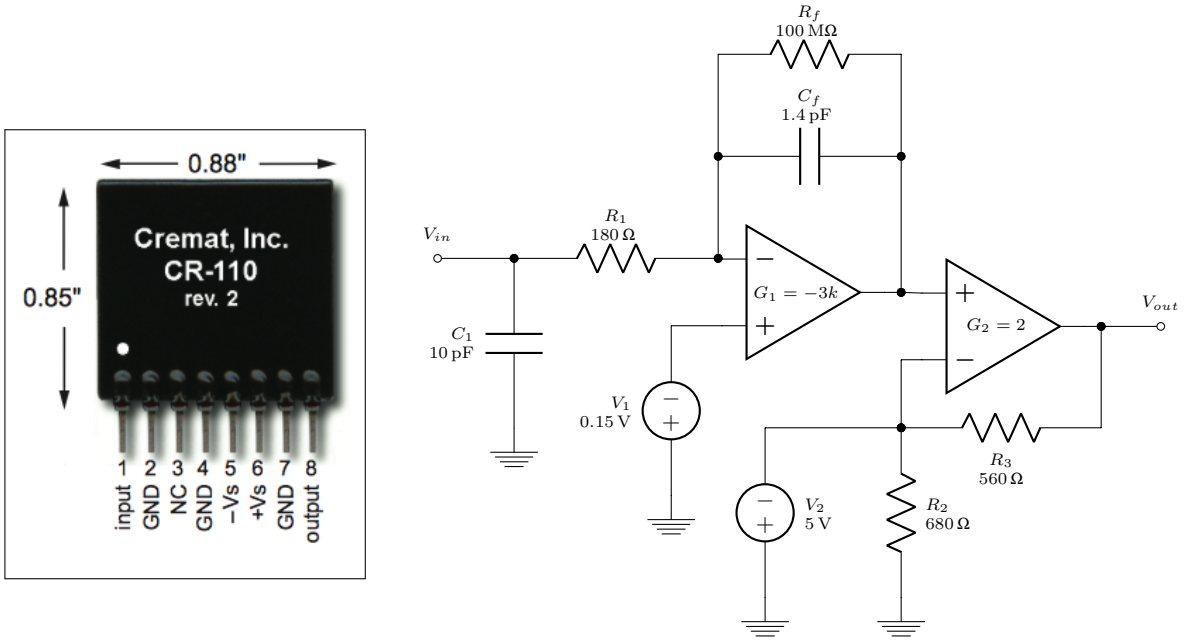
3.2 Early Detector Designs

The radiation detection system was designed around the sensing material, lithium indium diselenide (LISe), and the anticipated neutron radiation. At the most basic level, the detection system consists of the sensor, and the readout electronics used to convert the charge produced by the radiation interaction into electronic signals. During the prototyping phase, various enclosures and readout systems were tested in attempts to refine the signal produced from the LISe sensors.

3.2.1 Basic Readout System

The readout electronics provide the bias, collect the charge induced from the radiation event, process the charge into a current or voltage pulse, and generate a conditioned output for further signal processing. A charge sensitive preamplifier (CSP) handles the signal processing and must be carefully tailored to the charge produced from the radiation sensor. The following three CSPs were tested with LISe: the CAEN A1422, the CR-110 Preamplifier Module (CR-110), and the Amptek A250CF CoolFet featuring the optional Peltier cooled input field effect transistor (FET). The CR-110 (shown in Figure 3.1a) was selected for multiple reasons including: smaller size, circuit simplicity and low cost (∼$50). The basic function of the preamplifier (pre-amp) is to rapidly store the total charge created by the detector, as it generates a current pulse. The feedback capacitor and resistor, C_f and R_f respectively (see Figure 3.1), function as an alternating current (AC) op-amp integrator with direct current (DC) gain control, creating a slow discharge, at V_{out}, in the form of a tail pulse signal. The rise time of the output signal is rapid and typically on the same time scale as the detector charge collection. Ideally, the rise time of the pre-amp should be roughly equivalent to the pulse width of the current pulse from the detector. The decay time is much longer to ensure the total charge from the detector is collected, allowing the pre-amp to produce a voltage output proportional to the integrated charge.

While the pre-amp chip handles signal processing on the readout PCB, the supporting power electronics provide high-voltage bias to the detector via AC coupling, as shown in Figure 3.2. The use of AC coupling isolates the DC bias voltage from the pre-amp while still permitting the superimposed AC signal from the detection event to be passed to the pre-amp. The high-voltage bias is cleaned via passive filters following a ladder design; very large resistors ($R = 10\,\mathrm{M\Omega}$) are connected in series with the bias and small capacitors ($C = 0.01\,\mu\mathrm{F}$) are connected in parallel to the ground after each resistor. Regarding the interconnects,



(a) CR-110 chip

(b) CR-110 circuit schematic

Figure 3.1. Cremat CR-110 Preamplifier Module chip pinout and circuit diagram.

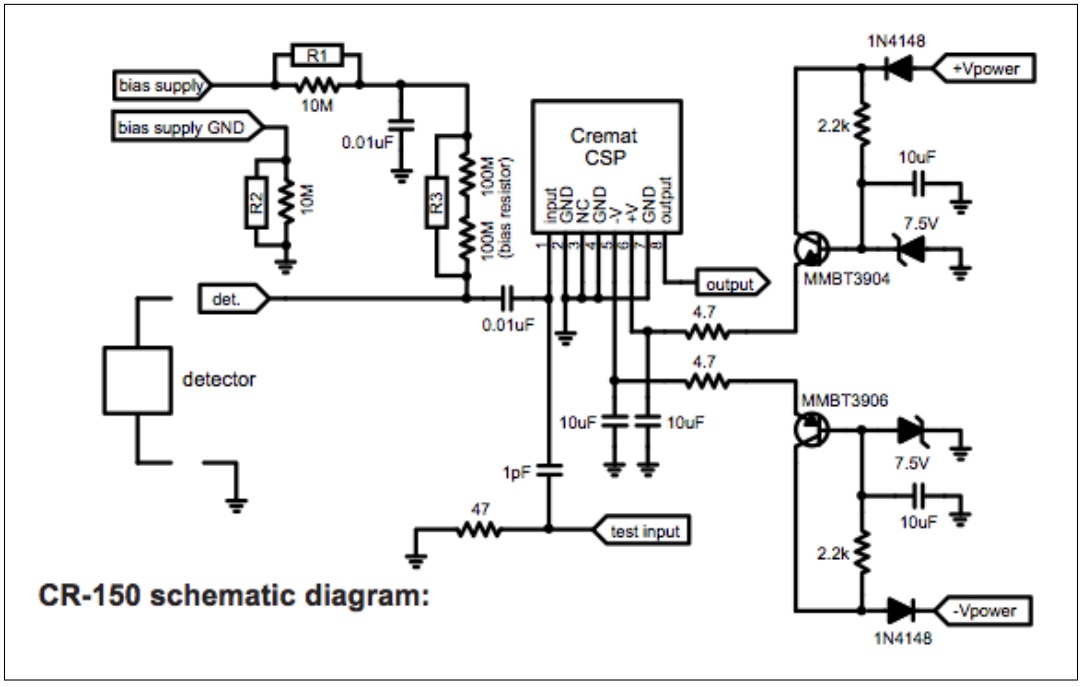


Figure 3.2. Cremat CR-150 Preamplifier PCB schematic diagram.

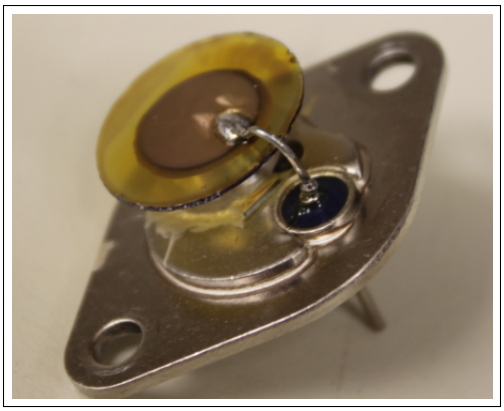


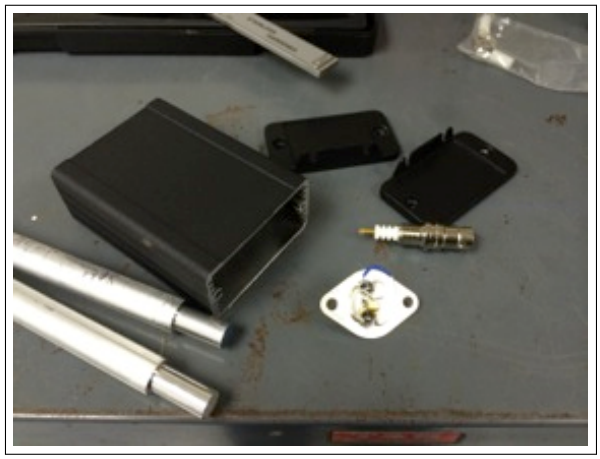
Figure 3.3. Original single channel LISe prototype using TO header.

the high-voltage bias is applied via safe high-voltage connector (SHV), permitting voltages exceeding 500 V, while the output signal uses the more traditional Bayonet Neill-Concelmann (BNC) (50 Ω). Low-voltage (±12 V) power supplies are used to drive the pre-amp circuitry and connectors vary based on user or designer preference.

3.2.2 Single Channel Counting Detector

The prototype LISe single channel detector was designed around a transistor outline (TO) header, shown in Figure 3.3. Commonly used for transistors, rectifiers, and integrated circuits, the TO-3 packaging specification provided an ample mounting pedestal for the LISe sensor, typically used by power electronics as a heatsink. Two signal leads are integrated into the packaging, backfilled with a glass insulator. The top of the leads serve as a bonding pad, facilitating wirebonds to the top contact. While the packaging was useful in handling the sensor, an enclosure was required for electromagnetic interference (EMI) shielding, as common with most radiation detectors.

A simple enclosure was designed to accommodate the specific TO header, shown in Figure 3.4. The enclosures fabricated in this work all utilized an aluminum construction with beveled flanges to create a light-tight seal. Both softer and lighter than steal, aluminum may be formed into rigid enclosures that are easy to machine and relatively neutron transparent. Standoffs were machined from aluminum cylinder stock (Figure 3.4a), providing the ground connection to the enclosure (Figure 3.4b). A bulkhead mounted SHV (Figure 3.4c) provided a matched connection to couple with one of the pre-amps discussed in Section 3.2.1. The center pin of the SHV connector carried the high-voltage bias, connected to the TO header via pin clamp, soldered to the back lead. The assembled enclosure is shown in Figure 3.4 along with the TO-3 package for reference.



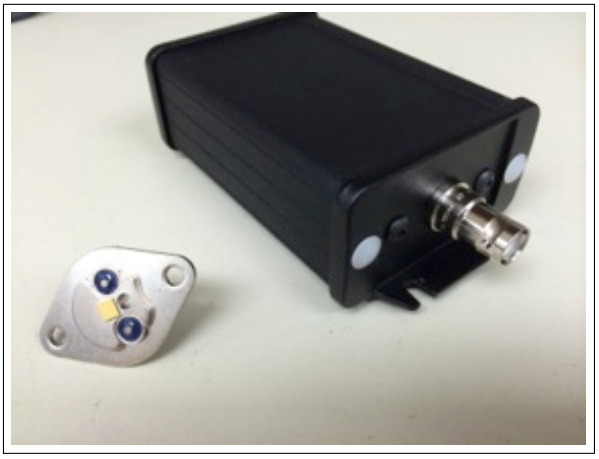
(a) raw enclosure components



(b) TO header connection



(c) exterior SHV connection



(d) assembled enclosure

Figure 3.4. Custom testing enclosure for TO header package.

3.2.3 Prototyping LISe Semiconductor Neutron Imager

A prototype pre-amp was fabricated to study the process of designing and manufacturing custom PCB electronics (see Figure 3.5). The design was similar to the commercially available CR-150 Preamplifier PCB (CR-150) used to drive the Cremat pre-amp. The circuit was drafted in EAGLE (Easily Applicable Graphical Layout Editor), a computer-aided design (CAD) software for circuit layouts and routing. A photomask was fabricated by using an inkjet printer to transfer the circuit design to a projector transparency sheet.

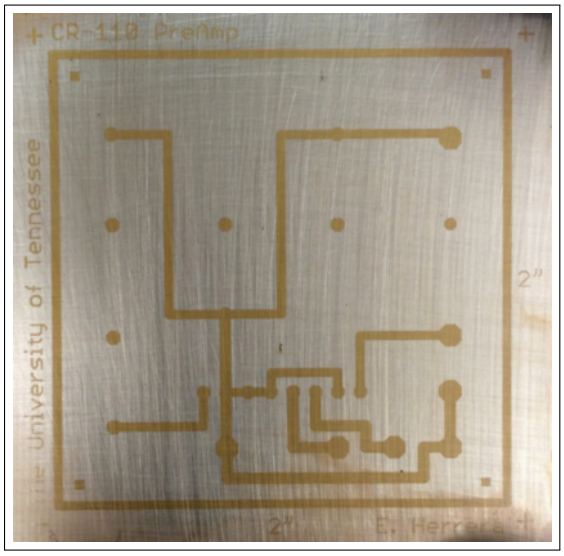
The pre-amp started as a single-sided Flame Retardant 4 (FR-4) board clad in 1 oz of copper. After coating the PCB in photoresist, the pattern was transferred using positive photolithography (see Appendix B.3), creating an etch resistant coating over the circuit traces (Figure 3.5a). A subsequent wet chemical etch (see Appendix A.2) removed the copper cladding from the PCB, leaving only the finalized circuit traces (Figure 3.5b). The board was drilled to create vias for through-hole components and polyethylene coated posts were installed to provide air insulated mounting for noise reduction (Figure 3.5c). Once the circuit components were solder to the PCB, the board installed in an aluminum enclosure equipped with appropriate signal and power bulkhead connectors as shown in Figure 3.6. The tight fitment of the board in the enclosure reduced the length of the interconnect wires to prevent signal loss and noise. A chip socket sized to the CR-110 allowed hot swapping in the event a chip was damaged or to test with other versions of Cremat CSPs. The standard SHV and BNC connectors were utilized for high-voltage bias and signal output respectively, along with banana sockets to directly connect the module to a voltage controlled DC power supply. In conjunction with the TO header detector module, these two components served as a proof of concept for the LISe pixel detector.

3.3 Pixelated 16-Channel Detection System

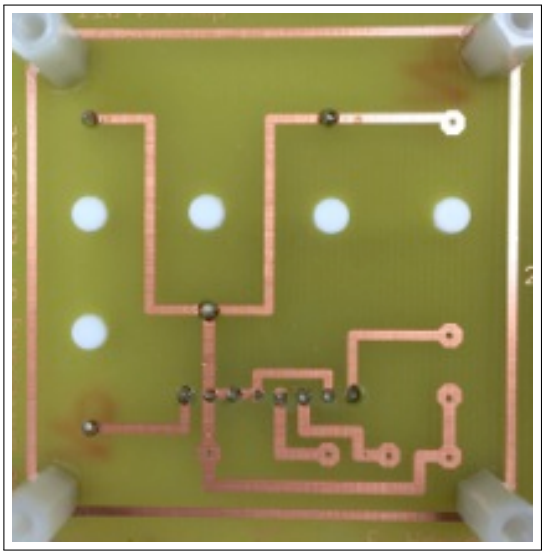
Expanding on the design of the single channel system, the LISe PD featured a multi-channel pixel array. Spanning a 4×4 grid, the LISe PD took the first steps towards solid-state neutron imaging. The new system required a redesign to incorporate the 16 individual CR-110s and a custom substrate PCB to accommodate wirebonding.

3.3.1 Electronic Readout System

As the system would house both the active sensor and the readout electronics, a larger aluminum enclosure was necessary. A split-body aluminum extruded enclosure was selected for its internal capacity as well as the PCB slots designed to secure circuit boards, show in Figure 3.7. The enclosure's external dimensions measured $8.5 \times 6.15 \times 3\,\text{in}^3$ with room for a 6 in wide board with up to a 0.070 in thickness. A CAD model of the system was generated prior to fabrication to ensure the narrow fitment would leave enough clearance for the bank of CR-110s. The pre-amps were connected to two identical 8-channel readout boards, installed



(a) photoresist pattern on PCB

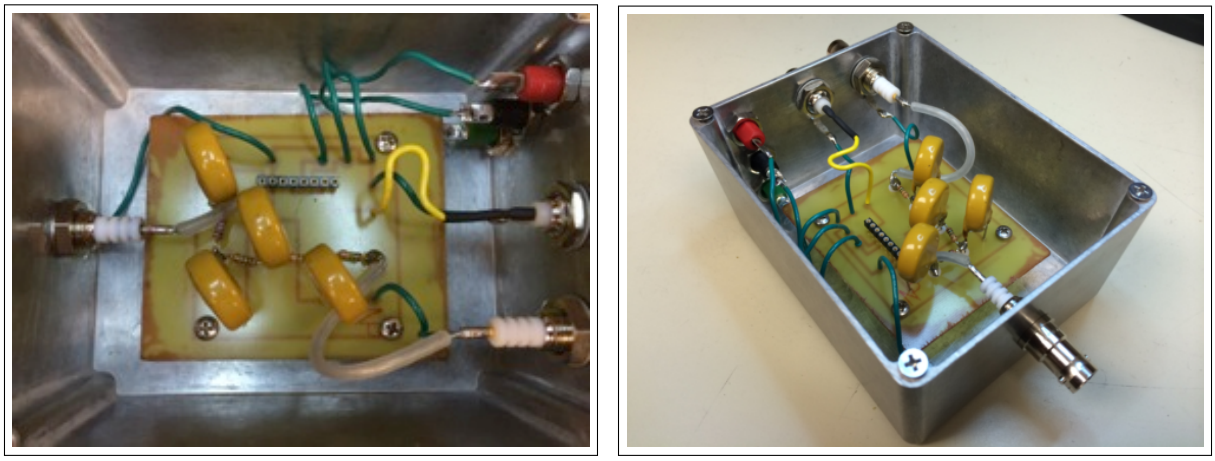


(b) etched and drilled PCB



(c) insulated through-hole components on PCB

Figure 3.5. Prototype single channel pre-amp PCB for Cremat CR-110 chip.



(a) internal circuitry (b) pre-amp assembly

Figure 3.6. Prototype single channel pre-amp. Readout PCB assembled in EMI shielded enclosure (lid not shown).

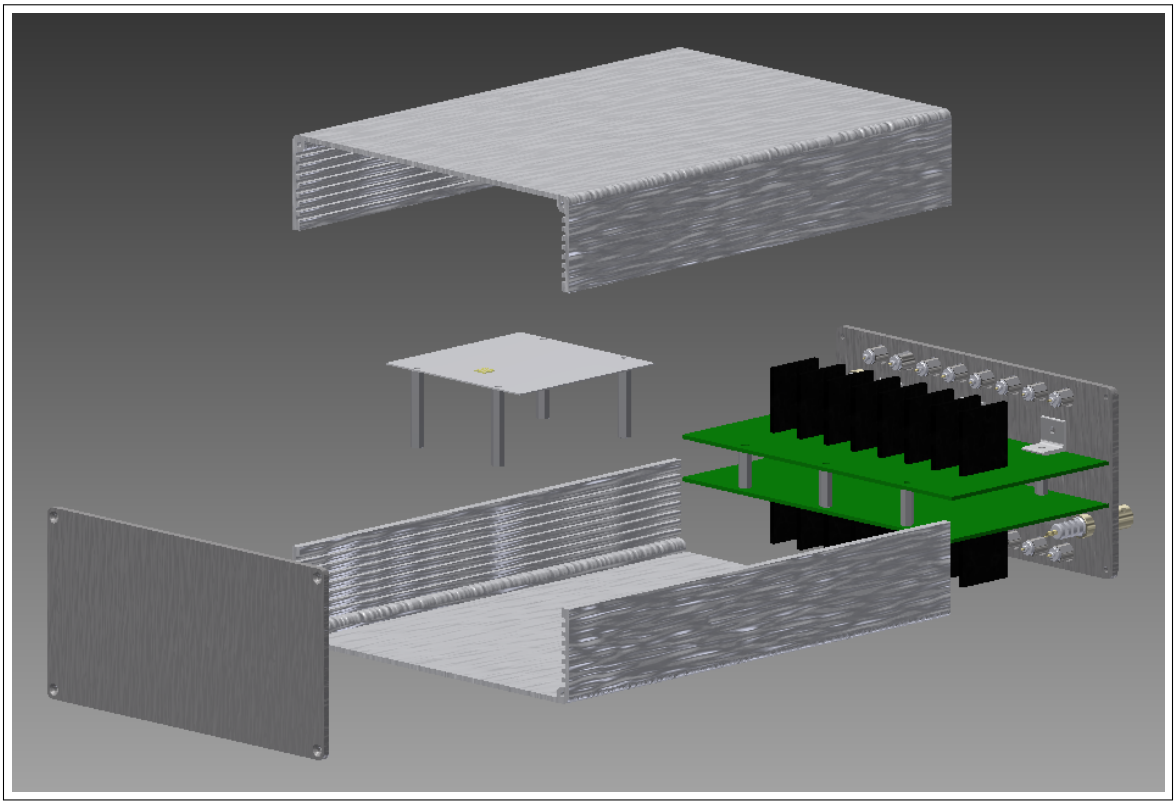


Figure 3.7. LISe PD CAD model illustrating components and assembly.

in an opposing configuration. With this design, the entire pre-amp assembly was fabricated outside of the enclosure, attached to one of the enclosure end caps. The high-voltage and signal lines were routed on top and bottom of the PCBs while the low-voltage chip power was routed between the boards, as shown in Figure 3.8. Keeping the power and signal lines separate helped to reduce potential sources of noise in the board, as well as isolating their corresponding circuit traces to the inside and outside layers respectively.

The ground planes of the two PCBs were connected via aluminum standoffs, also acting as structural elements. Joining the PCB assembly to the end cap, six aluminum angle brackets formed a ground connection between the PCBs and the bulkhead connections, securing the boards in place. Low-voltage power was again supplied via banana sockets for direct connection to a variable DC power supply. Independent high--voltage bias lines were routed to each PCB via SHV connectors, requiring two external power supplies at matched voltage. Due to their large form factor, BNC connectors were replaced with LEMO 00 coaxial connectors (LEMO 00s), another standard $50\,\Omega$ terminator used in the nuclear industry for high density cabling applications.

The original sensor board concept is depicted in Figure 3.7, featuring a thin alumina substrate. The substrate was to be mounted directly to the base of the enclosure and wires would be solder between the substrate board and the pre-amp PCBs. Eventually this design was shelved for a standard PCB approach as described in the following Section 3.3.2. In both iterations, the sensor board was placed on the opposite side of the enclosure, locating the pre-amp assembly outside of the neutron beam. Because the enclosure is aluminum, little neutron shielding would be offered to the readout electronics, potentially damaging the circuits, creating secondary radiation noise, and activating various constituent components.

3.3.2 Sensor Board Design

The sensor board or substrate PCB provides the physical mount for the radiation sensor while also containing the electronic traces needed to couple the readout electronics. In attempts to minimize the neutron interactions with the sensor board itself, a thin alumina substrate was fabricated into a sensor board. The alumina board (Figure 3.9), measuring $3 \times 3\,\text{in}^2$ and $635\,\mu\text{m}$ thickness was first metalized using the negative photolithography process and subsequent plasma sputtering (see Appendix B.2). The board design was routed in EAGLE with emphasis on shallow bends and near equivalent length signal traces. A standard quartz photomask (see Figure B.1a) was generated from the circuit design (see Figure 3.9a) and a thin layer of aluminum was deposited on a single side of the PCB. The initial aluminum metalization offered a relatively inexpensive pattern guide for locating the circuit vias. Using a 2 mm diameter diamond studded ceramic drill, each hole was manually carved through the ultra hard alumina substrate. Holes were drilled while submerged in a water bath to remove heat and debris from the drilling site while also lubricating the cutting surface. Even so, some boards cracked during this fabrication step and the process had to be restarted. After successfully drilling all vias in the substrate, the board was polished to remove the guide metal and a second photolithograhy run was used to deposit the final gold layering as shown in Figure 3.9b.

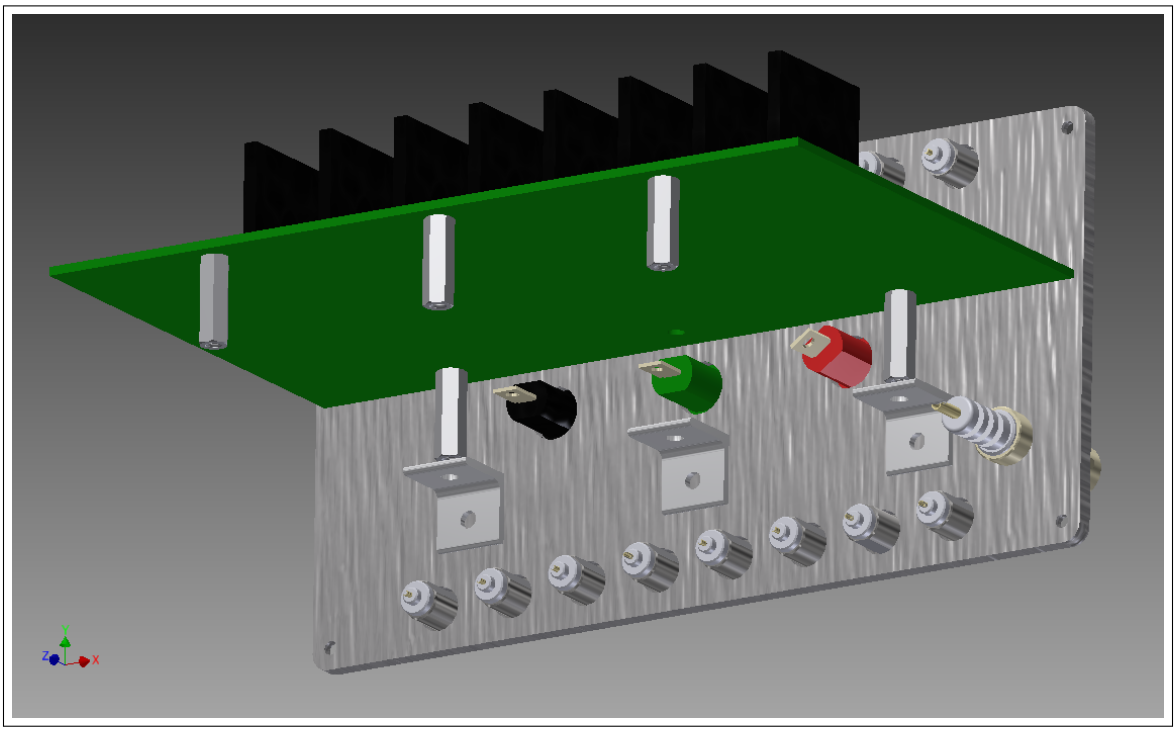
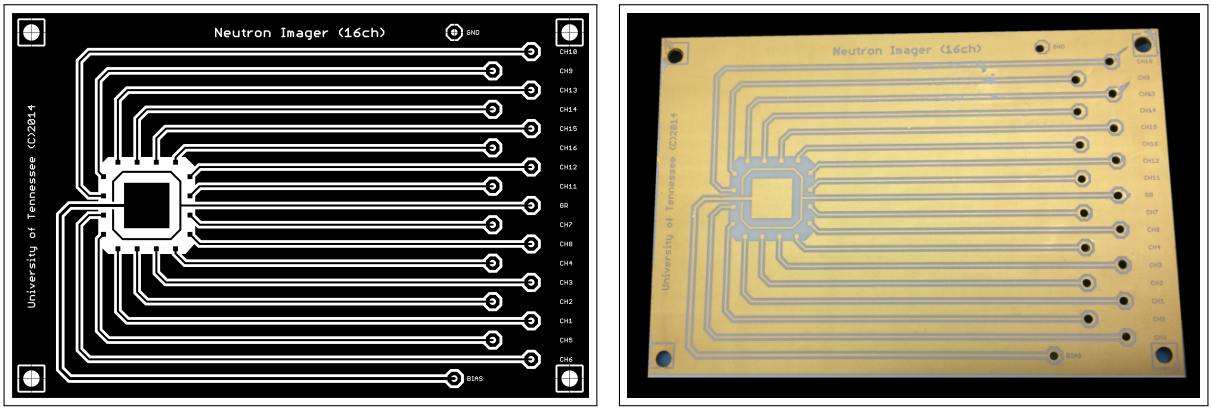


Figure 3.8. LISe PD pre-amp assembly (upper PCB shown).



(a) negative photomask for PCB fabrication

(b) gold plated alumina PCB

Figure 3.9. Neutron transparent readout PCB for LISe PD.

While a prototype alumina substrate board was successfully fabricated, the final product did not exhibit favorable electronic characteristics. The line resistances across the surface were considerably large due to the trace layer thickness, measuring <1 µm versus 34.79 µm for a 1 oz copper clad FR-4 board. Soldering to the board also proved incredibly difficult, with only limited wetting occurring between the copper wire and the solder vias. These disadvantages outweighed the benefits of the alumina board, and a standard FR-4 board was elected as the replacement. The revised substrate board was sized similar to the professionally manufactured pre-amp boards, fitting in the enclosure PCB slots for easier mounting. High-voltage bias lines (red) were routed on the top of the board, shown in Figure 3.10, while the signal output traces (blue), run perpendicular across the bottom of the board. The bond pads form a circle around the main sensor mounting pad, abruptly connected to a via traversing the PCB to the signal trace on the bottom of the board. Furthermore, top and bottom ground planes filled the remaining space around the traces to eliminate stray current leaking between signal lines.

Both ground planes feature a cutout region surrounding the sensor bonding pad, minimizing the amount of material immediately next to the sensor. Copper is used in neutron activation experiments due to its appreciable cross section, and activating the copper cladding on both sides of the board would introduce undesirable γ-ray background (see Appendix D.3). The light green circle surrounding the sensor in Figure 3.11 represents the cutout region. The primary experimental beamline at HFIR offered an adjustable beam window via attenuating slits, so neutrons could be directed to only the cutout region and crystal. The nine red copper wires at the top of the image correspond to the signal and guard ring lines, soldered directly between the substrate and pre-amp PCBs. Not shown are the eight matching white wires connecting the remaining channels to the second pre-amp PCB.

3.3.3 Sensor Design

The raw LISe crystal becomes a semiconductor detector through the negative photolithography process outlined in Appendix B.2. A photomask template is drawn using a CAD editor such as AutoCAD® and the schematic file is professionally processed into a 5 in quartz photomask. A completed sensor undergoes two rounds of lithography, one side producing the broadface contact and the other side receiving the pixel array and guard ring, shown in Figure 3.12. The LISe PD sensor measured $5 \times 5\,\mathrm{mm}^2$ with a 560 µm thickness as reported for the second version of the 4×4 array [145]. The sensor was bonded to the substrate PCB using silver paste and the pixel metalization was wirebonded to the PCB bond pads using the Kulicke and Soffa (K&S) 4500 Digital Series Manual Wire Bonder (wire bonder) following the process described in Appendix B.4. The first version of the sensor used larger 1,000 µm pixels to span the majority of the active area as shown in Figure 3.13. Initially, gold contacts demonstrated poor adhesion during wirebonding, due to the unrefined fabrication process. To overcome this issue, In_2Se_3 contacts were deposited in attempts to form stronger covalent bonds with the crystal bulk. While the first version of the sensor was bonded at each channel, some bonds did not make adequate electrical connection and others eventually broke during

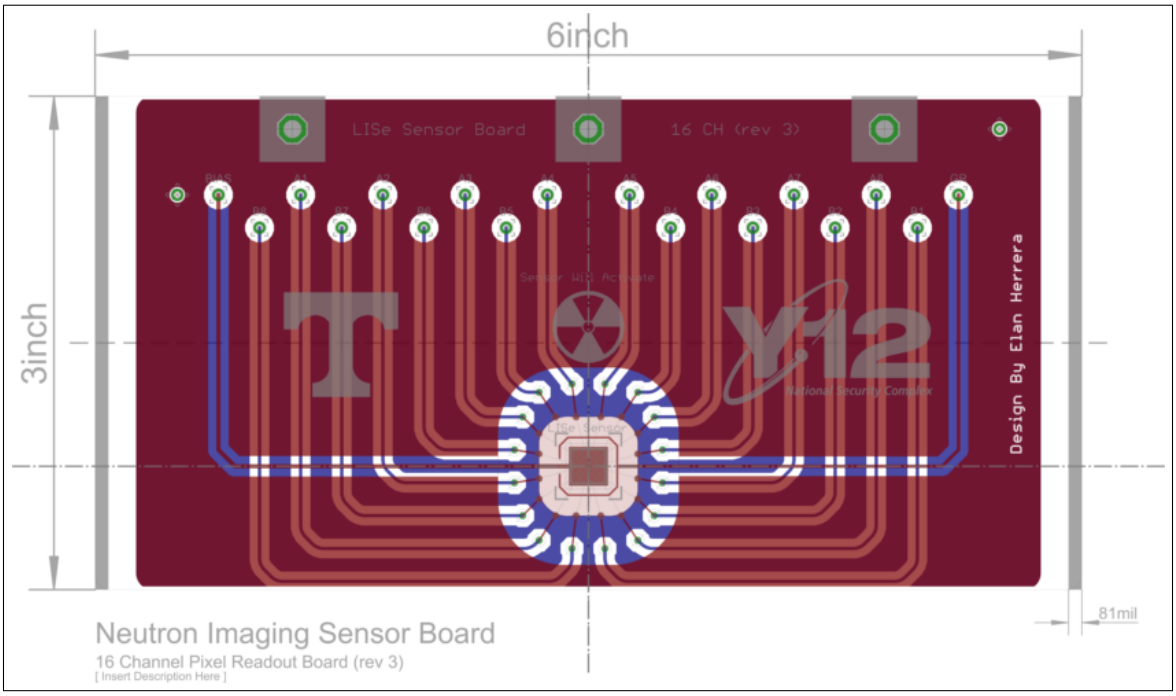


Figure 3.10. Layer diagram of LISe PD generated using EAGLE for PCB manufacturing (board dimensions $6 \times 3\,\mathrm{in}^2$).

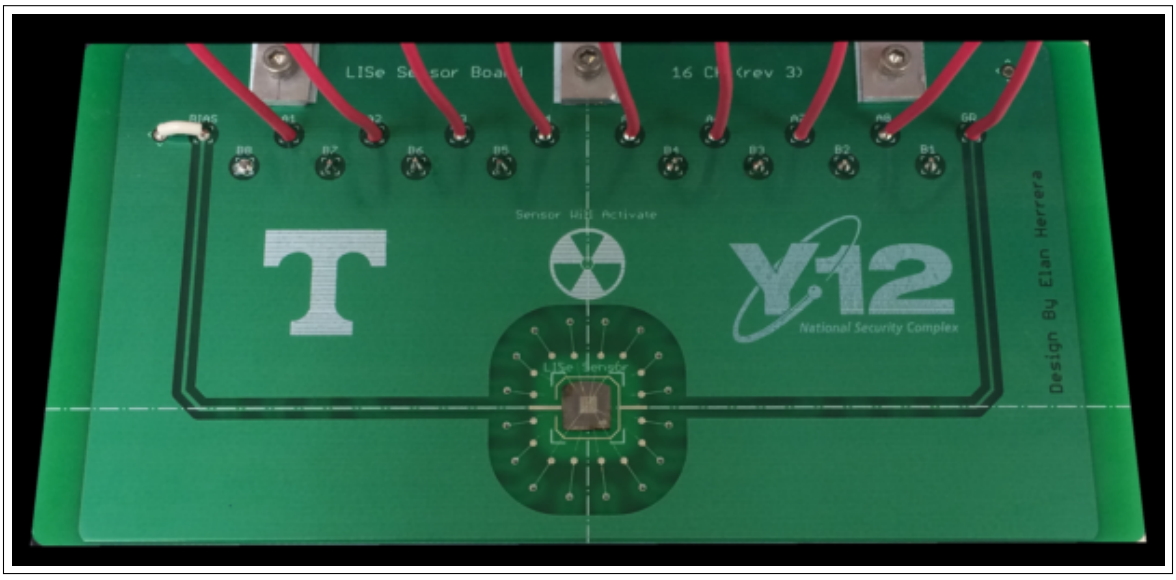


Figure 3.11. Assembled LISe PD sensor readout board with v2 sensor (board rev. 3).

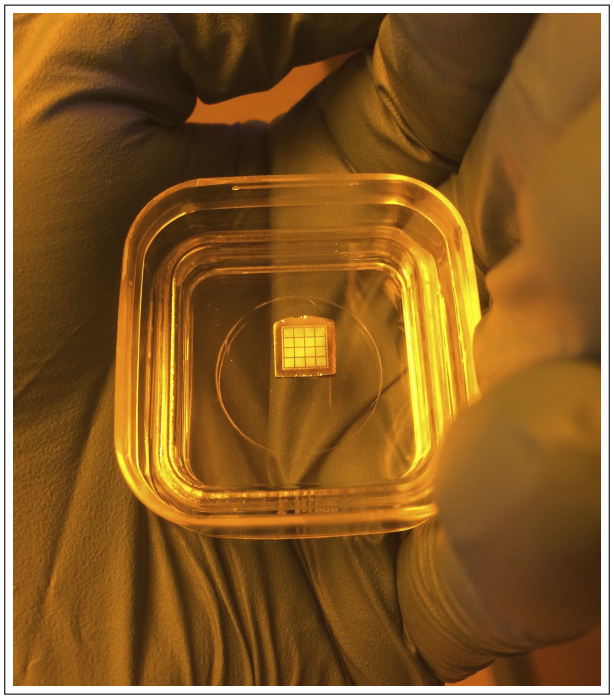
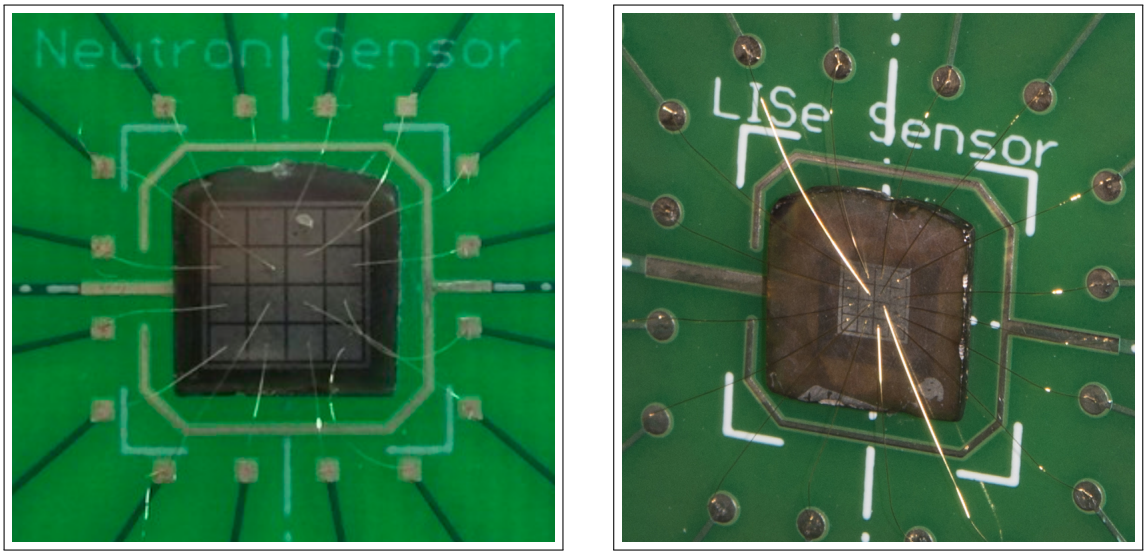


Figure 3.12. Photo of LISe PD sensor (v1) after photolithography process in sensor carrying case.



(a) LISe PD (v1): lithium selenide contacts, 1,150 µm pitch, 1,000 µm pixels, 150 µm guard ring

(b) LISe PD (v2): gold contacts, 550 µm pitch, 500 µm pixels, 100 µm guard ring [145]

Figure 3.13. LISe PD electronically coupled using 25 µm gold wire bonds.

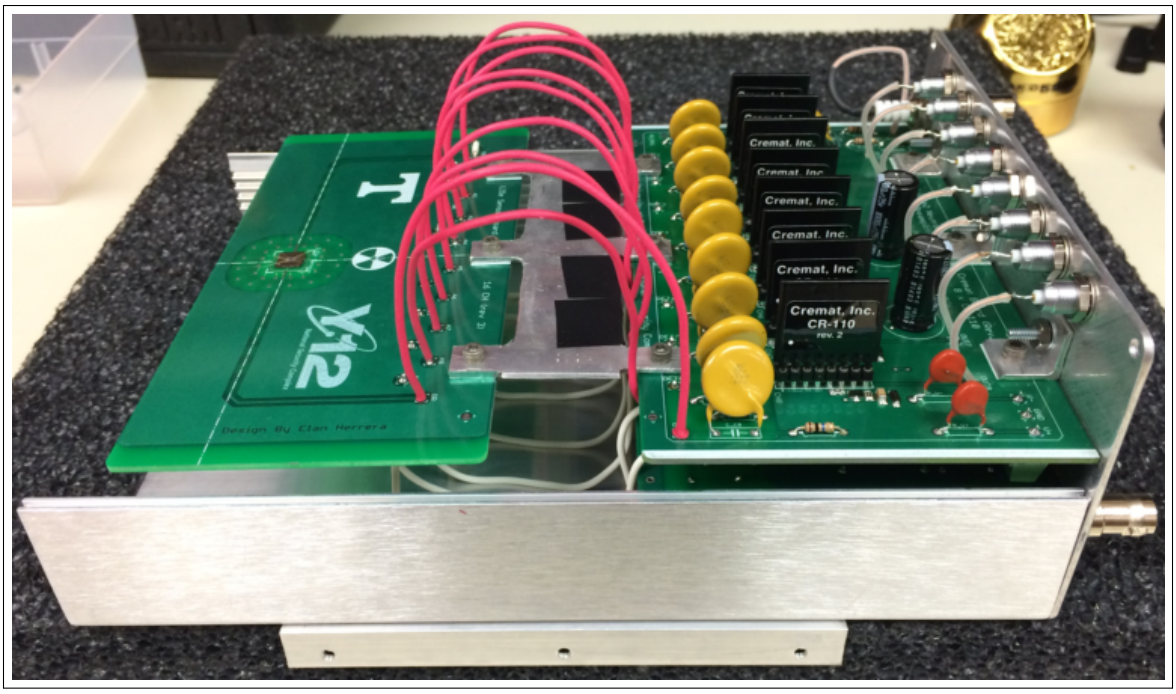


Figure 3.14. LISe PD with open lid to expose internal circuitry [145].

transport or operation; only two channels were able to effectively collect neutron data.

Serving as a proof of concept, the v1 sensor demonstrated functional neutron detection paired with the pre-amp and external acquisition electronics. Lessons learned during processing and fabrication were applied in the second version sensor, shown in Figure 3.13b. A refined polishing and wet etch process resulted in reduced surface roughness and presence of scratching (see Appendix B). Fine tuning the plasma sputtering process parameters, including substrate heating, improved the gold contact adhesion on the LISe crystal, returning to the original design. Reducing the pixel pitch to 500 µm focused the active array to the center of the crystal, far enough from the edge to avoid field effects. Depositing a layer of gold roughly 150 nm thick proved sufficient to successfully wirebond all 16 channels and the surrounding guard ring.

3.3.4 LISe Pixel Detector Assembly

The operational LISe PD offers a modular design, shown in Figure 3.14. With the top lid removed, the sensor PCB floats above the bottom half of the enclosure, suspended by the aluminum grounding bracket. The lid is slid on from the left, firmly securing the sensor PCB in one of the slots cut into the sidewall. Arching jumper wires were used to connect the sensor PCB and the pre-amp module, preventing high resistivity pinch points. The large yellow input capacitors were rated for high-voltage applications, supporting the use of highly resistive sensors biased up to 2 kV. In this configuration, each CR-110 module could be visually inspected for damage (usually indicated by bubbling under the polymer film coating) and quickly replaced.

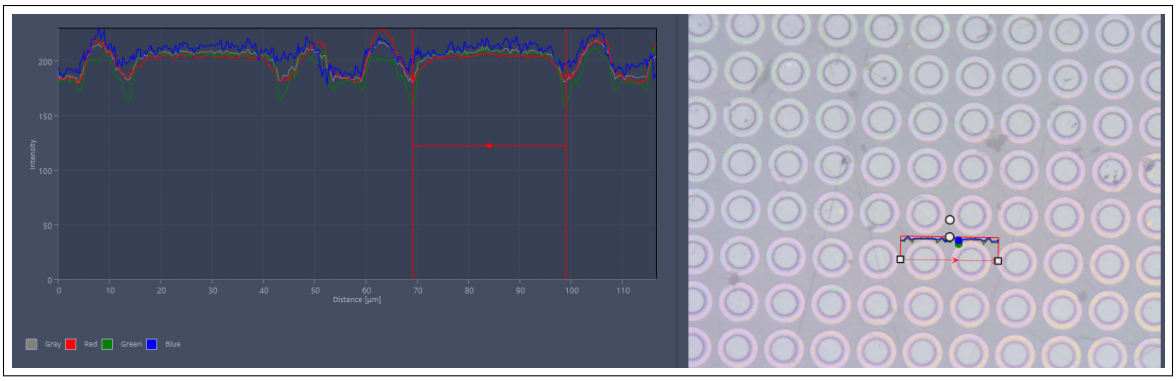


Figure 3.15. Micrograph analysis of exposed photoresist pattern on LISePix sensor. Exposed sensor area corresponds to anticipated pixel diameter of 30 µm. Resist sidewalls exhibit deep undercut (∼ 8 µm), facilitating resist removal.

3.4 Timepix Coupled Neutron Imaging System

Coupling the LISe semiconductor neutron sensor to the Timepix formed a novel high-resolution neutron imaging platform [107]. The LISePix imager establishes the first high-resolution direct conversion semiconductor system for thermal neutron detection and imaging.

3.4.1 LISePix Sensor

Fabricating the LISePix sensor followed an identical process to the LISe PD sensor, however process control was critical in producing the microscopic 55 µm pitch pixels. Invisible to the naked eye, the 30 µm pixel contacts require micrograph analysis throughout the photolithography process to ensure proper pattern transfer and metallization. The undercut present in the resist sidewall contributed significantly to the resulting pixel diameter, shown in Figure 3.15. The deep undercut significantly increased the release rate during liftoff, cleanly removing the large perforated top layer of metal without damaging the contact pads. After removing the excess metal, the contact pads are inspected to ensure even deposition across the diameter and to very the size corresponds to the nominal value, shown in Figure 3.16. Carefully scrutinizing the full pixel array served as a final quality control measure before sending the LISePix sensor to be bump-bonded. Large defects are not suitable for such a device and required subsequent cleaning and reprocessing. Any small defects were noted to account for potential hot or dead pixels in the final device. Generally, a properly prepared surface produced consistent metallization across the sensor seen in Figure 3.17. Reflective light microscope (LM) images (Figure 3.17a) reveal pixels with thin metallization, generally characterized by their dull reflection and shift in emitted light spectrum. Meanwhile transmitted LM images (Figure 3.17b) offer stark contrast between the opaque metal and transparent crystalline regions, illuminating inconsistencies in pixel size or shape.

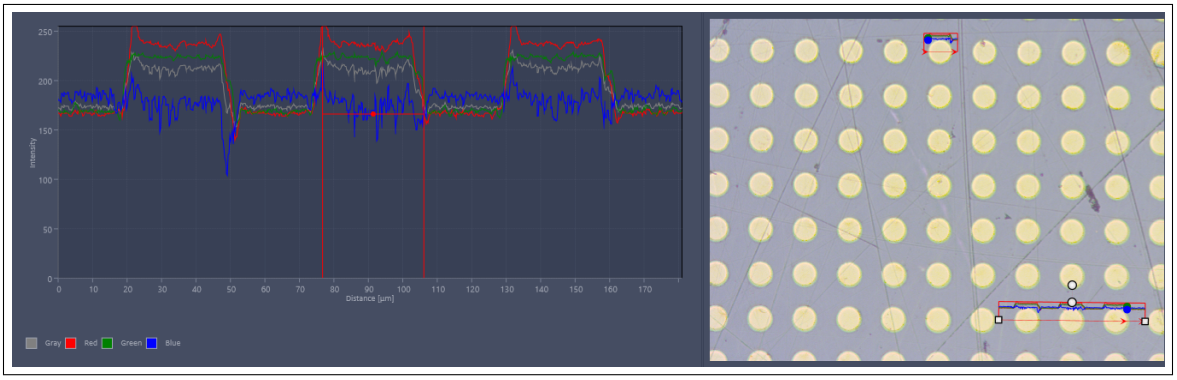
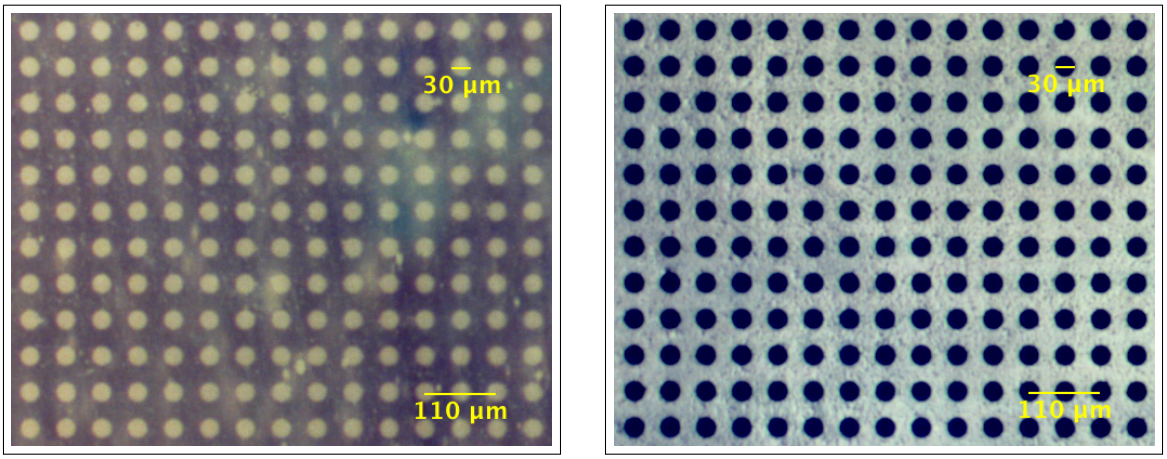


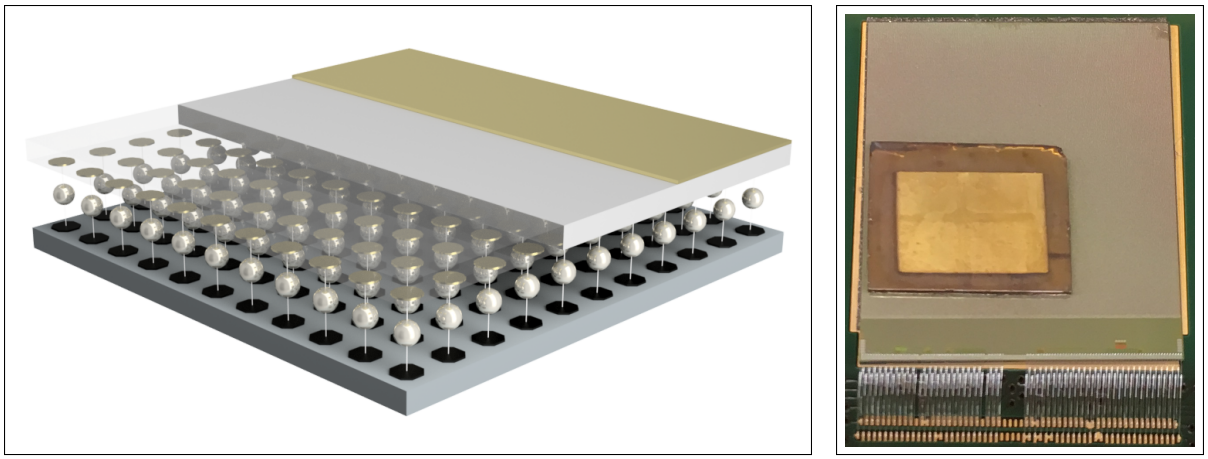
Figure 3.16. Micrograph analysis of gold contacts on metalized LISePix sensor. Pixel diameter correctly evaluated at 30 µm with a 55 µm pixel pitch.



(a) reflective light microscope

(b) transmitted light microscope

Figure 3.17. LISePix pattern with 30 µm diameter gold contacts (12 × 15 pixels shown).



(a) breakaway CAD model of LISePix sensor [107]

(b) photo of LISePix sensor bump-bonded to Timepix

Figure 3.18. LISePix sensor layering design.

3.4.2 Timepix ASIC

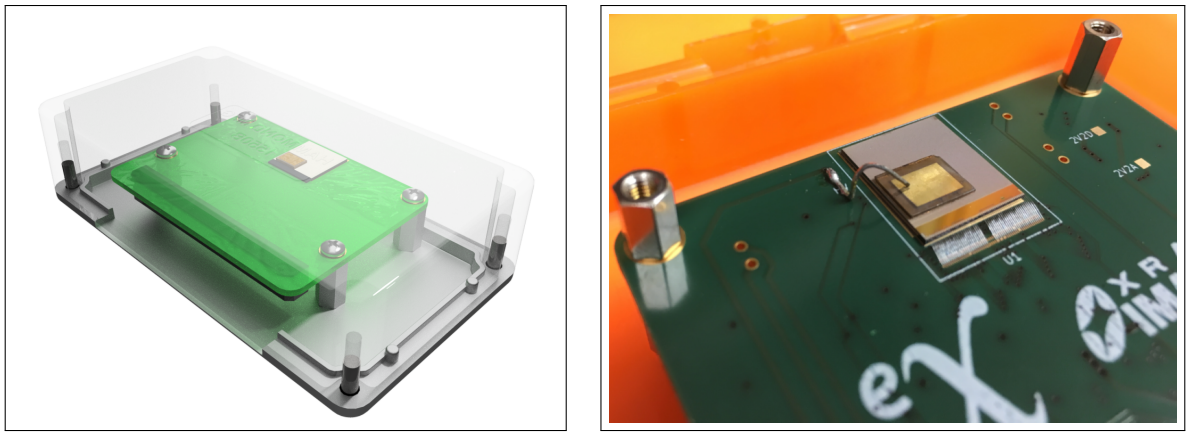
The Timepix v2 ASIC, derived from the Medipix2, offers a high-resolution multi-mode platform, applicable for neutron imaging. The ASIC contains a 256×256 array of pixels, each containing its own pre-amp and discriminator with threshold input. Consuming approximately 13.5 µW of power, each $55 \times 55\,\mu m^2$ pixel offers a dynamic counting range, spanning 0 to 11,810 in this system, registering events exceeding the threshold when operated in event counting mode. To electronically couple the ASIC, a 20 µm octagonal anode caps each pixel [188]. Shown in Figure 3.18, the ASIC electrodes (colored black) align with the corresponding 30 µm diameter gold LISe contacts (see File S1). Sandwiched between each pair of contacts, a 35 µm diameter indium bump bond (colored silver) created an electrical contact and the mechanical bond between the LISePix sensor and the Timepix ASIC. The gold pixels on the LISePix sensor measured 100 nm thick, while the broadface contact on the other side presented a slightly thicker 125 nm gold layer. Approximately $9.0 \times 7.0\,mm^2$ in size, the 550 µm thick crystal covered over a quarter of the available channels on the ASIC. After assessing the device response, the active area covered an effective array of 150×100 pixels, representing an area of $8.25 \times 5.50\,mm^2$, in accordance with the broadface contact dimensions [107]. The bonded LISePix sensor and ASIC are shown in Figure 3.18b, where the wirebonds at the bottom of the image connect the ASIC to the readout PCB.

3.4.3 LISePix Imaging Module

The LISePix imaging module, shown in Figure 3.19, contains the sensor, ASIC, and readout PCB (see File

Supplement 1. "Timepix-layer-diagram.pdf" : CAD model of LISePix layering diagram shown in Figure 3.18a. (*available online*)

Supplement 2. "LISe-Timepix-imager-module.pdf" : CAD model of LISePix imaging module shown in Figure 3.19a. (*available online*)



(a) CAD model of LISePix detection module

(b) bonded LISePix imager PCB

Figure 3.19. LISe high-resolution sensor mounted to Timepix [107].

S2). Designed by X-Ray Imatek, the readout PCB accommodates a single Timepix controlled by the readout electronics module, shown in Figure 3.20. As a prototyping PCB, the board was installed in a Hammond 1550B cast aluminum enclosure, providing EMI shielding. Using aluminum standoffs, the PCB was mounted to the lid, raising the sensor plane to approximately 2 mm offset from the 1.5 mm thick enclosure. A slot was machined into the enclosure and lid providing access for the 0.5 m long, high-channel density ribbon cable. The module was bolted to an aluminum plate with mounting holes spaced at 1.0 in intervals to mate with T-slotted aluminum extrusions.

3.5 HFIR CG-1D Beamline Testing

Close proximity to Oak Ridge National Laboratory (ORNL) offered unparalleled accessibility to their neutron radiation sources. As the primary location for neutron imaging experiments, HFIR is a specially designed 85 MW nuclear reactor used for isotope production and neutron experiments. The reactor offered direct access to one of the largest steady-state thermal neutron fluxes available globally [189].

3.5.1 Beamline Overview

The HFIR cold neutron source installed in the HB-4 beam tube contains a moderator vessel filled with 0.5 L of supercritical hydrogen gas. Installed in the beryllium reflector, the cryogenic moderating vessel maintains a temperature of only 20 K, surrounded by deuterated water for cooling and additional moderation. The cold neutrons scatter into the moderator vessel, losing energy, approaching 15 times lower energy than a thermal neutrons, eventually passing down the vacuum sealed beam tube to the experiment beamlines [39]. The heavily thermalized beam passes through the beam shutter, into the Cold Guide Hall (right side of Figure 3.21), feeding sub-thermal neutrons to multiple experimental stations. The the Cold Guide 1 Beamline (CG-1) houses multiple detector development experiments; the Cold Guide 1A Instrument (CG-1A) harbors

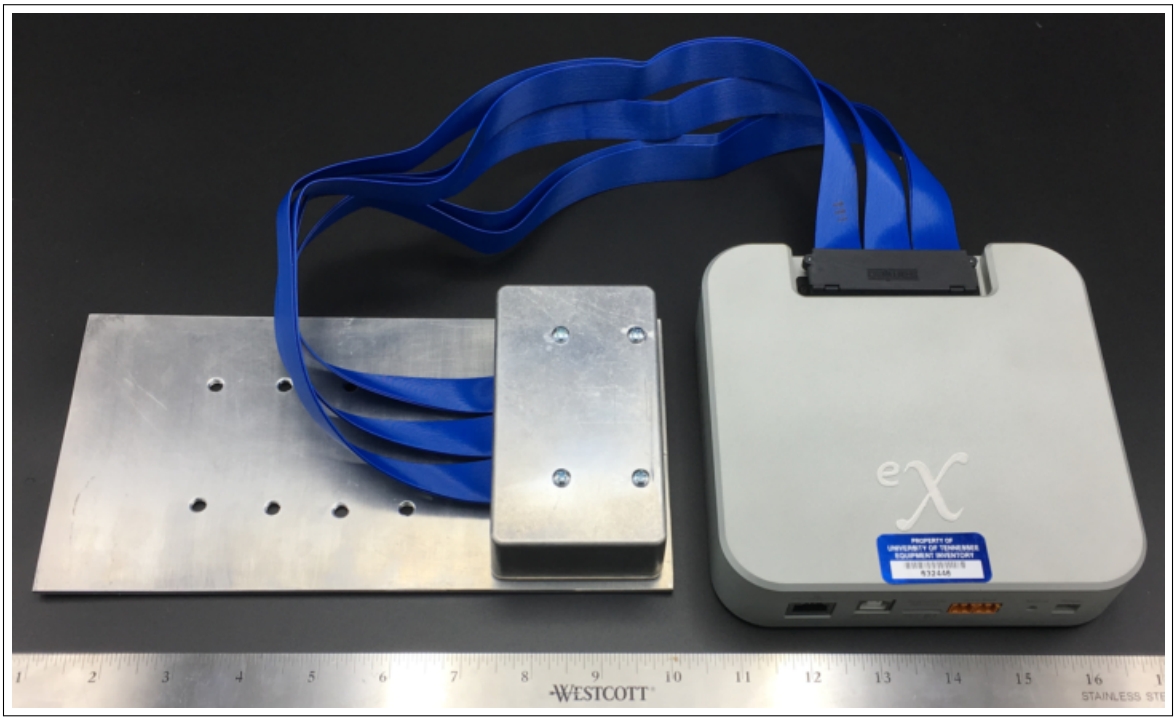
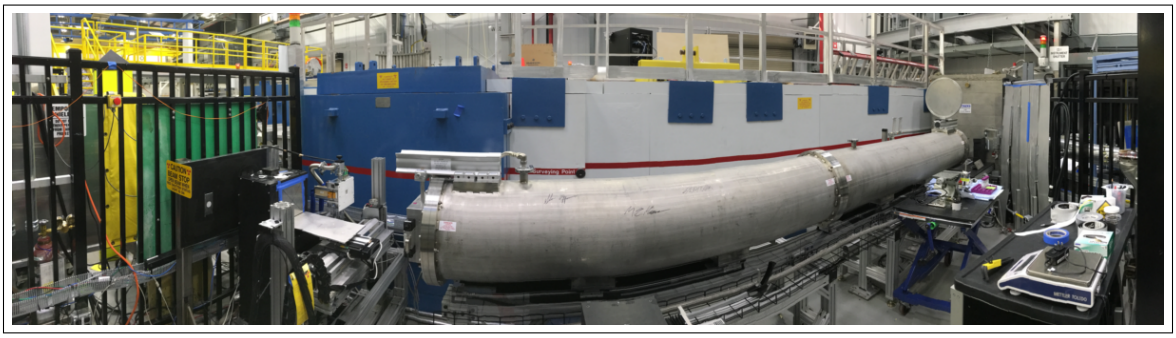


Figure 3.20. LISePix imaging module (left) connected via ribbon cable to readout electronics (right) [scale shown in inches]. Imaging module was mounted on adjustable aluminum plate for installation at CG-1D beamline.



(a) HFIR Cold Guide Hall



(b) CG-1D neutron imaging beamline

Figure 3.21. HFIR cold neutron guide hall, principal location for LISe neutron imaging and development.

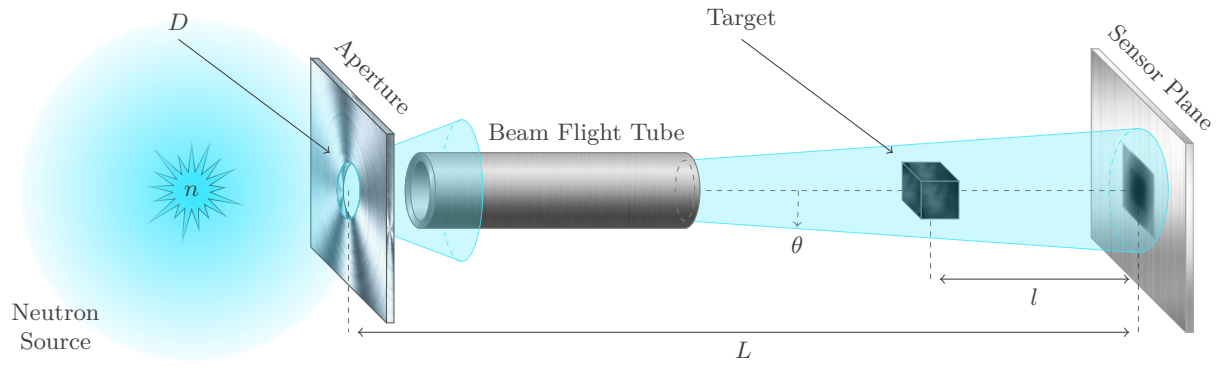


Figure 3.22. Generalized divergent beamline geometry for neutron imaging, given beam divergence angle, θ, aperture size, D, aperture to detector distance, L, and target to detector distance, l.

prototyping neutron detectors while CG-1D is dedicated to neutron imaging experiments (see Figure 3.21b). The beam guide exiting CG-1 measures $150 \times 25.4\,\mathrm{mm}^2$. The CG-1D aperture system is located downstream of the guide and is positioned to accept the highest neutron flux available at CG-1 [190].

The majority of LISe neutron imaging experiments were conducted on the CG-1D line, utilizing the fixed ^{6}LiF/ZnS screen based CCD imager for device comparison and positioning. At CG-1D, the neutron beam was transmitted through a 4.5 m helium filled flight tube, subject to a 600 mm diameter chopper, operating at rotational frequencies from 5 Hz to 100 Hz. The cold neutron beam spectrum followed a Maxwell-Boltzmann distribution with a cutoff near 0.81 Å and a peak at 2.6 Å. Minor Bragg edges are visible in the open beam, attributed to the aluminum windows in the reactor, cold neutron source, beam tube, and at the entrance and exit of the CG-1D flight tube. Across the multiple beam times, an average flux on the order of $10^7\,\mathrm{n/cm^2 \cdot s}$ provided significant contrast, forming images in a matter of ms to min [191].

The L/D ratio characterizes the geometry of neutron beamlines with, l, representing the target to detector plane distance, D, indicating the diameter of the source aperture, and the distance, L, spanning the length from the aperture and the detector image plane, illustrated in Figure 3.22 [192]. The beamline geometry creates a fixed detector distance ($L = 6.6\,\mathrm{m}$), while a motorized control system mechanically adjusts the aperture diameter ($D = 3.3$, 4.1, 8.2, 11 and 16 mm). The resulting L/D ratio spans from 400 to 2,000, depending on aperture selection [89]. To facilitate maximum resolution and edge contrast, the target distance, l, is kept to a minimum by positioning the target at the surface of the detector enclosure or imaging plate. The aperture is selected to adjust the neutron flux, helping to keep acquisition times low while preventing over saturation in the sensor.

3.5.2 Scintillator Operation

The CG-1D beamline features a fixed high-resolution, scintillator based imaging system installed at the end of the beam line (see Figure 3.23). A light-tight enclosure houses the ANDOR iKon-L DW936 CCD camera (ANDOR CCD), featuring a $7 \times 7\,\mathrm{cm}^2$ FOV, yielding a typical spatial resolution around 75 µm using the

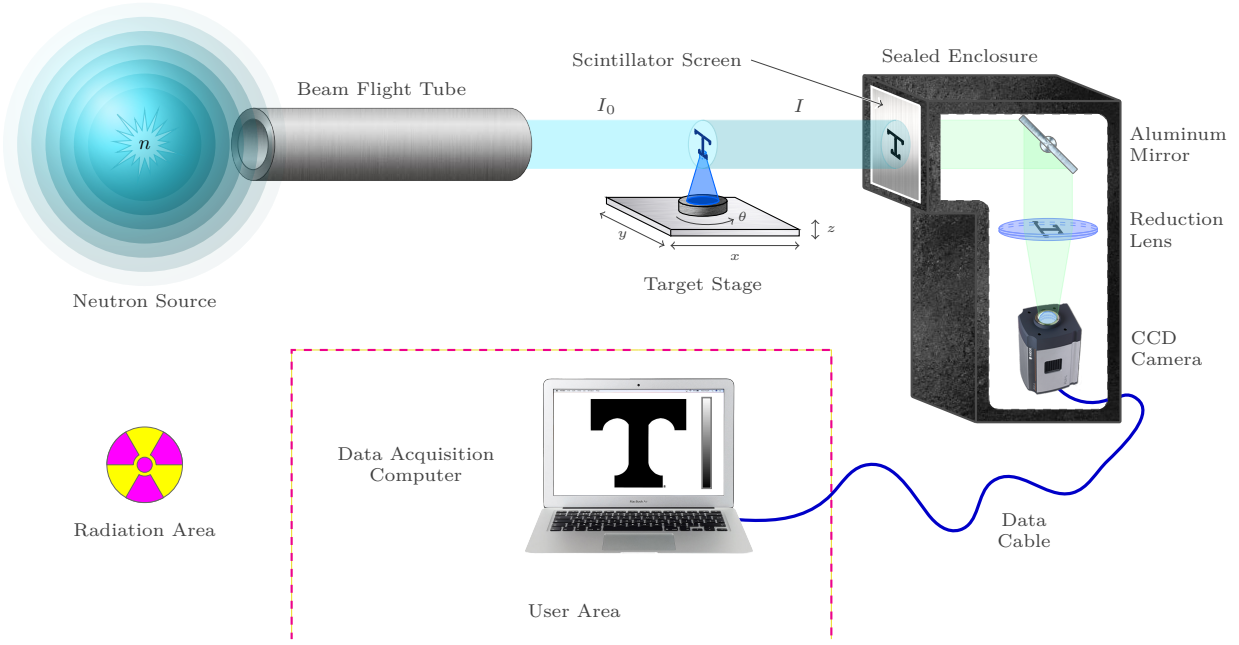
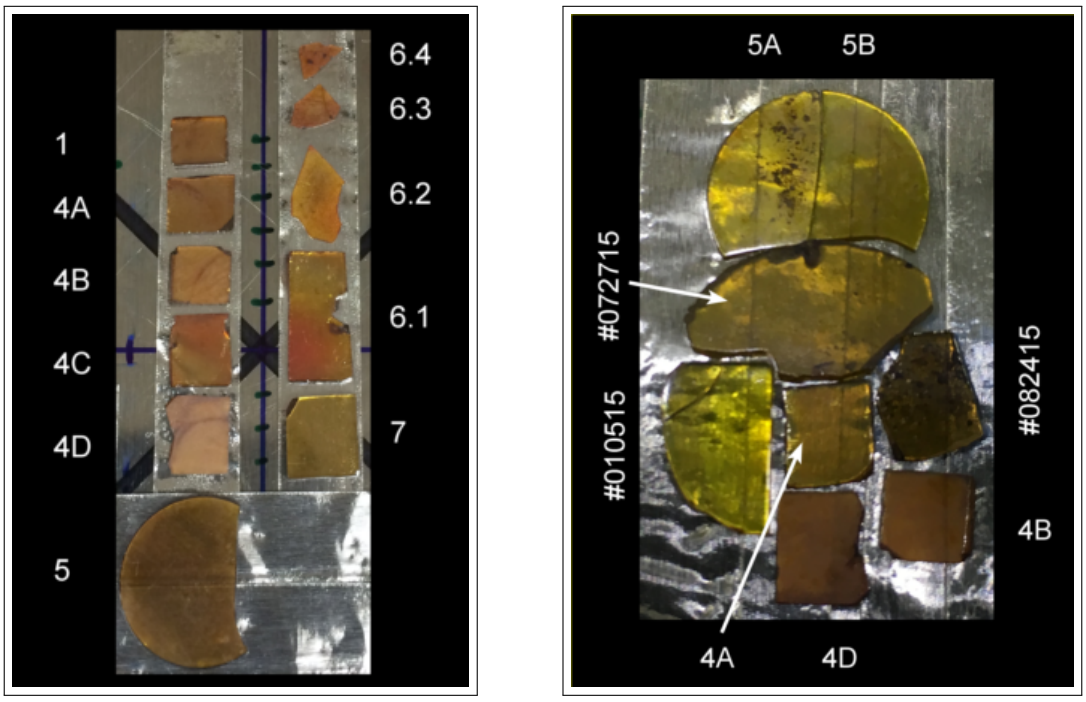


Figure 3.23. Scintillator experimental setup at the Cold Guide 1D Instrument (CG-1D) neutron beamline [193].

^{6}LiF/ZnS screen [89]. The ANDOR CCD rests at the bottom of the light-tight enclosure, aiming vertically towards an aluminum reflecting mirror. Oriented at a 90° angle to the ANDOR CCD, the ^{6}LiF/ZnS screen consists of a thin aluminum plate ($22 \times 22\,\text{cm}^2$ by 0.4 mm thick) coated in a neutron sensitive film mixture of a ^{6}LiF absorber, ZnS fluorescent pigment, and Cu activator, ranging from 50 µm to 200 µm thick [90]. When a neutron strikes the plate, an absorption reaction produces scintillation light that reflects off the 45° mirror, redirected downwards through a magnification lens to the ANDOR CCD [191]. In this research, a ^{6}LiF/ZnS screen with a 50 µm thick coating was used.

This neutron imaging system served as a standard for comparison against both LISe modes, as well as positioning the semiconductor systems in the neutron beam. Using the in-house optics stage, LISe scintillating sensors were attached to an identical aluminum plate (see Figure 3.24), installed in the CCD light-tight enclosure. Sensors were affixed using aluminum tape, minimizing neutron attenuation and scattering, with both transparent (reflective) and opaque (anti-reflective) coatings. Operating with an aperture of $D = 16\,\text{mm}$ and sitting at the full beamline distance, the light-tight enclosure produced an $L/D = 412$ [96]. The first version of the scintillator array (Figure 3.24a) tested the 11 available sensors to compare light output, measure spatial resolution, and test the super-sampling technique. Tested individually in an earlier experiment, sample LISe-1 provided the multi-position images used for image reconstruction [96]. In the second iteration of the scintillator array (Figure 3.24b) the sensors formed a pseudo open beam area, packing the crystals as close together as possible. To better asses the significance of surface finish and material thickness, the scintillators were specifically prepared at varying finishes, shown in Table 3.1. This experiment focused



(a) scintillator array (v1) [96]

(b) scintillator array (v2) [97]

Figure 3.24. LISe scintillator arrays used in HFIR imaging experiments.

Table 3.1. LISe scintillator sample identification, thickness, and measured surface roughness (R_a) within the array [97].

Sample ID	**Thickness** (µm)	$\boldsymbol{R_a}$ (µm)
LISe-4A	452	1.767
LISe-4B	409	0.331
LISe-4D	272	0.800
LISe-5A	427	0.050
LISe-5B	432	0.050
LISe-010515	1,824	0.787
LISe-072715	1,067	0.770
LISe-082415	904	0.659

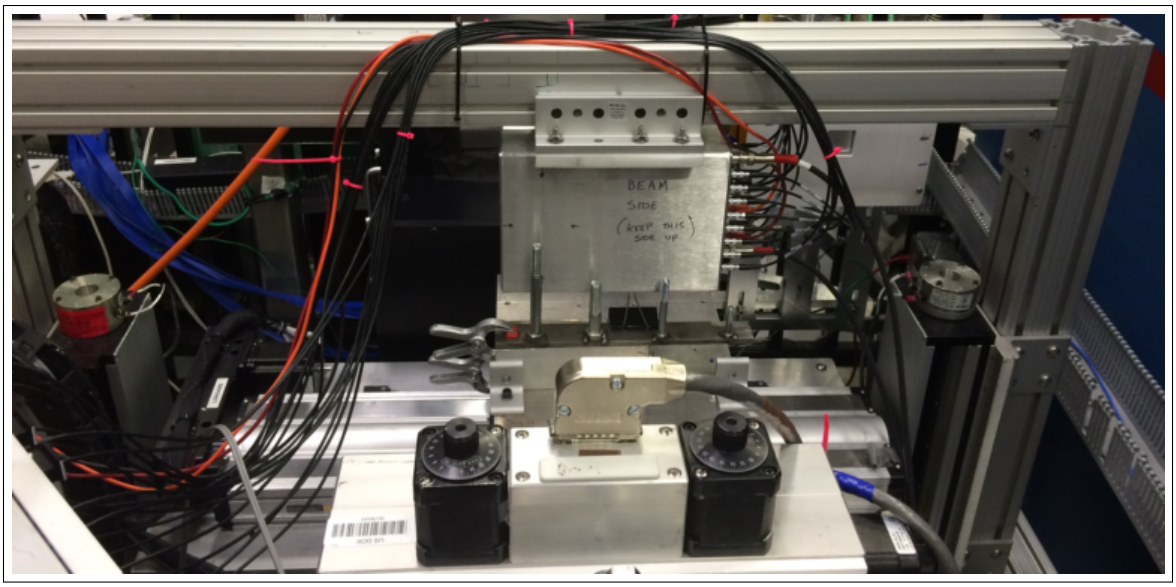
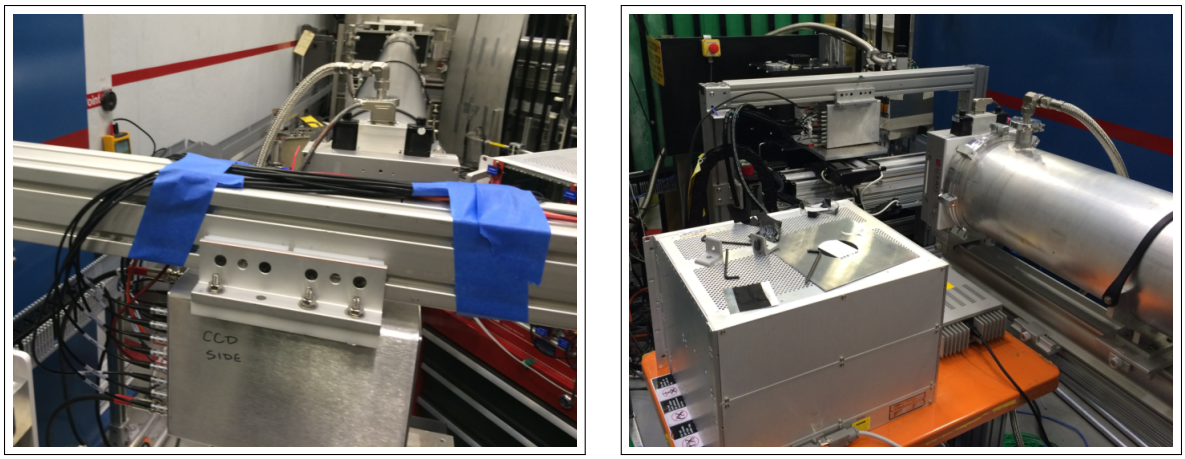


Figure 3.25. LISe PD running bolt super-sampling experiment.

on determining the spatial resolution limit of the scintillator mode, along with applications of neutron CT [97].

3.5.3 Semiconductor Operation

The CG-1D beamline offered a T-slotted aluminum extrusion frame, adjustable to accommodate a range of mounting configurations. Aluminum frames provided rigid, lightweight supports offering minimal neutron interaction to reduce background radiation. A sliding T-slot bracket was attached to the LISe PD enclosure, with a polyethylene spacer to electrically isolate the enclosure from the surrounding stage. Mounting the LISe PD from the top extrusion allowed the system to hang in front of the neutron beam, without obstructing the sample stage below, as demonstrate in the bolt experiment in Figure 3.25. The LISe PD was installed at an aperture distance of roughly $L = 6.3\,\mathrm{m}$ using the 16 mm aperture to give an $L/D = 394$. Cabling was secured to the frame, carrying the high-voltage, low-voltage and output signal lines to the supporting electronics, shown in Figure 3.26. An NHQ 203M High-Voltage Power Supply provided the $+250\,\mathrm{V}$ high-voltage bias, housed in an ORTEC 4001C NIM Bin. The low-voltage chip power came from a Keysight E3630A 35W Triple Output DC Power Supply operating at $\pm 12\,\mathrm{V}$ with a 170 mA current draw. The detection pulse generated by the CR-110 exited the enclosure via LEMO 00, routed to the micro coaxial connector (MCX) inputs on the digitizer using a converter cable. Housed in a CAEN VME 8010 Crate, the signals were processed by dual CAEN V1724 8-channel Digitizers featuring built-in digital pulse processing and pulse height analysis (DPP-PHA). A CAEN V2718 VME-PCIe Optical Link Bridge routed the processed spectra to the acquisition PC, via fiber optic cable, connecting to the CAEN A3818 PCIe CONET2 Controller. To control the acquisition timing and stage position, a custom LabVIEW (Lab Virtual Instrument Engineering



(a) LISe PD rear view looking upstream (v1)

(b) LISe PD and supporting electronics (v2)

Figure 3.26. LISe PD installed at the HFIR CG-1D beamline [145].

Workshop) module was designed and integrated with the CAEN supplied virtual instruments (VIs). The program connected to the in-house stage controls via ethernet, designating positional information used to index the output files. This automation made the super-sampling technique possible, requiring thousands of acquisitions across the translation sequence, lasting over 12 h [145].

3.5.4 Timepix Operation

The LISePix system maintained a smaller footprint than its predecessor, the LISe PD, shown in Figure 3.27. The data processing module sat on top of the T-slotted aluminum extrusions, safely out of the neutron beam to protect the sensitive electronics. The module only required two input cables, a standard ethernet patch cord to relay data to the acquisition computer, and a standard DC power supply running off 110 VAC. Hung from an aluminum mounting plate, the LISePix imaging module took position immediately behind the imaging targets, roughly centered on the beam axis. The blue, high-channel density ribbon cable connected the imaging PCB, carrying the high-voltage bias and ASIC data to the readout module. Positioned in front of the scintillator light-tight enclosure, the LISePix established an aperture distance of $L = 6$ m, tested with two aperture settings ($D = 8.2$ and 16 mm), resulting in L/D ratios of 732 and 375, respectively. Operating in Medipix2 event counting mode, the high-voltage bias of +300 V produced an internal electric field of 545 V/mm in the sensor [107].

3.5.5 Imaging Targets

At CG-1D, a motorized stage oriented samples in the beamline, giving the user fine position control while the beam was open. The base of the stage contained a large lift, capable of translating the sample vertically to raise or lower the position within the imager's FOV. Attached to the lift, two linear drives moved the stage parallel to the ground, one drive translating the sample left and right in the FOV and the other adjusting

the distance between the sample and detector. Operating the linear drives with step sizes as low as 25 µm yielded extremely fine positioning accuracy for the super-sampling technique. An optional fourth axis was attached to the stage for the neutron CT, rotating the sample about the vertical axis with 0.25° angular steps.

PSI Resolution Test Mask

Grünzweig *et al.* described a resolution test mask for neutron imaging designed and fabricated by PSI [57]. Shown in Figure 3.28, the target prescribes a Siemens Star design, a common resolution assessment tool in optical instrumentation. The Siemens Star is constructed from spokes radiating outwards from the center of a circle. The spokes form equally spaced, alternating bright and dark regions, typically on an attenuating background. The design used in the PSI Siemens star imaging mask (Siemens Star) utilizes 128 spokes across a 20 mm diameter. As the spokes get closer to the center, their period decreases, or the number of line pairs per unit length increases (in units of lp/mm). Concentric rings indicate spoke periods of 50, 100, 200, 300, 400 and 500 µm, used for estimating the resolution of the imaging system. In first approximation, the spatial resolution is determined by the period at the radius which no longer distinguishes transparent and attenuating spokes. To create transparent and attenuating regions, the quartz mask contains a 6 µm thin film of Gd sandwiched between a 25 nm adhesion layer and a 1 µm capping layer. The photo negatives in Figures 3.28 and 3.29 show the metalized layers as a reflective surface, with the transparent quartz mask indicated by the non-reflective regions. In beam, the Gd thin film heavily attenuates the thermal neutron flux, creating attenuating regions while the relatively neutron transparent quartz transmits with approximately open beam intensity. Also featured in the larger mask, a $24 \times 24\,\mathrm{mm}^2$ grid, spaced at 1 mm intervals, offers a means for measuring distortion and magnification [194]. The bottom of the mask contains a series of knife-edge line pairs, decreasing in spacing, to measure the MTF as described in Appendix C.4.

Additive Manufacturing

Additive manufacturing (AM) has become an increasingly popular engineering tool for prototyping and production of complex specialty parts [195]. Santamaria *et al.* used neutron imaging to actively investigate the water transport in a PEFC. In this assembly, the manifold housing was fabricated from acrylonitrile butadiene styrene (ABS) using AM [12]. Bilheux *et al.* reported on the design verification analysis of an Inconel 718 turbine using neutron radiography to investigate the internal structure of the AM part [196].

In the first set of AM samples, the *CNS-Y12* imaging target offered a low-cost, disposable, fused deposition modeling (FDM) part for neutron imaging experiments (see Figure 3.30). Printed on an Ultimaker 2^+ 3D printer (Ultimaker 2^+), the target was formed by melting polylactic acid (PLA) filament and tracing the $1.00 \times 0.75\,\mathrm{cm}^2$ logo, layer by layer, to gradually build a thickness of 1.0 cm. The nozzles on the Ultimaker 2^+ may be swapped to adjust the ejected fillament diameter including 0.25, 0.4, 0.6 and 0.8 mm hardware [197]. As the name implies, the filament fuses each successive layer into a semi-solid object, with some residual

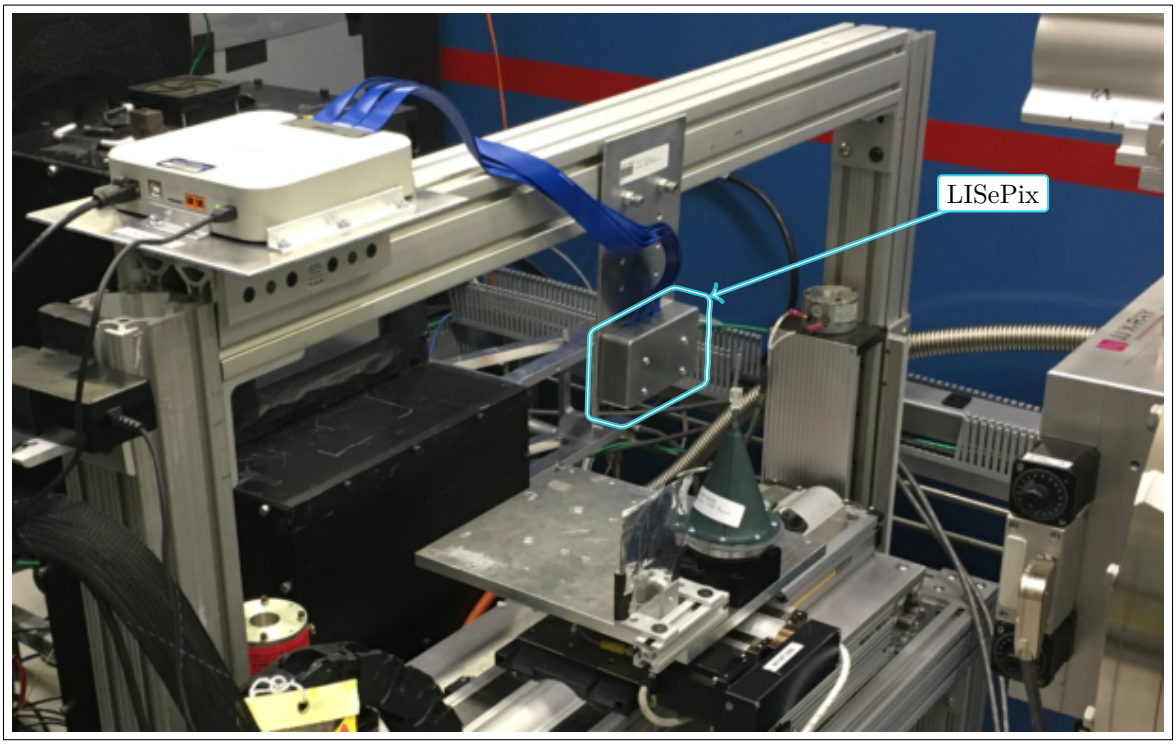


Figure 3.27. LISePix installed at HFIR CG-1D beamline.

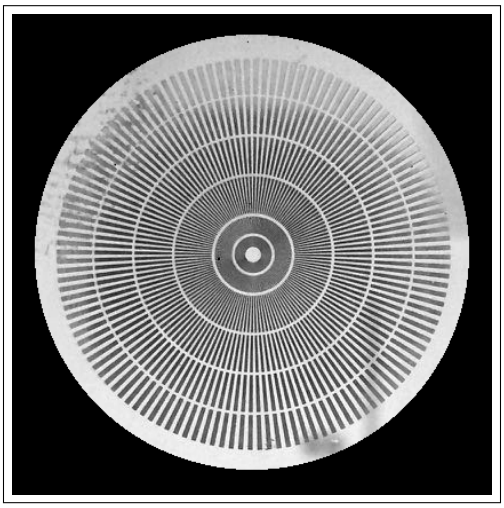


Figure 3.28. Small Siemens Star featuring only radial star pattern *(negative B/W photo to enhance contrast)* [107].

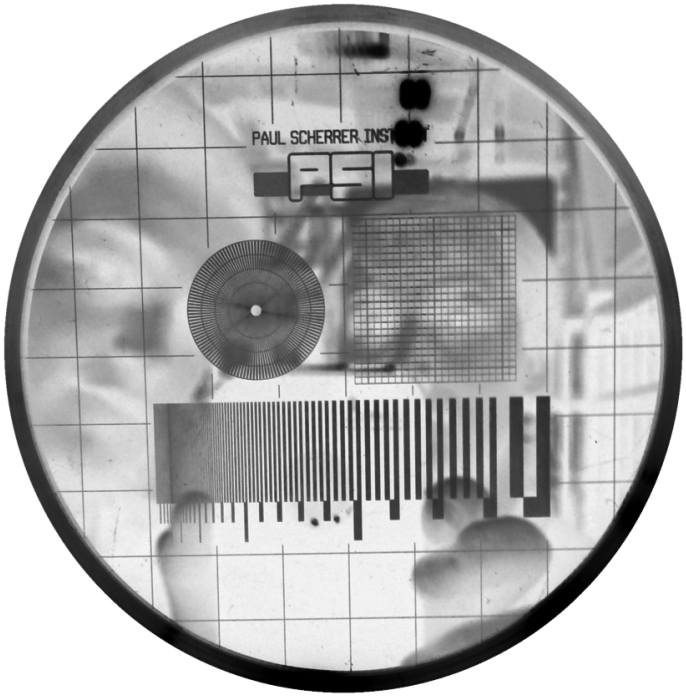
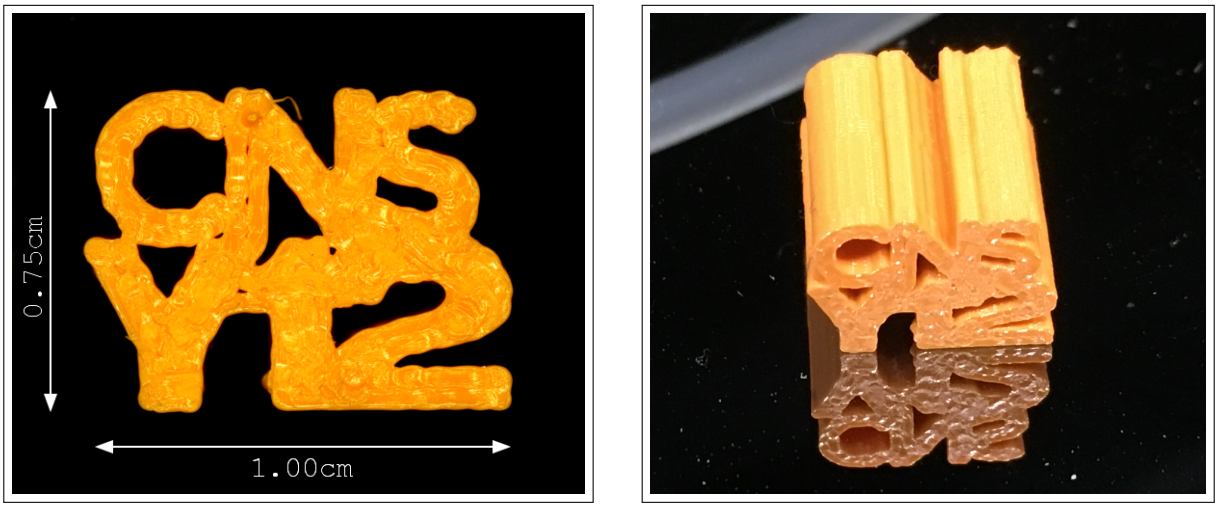


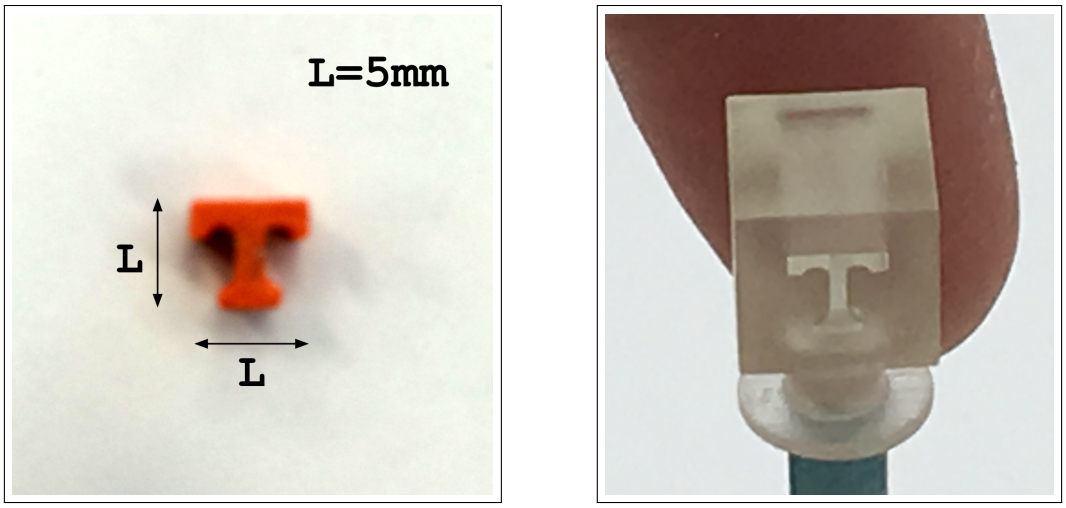
Figure 3.29. Large Siemens Star, featuring radial star, variable line pairs and Cartesian grid *(negative B/W photo to enhance contrast).*



(a) dimensions of *CNS-Y12* imaging target

(b) photo of *CNS-Y12* on silicon

Figure 3.30. FDM printed *CNS-Y12* neutron imaging target.



(a) low-detail FDM sample (b) high-detail SLA sample

Figure 3.31. Photographs of 3D printed *Power-T* neutron imaging targets [107].

inter-filament porosity. This method of construction creates unique internal density fluctuations similar to professionally manufactured AM parts. A smaller *Power-T* imaging target was also produced using the same AM process, shown in Figure 3.31. The *Power-T* exhibited rounding about the corners due to the smaller features approaching the resolution limits of the FDM printer. The target measured roughly $5 \times 5\,\mathrm{mm}^2$ and 5 mm thick, creating less attenuation and white field contrast than the *CNS-Y12* target. Both the *CNS-Y12* target and the *Power-T* target were used in the first LISe scintillator array experiments [96]. A revised set of AM imaging targets were produced for the LISePix experiments, using a higher fidelity stereolithography (SLA) printer. Shown in Figure 3.31b, the *Power-T* cube was printed on a Form-2 3D printer (Form-2), using the proprietary Formlabs v2 Clear Resin, at a 25 µm layer thickness (see File S3). The $1 \times 1 \times 1\,\mathrm{cm}^3$ cube had the *Power-T* logo inscribed the full thickness of the part, with the logo measuring 6 mm on a side [107]. Because the Form-2 uses a resin bath for feed material, the resulting part exhibits minimal porosity and functions as a uniform, dense, plastic part.

Biological

As an analog to X-ray imaging, neutron imaging can be used to explore the internal structure of biological samples. Bilheux *et al.* noted the use of CG-1D for imaging biological samples including bones, muscles and organ tissues [191]. In the second round of LISe scintillator array experiments, a neutron CT was conducted on a post mortem *halyomorpha halys*, shown in Figure 3.32. Observed as non-indigenous agricultural pest in Eastern Tennessee, *halyomorpha halys* frequently intrudes households during the winter, becoming trapped and dying from lack of resources. The female sample captured by Jones *et al.* measured over 16 mm in length,

Supplement 3. "Neutron-imaging-target-stand.pdf" : CAD model of target stand and *Power-T* neutron imaging target shown in Figure 3.31. (*available online*)

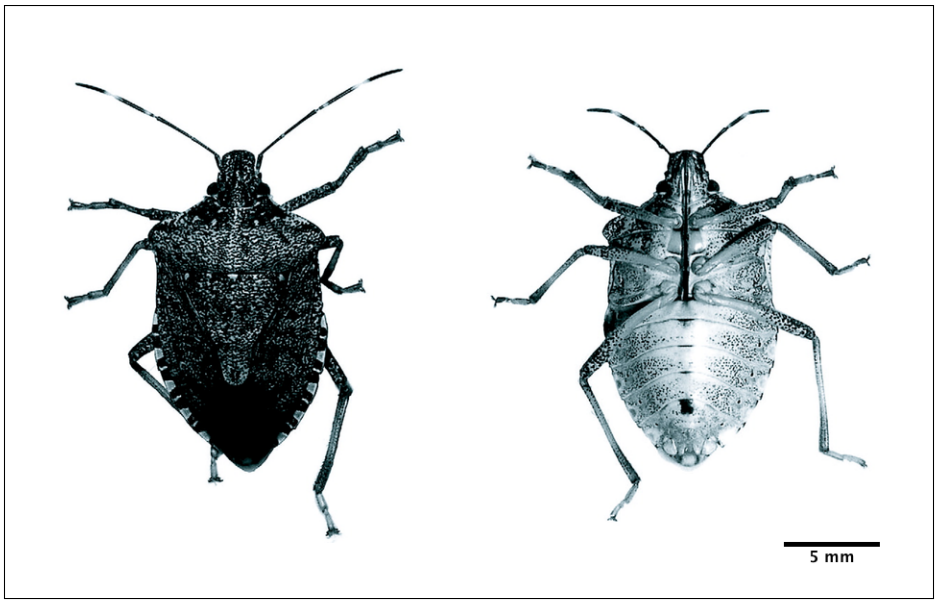


Figure 3.32. *Halyomorpha halys*: (left) dorsal view showing humeral angle of the pronotum rounded and abdominal margins with alternating light and dark banding, (right) ventral aspect showing legs with 3-segmented tarsi, abdominal sterna, and the genital capsule (photo courtesy Jones *et al.* (2009) [198]).

exhibiting the characteristic shield shaped thorax [198]. For the imaging experiment, a deceased insect was collected and preserved in an aluminum foil pouch, ready for neutron imaging. Using the rotational stage, the insect sample was imaged at multiple angles, and a 3D reconstruction was created using Octopus Imaging Software [97].

3.6 Imaging Techniques

The neutron imaging techniques in this section describe methods to analyze a detector's performance, and fuse raw output data into meaningful graphics. A more detailed mathematical description for the concepts discussed in this section is provided in Appendix C.

3.6.1 Super-Sampling

The super-sampling technique comprises a combination of experimental and analytically methods to enhance image resolution (see Appendix C.3). In general, a pixel based digital imaging device maintains a lower resolution limit based on the physical size of the pixels. The spatial sampling frequency, f_s, is related to the size of the pixels, D_p, by equation eq. (31a).

$$f_s = \frac{1}{D_p} \tag{31a}$$

$$f_N = \frac{1}{2D_p} \tag{31b}$$

To prevent distortion and accurately represent the analog signal in digital space, the Nyquist frequency, f_N, is defined as half the spatial frequency, shown in eq. (31b). The Nyquist frequency implies a physical resolution limit of twice the pixel pitch, requiring smaller pixels to achieve higher resolution. As a method to overcome this limitation, super-sampling achieves sub-pixel resolution by scanning a region at position intervals (or sub-steps) smaller than the pixel pitch. For a single pixel channel, each sub-step creates a virtual pixel of equivalent size, capturing the subtle changes in intensity unresolved by the larger physical pixel. The resulting map of virtual pixels contains the original image, sampled at a higher rate attributed to the pixel size reduction. The trade off for the enhanced resolution is increased imaging time, requiring N^2 samples where N is the ratio of sub-steps to pixel pitch, and the associated setup cost from high-fidelity positioning stages. This method was tested in simulations and physical experiments to obtain resolutions less than half the pixel pitch [145].

3.6.2 Contrast

A key parameter for any imaging system, contrast has been redefined over the past two centuries. In its simplest form, contrast relates the intensity difference of two objects in an image or FOV, giving rise to the concept of bright and dark regions. A basic definition of contrast, C, is shown in eq. (32) where the brightest region has an intensity, $I_{\max}$, and the darkest, $I_{\min}$.

$$C = \frac{I_{\max}}{I_{\min}} \tag{32}$$

An early definition of contrast was developed by Weber, who studied the physiology of the human eye and its ability to distinguish changes in sensory input. He found that the smallest discernible change from a baseline stimulus remained constant across the range of ocular sensitivity. Applying to scenarios where a small, luminous object of intensity, $I_{\max}$, is present among a broad background of lower intensity, $I_{\min}$, the Weber contrast uses a normalized intensity difference, shown in eq. (33) [199].

$$C_w = \frac{I_{\max} - I_{\min}}{I_{\min}} \tag{33}$$

In these types of images, a relatively uniform background produces an average intensity near one of the extremes, useful in applications such as astronomical images or on-screen text. Alternatively, Michelson developed a contrast, C_m, for imaging periodic features using the minimum and maximum intensities, $I_{\min}$ and $I_{\max}$, as described in eq. (34) [200].

$$C_m = \frac{I_{\max} - I_{\min}}{I_{\max} + I_{\min}} \tag{34}$$

The modulation based contrast proposed by Michelson applies to neutron imaging, where the noise is generated from a partially transparent target or mask obscuring the view of the open beam. This definition of contrast is applied in the modulation transfer function (MTF) technique used to evaluate the spatial resolution limit for an imaging system [201]. For less standard patterns and geometries, Peli described a root mean square (RMS) contrast method, relating the normalized gray level in a given pixel, x_i, to the average for the image, $\bar{x}$, shown in eq. (35), then applying advanced band-filtering routines to enhance feature visibility [202].

$$C_{rms} = \left[\frac{1}{n-1} \sum_{i=1}^{n} (x_i - \bar{x})^2 \right]^{1/2} \tag{35}$$

where,

$$\bar{x} = \frac{1}{n} \sum_{i=1}^{n} (x_i)$$

3.6.3 Modulation Transfer Function Resolution Calculation

The contrast in an imaging system may be evaluated using the experimental technique shown in Figure 3.33, followed by MTF analysis as detailed in Appendix C.4. The left column of the process diagram represents conditions where the spatial period, P_s, (or inverse spatial frequency, f_s^{-1}), is equivalent or greater than the resolution limit, R_{lim}, of the imaging device. As the spatial frequency increases past the resolution limit, the response will follow the right column, where contrast reduction limits the ability to fully resolve image features. The resolution experiment begins with the selection of an appropriate line pair pattern or sharp knife-edge feature, shown in Step (a). An idealized knife-edge feature fully attenuates the incident beam, providing a sudden change in response ranging from the fully open beam of maximum intensity, to the dark field of minimum intensity. Step (b) shows the attenuating mask in the neutron radiation field, where a highly absorbing film (such as Gd) of given thickness, x, removes a significant portion of the incident beam, I_0, resulting in a modulated output, I_m, captured by the imaging system. The resulting output image, shown in Step (c), follows a periodic shift from open beam (white) to the dark field (black), where minimal gray region indicates high contrast. While the left image demonstrates fully black regions along the centerline of attenuating mask, the right image only achieves a gray color, indicative of contrast deficit. This concept is further illustrated in Step (d), where the image is flattened to yield the repeating edge spread function (ESF). Again, the sinusoidal ESFs (blue) on the left span the full contrast range, in close agreement with the idealized step response (gray), while those on the right side cover a shallow contrast range, significantly above the dark field level. The experimentally determined ESF serves as the input for MTF analysis to calculate the resolution limit.

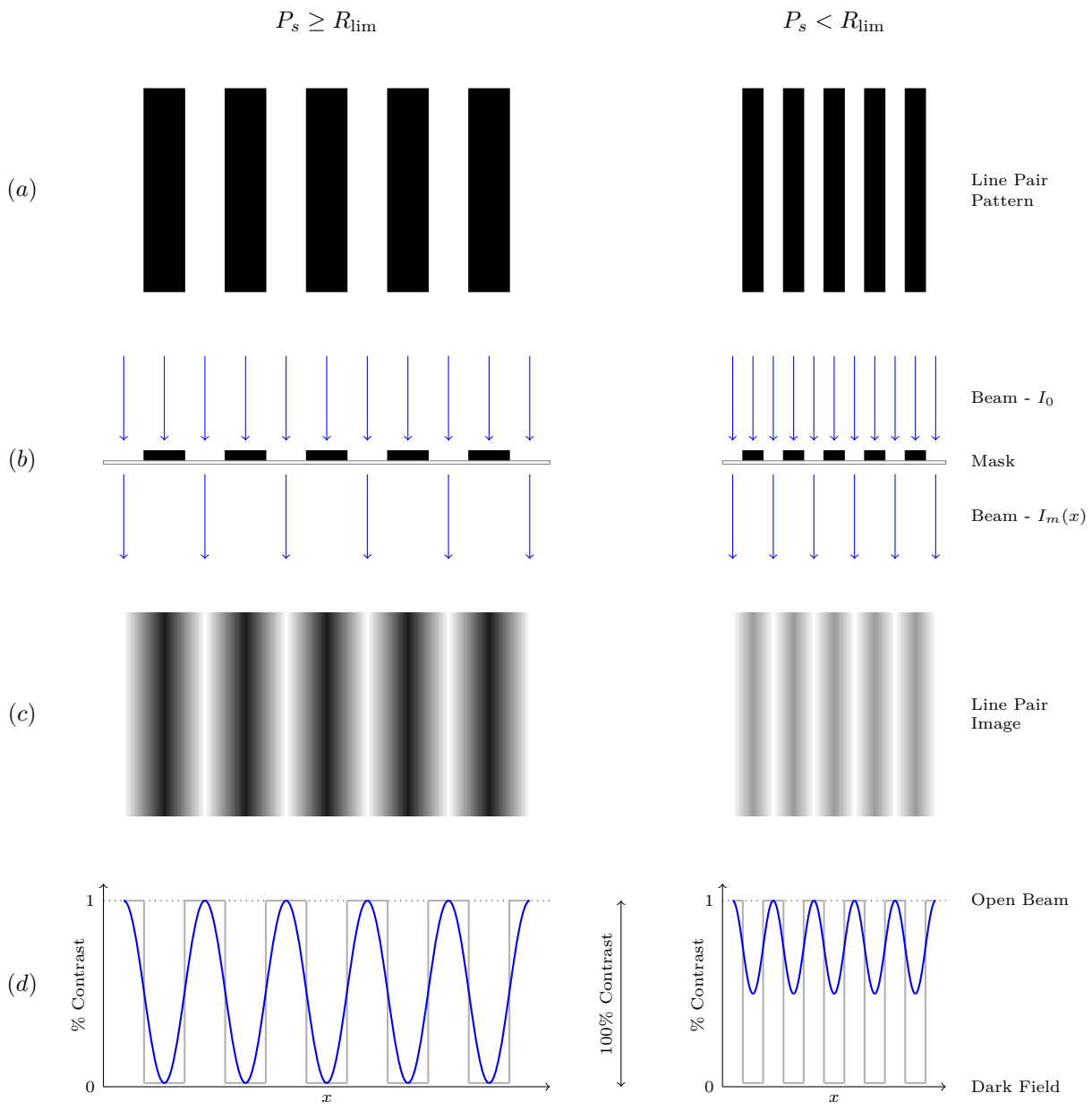


Figure 3.33. Determining the edge spread function from a line pair mask.

3.6.4 Full Width at Half Maximum Resolution Calculation

Another common technique for evaluating the spatial resolution, the FWHM measures the sharpness of a normally distributed signal. The parameter describes the width of a normal distribution at an intensity equivalent to half the maximum intensity, evaluated at the mean. For a given signal of sample data, x, with a mean, x_0, and standard deviation, σ, the normal distribution is given by the function, $f(x)$, shown in eq. (36).

$$f(x) = \frac{1}{\sigma\sqrt{2\pi}} \exp\left[-\frac{(x - x_0)^2}{2\sigma^2}\right] \tag{36}$$

As with the MTF experiment, the step function from a line pair mask produces a smooth, periodic ESF. Following the MTF analysis in Appendix C.4, the differentiated LSF follows a normal distribution. Applying a Gaussian fit to the LSF, the standard deviation for the experimental distribution is used to evaluate the FWHM, shown in eq. (37a).

$$\text{FWHM} = 2\sqrt{2\ln 2}\sigma \tag{37a}$$

$$\text{FWHM} \approx 2.355\sigma \tag{37b}$$

The approximate value of the FWHM is given by eq. (37b), and may be evaluated using numerical methods as part of the image processing algorithm. The spatial resolution calculated using the FWHM is presented along with the MTF calculation for complete performance comparison.

3.6.5 Simulation

During the construction of the single channel LISe neutron detector, the anticipated Siemens Star experiment using the LISe PD was simulated using MCNP. Because the experiment would require beamline time at HFIR to obtain an appropriate neutron flux, the simulation served as a method to justify the experiment, inspect the pixel array geometry prior to fabrication, and create an idealized output image for reference. Compared against a photo of the Siemens Star on the left of Figure 3.34, the right side depicts the experimental geometry. The green array illustrates the sensor starting position while the red array represents the final scan position, with the black outline representing the swept area covered during the scan. The blue lines, corresponding to spoke cutouts in the Gd mask, extend into the swept area, with the outer two concentric rings (400 and 500 µm) spanning the scan area.

The pixel detector design reflected dimensions closer to the first iteration of the LISe PD, using 900 µm pixels. For design simplicity, the pixels were simulated edge-to-edge, omitting inter pixel spacing and the surrounding guard ring necessary for real detector electronic operation. A plane wave neutron source, positioned 15 cm from the detector surface along the z-axis, simulated the transport of 10^9 neutrons at 25 meV for each position. The detector was translated in the x and y-directions at 50 µm steps, resulting in a total of 5,329 individual simulations [145]. To generate the large number of input deck files, a single

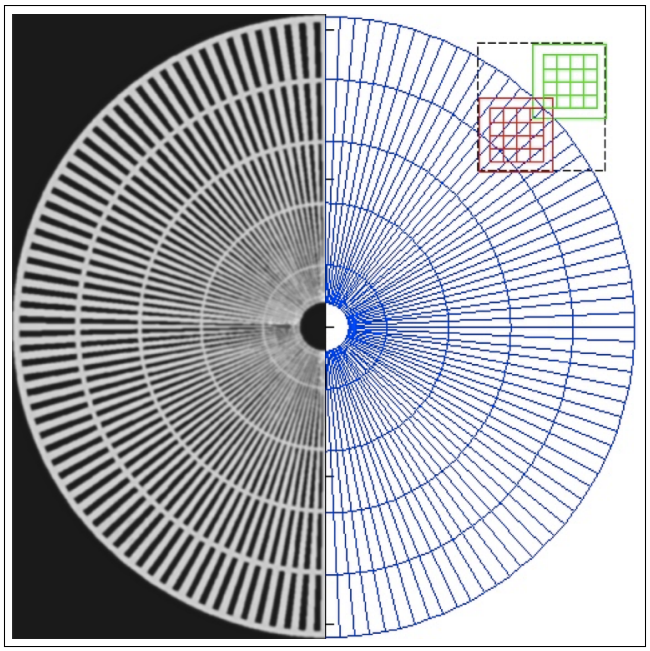


Figure 3.34. Optical microscope image of Siemens Star (left) [194] and experimental interrogation area of the LISe PD (right) [145].

file using the starting geometry provided the template. Reading this template into MATLAB (Matrix Laboratory), a series of near identical files were created, modifying the detector geometry for each input deck, indexing the file name with the positional coordinates. These simulations exploited the computational power of the Nuclear Engineering Department Cluster, batch processing the large file set [203]. The output files were again processed in MATLAB, first rendering 16 individual super-sampled images for each channel, composed of a 73×73 array of $50 \times 50\,\mu m^2$ virtual pixels, as described in Appendix C.3. Afterwards, the super-sampled images were recombined, following the methods in Appendix C.2, to produce a single image of the Siemens Star super-sampling experiment, shown in Figure 3.35. The simulated LISe PD response confirmed the application of super-sampling to achieve sub-pixel pitch resolution with a limited number of readout channels. The line pairs are distinctly visible between the 400 and 500 µm rings, indicating a resolution 2.25× smaller than the 900 µm pixel pitch. As an idealized response, the dark field appears uniform after averaging the images together, while the radial markers exhibit smooth curvature across the FOV. Furthermore, noticeable rounding occurs near the spoke to ring interface, deviating from the sharp geometry in the physical mask and the ideal edges created by the simulated mask. Shown as the darkest red spots where the spokes perpendicularly meet the ring, these artifacts can be attributed to diffraction effects at the edge of the sharp attenuating feature. The presence of these rounded features near the spoke/ring union is likely exacerbated by the use of super-sampling with a large pixel, and should also appear to some degree in the physical experiments.

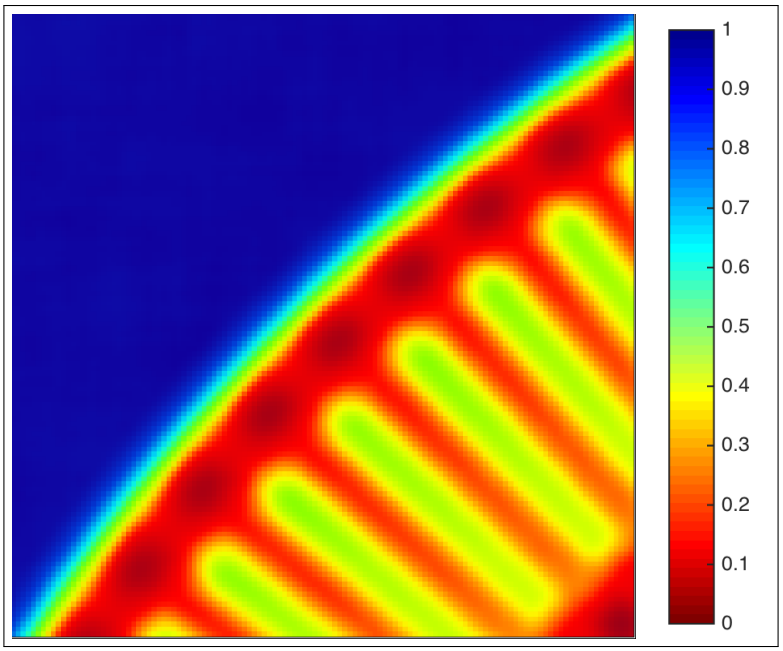


Figure 3.35. MCNP simulation of Siemens Star neutron image using LISe PD with 900 µm pixels and a 50 µm super-sampling step size. The two outer most rings are shown, resolving line pairs from the 400 µm to 500 µm radial marker [145].

3.6.6 Computational Tomography w/ Scintillator

One of the most instrumental applications of neutron imaging, neutron computed tomography (nCT) investigates the internal structure of materials. Along with X-ray computed tomography (xCT) and electron computed tomography (eCT), nCT offers a complementary set of NDT techniques. The experimental setup at CG-1D operates as a cone beam micro computed tomography (μCT) system, using the neutron beam to project 2-dimensional (2D) image slices of the target on the detector plane. Rotating the target stage at fixed intervals provided multiple image cross-sections for reconstruction of a 3D solid object. In the second round of LISe scintillator array experiments, the top two samples (5A and 5B in Figure 3.24b) represented the largest continuous FOV to date. Having demonstrated similar capabilities as the in-house ANDOR CCD, these two LISe samples were selected for the first nCT experiment. Using a *halyomorpha halys* specimen encased in aluminum foil as the target, the nCT scan covered 183° of rotation at 0.25° increments, at 30 s per frame. The experiment produced 734 tomographic slices, processed on the ORNL Neutron Sciences server for facilities users, after image cleanup [204].

On the ORNL server, Octopus provided a variety of tools for compiling raw CT data into 3D solid bodies. While the software provided basic pre-processing functionality, the non-standard data set created by a curved detection area required additional correction. The standard Octopus pre-preprocess includes: image cropping, spot filtering, and image normalization, similar to general neutron radiography (see Appendix C.1). An additional feature removes ring artifacts, caused by aberrations in pixel performance near edge transitions,

producing unusual intensity fluctuations and ghosting. After pre-processing, the software generates one or more sinograms for each input image by applying the Radon transform, as described by Kak *et al.* shown in Figure 3.36. As a basic example, a projection at an angle, θ, may be described by a set of parallel lines, t_i, perpendicularly intersecting the projection plane, given by the expression shown in eq. (38).

$$t_i = x\cos\theta + y\sin\theta \tag{38}$$

The Radon transform, $P_\theta(t)$, describes the line integral for the object defined by $f(x, y)$ at a distance, s, from the projection plane, taking the form shown in eq. (39).

$$P_\theta(t) = \int_{(\theta,t)\text{line}} f(x, y)\ ds \tag{39a}$$

Applying a delta function, the equation can be rewritten,

$$P_\theta(t) = \int_{-\infty}^{\infty}\int_{-\infty}^{\infty} f(x, y)\delta(x\cos\theta + y\sin\theta - t)\ dx\ dy \tag{39b}$$

Spanning the (θ, t) space, the sinograms measure the object density across various projections. The sinograms were processed by the software using a filtered back-projection formula (or inverse Radon transform) to rebuild the object [205, 206].

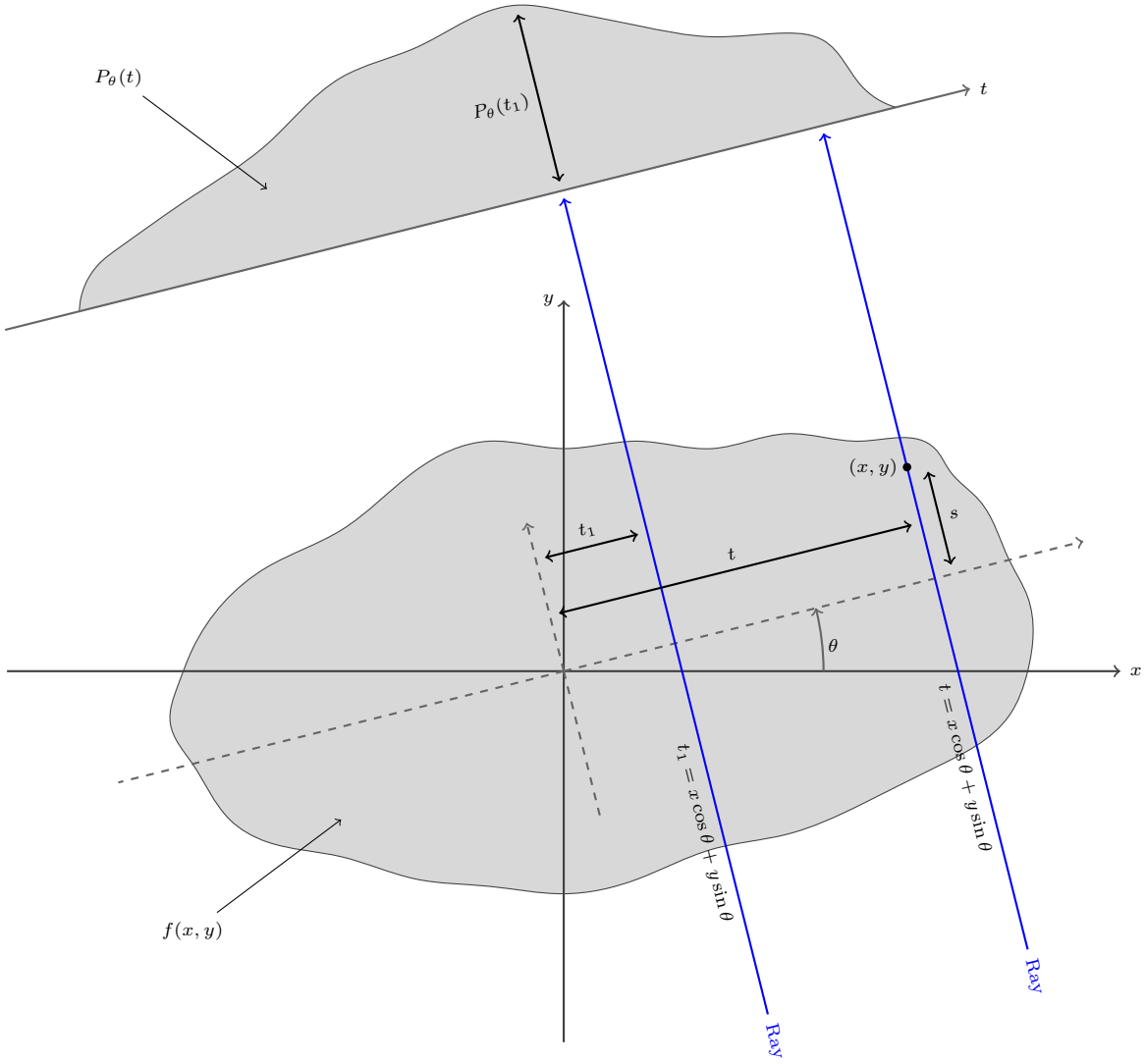


Figure 3.36. Example of object projection used for nCT (recreated from Kak *et al.* (2002)) [205].

Chapter 4

Results and Discussion

This chapter presents the results of the LISe scintillator and LISe semiconductor neutron imaging experiments. The LISe scintillator demonstrated practical application as a neutron imaging conversion screen when coupled to a high-resolution CCD. An analysis of spatial resolution is presented along with imaging results, including usage of the mosaic stitching technique and nCT. The radiation response and sensitivity in LISe semiconductors verified the usage of this technology in mixed radiation fields for neutron imaging. A progression from the LISe PD to the LISePix documented increasing spatial resolution, approaching operational characteristics on par with state-of-the-art technologies.

4.1 Scintillator: Single Sensor

The single crystal LISe scintillator provided a set of introductory experiments, qualifying the scintillation response to cold neutrons at HFIR. Using the in-house CCD optics, the sensor was easily coupled to the high-resolution imaging system. These experiments demonstrated the mosaic stitching technique, allowing the prototype sensor to image an area significantly larger that itself, overcoming the current growth related size limits.

4.1.1 Open Beam

In early testing, the LISe samples were found to demonstrate scintillation properties, generating light in response to a neutron field. While testing the early LISe single channel counter at CG-1D, a set of complementary scintillator experiments were also conducted using a single LISe sample (**LISe-1**). The open beam image is shown in Figure 4.1 captured using 20 frames at a 120 s exposure time. This image immediately verified the scintillator potential for LISe, with the open beam showing distinct contrast from the dark field baseline, and a clear outline of the sensor edge. While the light-tight enclosure at CG-1D was specifically engineered for the ^{6}LiF/ZnS screen, a direct replacement with the LISe scintillator produced positive re-

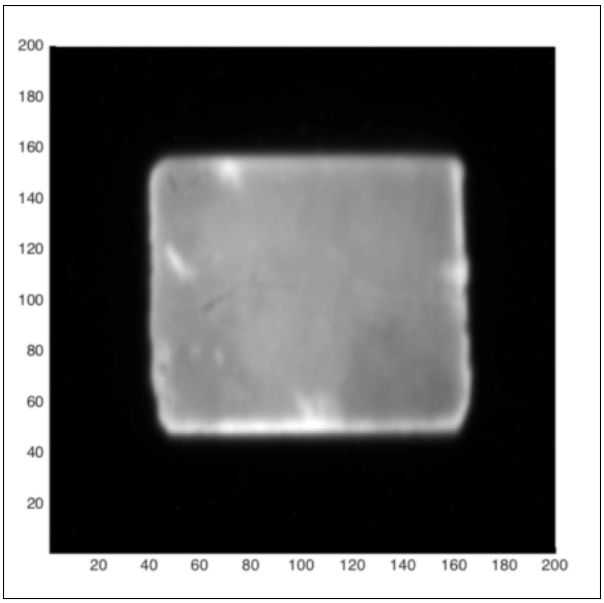
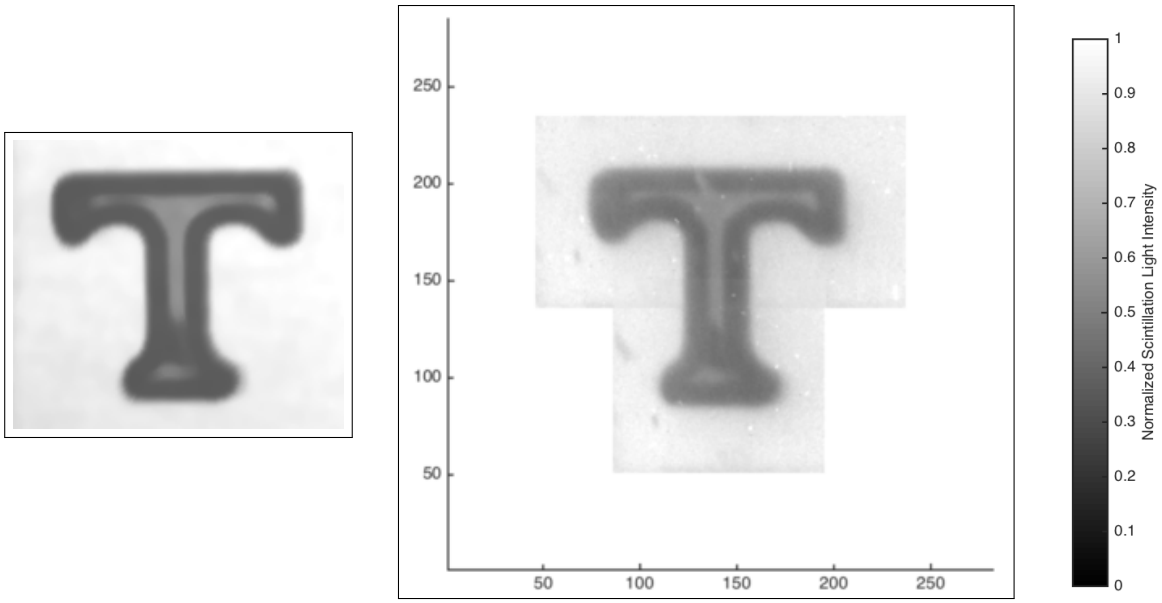


Figure 4.1. Open beam image of single LISe scintillator [96].

sults. At only 650 µm thick, the sensor boasted a neutron absorption efficiency over 70 %, measured with the ^{6}LiF/ZnS screen [96].

4.1.2 Power-T Target

The FDM *Power-T* imaging target was the first object to be imaged with the LISe scintillator. With a simple geometry, large feature size, and relatively uniform density, the object served as a preliminary test for comparing the response of the ^{6}LiF/ZnS screen and *LISe-1*, shown in Figure 4.2. The image captured with the ^{6}LiF/ZnS screen used 5 frames at 60 s exposures at a single location, using only a small fraction of the much larger FOV. Because **LISe-1** had an area slightly smaller than the *Power-T* dimensions, a simple mosaic stitching experiment used 3 different positions, each capturing 2 frames at 60 s exposures. The outline of each open beam section from **LISe-1** is visible in Figure 4.2b, cropped to remove the inhomogeneous light output near the edges of the sensor. While the image clarity is comparable at equivalent exposure windows, the ^{6}LiF/ZnS screen produced a higher LY and thus more contrast, creating a darker *Power-T* (see Figure 4.2a), when the two images are normalized to the same scale. In both images, the internal voiding is visible as a more transparent region in the center of the logo [96]. When parts are 3D printed using a FDM process, the outer profile is traced in plastic filament, creating a continuous surface perpendicular to the build plate (the page in this case). To conserve material and minimize sagging of the part as layers build and the plastic cools, the internal area is only partially filled using a varying web of plastic filament. This web effectively creates a porous, internal structure (visible in larger objects), producing less neutron attenuation and a more transparent image. The outline of the *Power-T* corresponds to the solid filament outline, effectively measuring the thickness of the part's sidewall, with only a small attenuating region in the lower leg of the



(a) LiF/ZnS screen image (b) LISe scintillator image using mosaic stitching

Figure 4.2. Scintillator performance comparison of *Power-T* transmission neutron imaging target (CCD effective pixel size = 36.5 µm) [96].

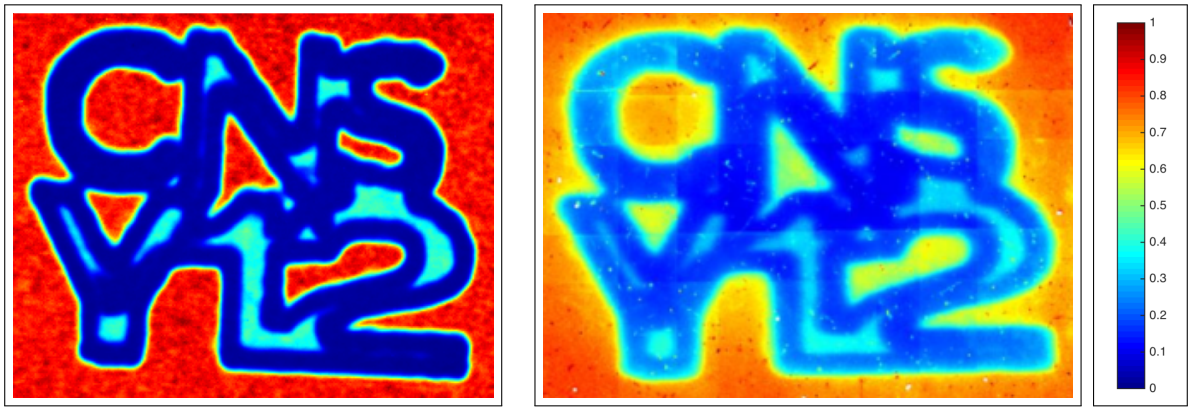
object, likely due to a cross-over point along the nozzle tracing path.

4.1.3 CNS-Y12 Target

The *CNS-Y12* target was manufactured using the same FDM process, however the part is both thicker and covers more imaging area (see Figure 3.30). The unique shape, internal voiding, and hollowed regions between the lettering created a more complex set of features, seen in Figure 4.3. Again using the ^{6}LiF/ZnS screen as a baseline, the neutron image averaged 5 frames at 60 s exposures. The larger target required 15 sampling positions with **LISe-1**, each with 2 frames at 60 s exposures. This experiment, along with the *Power-T*, further confirmed the mosaic stitching technique for imaging large areas using a smaller prototype sensor. Both scintillators reveal the internal voiding from the filament webbing, clearly visible in the number '12', while also showing the letter 'C' was almost entirely solid plastic based on the circular path required to create the shape. The more gradual color change in the LISe scintillator image (Figure 4.3b) can again be attributed to lower LY and contrast. The contrast is more prominent in the center of the part, where multiple position data overlaps, improving the data average.

4.1.4 PSI Siemens Star

As a final performance comparison between the ^{6}LiF/ZnS screen and the single LISe scintillator, the Siemens Star was imaged with both systems. Shown in Figure 4.4, the LISe scintillator images are superimposed on the larger ^{6}LiF/ZnS screen image, offering a direct visual comparison. The ^{6}LiF/ZnS screen image (blue)



(a) LiF/ZnS scintillator screen (b) LISe scintillator sensor

Figure 4.3. Scintillator performance comparison of *CNS-Y12* neutron imaging target (CCD effective pixel size = 36.5 µm) [96].

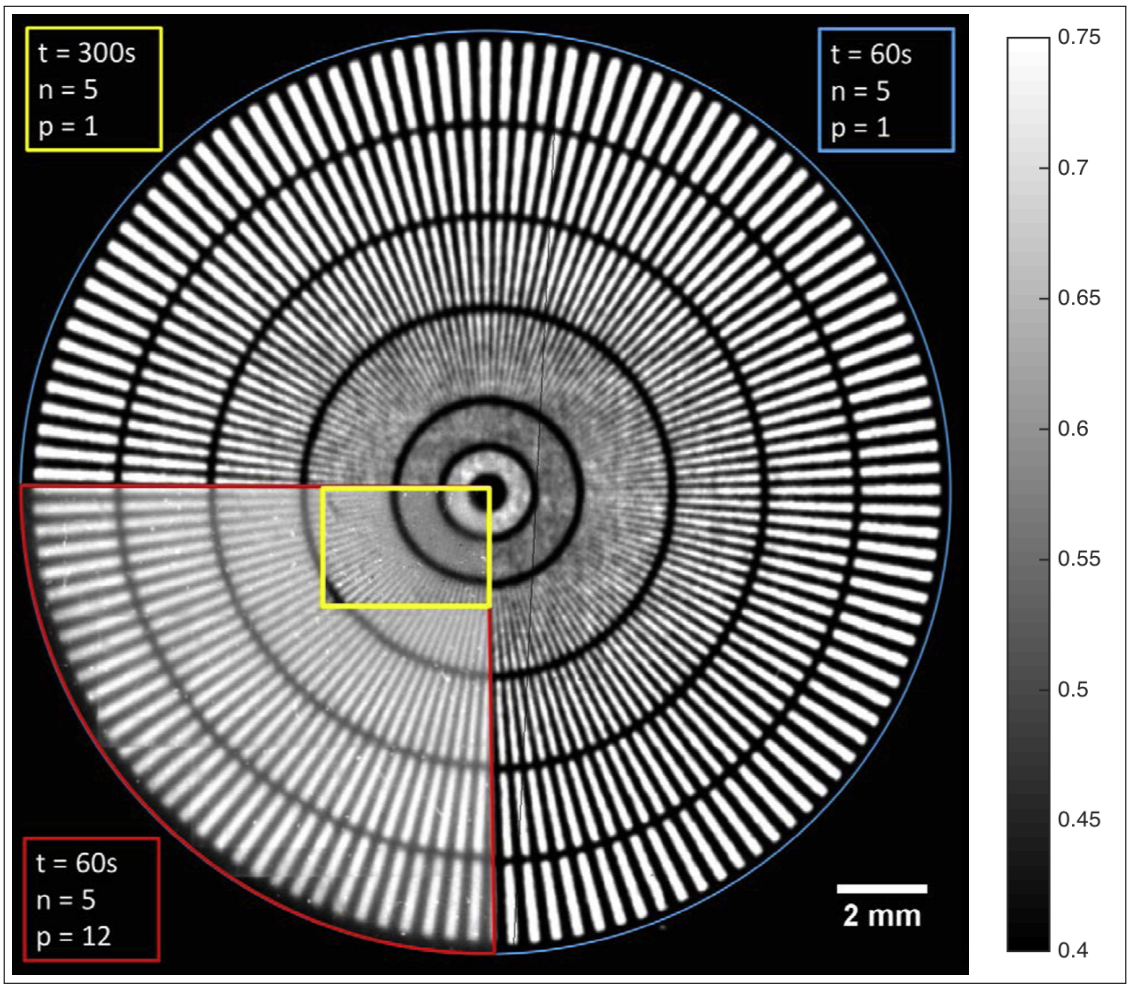


Figure 4.4. Radiograph taken of the Siemens Star with the 50 µm LiF/ZnS scintillation screen. The overlay data from the LISe scintillator is outlined in red, with an extended count in yellow. In the colored regions, the integration time (t), number of images taken to define the median image (n), and the number of positions (p) [96].

consisted of 5 frames counted for 60 s exposures, a standard acquisition for resolution estimation. In the lower, left-hand corner of the image, the LISe scintillator mosaic is outlined in red, covering approximately 1/4 of the mask using 12 different positions, with 5 frames each at 60 s exposures. Towards the center of the mask, a single position (yellow) was captured with 5 frames at an extended 300 s exposure, providing the necessary contrast to resolve the fine line pairs. The difference between the center image and the large mosaic can be seen in the bottom left corner of the yellow outline, where the radial marker is much darker than the rest of the LISe scintillator. Between the 200 and 100 µm radial markers, the line pairs are well distinguished, with some line pairs still resolvable just inside the 100 µm radial marker. A concurrent experiment using a separate LISe scintillator at PSI produced a similar spatial resolution at their neutron imaging line. Visual inspection indicates an equivalent spatial resolution limit between the ^{6}LiF/ZnS screen and the LISe scintillator for this experiment, coupled to the same optics and acquisition system [96].

4.2 Scintillator: Sensor Array

The LISe scintillator array offered a test for quantifying the scintillation performance of multiple samples, from different crystal growth boules. With an active area much smaller than the ^{6}LiF/ZnS screen, the samples were readily positioned in the center of the neutron beam and the FOV of the CCD , providing a direct performance comparison under near identical operating conditions. Furthermore, the larger open beam window, created by tiling multiple sensors, allowed neutron imaging of larger target objects.

4.2.1 Open Beam

The first version LISe scintillator array predominately measured LY and neutron absorption efficiency. The sensors were spread further apart and functioned as independent open beam areas. In the second version of the LISe scintillator array experiment, the sensors were attached to the aluminum backing plate in close proximity to one another. The resulting array provided a pseudo open beam area, shown in Figure 4.5, demonstrating the concept of tiling multiple, smaller scintillators together to create a large FOV. Each open beam was produced from a series of 20 frames at 15 s exposures. In the earlier LISe scintillator imaging experiments, the sensors were attached with reflective, aluminum tape, boosting the LY by reflecting any photons traveling in the opposite direction of the beam. It was hypothesized that the reflective backing, while increasing the LY, would also introduce blurring from the back scattered photons. To test this hypothesis, two parallel experiments were conducted using the reflective aluminum backing as well as an anti-reflective, theatrical tape featuring a highly absorbing black coating [97].

The LISe samples used in the experiment ranged from 5 to well over 20 times the thickness of the 50 µm ^{6}LiF/ZnS screen. While LiF/ZnS is traditionally applied as a thin film, being relatively opaque to its own scintillation light, LISe is optically transparent, favoring photon transport in the visible spectrum. Nonetheless, a back scattered photon must travel an additional distance at least the thickness of the LISe

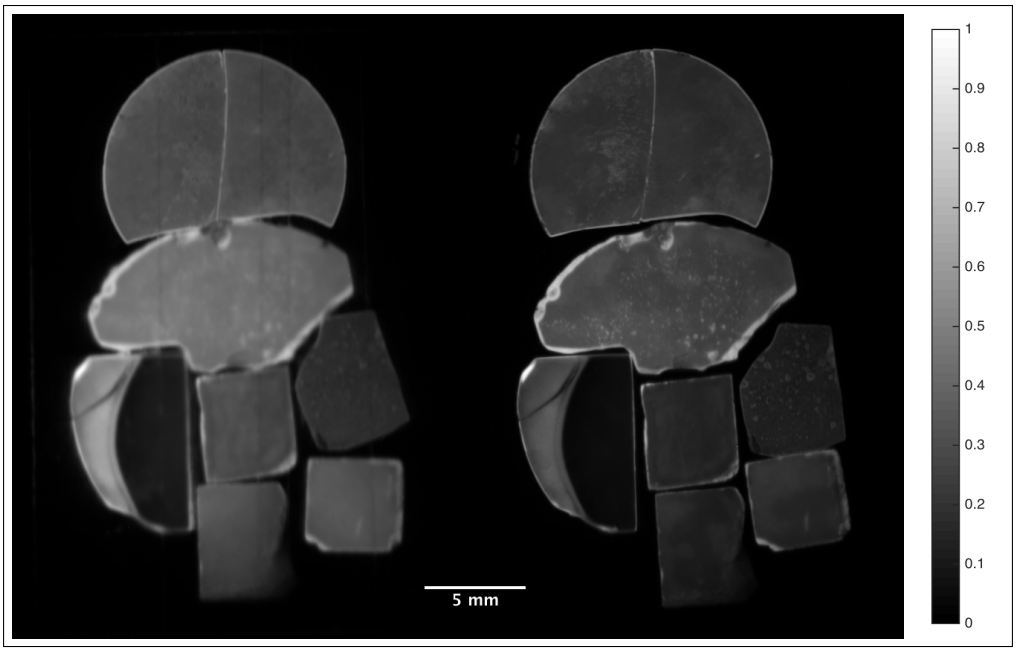


Figure 4.5. Open beam image of LISe scintillator array (v2) using reflective backing (left) and anti-reflective backing (right) [97].

crystal, increasing the probability of scattering before exiting the sensor. The experimental LY, listed in Table 4.1, confirms the theory that back scattered scintillation light boosts overall LY, which can also be seen in the open beam comparison image. The light yield was calculated using a large, rectangular ROI across each LISe sample, with an identical ROI evaluated in the open beam image using the ^{6}LiF/ZnS screen. Because the exact positioning would be impossible to replicate when exchanging the adhesive, this comparison eliminates variation due to positioning and nonuniformities in the beam [97].

As an observational note, in **LISe-010515** there is a smoothly curved response edge, showing a significant drop in light yield across an abnormally sharp edge. This aberation exists inside the material, the phenomena being previously identified in the top half of **LISe-6.1** and in **LISe-6.3**, also originating from boule #010515 (see Figure 3.24a). Evaluated with the MTF method, the edge response in **LISe-6.1** fell off within 80 µm, exhibiting a broader change in color from reddish to chartreuse over the length of the crystal. A similar LY transition edge was evaluated in **LISe-010515**, showing an additional parallel band following the primary transition edge. In both samples, this abrupt LY edge produces a dark region on the concave side, and a noticeably brighter region on the convex side. Based on the geometry and curvature of the internal transition, this specific growth produced a higher grade scintillator material on the outsie of the boule, with a redder, lower LY material towards the center [96].

Table 4.1. LISe scintillator neutron absorption efficiency and LY measured with reflective and anti-reflective backing [97].

Sample ID	$\varepsilon_{\mathbf{int}}$ (%)	**LY - Reflective**†		**LY - Anti-Reflective**†	
		LISe	LiF/ZnS*	LISe	LiF/ZnS*
LISe-4A	62 ± 4	2.79 ± 0.14	5.92 ± 0.20	1.39 ± 0.05	5.98 ± 0.27
LISe-4B	59 ± 4	2.99 ± 0.14	5.46 ± 0.20	1.44 ± 0.08	5.26 ± 0.20
LISe-4D	45 ± 5	2.70 ± 0.25	6.13 ± 0.18	1.31 ± 0.08	5.80 ± 0.24
LISe-5A	61 ± 4	2.86 ± 0.01	5.79 ± 0.18	1.57 ± 0.07	5.69 ± 0.23
LISe-5B	62 ± 3	2.70 ± 0.15	5.39 ± 0.16	1.53 ± 0.08	5.38 ± 0.19
LISe-010515	88 ± 4	4.4 ± 0.6	6.83 ± 0.18	1.89 ± 0.14	6.88 ± 0.22
LISe-072715	83 ± 4	3.74 ± 0.14	6.05 ± 0.18	1.77 ± 0.11	6.0 ± 0.3
LISe-082415	83 ± 3	2.02 ± 0.08	5.16 ± 0.19	1.30 ± 0.05	5.23 ± 0.02

* Values for the ^{6}LiF/ZnS screen correspond to ROI for associated LISe scintillator.

† LY values are reported as $\times 10^3$ counts.

4.2.2 Resolution Calculations

In previous experiments, the resolution was qualified using the Siemens Star to be near 100 µm. To determine the calculated spatial resolution of each sample, a knife-edge test was conducted using the thin film gadolinium edge provided on the large Siemens Star mask (see Figure 3.29). Four vertical edge positions were captured with each backing to provide a sharp transition across all samples in the array, each acquired using 5 frames at 30 s exposures. Following the methodology described in Section 3.6.3, a MTF calculation was run for each backing material, shown in Table 4.2. As expected, the anti-reflective backing provided a spatial resolution approximately half that of the reflective aluminum tape, as calculated with the MTF method [97].

Furthermore, the spatial resolution was weakly dependent on the surface roughness and scintillator thickness, with the three highest performing samples spanning the range of thicknesses: **LISe-5B** (432 µm), **LISe-082415** (904 µm), and **LISe-010515** (1,824 µm). For sample thicknesses over 300 µm, the resolution consistently approached the mid-30 µm range (MTF method), suggesting a minimum thickness required to prevent charged particle escape, while also confirming superior optical transparency to internally generated scintillation light. The MTF results prove the functionality of the LISe scintillator as a high-resolution neutron imager, with optimization in growth and preparation potentially seeing even further refinement in the spatial resolution [97].

Table 4.2. LISe scintillator spatial resolution measurements using reflective and anti-reflective backing, calculated with the FWHM and MTF methods [97].

Sample ID	Reflective		Anti-Reflective	
	FWHM	MTF	FWHM	MTF
LISe-4A	201.32	81.99	136.06	41.49
LISe-4B	237.88	88.70	152.64	56.55
LISe-4D	274.35	103.60	147.58	60.62
LISe-5A	132.13	52.05	147.07	40.17
LISe-5B	126.45	50.84	142.88	38.76
LISe-010515	157.36	53.55	92.20	37.29
LISe-072715	234.72	103.60	116.15	52.13
LISe-082415	145.20	57.80	111.17	34.06

Note: Spatial resolution value is given in units of µm.

4.2.3 Computed Tomography

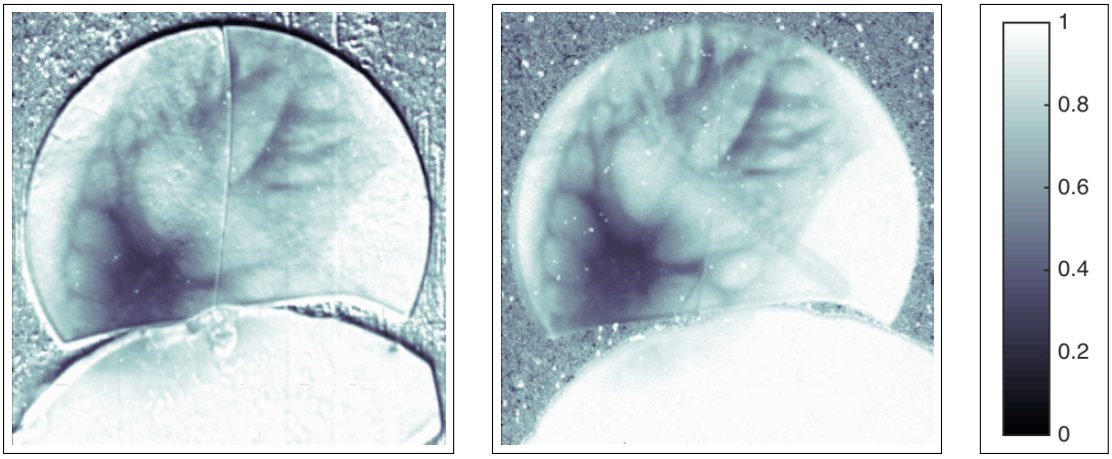
One of the most bold objectives in the LISe neutron imaging experiments was producing a nCT scan. Using samples **LISe-5A**, **LISe-5B** and **LISe-072715**, a large enough area was available to capture the bulk of a *halyomorpha halys* specimen. The scan used the rotational stage at CG-1D, sweeping 183° at 0.25° increments for a total of 733 projections, each across a 60 s exposure window. A scan was performed with each backing, lasting around 13 h a piece. For comparison, a nCT was also conducted with the ^{6}LiF/ZnS screen across the same intervals at 15 s exposures.

A sample of the raw LISe scintillator scan is shown in Figure 4.6, with the full scan available for download (File S4). The raw image exhibited significant salt-and-pepper (speckling) noise, as well as shadowing and overexposure along the crystal edges. The reflective backing also highlighted the split between **LISe--5A** and **LISe-5B**, along with a surface chip in **LISe-072715**. Initial attempts to use this data with the Octopus imaging software produced abnormal volume artifacts, encapsulating the insect volume inside a shell corresponding to the edge of the crystals. To overcome the deficit in imaging area, the image data was cleaned, removing the regions around the edges of the sensors and the dark field region (see File S5). After cropping the outlying region and replacing their values with a saturated open beam, a despeckling filter was applied, producing the sample projection shown in Figure 4.7. The final cleaned and filtered data

Supplement 4. "CT-scan-raw.gif" : Full sweep animation of neutron computed tomography of *halyomorpha halys* specimen as shown in Figure 4.6. (*available online*)

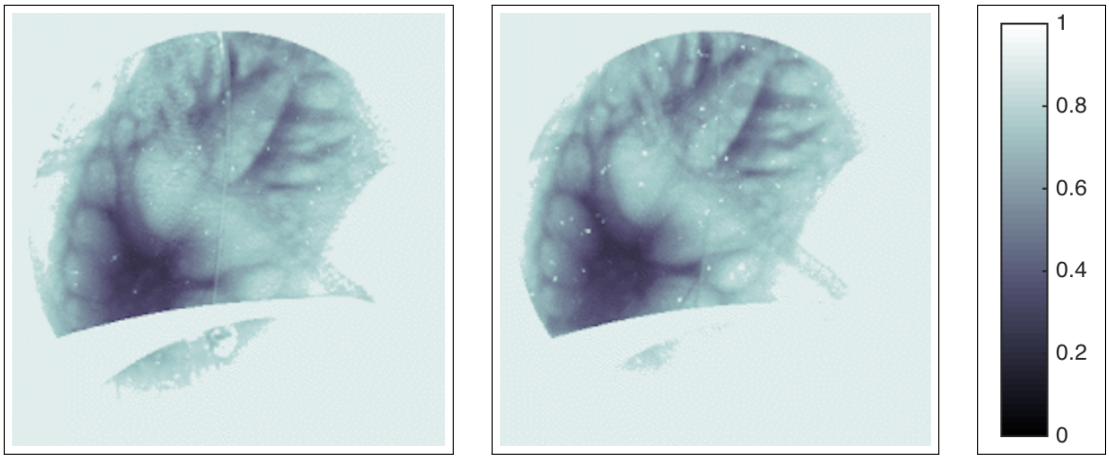
Supplement 5. "CT-scan-cleaned.gif" : Full sweep animation of neutron neutron computed tomography of *halyomorpha halys* specimen after white field cleanup. (*available online*)

Supplement 6. "CT-scan-filtered.gif" : Full sweep animation of neutron neutron computed tomography of *halyomorpha halys* specimen as shown in Figure 4.7. (*available online*)



(a) reflective (b) anti-reflective

Figure 4.6. NCT slice comparing raw LISe scintillator neutron radiographs of *halyomorpha halys* specimen.



(a) reflective (b) anti-reflective

Figure 4.7. NCT slice comparing cleaned and filtered LISe scintillator neutron radiographs of *halyomorpha halys* specimen [97].

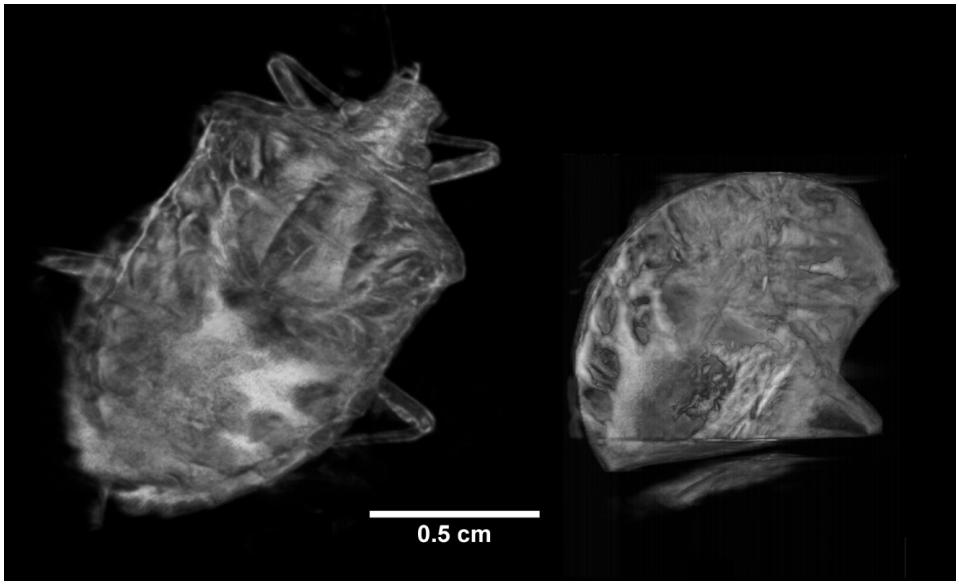


Figure 4.8. Neutron computed tomography using ^{6}LiF/ZnS screen (left) and LISe scintillator array (v2) after cleaning and filtering sensor array data (right) [97].

was sufficient to run the CT analysis in Octopus (see File S6). A comparison between the ^{6}LiF/ZnS screen and the LISe scintillator array is shown in Figure 4.8. The legs and lower abdominal features are visible in both reconstructed volumes. The internal structure of the shield shaped body can also be seen, as well as the rostrum (probing mouth part) in the LISe scintillator reconstruction.

4.3 Semiconductor Response and Sensitivity

Neutron imaging systems must be sensitive to neutrons, however, their ability to detect or discriminate against other types of radiation is important for real world usage. In most neutron experiments, a mixed radiation field is present, requiring robust system capable of handling a variety of conditions. For the LISe semiconductor technology, a gambit of radiation exposure studies have been conducted to evaluate the sensitivity to other classes of radiation.

Alpha Exposures

A convenient way of testing semiconductor signal generation and energy resolution, α injection introduces the large charged particle into the sensor bulk without the need for a neutron source. Because the $^{6}\mathrm{Li}(n,\alpha)^{3}\mathrm{H}$ reaction spawns T's and α's, directly injecting an α of equivalent energy serves as an analog for charge collection. Shown in Figure 4.9, this type of experiment was used to evaluate whether a new semiconductor sample exhibited sufficient electrical performance, assuming appropriate ^{6}Li enrichment would ensure the precursory reaction in the presence of neutrons. The natural decay of ^{234}U, following eq. (40), releases a highly energetic α, with over double the energy of the α released in the $^{6}\mathrm{Li}(n,\alpha)^{3}\mathrm{H}$ reaction.

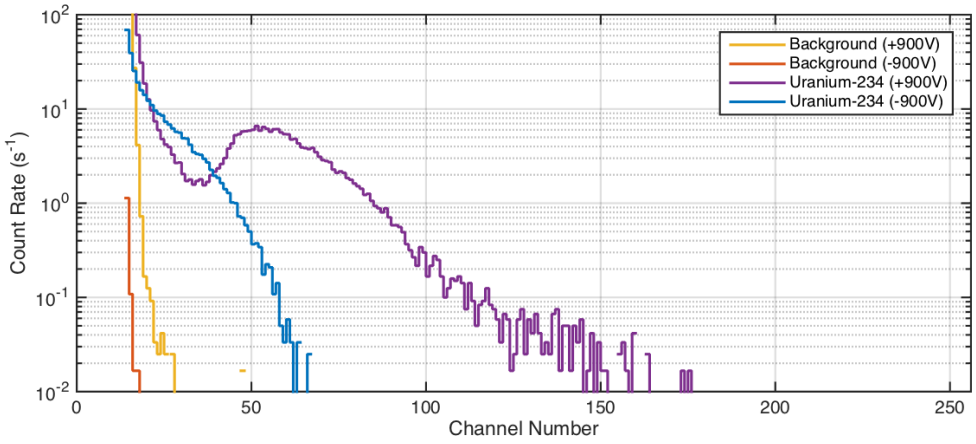


Figure 4.9. Bias polarity effects on LISe response to ^{234}U alpha source.

$$^{234}_{92}\mathrm{U} \rightarrow {}^{230}_{90}\mathrm{Th} + \alpha \qquad \underline{Q\text{-value}} \quad 4.860\,\mathrm{MeV} \tag{40}$$

Operating in a vacuum at close proximity to the detector surface, the higher energy α's will penetrate into the sensor bulk, generating a large number of charge carriers, comparable to or exceeding the actual neutron reaction, near the incident electrode. In this way, it was determined that LISe has significantly better electron charge carrier properties compared to those for the holes. With both positive and negative polarity high-voltage bias, the sensor generates minimal background signal, as expected from a high resistivity ohmic semiconductor. Introducing the α from a ^{234}U electroplated button source, the positive bias exhibits a much larger tail, extending into the higher energy channels and creating a broad energy peak. Under a negative bias, the spectrum is compressed to the lower energies, covering less integrated area, without exhibiting an energy peak. A similar spectra was captured using other actinide series alpha emitters including: ^{238}Pu (5.593 MeV), ^{241}Am (5.637 MeV), and ^{244}Cm (5.901 MeV), as well as ^{210}Po (5.407 MeV).

Beta Sensitivity

As a neutron imaging sensor, LISe is subjected to extremely high neutron fluences, producing a series of neutron reactions, including neutron capture (n, γ), generating heavier isotopes. In the compound ^{6}LiInSe$_2$, isotopes of lithium and indium provide the majority of neutron interacting species. Mostly present as ^{6}Li, the lithium component interacts following the desirable $^{6}\mathrm{Li}(n, \alpha)^{3}\mathrm{H}$ as discussed in Section 2.1.3 (see Figures D.7 and D.8). Alternatively, the natural indium component, consisting of isotopes ^{113}In and ^{115}In (4.28 % and 95.71 % respectively), also possesses a significant neutron cross section, competing with the lithium reaction. For the low neutron energies present at CG-1D, the indium isotopes will account for approximately 20 % of the reactions in the LISe sensor [96]. The neutron interaction cross sections for both indium isotopes

are dominated by capture reactions (see Figures D.9 and D.9) producing γ-rays, such as the ^{113}In neutron capture reactions shown in eq. (41).

	Q-value	
$^{113}_{49}\mathrm{In} + n \rightarrow {}^{114}_{49}\mathrm{In} + \gamma$	7.274 MeV	(41a)
$^{113}_{49}\mathrm{In} + n \rightarrow {}^{114m1}_{49}\mathrm{In} + \gamma$	7.084 MeV	(41b)
$^{113}_{49}\mathrm{In} + n \rightarrow {}^{114m2}_{49}\mathrm{In} + \gamma$	6.772 MeV	(41c)

The ground state, ^{114}In, and the meta-stable isomeric states ^{114m}In and ^{114m2}In are shown with their associated half-lives, branching ratios, and decay reactions in the eq. (42) series [207].

$t_{1/2}$	$B.R.$		Q-value	
43.1 ms	100 %	$^{114m2}_{49}\mathrm{In} \rightarrow {}^{114}_{49}\mathrm{In} + \gamma(502\,\mathrm{keV})$	(IT)	(42a)
49.51 d	96.75 %	$^{114m1}_{49}\mathrm{In} \rightarrow {}^{114}_{49}\mathrm{In} + \gamma(190\,\mathrm{keV})$	(IT)	(42b)
	3.25 %	$^{114m1}_{49}\mathrm{In} + e^- \rightarrow {}^{114}_{48}\mathrm{Cd} + \nu_e$	1.447 MeV	(42c)
71.9 s	99.5 %	$^{114}_{49}\mathrm{In} \rightarrow {}^{114}_{50}\mathrm{Sn} + \beta^- + \bar{\nu}_e$	1.989 MeV	(42d)
	0.5 %	$^{114}_{49}\mathrm{In} + e^- \rightarrow {}^{114}_{48}\mathrm{Cd} + \nu_e$	1.447 MeV	(42e)

The β produced in eq. (42d) has a mean energy of 778 keV along with a 1.3 MeV γ-ray. Following suit, the neutron capture reactions for ^{115}In are shown in eq. (43).

	Q-value	
$^{115}_{49}\mathrm{In} + n \rightarrow {}^{116}_{49}\mathrm{In} + \gamma$	6.785 MeV	(43a)
$^{115}_{49}\mathrm{In} + n \rightarrow {}^{116m1}_{49}\mathrm{In} + \gamma$	6.657 MeV	(43b)
$^{115}_{49}\mathrm{In} + n \rightarrow {}^{116m2}_{49}\mathrm{In} + \gamma$	6.495 MeV	(43c)

The ground and isomeric states for indium-116 are shown below in eq. (44), with their associated decay schemes [208].

$t_{1/2}$	*B.R.*		*Q*-value	
2.18 s	100 %	$^{116m2}_{49}\mathrm{In} \rightarrow {}^{116m1}_{49}\mathrm{In} + \gamma(162\,\mathrm{keV})$	(IT)	(44a)
54.29 min	100 %	$^{116m1}_{49}\mathrm{In} \rightarrow {}^{116}_{50}\mathrm{Sn} + \beta^- + \bar{\nu}_e$	3.278 MeV	(44b)
14.10 s	99.977 %	$^{116}_{49}\mathrm{In} \rightarrow {}^{116}_{50}\mathrm{Sn} + \beta^- + \bar{\nu}_e$	3.278 MeV	(44c)
	0.023 %	$^{116}_{49}\mathrm{In} + e^- \rightarrow {}^{116}_{48}\mathrm{Cd} + \nu_e$	0.467 MeV	(44d)

The β produced in eq. (44b) has a mean energy of 309 keV while the β in eq. (44c) has a much larger mean energy of 1.365 MeV, with both reactions producing highly energetic electrons (>1 MeV) and γ-rays (>2 MeV). The indium interaction rate, compared to ^{6}Li, comprises approximately 20 % of the total neutron interactions at thermal neutron energies. Therefor the higher isomer decay energy will manifest itself around 4 % of the time in all neutron interactions at CG-1D [96]. The range for 1 MeV β's in LISe is roughly 1.5 mm, linearly increasing at a rate of around 1.25 mm/MeV, significantly distributing charge carrier generatation across a large fraction of the sensor active area. The low production rate, along with their significant range, minimizes noise caused by β's in the neutron images [106]. The significance of the X-rays and γ-rays produced from indium isotopes will be discussed in the following section.

Gamma-ray Sensitivity

A major feature requirement of a robust neutron detector is the ability to discriminate between neutrons and γ-rays. Kouzes *et al.* specified a set of criteria for evaluating the effects of intrinsic γ-ray sensitivity, with a 10 % limit imposed on the deviation between the intrinsic efficiency for neutrons and mixed neutron/γ--ray fields, necessary in national security applications [29]. Applied across a wide range of liquid and plastic scintillators, neutron/γ-ray discrimination has been achieved through a few different techniques. McBeth *et al.* described a zero-crossing (ZC) PSD technique for distinguishing particle types based on their scintillation profiles. Pulse shape will vary between different types of radiation, corresponding to the decay time characteristic for each particle or photon. Using a series of analog nuclear instrumentation module (NIM) modules, the timing is converted to an amplitude for processing using a multi-channel analyzer (MCA) [209]. Charge comparison is another method for discrimination, integrating the slow and fast components of the scintillation pulse to determine the associated particle type [210].

In neutron imaging, such techniques are not practical, instead favoring a material with low γ-ray detection efficiency, or the capability of direct energy discrimination. Using MCNP simulations, it was shown that LISe demonstrated poor γ-ray detection efficiency at thicknesses used for the semiconductor systems. For samples less than 1 mm thickness, the γ-ray detection efficiency was less than 5 % for energies >100 keV. This feature helps to explain why the higher energy γ-rays produced from the various indium reactions did not contribute significant noise in any of the imaging experiments in either mode [106]. Furthermore, under

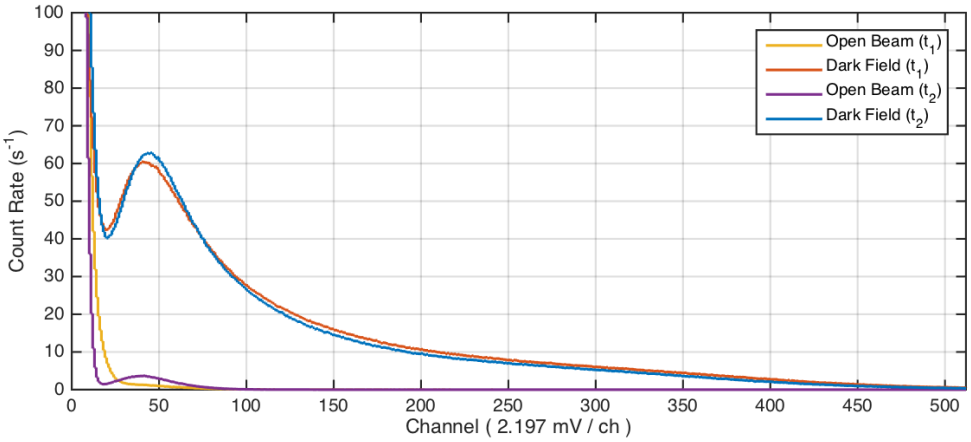


Figure 4.10. Neutron spectra at CG-1D from channel 15 of LISe PD at the beginning (t_1) and end (t_2) of experiments [145].

full charge collection a neutron interaction produces energetic particles an order of magnitude larger than the 100 keV limit: 2.73 MeV for the T, 2.05 MeV for the α and 4.78 MeV for the full event deposition.

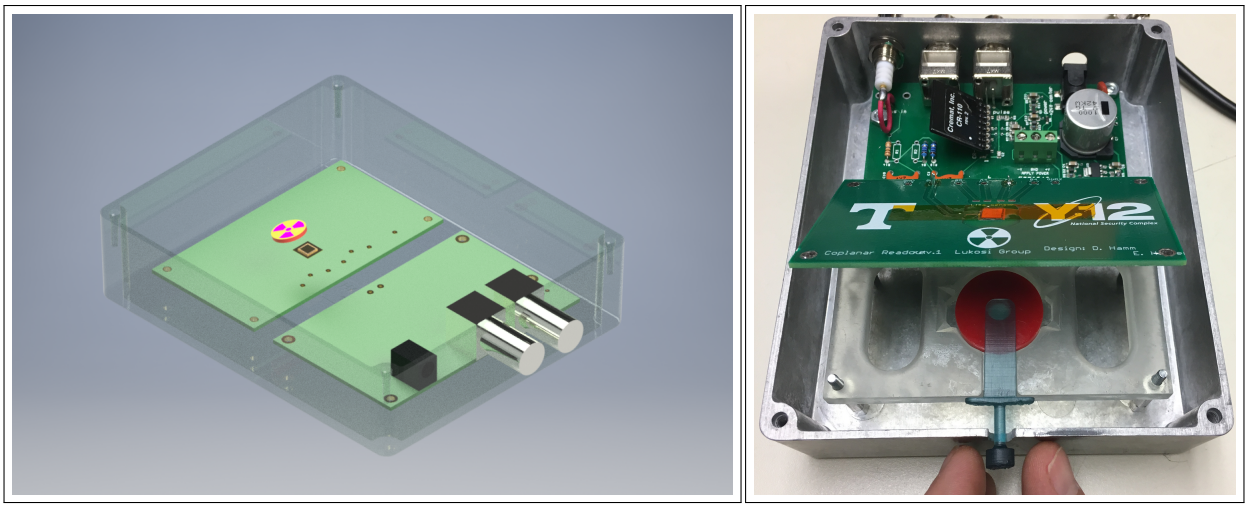
Neutron Detection

The neutron response for LISe was routinely tested using the Pu/Be source at University of Tennessee (UTK) before imaging experiments at HFIR. The moderated source provided a characteristic thermal/cold neutron spectrum, producing a broad continuum response over the background (dark field). At CG-1D the LISe PD produced a single, broad energy peak with an extended tail, shown in Figure 4.10 (half the digitizer range shown) [145]. A digital threshold was implemented on the digitizer to eliminate signal pile-up from low energy noise and pulses. Over the course of the experiment, the pulse height spectrum remained relatively consistent.

4.3.1 Fast Neutron Detection

As a natural extension to the neutron detection capabilities of LISe, fast neutron detection typically presents a greater challenge across most materials. Generally, neutron interaction cross sections tend to follow a $1/v$ relationship, with many of the prominent thermal neutron absorbers exhibiting orders of magnitude drop in performance at fast neutron energies (see Appendix D.1). Comparing Figures D.7 and D.8 it becomes apparent that as the neutron energy exceeds $\sim 10^4$ eV, the neutron interaction cross sections for ^{6}Li and ^{7}Li are roughly equivalent, within a factor of 2. Using LISe with natural concentrations of ^{6}Li will lower the sensor price and while increasing the accessibility, using the same refined growth process as lithium-6 indium diselenide (^{6}LISe).

A multi-source exposure system, shown in Figure 4.11, was designed and constructed to test LISe and ^{6}LISe samples, integrating a 3D printed button source holder within the enclosure. With the sensor attached



(a) fast sensor enclosure CAD model (b) fabricated testing enclosure

Figure 4.11. LISe fast neutron testing enclosure.

to the PCB using silver paste and wirebonds, the sample could be repeatedly tested without interrupting the contact or damaging the sensor. The enclosure was designed to support swappable sensor PCBs, each carrying a discrete sample. By desoldering the board wires, the wirebond and sensor were left untouched for later reuse, facilitating experimental repeatability. The enclosure featured an integrated CR-110 and CR--150 for versatile use with standard NIM or Versa Module Europa communication bus (VME) electronics. The button source carrier tray mounted directly underneath the sensor PCB, aligning the source with a via running through the base contact underneath the sensor. Using the 3D printed shutter (blue sword shape), the underlying α or β source could be blocked. This enclosure was meant to test a variety of LISe sensors with Pu/Be neutrons, facilitating a variety of combinations using the moderated or bare Pu/Be source, with and without the addition of injected charged particles. Initial exposures with natural lithium showed a response to α injection, as expected for a semiconductor grade sample, as well as a broad spectrum for various Pu/Be configurations. The signal was not as prominent as the ^{6}LISe testing and the results remain inconclusive, requiring further testing.

4.4 Semiconductor: 16 Channel Imager

In this semiconductor experiment, the LISe PD validated the hypothesis that LISe could be used as a pixelated neutron detector. Using a limited number of channels helped to reduce complexity of the build, focusing on the fabrication of the sensor and ensuring the basic system could be constructed and operated in a high flux neutron environment across a practical exposure timeline. The automated acquisition sequence provided the groundwork for a control intensive super-sampling scan, as well as other position dependent exposure experiments within the research group. The lessons learned in the two iterations of the LISe PD

were directly applied in the fabrication process of the LISePix as its high-resolution successor.

4.4.1 LISe Pixel Detector v1

In the first LISe PD experiments, a large portion of the allotted experiment time consisted of system setup and calibration. At the time, the CAEN acquisition electronics were brand new, switching from the previous analog electronics to a fully digital pulse processing system. Because the flux at CG-1D was significantly higher than the Pu/Be source at UTK, the threshold settings were completely different. After manually calibrating the set points to correctly register spectra for each of the 16 channels, the automated acquisition system was ready. As mentioned, a custom LabVIEW application controlled both the acquisition timing as well as the linear drives for the sample positioning stage. Interfacing with the in-house motor controller required some on-site changes to the control software, but the final result was a fully automated acquisition system for neutron imaging with the super-sampling technique. The scan consisted of 200 µm steps across a 101×9 array, generating a total of 909 acquisition locations, covering an area of $20 \times 1.6\,\mathrm{mm}^2$. With each exposure lasting 10 s and a generous 5 s slew window, the total experiment run time lasted right at 4 h [145].

The LISe PD scanned the stainless steel bolt, shown in Figure 4.12, receiving an estimated neutron fluence of $\sim 4 \times 10^{11}\,\mathrm{n/cm}^2$ across the duration of experimentation. Artificial color has been added to the image to contrast the open beam region (green) from the bolt attenuated region (yellow). The two regions are separated with bands of black to enhance the overall contrast and show clear transition between the open beam and object image. The semiconductor data from the LISe PD is outlined in red and superimposed on the comparison image captured using the ^{6}LiF/ZnS screen. Two data points have been marked in red to capture the edge profile of the bolt and the center of the bolt where attenuation is greatest. Approximately half-way through the automated experiment, the in-house motor control system power failed and had to be manually reset upon return to the line, leaving the system exposed to the open beam for 10.5 h before subsequent acquisition resumed. The resulting reduction in signal is seen in the intensity profile overlaid on the bottom of the bolt. The roughly 20 % decrease in efficiency was attributed to a combination of positive bias on the beam facing contact, where the interaction rate was highest, and the poor charge carrier transport properties for holes in this material. Because the electrons provided the majority of the detection pulse, damage induced on the beam side during extended operation magnified performance degradation, specifically interfering with electron collection [145].

4.4.2 LISe Pixel Detector v2

Having confirmed the functionality of the readout electronics and worked through debugging issues with the acquisition and control software, the primary focus in the second system iteration was the sensor. After the first set of experiments, the sensor PCB was removed from the imaging system and tested to determine the source of channel performance issues. Using a combination of current-voltage (IV) curve tests to determine

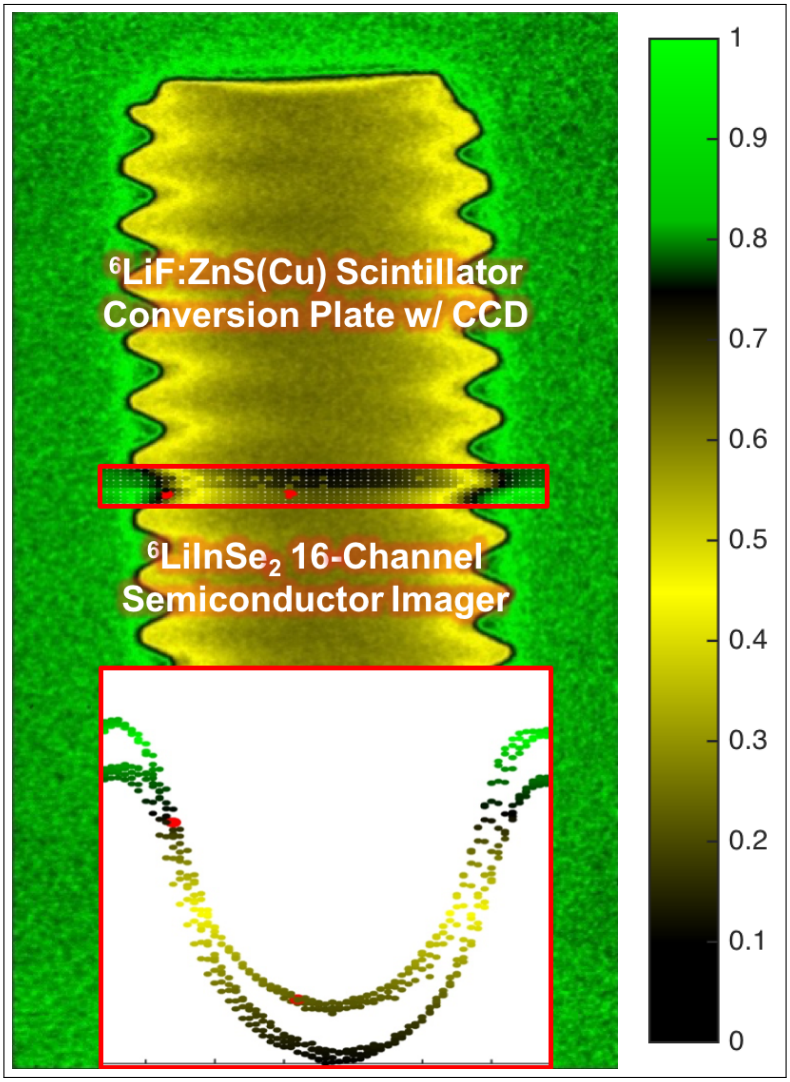


Figure 4.12. Image of a stainless steel bolt generated with the LISe PD overlaid on the radiograph taken with the 50 µm LiF/ZnS scintillation screen. Image is normalized to the mean white field [145].

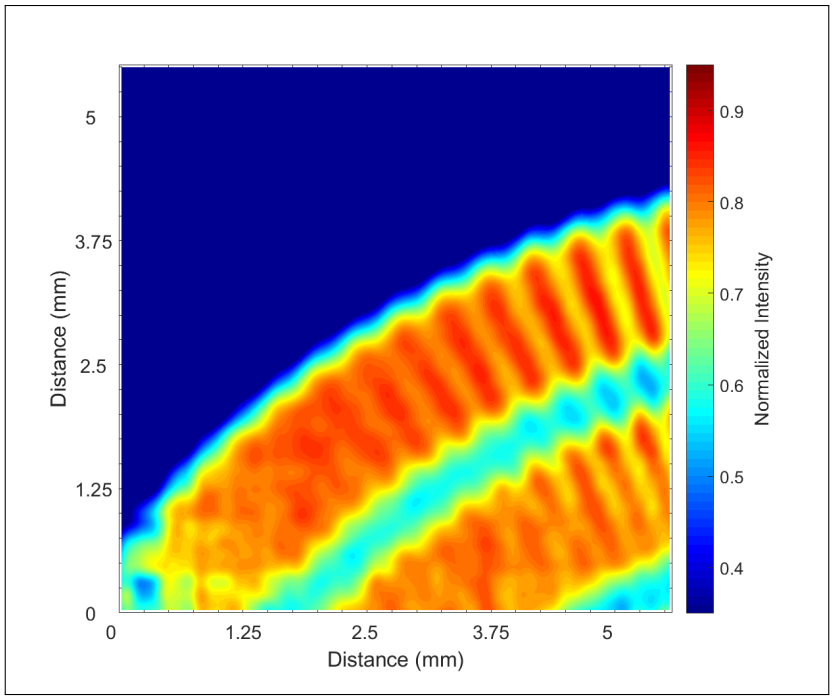


Figure 4.13. Reconstructed image of the Siemens Star using the LISe PD with a 550 µm pixel pitch and the super-sampling technique (125 µm step size) [145].

electrical response and visual inspection under the LM, the sensor showed signs of electronic decoupling. With an improved fabrication process, the sample was polished, stripping all previous metallization, and completely repackaged with a new sensor PCB to facilitate wirebonding. A combination of properly deposited contact metal and properly formed wirebonds ensured the mechanical stability of the electrical connections.

The super-sampling scan used 125 µm steps across a 33×33 array generating a total of 1,089 acquisition positions. Each position consisted of a 10 s exposure, and an additional 2 s window for stage position adjustment, running for a total experiment time of 3 h:37 min. Covering a $4 \times 4\,\mathrm{mm}^2$ sweep area, the scan captured the two outermost radial marking rings, shown in Figure 4.13. The reconstructed neutron image was able to resolve line pairs at the 500, 400 and 300 µm line pair spacings. At the 300 µm limit, the technique provided a spatial resolution roughly 55 % of the pixel size, corroborating the efficacy of the super-sampling technique in achieving sub-pixel size resolution. Furthermore, in this experiment, the rejuvenated sensor showed minimal performance degradation over the exposure period, with each channel consistently performing through the duration of the experiment. It is hypothesized the performance degradation in the first iteration was incurred as a result of electrical decoupling from weak wirebonds, or delamination of pixels. While all channels were able to generate an image signal, a few showed poorer performance than the others (see Figure C.3), possibly due to material defects, fabrication or a combination of the two. At the neutron energies seen in CG-1D, the anticipated efficiency should have approached 59 %, however the inefficiencies seen across the devices channels only measured between 35 % to 55 %. The performance deviation from the

idealized value was again attributed to the poor hole charge collection with the sensor bulk, present across all channels [145].

4.5 Semiconductor: Timepix Imager

The preliminary results of the LISePix system provided insight into the capabilities of the technology and proved the application of LISe as a high-resolution semiconductor detector. At the time of fabrication, the current growth system did not provide for a single sensor of adequate area to cover the entire Timepix, limiting the number of functional channels on the ASIC. Furthermore, the prototype LISePix sensor received a contact pattern treatment across the entire surface to maximize usable area, omitting a guard ring in this design. Typically, a guard ring is implemented to stabilize the internal electrical field, however, without a sensor large enough to cover the entire ASIC, a matching sensor guard ring would have been rendered ineffective [211]. The device also exhibited channel and regional defects, likely due to imperfects in the novel fabrication process. Most notably, a large area of dead pixels occurs in the upper right corner of the following neutron radiographs. A long streak of dead pixels is also visible along the horizontal direction [107]. The bottom left corner of the active area shows a reduction in signal output, a phenomenon similar to the response variation seen in the scintillator sensors and still under investigation [96]. The reasoning behind these defects and their effects on the output response will be described later in this section.

4.5.1 Plutonium / Beryllium Source

Preliminary testing for the LISePix system was conducted in the neutron irradiation laboratory at UTK. The 2 Ci Pu/Be source provided an isotropic neutron field of around 2×10^6 n/s. Shown in Figure 4.14, each frame counted interactions for a 600 s window, averaging a series of 150 frames to produce a single neutron radiograph. While this configuration is not suited for neutron imaging, an overnight count helps to ensure the sensor response, system automated functionality, and assess any potential for signal drift over extended periods of operation.

For safety reasons, the Pu/Be source is typically stored in a shielded safe or in a thick (> 6 in) polyethylene (PE) moderating enclosure, surrounded by 2 in thick paraffin wax blocks to provide significant thermalization and shielding. Under special circumstances, the source may be uncovered, exposing the detector to the raw spectrum emitted from the Pu/Be source. The LISePix system was tested in both configurations, measuring a thermal baseline, and a higher energy mixed spectrum to test the sensitivity to fast neutrons. A clear neutron baseline signal is established in the thermalized response (Figure 4.14a) with the raw intensity scale given to offer an absolute comparison with the less resolved bare response (Figure 4.14b). Lukosi *et al.* simulated the expected response across varying energy ranges, anticipating a drop in overall interaction by a factor of 1,000 at higher neutron energies [106]. Because the spectra emitted from the source and enclosure are not true thermal or fast energy spectrum, and certainly not mono-energetic, a MCNP simulation would

be required to evaluate a more representative flux in each configuration, providing a quantifiable comparison of device efficiency across each energy range. The selected ROI (shown in Figure 4.14c) was evaluated in ImageJ to provide a measure of uniformity across the broader active area, with an average intensity value of 0.00140 ± 0.00049. This experiment illustrates the broad sensitivity to neutrons across the entire energy spectrum, however, the usage of heavily ^{6}Li enriched material predisposes this specific composition for thermal neutron detection [107].

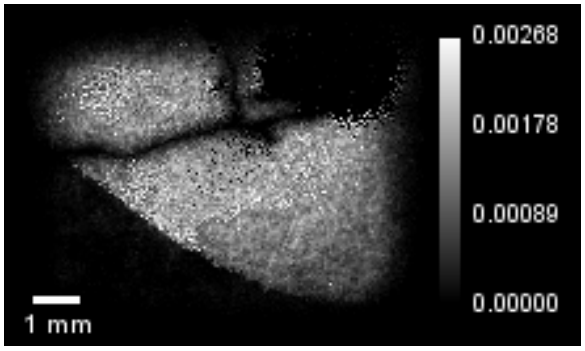
4.5.2 Open Beam

As with previous experiments, the LISePix system was tested at HFIR on CG-1D. With prototype systems, the first experiment captures the open beam image, verifying neutron response, pixel electronic operation and exposure window timing. The neutron source at HFIR provided a neutron fluence of $4.5 \times 10^{6}\,\mathrm{n/cm^2}$ across the sensor area, or $300\,\mathrm{n/s}$ across each $55 \times 55\,\mu\mathrm{m}^2$ pixel. Shown in Figure 4.15, the imager responded to the neutron beam across the active sensor area, with a diminished response in the lower left corner. The acquisition settings used were 50 frames at 1 s exposures with the sensor biased at $+300\,\mathrm{V}$. Configured with the 16 mm beam aperture to maximize neutron flux, $L/D = 375$ for this setup [107]. The smooth curvature and abrupt transition in contrast suggested a material or phase gradient, similar to Figure 3.24, instead of a mechanical defect. A key difference is the direction of contrast transition, with the inner concave region creating a more intense semiconductor signal and the outer, convex region exhibiting a weaker electronic pulse. This behavior functions opposite of the same phenomena observed in the LISe scintillators, suggesting the scintillation and semiconductor mechanisms are complementary constituents of the total neutron response.

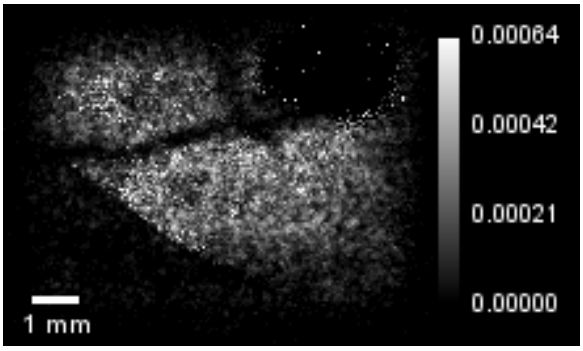
The variation between bright and dark response regions was characterized to determine relative intensity difference and intensity homogeneity, shown in Figure 4.15b. Each ROI consists of approximately equivalent number of pixels, with the bright ROI concentrated around the same area as in the Pu/Be analysis, demonstrating the largest contrast and smoothest response. The bright ROI yielded a mean intensity of 0.0086 ± 0.0008, while the dark ROI returned a more modest 0.00520 ± 0.00178, equating to a 40 % intensity reduction across the sharp gradient. The open beam response image showed less deviation in intensity across the sensor, as expected, due to the energy and spatial uniformity of the neutron beam. Furthermore, the more luminous beam and lower neutron energies highlighted the true functional edge of the sensor area, not visible in the Pu/Be experiments. The gradual drop off and rounded corners at the periphery are likely attributed to the omission of a guard ring as previously noted [107].

4.5.3 Resolution Calculation

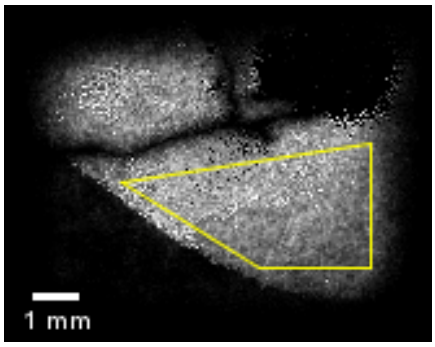
In accordance with neutron imaging resolution experiments, the Siemens Star was imaged using the LISePix, shown in Figure 4.16. After confirming a suitable exposure window using the neutron flux at the largest



(a) thermalized Pu/Be source

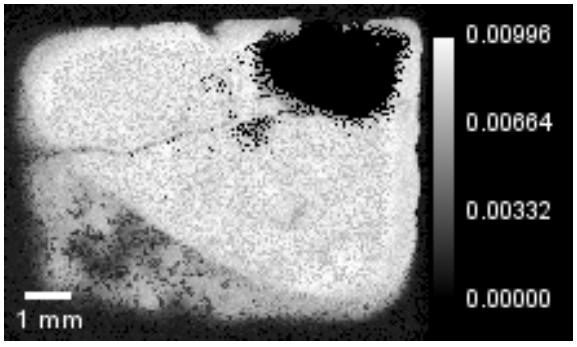


(b) bare Pu/Be source

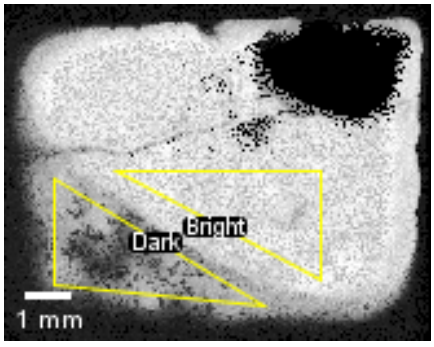


(c) thermalized Pu/Be source ROI

Figure 4.14. LISePix neutron field response image to 2 Ci Pu/Be neutron source [107].



(a) open beam response



(b) open beam ROI

Figure 4.15. LISePix neutron response image of HFIR CG-1D open beam [107].

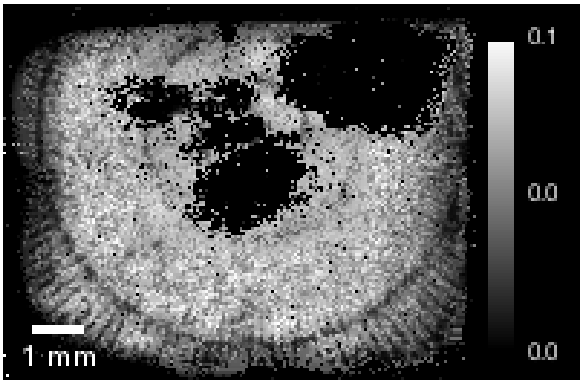
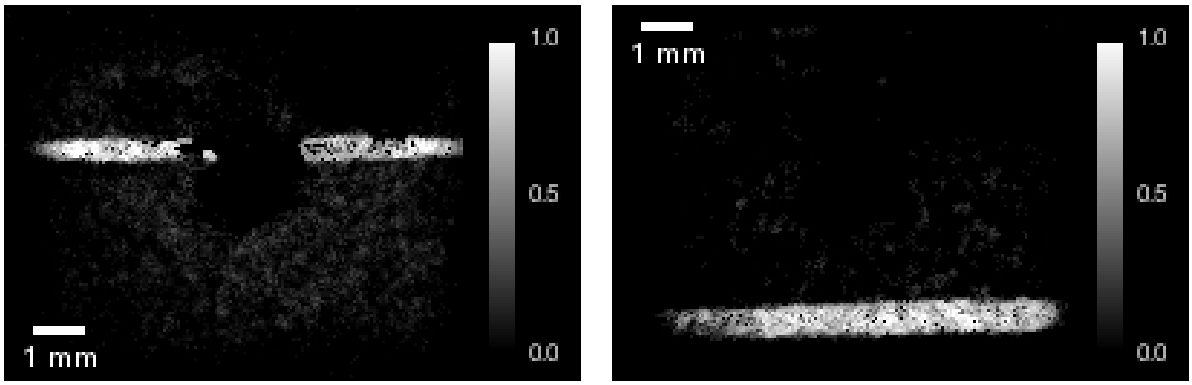


Figure 4.16. LISePix neutron image of Siemens Star [107].

aperture, the beam was reconfigured with the 8.2 mm aperture to enhance resolution. The configuration provided a larger, $L/D = 732$, with a target distance measured at, $l = 7$ mm. The Siemens Star image was captured across 400 frames at 1 s exposures, with the larger frame count providing additional statistics to overcome the now heavily obstructed beam. The 200 µm indication ring is circumscribed across the bottom and left side of the sensor, with clearly separated line pairs on the outside of the ring, and some line pairs extending inwards towards the 100 µm ring. Shown in the center of the imaging area, the 100 µm radius marker is partially visible (∼75 %) while the innermost 50 µm ring is identifiable (∼25 %). It should also be noted, the darker ROI in the lower left corner provides approximately equivalent performance in the cleaned and normalized output image, suggesting the isotopic composition and electronic performance remains consistent across the sensor. As a preliminary qualitative assessment, this experiment indicates the spatial resolution of the system is at a minimum equivalent or better than 200 µm, even with sub-optimized fabrication [107].

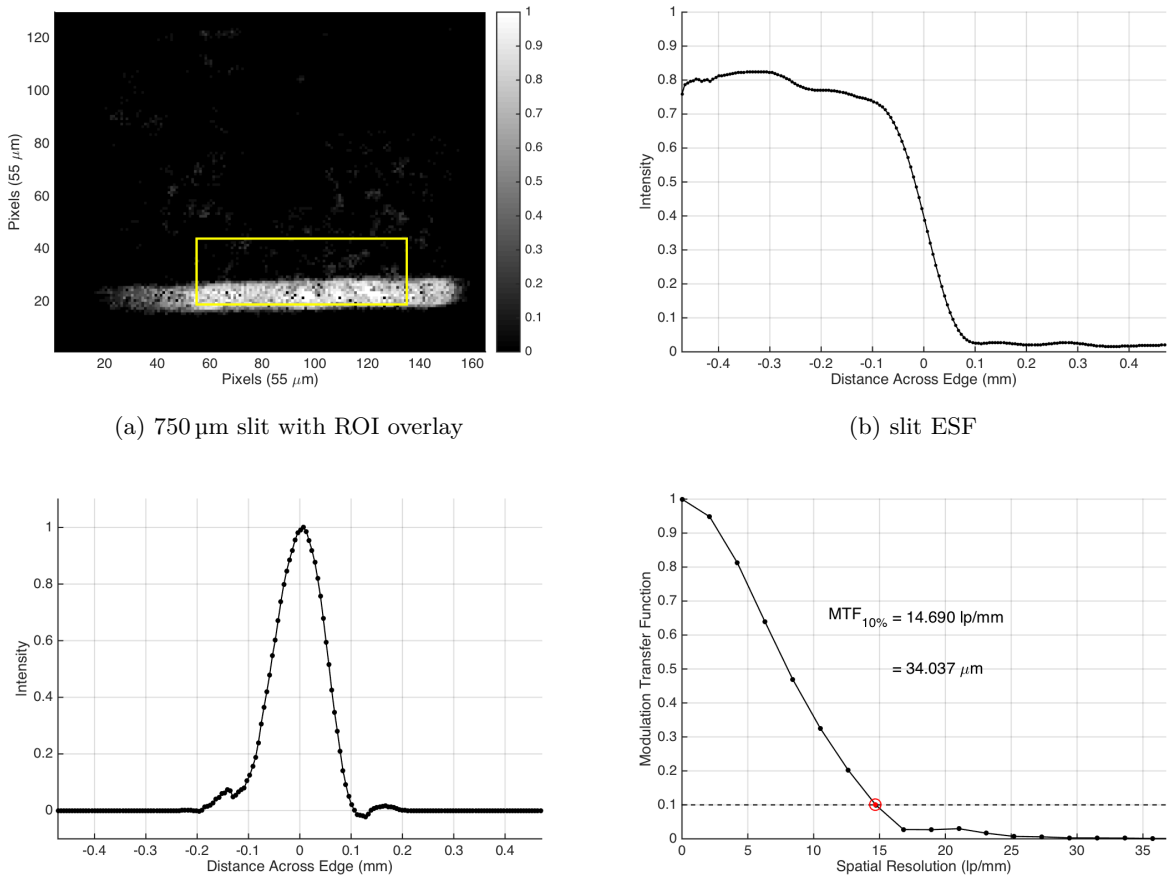
A knife-edge experiment provided data for use with the MTF technique to quantitatively evaluate the operational spatial resolution. The experiment follows the same principals as described in Section 3.6.3, creating an abrupt change in the beam intensity to determine the edge resolution across the full contrast, from open beam to fully attenuated (dark field) intensity. Two long slits, shown in Figure 4.17, provided the sharp edge at widths of 500 µm and 750 µm, captured using 50 frames at 1 s exposures. Extending past the width of the detector, the slits were milled into a 1/16 in thick aluminum sheet, treated in a borated coating to heavily attenuate the cold neutron beam. The aluminum plate was installed at distance of $l = 10$ mm from the detector. The 500 µm wide slit (Figure 4.17a) showed uniform open beam intensity across the horizontal direction, broken in the middle corresponding to the dead pixel region. Alternatively, the 750 µm wide slit (Figure 4.17b) ran the entire length of the sensor area, showing a slight drop in intensity in the bottom corner as seen in the previous figures. Both slits were imaged at a slight angle, rotated approximately 2° counterclockwise from horizontal, to overcome the pixel size limit in the MTF analysis [107].

For the MTF analysis, the 750 µm slit was used, offering a continuous edge profile. Shown in Figure 4.18, the edge profile consisted of a ROI 80 pixels long by 25 pixels wide across the edge transition, outlined



(a) slit: 500 µm (b) slit: 750 µm

Figure 4.17. LISePix neutron image of knife edge slit in thin borated aluminum attenuating sheet [107].



(a) 750 µm slit with ROI overlay (b) slit ESF

(c) slit LSF profile (d) slit MTF profile

Figure 4.18. MTF method to calculate edge resolution [107].

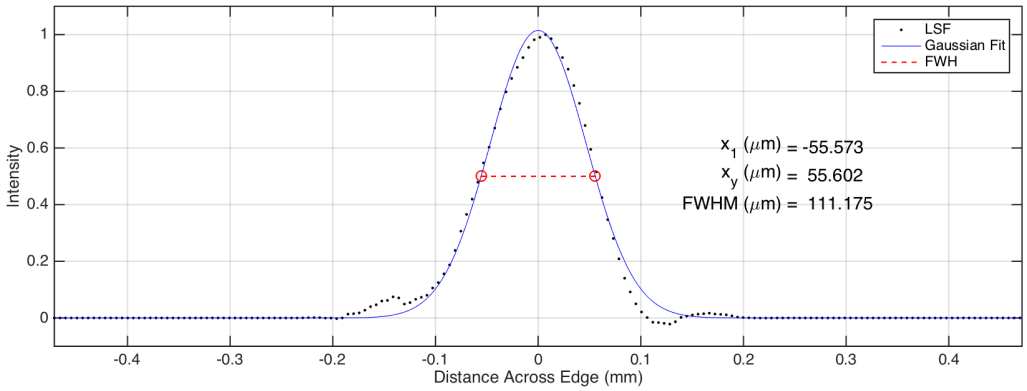
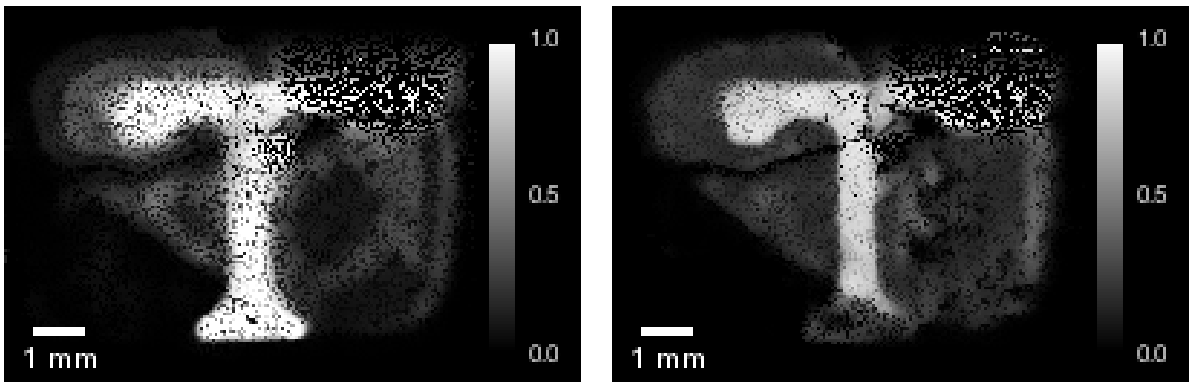


Figure 4.19. Centered LSF with Gaussian fit and FWHM.

in yellow. The averaged ESF and LSF are also shown (Figures 4.18c and 4.18d), processed following the methodology described in Appendix C.4. Applying a fast Fourier transform (FFT) to the LSF produced the final MTF curve, providing a spatial resolution of 14.7 lp/mm, assessed at the 10 % cutoff limit. Converting this spatial resolution from the frequency domain corresponds to an experimental material resolution limit of approximately 34 µm, around 2/3 of the 55 µm pixel pitch [107]. For comparison, a spatial resolution of 111 µm was found using the FWHM, shown in Figure 4.19.

4.5.4 Feature Detection

Along with resolution measurements, object identification experiments offered a practical example of the imaging systems capabilities for neutron imaging in other scientific areas of study. While a biological specimen, an adult red paper wasp (*Polistes carolina*), was prepared for imaging, the specimen did not exhibit the same depth of contrast as seen in the brown marmorated stink bug (*Halyomorpha halys*) specimen, and was omitted from further testing. A series of 3D printed imaging targets were investigated, providing simple geometric features to qualify the LISePix system. The *Power-T* target, shown in Figure 4.20, provided the best preliminary performance and was selected at the beam line for extended exposures. The 1 cm^3 target block provided a thick medium for neutron attenuation, with the *Power-T* inscription permitting an unobstructed view of the open beam. The logo, following the university template, measured approximately 6 mm tall, and less than 1 mm at the most narrow points (see Section 3.5.5). Two different image sequences were acquired, each for 50 frames at 10 s, to test the effects of signal threshold adjustment. The longer acquisition time was used to account for the decreases in count rate due to heavy attenuation as well as signal rejection. The lower threshold setting (+4 V) provided higher contrast and accommodated shorter exposure windows, thus being used for the bulk of the experiments. The higher threshold setting (+24 V) significantly enhanced overall resolution, even cleaning the areas surrounding dead pixels, at the cost of contrast and timing. Furthermore, the higher threshold had significant reduction in signal along the dark ROI in the lower left corner, suggesting the neutron interaction rate may have been equivalent, while the charge carrier



(a) threshold: +4 mV (b) threshold: +24 mV

Figure 4.20. LISePix neutron image of 3D printed *Power-T* [107].

transport and pulse production suffered. At the higher threshold, the geometric structure in the 3D printed part is visible, with minor rounding along the sharp outer edges.

Chapter 5

Conclusion

This work documents the successful implementation of lithium indium diselenide in high-resolution solid-state neutron imaging devices. Having tested the material as both a scintillator and semiconductor detector, LISe offers promising characteristics for neutron imaging and nCT, supporting their growing scientific utilization.

5.1 Project Outcomes

The principal aim of this research was accomplished, having fabricated and tested a high-resolution neutron imager. Operating in semiconductor mode, LISe introduces a novel platform for direct conversion semiconductor neutron detection. The LISePix system successfully combined the proprietary neutron sensitive compound, $^{6}LiInSe_2$, with the industry standard Timepix, to produce a neutron imaging system capable of resolving features down to the device limit prescribed by the 55 µm pixel pitch. Furthermore, in this research, LISe achieved a material spatial resolution of 34 µm with the MTF (111 µm using the FWHM) operating in both scintillator and semiconductor modes, requiring only 150 s and 400 s exposures, respectively.

5.1.1 Fabrication Techniques

A major outcome of this research was laying the foundation for LISe device fabrication. With the LISe scintillators offering a simpler approach to imaging, the basic polishing and etching requirements to prepare an optically smooth surface have been documented. Handling the relatively delicate samples required special provisions to ensure that each semiconductor fabrication step would not induce residual mechanical stresses in the sensor, degrading operational performance. The photolithography and packaging processes exposed the material to a broader range of chemicals and physical stresses, some resulting in poorer device performance or sample destruction. Sequentially eliminating the incompatibilities provided a regimen for successfully producing semiconductor detectors without incurring sample harm or loss. Most importantly, the material showed compatibility with semiconductor fabrication equipment typically utilized with silicon

wafers, including: spin-coating, photolithography, wirebonding and flip-chip bump bonding.

5.1.2 Operational Modes

One of the most interesting aspects of LISe is its operational duality, functioning as both semiconductor and scintillator. The 34 µm material spatial resolution, as evaluated with the MTF, is in fact smaller than the range of T's in the material (39.4 µm), attributed to the non-zero kinetic energy of the real incident neutron. Furthermore, the optical self transparency demonstrated in the LISe scintillators led a wide range of sample thicknesses to provide a similar spatial resolution, unlike the ^{6}LiF/ZnS screen, which has a spatial resolution that trends proportionally with thickness, optimized near 50 µm.

A potential clue in understanding the difference between scintillation and biased charge carrier transport mechanisms was revealed in the LISePix experiments. As a scintillator, LY was more intense towards the outer region (concave side) of the response transition edge, presumably corresponding to the outside of the boule, as grown. Contrarily, the LISePix semiconductor showed more intense charge collection towards the inner region (convex side), corresponding to the internal region of the boule following the same logic. As a rule of thumb, the coloration of the material was considered to be a loose indicator of device performance, with low inclusion, yellow to chartreuse sensors providing the maximum performance. However, the sensors exhibiting the response transition were an almost uniform yellow color across the edge, nearly indistinguishable by visible observation. The transition edge still remains a point of debate in LISe research and further investigation may offer new insights towards optimizing for either scintillation or semiconductor operation.

5.1.3 Resolution Limits

Based on the construction of the LISePix system and the material optimization at the time of LISe scintillator experiments, it remains unclear if the maximum achievable material resolution has been reached. Recently, the TC chemistry was modified to incorporate gallium, reducing the isotopic concentration of indium in the compound while tuning the scintillation properties. Furthermore, Wiggins *et al.* showed the 512 nm emission peak from X-ray excited optical luminescence (XEOL) measurements overlapped with the tail end of the absorption spectrum [95]. Refinements in the chemical composition and growth process may be able to tune the LISe scintillator, providing equivalent results as tested in this research, while offering higher light output to increase contrast and reduce exposure time.

The single prototype LISePix system may also see improvements in spatial resolution through fabrication refinement along with the potential for super-sampling. As a basic concept, the super-sampling technique was able to achieve resolutions roughly half the size of the pixel pitch, implying a super-sampling experiment with a 55 µm pixel pitch, such as the LISePix, could provide resolution beyond 34 µm and the theoretical material limit. While the computational load could be handled by present single server grade personal computers (PCs), the mechanical positioning would present the major obstacle. Motorized linear drives and stages

Table 5.1. Estimated cost for hypothetical LISePix (4×) high-resolution neutron imaging system.

Item 1	Unit Cost (US$)	Qty	Total Cost (US$)
Timepix Readout			
main processing module†	10,000.00	1	10,000.00
Timepix (4×) detector module	150.00	1	150.00
detector dock and data bus cabling	400.00	1	400.00
A-Class Timepix ASIC	625.00	4	2,500.00
LISe Sensor			
material (cost/cm^2)*	100.00	8	800.00
contact metallizaton: gold (cost/h)	40.00	20	800.00
flip-chip bump bonding	150.00	4	600.00
Acquisition PC	1,000.00	1	1,000.00
Total Estimated Cost			16,250.00

* Projected cost of ^{6}LISe following commercialization of material growth

† Supports up to 16 Timepix modules, configured for 4 in this design

are commercially available with sub micron resolution, with the popularity of 3D printing driving down the cost and improving the device performance [212]. Hypothetically, a pristine LISePix system using current technology could operate in tandem with a micro-positioning stage, sweeping a 11×11 array of positions at 5 µm intervals perpendicular to a neutron beam line. Using a 1 s exposure window with 10 frames would result in a total experiment run time of 20 min, potentially achieving a spatial resolution around 20 µm or less. Compared to the cost, complexity, and acquisition time of current ultra high-resolution neutron imagers, this avenue may present a more fiscally sensible option for beam line facilities to enhance their imaging capabilities.

5.2 Moving Forward

The validation of a direct semiconductor neutron detector technology serves as a milestone for future neutron imaging and portable detection systems. While many of the high-resolution systems are semi-permanently installed in their home beam line, the LISePix system maintains the portability of similar devices built on the Timepix platform, including universal serial bus (USB) stick devices and CubeSats [213–215]. A rough estimate of the projected equipment cost for a hypothetical 4× LISePix instrument, extrapolated from a single Timepix system, has been listed in Table 5.1. These costs may be reduced by access to fabrication facilities and/or collaboration with manufacturers. It should also be noted that the bulk of the cost stems from the upfront purchase of the main processing module required to drive the Timepix ASICs. This cost may be mitigated or eliminated if an alternative system is already available or a custom design is implemented by the production team.

5.2.1 LISe Timepix Device Improvements

The LISePix fabrication still requires the following processing improvements: optimized sensor thickness, usage of a guard ring to stabilize electrical field, material growth to reduce inclusions and improve hole carrier transport, and bump bonding consistency. Perfecting the fabrication process is the first critical step in continuing with the LISePix technology. The LISe scintillator array demonstrated the ability to tile multiple sensors together to create a large active area, which may offer a temporary avenue for covering an entire Timepix surface while the growth diameter improves. Upon successfully utilizing an entire single ASIC, the next logical step would be to move towards a multi-Timepix module described in Table 5.1. The readout platform used in the LISePix prototype currently supports 4 ASICs running in tandem using the provided multi-Timepix detector PCB. Currently, this technology avenue has been pursued by the company ADVACAM, collaborating with the Medipix team at European Organization for Nuclear Research (CERN). Pushing the commercialization of high-resolution radiography platforms, ADVACAM has demonstrated a unique 10×10 Timepix array device, known as the WidePIX, shown in Figure 5.1. The state-of-the-art system boasts a 6.5 MP ($14.3 \times 14.3\,\mathrm{cm}^2$) FOV used for high-resolution X-ray imaging at a maximum 20 FPS [216].

5.2.2 Coplanar Device

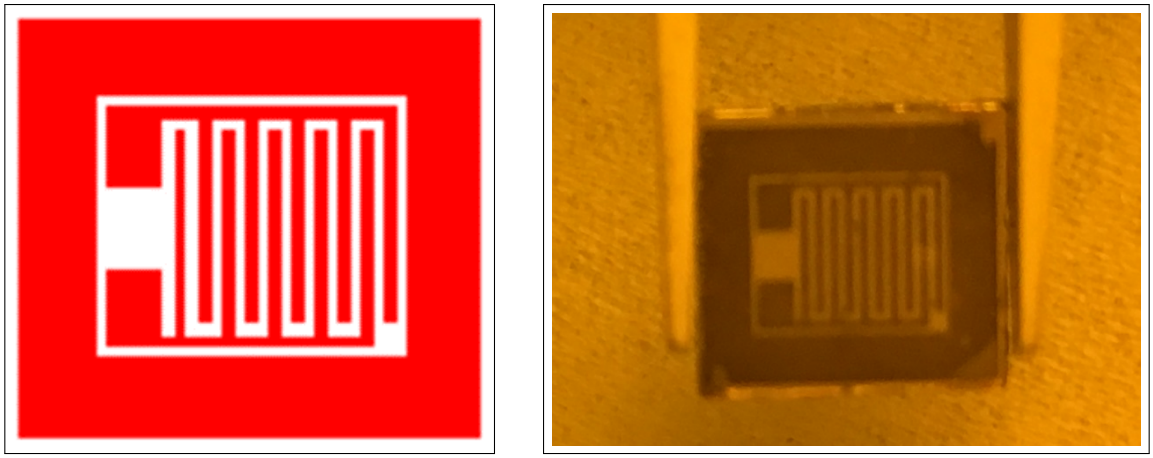
A common technique for improving the energy resolution in radiation detectors is the usage of coplanar electrodes. Functioning similar to Frisch grids, this semiconductor elctrode structure is designed to accomodate the charge carrier with better transport properties (electrons for LISe), not relying on the other carrier for signal production [187, 217]. A prototype detector using the interdigitated electrode design was fabricated, shown in Figure 5.2. Each electrode featured 5 digits of 200 µm width at a 400 µm spacing and 5 mm length, surrounded by a 1.5 mm guard ring. These type of sensors have shown to improve the spectroscopic performance in other semiconductor detectors, increasing the energy peak resolution [218–220].

5.2.3 Time of Flight Measurements

The TOF technique offers a method for distinguishing neutrons based on their kinetic energy. The basic structure of a TOF experiment involves a neutron source, a crystalline monochromator (effecitvely a neutron mirror), a chopper, the sample and the detector array. Neutrons are generated and directed as in other beam lines, however they are Bragg reflected off the monochromator, and pulsed using a chopper (a revolving neutron attenuator periodically interupting the beam). By changing the momentum and wavelength of the neutrons with a well documented experiment geometry, the energy of the neutrons striking the target may be calculated [221]. To properly utilize such measurements, the pulse rise time must be sufficiently fast to distinguish between neutron arrival times. Wiggins *et al.* measured a fast and slow time constant for the LISe scintillator at 31 ± 1 and 143 ± 9 ns, respectively, meanwhile Hamm *et al.* measured a time constant



Figure 5.1. WidePIX, an advanced design utilizing a 10×10 Timepix array in a single readout system for wide-area, high-resolution X-ray imaging (photo courtesy Jakubek *et al.* (2014)) [216].



(a) sensor mask

(b) LISe sensor

Figure 5.2. Coplanar strip detector design and fabricated LISe prototype using 200 µm strips at 400 µm spacing and 5 mm length.

of 100 ns to 150 ns for a range of semiconductor sensors [95, 187, 220]. With these timing charactersistics, refined LISe neutron detectors exhibiting neutron sensitivity across the broader neutron energy spectrum may find application as a spectrometer in new TOF experiments such as the Versatile Neutron Imaging Instrument (VENUS) [222]. This type of measurement is particularly useful in differentiating materials where the attenuation cross section is largely energy dependent. Some areas of research include materials science, AM, engineering materials and failure studies, and biological systems.

5.3 Closing Remarks

Lithium indium diselenide offers tremendous potential for neutron sciences including detection, imaging, neutron computed tomography and potentially spectroscopy. Demand continues to grow for access to neutron imaging facilities for materials engineering, biological and pharmaceutical studies, and fundamental nuclear physics sciences, among many others. As technology progresses, neutron beam lines will be able to produce more refined fluxes with higher intensity, while compact accelerator-driven neutron sources will dramatically boost the accessibility of neutron imaging to the broader scientific community. The utility of lithium indium diselenide will come at the intersection of supporting high-resolution imaging, while offering a sustainable, portable neutron detection platform, crucial for national security applications.

References

[1] I. S. Anderson, H. Z. Bilheux, and R. McGreevy, Eds., *Neutron Imaging and Applications*. New York, NY: Springer US, May 7, 2009, 341 pp., ISBN: 0387786929. DOI: 10.1007/978-0-387-78693-3.

[2] J. Brenizer, "A review of significant advances in neutron imaging from conception to the present," *Physics Procedia*, vol. 43, pp. 10–20, 2013, ISSN: 1875-3892. DOI: 10.1016/j.phpro.2013.03.002.

[3] I. Anderson, C. Andreani, J. Carpenter, *et al.*, "Research opportunities with compact accelerator-driven neutron sources," *Physics Reports*, vol. 654, pp. 1–58, Oct. 2016, ISSN: 0370-1573. DOI: 10.1016/j.physrep.2016.07.007.

[4] M. Taylor, E. Sengbusch, C. Seyfert, E. Moll, and R. Radel, "Thermal neutron radiography using a high-flux compact neutron generator," *Physics Procedia*, vol. 88, no. Supplement C, pp. 175–183, 2017, Neutron Imaging for Applications in Industry and Science Proceedings of the 8th International Topical Meeting on Neutron Radiography (ITMNR-8) Beijing, China, September 4-8, 2016, ISSN: 1875-3892. DOI: 10.1016/j.phpro.2017.06.024.

[5] E. Lehmann, D. Mannes, A. Kaestner, and C. Grünzweig, "Recent applications of neutron imaging methods," *Physics Procedia*, vol. 88, pp. 5–12, 2017, Neutron Imaging for Applications in Industry and Science Proceedings of the 8th International Topical Meeting on Neutron Radiography (ITMNR-8) Beijing, China, September 4-8, 2016, ISSN: 1875-3892. DOI: 10.1016/j.phpro.2017.06.055.

[6] P. Trtik and E. H. Lehmann, "Isotopically-enriched gadolinium-157 oxysulfide scintillator screens for the high-resolution neutron imaging," *Nuclear Instruments and Methods in Physics Research Section A: Accelerators, Spectrometers, Detectors and Associated Equipment*, vol. 788, pp. 67–70, Jul. 2015, ISSN: 0168-9002. DOI: 10.1016/j.nima.2015.03.076.

[7] E. Lehmann, P. Vontobel, and N. Kardjilov, "Hydrogen distribution measurements by neutrons," *Applied Radiation and Isotopes*, vol. 61, no. 4, pp. 503–509, Oct. 2004, Proceedings of the Fourth International Topical Meeting on Neutron Radiography. Advances in Neutron Imaging for the 21st Century, ISSN: 0969-8043. DOI: 10.1016/j.apradiso.2004.03.075.

[8] M. Kang, H. Bilheux, S. Voisin, *et al.*, "Water calibration measurements for neutron radiography: Application to water content quantification in porous media ☆," *Nuclear Instruments and Methods in Physics Research Section A: Accelerators, Spectrometers, Detectors and Associated Equipment*, vol. 708, no. 0, pp. 24–31, Apr. 2013, ISSN: 0168-9002. DOI: 10.1016/j.nima.2012.12.112.

[9] L. Poulikakos, M. S. Gilani, D. Derome, I. Jerjen, and P. Vontobel, "Time resolved analysis of water drainage in porous asphalt concrete using neutron radiography," *Applied Radiation and Isotopes*, vol. 77, pp. 5–13, Jul. 2013, ISSN: 0969-8043. DOI: 10.1016/j.apradiso.2013.01.040.

[10] E. Perfect, C.-L. Cheng, M. Kang, *et al.*, "Neutron imaging of hydrogen-rich fluids in geomaterials and engineered porous media: A review," *Earth-Science Reviews*, vol. 129, pp. 120–135, Feb. 2014, ISSN: 0012-8252. DOI: 10.1016/j.earscirev.2013.11.012.

[11] P. Boillat, D. Kramer, B. Seyfang, *et al.*, "*In situ* observation of the water distribution across a PEFC using high resolution neutron radiography," *Electrochemistry Communications*, vol. 10, no. 4, pp. 546–550, Apr. 2008, ISSN: 1388-2481. DOI: 10.1016/j.elecom.2008.01.018.

[12] A. D. Santamaria, M. K. Becton, N. J. Cooper, A. Z. Weber, and J. W. Park, "Effect of cross-flow on PEFC liquid-water distribution: An in-situ high-resolution neutron radiography study," *Journal of Power Sources*, vol. 293, pp. 162–169, Oct. 2015, ISSN: 0378-7753. DOI: 10.1016/j.jpowsour.2015.05.016.

[13] B. Schillinger, H. Abele, J. Brunner, *et al.*, "Detection systems for short-time stroboscopic neutron imaging and measurements on a rotating engine," *Nuclear Instruments and Methods in Physics Research Section A: Accelerators, Spectrometers, Detectors and Associated Equipment*, vol. 542, no. 1-3, pp. 142–147, Apr. 2005, Proceedings of the Fifth International Topical Meeting on Neutron Radiography, ISSN: 0168-9002. DOI: 10.1016/j.nima.2005.01.091.

[14] N. Kardjilov, A. Hilger, I. Manke, *et al.*, "Industrial applications at the new cold neutron radiography and tomography facility of the HMI," *Nuclear Instruments and Methods in Physics Research Section A: Accelerators, Spectrometers, Detectors and Associated Equipment*, vol. 542, no. 1, pp. 16–21, Apr. 2005, Proceedings of the Fifth International Topical Meeting on Neutron Radiography, ISSN: 0168-9002. DOI: 10.1016/j.nima.2005.01.005.

[15] L. G. Butler, E. H. Lehmann, and B. Schillinger, "Neutron radiography, tomography, and diffraction of commercial lithium-ion polymer batteries," *Physics Procedia*, vol. 43, pp. 331–336, 2013, ISSN: 1875-3892. DOI: 10.1016/j.phpro.2013.03.039.

[16] K. Beyer, T. Kannengiesser, A. Griesche, and B. Schillinger, "Study of hydrogen effusion in austenitic stainless steel by time-resolved in-situ measurements using neutron radiography," *Nuclear Instruments and Methods in Physics Research Section A: Accelerators, Spectrometers, Detectors and Associated Equipment*, vol. 651, no. 1, pp. 211–215, 2011, Proceeding of the Ninth World Conference on Neutron radiography ("The Big-5 on Neutron Radiography"), ISSN: 0168-9002. DOI: 10.1016/j.nima.2011.02.010.

[17] M. Grosse, M. van den Berg, C. Goulet, E. Lehmann, and B. Schillinger, "In-situ neutron radiography investigations of hydrogen diffusion and absorption in zirconium alloys," *Nuclear Instruments and Methods in Physics Research Section A: Accelerators, Spectrometers, Detectors and Associated Equipment*, vol. 651, no. 1, pp. 253–257, Sep. 2011, Proceeding of the Ninth World Conference on Neutron radiography ("The Big-5 on Neutron Radiography"), ISSN: 0168-9002. DOI: 10.1016/j.nima.2010.12.070.

[18] L. G. Butler, B. Schillinger, K. Ham, *et al.*, "Neutron imaging of a commercial Li-ion battery during discharge: Application of monochromatic imaging and polychromatic dynamic tomography," *Nuclear Instruments and Methods in Physics Research Section A: Accelerators, Spectrometers, Detectors and Associated Equipment*, vol. 651, no. 1, pp. 320–328, Sep. 2011, Proceeding of the Ninth World Conference on Neutron radiography ("The Big-5 on Neutron Radiography"), ISSN: 0168-9002. DOI: 10.1016/j.nima.2011.03.023.

[19] L. G. Butler and E. H. Lehmann, "Edge enhancement in cold neutron imaging: A comparison of experiments at edges and interfaces with ray-tracing based on refraction and reflection," *Physics Procedia*, vol. 43, pp. 149–160, 2013, ISSN: 1875-3892. DOI: 10.1016/j.phpro.2013.03.018.

[20] E. Deschler-erb, E. H. Lehmann, L. Pernet, P. Vontobel, and S. Hartmann, "The complementary use of neutrons and x-rays for the non-destructive investigation of archaeological objects from swiss collections*," *Archaeometry*, vol. 46, no. 4, pp. 647–661, Nov. 2004, ISSN: 0003-813X. DOI: 10.1111/j.1475-4754.2004.00180.x.

[21] J. Rant, Z. Milič, J. Istenič, *et al.*, "Neutron radiography examination of objects belonging to the cultural heritage," *Applied Radiation and Isotopes*, vol. 64, no. 1, pp. 7–12, Jan. 2006, ISSN: 0969-8043. DOI: 10.1016/j.apradiso.2005.06.003.

[22] F. Hameed, B. Schillinger, A. Rohatsch, M. Zawisky, and H. Rauch, "Investigations of stone consolidants by neutron imaging," *Nuclear Instruments and Methods in Physics Research Section A: Accelerators, Spectrometers, Detectors and Associated Equipment*, vol. 605, no. 1-2, pp. 150–153, Jun. 2009, ITMNR 08, ISSN: 0168-9002. DOI: 10.1016/j.nima.2009.01.139.

[23] M. Schulz and B. Schillinger, "ANTARES: Cold neutron radiography and tomography facility," *Journal of large-scale research facilities JLSRF*, vol. 1, p. 17, Aug. 2015. DOI: 10.17815/jlsrf-1-42.

[24] E. Lehmann, S. Hartmann, and M. O. Speidel, "Investigation of the content of ancient Tibetan metallic Buddha statues by means of neutron imaging methods," *Archaeometry*, vol. 52, no. 3, pp. 416–428, Sep. 2009. DOI: 10.1111/j.1475-4754.2009.00488.x.

[25] K. Ryzewski, S. Herringer, H. Bilheux, *et al.*, "Neutron imaging of archaeological bronzes at the Oak Ridge National Laboratory ☆," *Physics Procedia*, vol. 43, pp. 343–351, 2013, The 7th International Topical Meeting on Neutron Radiography (ITMNR-7), ISSN: 1875-3892. DOI: 10.1016/j.phpro.2013.03.041.

[26] U.S. Department of Energy. (2018). Isotope development & production for research and applications (IDPRA), Supply and demand of helium-3, U.S. Department of Energy, [Online]. Available: https://science.energy.gov/np/research/idpra/3he-fact-sheet/.

[27] R. T. Kouzes, A. T. Lintereur, and E. R. Siciliano, "Progress in alternative neutron detection to address the helium-3 shortage," *Nuclear Instruments and Methods in Physics Research Section A: Accelerators, Spectrometers, Detectors and Associated Equipment*, vol. 784, pp. 172–175, Jun. 2015, Symposium on Radiation Measurements and Applications 2014 (SORMA XV), ISSN: 0168-9002. DOI: 10.1016/j.nima.2014.10.046.

[28] R. T. Kouzes, J. H. Ely, L. E. Erikson, *et al.*, "Neutron detection alternatives to ^{3}He for national security applications," *Nuclear Instruments and Methods in Physics Research Section A: Accelerators, Spectrometers, Detectors and Associated Equipment*, vol. 623, no. 3, pp. 1035–1045, Nov. 2010, ISSN: 0168-9002. DOI: 10.1016/j.nima.2010.08.021.

[29] R. T. Kouzes, J. H. Ely, A. T. Lintereur, *et al.*, "Neutron detection gamma ray sensitivity criteria," *Nuclear Instruments and Methods in Physics Research Section A: Accelerators, Spectrometers, Detectors and Associated Equipment*, vol. 654, no. 1, pp. 412–416, Oct. 2011, ISSN: 0168-9002. DOI: 10.1016/j.nima.2011.07.030.

[30] F. Mittelbach, M. Goossens, J. Braams, D. Carlisle, and C. Rowley, *The LaTeX companion*. Addison-Wesley Professional, 2004.

[31] F. Mittelbach. (2018). The LaTeX Project, [Online]. Available: https://www.latex-project.org.

[32] U.S. Nuclear Regulatory Commission. (2017), U.S. Governmnet, [Online]. Available: https://www.nrc.gov.

[33] C. Leroy and P.-G. Rancoita, *Principles of Radiation Interaction in Matter and Detection*. World Scientific, Nov. 11, 2004, 698 pp., ISBN: 9812389091.

[34] E. B. Podgorsak, *Radiation Physics for Medical Physicists*, ser. Biological and Medical Physics, Biomedical Engineering. Springer, 2006, pp. 1–457, ISBN: 9783540250418.

[35] G. F. Knoll, *Radiation Detection and Measurement*. John Wiley & Sons, Aug. 11, 2010, 830 pp., ISBN: 9780470131480.

[36] C. J. Christensen, A. Nielsen, A. Bahnsen, W. K. Brown, and B. M. Rustad, "Free-neutron beta-decay half-life," *Phys. Rev. D*, vol. 5, no. 7, pp. 1628–1640, 7 Apr. 1972. DOI: 10.1103/physrevd.5.1628.

[37] R. A. Knief, *Nuclear Engineering, Theory and Technology of Commercial Nuclear Power*, 2nd. American Nuclear Society, 2014, p. 770, ISBN: 9780894484582.

[38] J. E. Turner, *Atoms, Radiation, and Radiation Protection*, 2nd. New York: John Wiley & Sons, Inc., 1995, ISBN: 9780471595816.

[39] K. Farrell, "Materials selection for the HFIR cold neutron source," Office of Scientific and Technical Information, Aug. 2001. DOI: 10.2172/786477.

[40] D. Quach, R. Aldredge, H. Liu, and W. Richards, "Thermal design study of a liquid hydrogen-cooled cold-neutron source," *Applied Thermal Engineering*, vol. 27, no. 11-12, pp. 1817–1822, Aug. 2007, ISSN: 1359-4311. DOI: 10.1016/j.applthermaleng.2007.01.010.

[41] A. Anghel, F. Atchison, B. Blau, *et al.*, "The PSI ultra-cold neutron source," *Nuclear Instruments and Methods in Physics Research Section A: Accelerators, Spectrometers, Detectors and Associated Equipment*, vol. 611, no. 2, pp. 272–275, Dec. 2009, Particle Physics with Slow Neutrons, ISSN: 0168-9002. DOI: 10.1016/j.nima.2009.07.077.

[42] J. R. Lamarsh and A. J. Baratta, *Introduction to Nuclear Engineering*, 3rd. Pearson, 2001, pp. 1–801, ISBN: 9780201824988.

[43] P. D. Biévre, M. Gallet, N. E. Holden, and I. L. Barnes, "Isotopic abundances and atomic weights of the elements," *Journal of Physical and Chemical Reference Data*, vol. 13, no. 3, pp. 809–891, Jul. 1984. DOI: 10.1063/1.555720. eprint: https://doi.org/10.1063/1.555720.

[44] H. Zerriffi, "Tritium: The environmental, health, budgetary, and strategic effects of the Department of Energy's decision to produce tritium," Institute for Energy and Environmental Research, Tech. Rep., Jan. 1996.

[45] M. Chadwick, M. Herman, P. Obložinský, *et al.*, "ENDF/B-VII.1 nuclear data for science and technology: Cross sections, covariances, fission product yields and decay data," *Nuclear Data Sheets*, vol. 112, no. 12, pp. 2887–2996, 2011. DOI: 10.1016/j.nds.2011.11.002.

[46] J. Dawidowski, J. R. Granada, J. R. Santisteban, F. Cantargi, and L. A. R. Palomino, "Appendix - Neutron scattering lengths and cross sections," in *Neutron Scattering - Fundamentals*, ser. Experimental Methods in the Physical Sciences, F. Fernandez-Alonso and D. L. Price, Eds., vol. 44, Academic Press, 2013, pp. 471–528. DOI: 10.1016/B978-0-12-398374-9.09989-7.

[47] R. T. Kouzes, "The ^{3}He supply problem," Office of Scientific and Technical Information, May 2009. DOI: 10.2172/956899.

[48] R. W. Pringle, H. W. Taylor, and K. I. Roulston, "Radiative capture of thermal neutrons by ^{113}Cd," *Phys. Rev.*, vol. 87, no. 6, pp. 1016–1017, 6 Sep. 1952. DOI: 10.1103/physrev.87.1016.

[49] G. Rusev, M. Jandel, M. Krtička, *et al.*, "Cascade γ rays following capture of thermal neutrons on ^{113}Cd," *Phys. Rev. C*, vol. 88, no. 5, p. 057 602, 5 Nov. 2013. DOI: 10.1103/physrevc.88.057602.

[50] J. Godt, F. Scheidig, C. Grosse-Siestrup, *et al.*, "The toxicity of cadmium and resulting hazards for human health," *Journal of Occupational Medicine and Toxicology*, vol. 1, no. 1, p. 22, Sep. 10, 2006, ISSN: 1745-6673. DOI: 10.1186/1745-6673-1-22.

[51] B. A. Fowler, "Monitoring of human populations for early markers of cadmium toxicity: A review ☆," *Toxicology and Applied Pharmacology*, vol. 238, no. 3, pp. 294–300, Aug. 2009, New Insights into the Mechanisms of Cadmium Toxicity, ISSN: 0041-008X. DOI: 10.1016/j.taap.2009.05.004.

[52] R. C. Semelka, M. Ramalho, and M. Jay, "Summary of special issue on gadolinium bioeffects and toxicity with a look to the future," *Magnetic Resonance Imaging*, vol. 34, no. 10, pp. 1399–1401, Dec. 2016, Gadolinium Bioeffects and Toxicity, ISSN: 0730-725X. DOI: 10.1016/j.mri.2016.09.002.

[53] M. Rogosnitzky and S. Branch, "Gadolinium-based contrast agent toxicity: A review of known and proposed mechanisms," *BioMetals*, vol. 29, no. 3, pp. 365–376, Apr. 2016, ISSN: 1572-8773. DOI: 10.1007/s10534-016-9931-7.

[54] P. B. Riesz, "The life of Wilhelm Conrad Roentgen," *American Journal of Roentgenology*, vol. 165, no. 6, pp. 1533–1537, Dec. 1995, ISSN: 0361-803X. DOI: 10.2214/ajr.165.6.7484601.

[55] L. M. Bollinger, G. E. Thomas, and R. G. Ginther, "Glass scintillators for neutron detection," *Review of Scientific Instruments*, vol. 30, no. 12, pp. 1135–1136, Dec. 1959. DOI: 10.1063/1.1716471. eprint: 10.1063/1.1716471.

[56] F. Firk, G. Slaughter, and R. Ginther, "An improved ^{6}Li-loaded glass scintillator for neutron detection," *Nuclear Instruments and Methods*, vol. 13, pp. 313–316, Aug. 1961, ISSN: 0029-554X. DOI: 10.1016/0029-554x(61)90221-x.

[57] Paul Scherrer Institut. (2017), [Online]. Available: https://www.psi.ch.

[58] J. Banhart, *Advanced Tomographic Methods in Materials Research and Engineering*. Oxford University Press, 2008, ISBN: 9780199213245.

[59] M. Katagiri, K. Sakasai, M. Matsubayashi, *et al.*, "Scintillation materials for neutron imaging detectors," *Nuclear Instruments and Methods in Physics Research Section A: Accelerators, Spectrometers, Detectors and Associated Equipment*, vol. 529, no. 1-3, pp. 274–279, Aug. 2004, ISSN: 0168-9002. DOI: 10.1016/j.nima.2004.04.165.

[60] K. Mizukami, S. Sato, H. Sagehashi, *et al.*, "Measurements of performance of a pixel-type two-dimensional position sensitive Li-glass neutron detector," *Nuclear Instruments and Methods in Physics Research Section A: Accelerators, Spectrometers, Detectors and Associated Equipment*, vol. 529, no. 1-3, pp. 310–312, Aug. 2004, Proceedings of the Joint Meeting of the International Conference on Neutron Optics (NOP2004) and the Third International Workshop on Position-Sensitive Neutron Detectors (PSND2004), ISSN: 0168-9002. DOI: 10.1016/j.nima.2004.05.001.

[61] M. Ishii, Y. Kuwano, T. Asai, *et al.*, "Boron based oxide scintillation glass for neutron detection," *Nuclear Instruments and Methods in Physics Research Section A: Accelerators, Spectrometers, Detectors and Associated Equipment*, vol. 537, no. 1-2, pp. 282–285, Jan. 2005, Proceedings of the 7th International Conference on Inorganic Scintillators and their Use in Scientific adn Industrial Applications, ISSN: 0168-9002. DOI: 10.1016/j.nima.2004.08.027.

[62] T. Matsumoto, H. Harano, T. Shimoyama, *et al.*, "Development of a novel small-sized neutron detector based on a ^{6}Li-glass scintillator," in *IEEE Nuclear Science Symposium Conference Record, 2005*, vol. 3, IEEE, Oct. 2005, pp. 1291–1293. DOI: 10.1109/nssmic.2005.1596556.

[63] G. Ban, K. Bodek, T. Lefort, *et al.*, "UCN detection with ^{6}Li-doped glass scintillators," *Nuclear Instruments and Methods in Physics Research Section A: Accelerators, Spectrometers, Detectors and Associated Equipment*, vol. 611, no. 2, pp. 280–283, 2009, Particle Physics with Slow Neutrons, ISSN: 0168-9002. DOI: 10.1016/j.nima.2009.07.083.

[64] J. Park, D. Ha, S. Kaewjeang, *et al.*, "Luminescence properties of Ce^{3}+ doped gadolinium-calcium-silicaborate glass scintillator," *Radiation Measurements*, vol. 90, pp. 166–169, Jul. 2016, Proceedings of the 9th International Conference on Luminescent Detectors and Transformers of Ionizing Radiation (LUMDETR 2015), ISSN: 1350-4487. DOI: 10.1016/j.radmeas.2015.12.028.

[65] R. Breukers, C. Bartle, and A. Edgar, "Transparent lithium loaded plastic scintillators for thermal neutron detection," *Nuclear Instruments and Methods in Physics Research Section A: Accelerators, Spectrometers, Detectors and Associated Equipment*, vol. 701, pp. 58–61, 2013, ISSN: 0168-9002. DOI: 10.1016/j.nima.2012.10.080.

[66] N. J. Cherepy, R. D. Sanner, P. R. Beck, *et al.*, "Bismuth- and lithium-loaded plastic scintillators for gamma and neutron detection," *Nuclear Instruments and Methods in Physics Research Section A: Accelerators, Spectrometers, Detectors and Associated Equipment*, vol. 778, pp. 126–132, Apr. 2015, ISSN: 0168-9002. DOI: 10.1016/j.nima.2015.01.008.

[67] A. N. Mabe, M. J. Urffer, D. Penumadu, G. K. Schweitzer, and L. F. Miller, "Transparent lithium-6 based polymer scintillation films containing a polymerizable fluor for neutron detection," *Radiation Measurements*, vol. 66, pp. 5–11, Jul. 2014, ISSN: 1350-4487. DOI: 10.1016/j.radmeas.2014.04.023.

[68] A. N. Mabe, A. M. Glenn, M. L. Carman, N. P. Zaitseva, and S. A. Payne, "Transparent plastic scintillators for neutron detection based on lithium salicylate," *Nuclear Instruments and Methods in Physics Research Section A: Accelerators, Spectrometers, Detectors and Associated Equipment*, vol. 806, pp. 80–86, Jan. 2016, ISSN: 0168-9002. DOI: 10.1016/j.nima.2015.09.111.

[69] S. Normand, B. Mouanda, S. Haan, and M. Louvel, "Study of a new boron loaded plastic scintillator (revised)," *IEEE Transactions on Nuclear Science*, vol. 49, no. 4, pp. 1603–1608, Aug. 2002, ISSN: 0018-9499. DOI: 10.1109/tns.2002.805282.

[70] I. Pawełczak, A. Glenn, H. Martinez, *et al.*, "Boron-loaded plastic scintillator with neutron-γ pulse shape discrimination capability," *Nuclear Instruments and Methods in Physics Research Section A: Accelerators, Spectrometers, Detectors and Associated Equipment*, vol. 751, pp. 62–69, Jul. 2014, ISSN: 0168-9002. DOI: 10.1016/j.nima.2014.03.027.

[71] A. Mahl, H. A. Yemam, J. Stuntz, *et al.*, "Bis(pinacolato)diboron as an additive for the detection of thermal neutrons in plastic scintillators," *Nuclear Instruments and Methods in Physics Research Section A: Accelerators, Spectrometers, Detectors and Associated Equipment*, vol. 816, pp. 96–100, 2016, ISSN: 0168-9002. DOI: 10.1016/j.nima.2016.01.073.

[72] A. Mahl, H. A. Yemam, R. Fernando, *et al.*, "^{10}B enriched plastic scintillators for application in thermal neutron detection," *Nuclear Instruments and Methods in Physics Research Section A: Accelerators, Spectrometers, Detectors and Associated Equipment*, vol. 880, pp. 1–5, Feb. 2018, ISSN: 0168-9002. DOI: 10.1016/j.nima.2017.10.042.

[73] L. Ovechkina, K. Riley, S. Miller, Z. Bell, and V. Nagarkar, "Gadolinium loaded plastic scintillators for high efficiency neutron detection," *Physics Procedia*, vol. 2, no. 2, pp. 161–170, Aug. 2009, The 2008 International Conference on Luminescence and Optical Spectroscopy of Condensed Matter, ISSN: 1875-3892. DOI: 10.1016/j.phpro.2009.07.008.

[74] A. Bedrik, Y. S. Velmozhnaya, P. Zhmurin, *et al.*, "Plastic scintillator with gadolinium phenylpropionate," *Functional Materials*, vol. 18, no. 4, pp. 470–473, 2011.

[75] J. Dumazert, R. Coulon, F. Carrel, *et al.*, "Sensitive and transportable gadolinium-core plastic scintillator sphere for neutron detection and counting," *Nuclear Instruments and Methods in Physics Research Section A: Accelerators, Spectrometers, Detectors and Associated Equipment*, vol. 828, pp. 181–190, Aug. 2016, ISSN: 0168-9002. DOI: 10.1016/j.nima.2016.05.054.

[76] N. D'Olympia, P. Chowdhury, C. Lister, *et al.*, "Pulse-shape analysis of CLYC for thermal neutrons, fast neutrons, and gamma-rays," *Nuclear Instruments and Methods in Physics Research Section A: Accelerators, Spectrometers, Detectors and Associated Equipment*, vol. 714, pp. 121–127, Jun. 2013, ISSN: 0168-9002. DOI: 10.1016/j.nima.2013.02.043.

[77] J. Glodo, R. Hawrami, and K. Shah, "Development of Cs_2LiYCl_6 scintillator," *Journal of Crystal Growth*, vol. 379, no. 0, pp. 73–78, Sep. 2013, ISSN: 0022-0248. DOI: 10.1016/j.jcrysgro.2013.03.023.

[78] M. Smith, M. McClish, T. Achtzehn, *et al.*, "Assessment of photon detectors for a handheld gamma-ray and neutron spectrometer using Cs_2LiYCl_6:Ce (CLYC) scintillator," *Nuclear Instruments and Methods in Physics Research Section A: Accelerators, Spectrometers, Detectors and Associated Equipment*, vol. 715, no. 0, pp. 92–97, Jul. 2013, ISSN: 0168-9002. DOI: 10.1016/j.nima.2013.03.023.

[79] M. Bourne, C. Mussi, E. Miller, *et al.*, "Characterization of the CLYC detector for neutron and photon detection," *Nuclear Instruments and Methods in Physics Research Section A: Accelerators, Spectrometers, Detectors and Associated Equipment*, vol. 736, pp. 124–127, Feb. 2014, ISSN: 0168-9002. DOI: 10.1016/j.nima.2013.10.030.

[80] R. Machrafi, N. Khan, and A. Miller, "Response functions of Cs_2LiYCl_6:Ce scintillator to neutron and gamma radiation," *Radiation Measurements*, vol. 70, no. 0, pp. 5–10, Nov. 2014, ISSN: 1350-4487. DOI: 10.1016/j.radmeas.2014.07.010.

[81] C. M. Whitney, L. Soundara-Pandian, E. B. Johnson, *et al.*, "Gamma-neutron imaging system utilizing pulse shape discrimination with CLYC ☆," *Nuclear Instruments and Methods in Physics Research Section A: Accelerators, Spectrometers, Detectors and Associated Equipment*, vol. 784, pp. 346–351, 2015, Symposium on Radiation Measurements and Applications 2014 (SORMA XV), ISSN: 0168-9002. DOI: 10.1016/j.nima.2014.09.022.

[82] A. Giaz, L. Pellegri, F. Camera, *et al.*, "The CLYC-6 and CLYC-7 response to γ-rays, fast and thermal neutrons," *Nuclear Instruments and Methods in Physics Research Section A: Accelerators, Spectrometers, Detectors and Associated Equipment*, vol. 810, pp. 132–139, 2016, ISSN: 0168-9002. DOI: 10.1016/j.nima.2015.11.119.

[83] R. Stedman, "Scintillator for thermal neutrons using Li^6F and ZnS (Ag)," *Review of Scientific Instruments*, vol. 31, no. 10, pp. 1156–1156, Oct. 1960. DOI: 10.1063/1.1716833. eprint: 10.1063/1.1716833.

[84] F. H. Helm, "Experiments with neutron scintillators made of lithium fluoride, zinc sulfide, and Lucite," *Review of Scientific Instruments*, vol. 33, no. 6, pp. 687–688, Jun. 1962. DOI: 10.1063/1.1746660. eprint: 10.1063/1.1746660.

[85] H. Iikura, N. Tsutsui, T. Nakamura, *et al.*, "Evaluations of the new LiF-scintillator and optional brightness enhancement films for neutron imaging," *Nuclear Instruments and Methods in Physics Research Section A: Accelerators, Spectrometers, Detectors and Associated Equipment*, vol. 651, no. 1, pp. 100–104, Sep. 2011, ISSN: 0168-9002. DOI: 10.1016/j.nima.2011.01.010.

[86] N. Kawaguchi, K. Fukuda, T. Yanagida, *et al.*, "Fabrication and characterization of large size $^6LiF/CaF_2$:Eu eutectic composites with the ordered lamellar structure," *Nuclear Instruments and Methods in Physics Research Section A: Accelerators, Spectrometers, Detectors and Associated Equipment*, vol. 652, no. 1, pp. 209–211, 2011, Symposium on Radiation Measurements and Applications (SORMA) XII 2010, ISSN: 0168-9002. DOI: 10.1016/j.nima.2011.02.009.

[87] M. Matsubayashi, A. Faenov, T. Pikuz, *et al.*, "LiF crystals as high spatial resolution neutron imaging detectors," *Nuclear Instruments and Methods in Physics Research Section A: Accelerators, Spectrometers, Detectors and Associated Equipment*, vol. 651, no. 1, pp. 90–94, Sep. 2011, ISSN: 0168-9002. DOI: 10.1016/j.nima.2011.01.072.

[88] W. Yang, T. Bin, H. Heyong, *et al.*, "The study of zinc sulphide scintillator for fast neutron radiography ☆," *Physics Procedia*, vol. 43, pp. 205–215, 2013, The 7th International Topical Meeting on Neutron Radiography (ITMNR-7), ISSN: 1875-3892. DOI: 10.1016/j.phpro.2013.03.024.

[89] L. Santodonato, H. Bilheux, B. Bailey, *et al.*, "The CG-1D neutron imaging beamline at the Oak Ridge National Laboratory High Flux Isotope Reactor," *Physics Procedia*, vol. 69, pp. 104–108, 2015, ISSN: 1875-3892. DOI: 10.1016/j.phpro.2015.07.015.

[90] RC TRITEC, Ltd. (2018), [Online]. Available: http://www.rctritec.com/en/home.html.

[91] S. Stave, M. Bliss, R. Kouzes, *et al.*, "LiF/ZnS neutron multiplicity counter," *Nuclear Instruments and Methods in Physics Research Section A: Accelerators, Spectrometers, Detectors and Associated Equipment*, vol. 784, no. 0, pp. 208–212, Jun. 2015, ISSN: 0168-9002. DOI: 10.1016/j.nima.2015.01.039.

[92] A. Stoykov, J. Mosset, U. Greuter, M. Hildebrandt, and N. Schlumpf, "A SiPM-based ZnS:^{6}LiF scintillation neutron detector," *Nuclear Instruments and Methods in Physics Research Section A: Accelerators, Spectrometers, Detectors and Associated Equipment*, vol. 787, no. 0, pp. 361–366, Jul. 2015, ISSN: 0168-9002. DOI: 10.1016/j.nima.2015.01.076.

[93] E. Tupitsyn, P. Bhattacharya, E. Rowe, *et al.*, "Single crystal of $LiInSe_2$ semiconductor for neutron detector," *Applied Physics Letters*, vol. 101, no. 20, p. 202 101, Nov. 2012. DOI: 10.1063/1.4762002.

[94] E. Tupitsyn, P. Bhattacharya, E. Rowe, *et al.*, "Lithium containing chalcogenide single crystals for neutron detection," *Journal of Crystal Growth*, vol. 393, pp. 23–27, May 2014, ISSN: 0022-0248. DOI: 10.1016/j.jcrysgro.2013.10.054.

[95] B. Wiggins, M. Groza, E. Tupitsyn, *et al.*, "Scintillation properties of semiconducting $^{6}LiInSe_2$ crystals to ionizing radiation," *Nuclear Instruments and Methods in Physics Research Section A: Accelerators, Spectrometers, Detectors and Associated Equipment*, vol. 801, pp. 73–77, Nov. 2015, ISSN: 0168-9002. DOI: 10.1016/j.nima.2015.08.035.

[96] E. Lukosi, E. Herrera, D. Hamm, *et al.*, "Lithium indium diselenide: A new scintillator for neutron imaging," *Nuclear Instruments and Methods in Physics Research Section A: Accelerators, Spectrometers, Detectors and Associated Equipment*, vol. 830, pp. 140–149, Sep. 2016, ISSN: 0168-9002. DOI: 10.1016/j.nima.2016.05.063.

[97] E. D. Lukosi, E. H. Herrera, D. S. Hamm, A. Burger, and A. C. Stowe, "Neutron imaging with lithium indium diselenide: Surface properties, spatial resolution, and computed tomography," *Nuclear Instruments and Methods in Physics Research Section A: Accelerators, Spectrometers, Detectors and Associated Equipment*, vol. 872, no. Supplement C, pp. 181–186, Nov. 2017, ISSN: 0168-9002. DOI: 10.1016/j.nima.2017.08.028.

[98] C. Tözke, I. Manke, A. Hilger, *et al.*, "Large area high resolution neutron imaging detector for fuel cell research," *Journal of Power Sources*, vol. 196, no. 10, pp. 4631–4637, May 2011, ISSN: 0378-7753. DOI: 10.1016/j.jpowsour.2011.01.049.

[99] T. Yanagida, N. Kawaguchi, Y. Fujimoto, *et al.*, "Basic study of europium doped $LiCaAlF_6$ scintillator and its capability for thermal neutron imaging application," *Optical Materials*, vol. 33, no. 8, pp. 1243–1247, Jun. 2011, ISSN: 0925-3467. DOI: 10.1016/j.optmat.2011.02.016.

[100] T. Yanagida, Y. Fujimoto, K. Watanabe, and K. Fukuda, "Dosimeter properties of Ce and Eu doped $LiCaAlF_6$," *Radiation Measurements*, vol. 71, pp. 148–152, 2014, Proceedings of the 17th Solid State Dosimetry Conference (SSD17), ISSN: 1350-4487. DOI: 10.1016/j.radmeas.2014.02.021.

[101] Y. Wu, E. D. Lukosi, M. Zhuravleva, A. C. Lindsey, and C. L. Melcher, "A novel $LiCl\text{-}BaCl_2:Eu^{2+}$ eutectic scintillator for thermal neutron detection," *Nuclear Instruments and Methods in Physics Research Section A: Accelerators, Spectrometers, Detectors and Associated Equipment*, vol. 797, pp. 319–323, Oct. 2015, ISSN: 0168-9002. DOI: 10.1016/j.nima.2015.06.064.

[102] A. Owens, *Compound Semiconductor Radiation Detectors*. CRC Press, Apr. 19, 2016, 567 pp., ISBN: 9781439873137.

[103] N. Tsoulfanidis and S. Landsberger, *Measurement and Detection of Radiation*, 3rd. CRC Press, 2010, p. 518, ISBN: 1420091859.

[104] A. Das and T. Ferbel, *Introduction to Nuclear and Particle Physics*, 2nd. World Scientific Publishing Company, Dec. 23, 2003, 416 pp., ISBN: 9812387447.

[105] J. F. Ziegler, M. Ziegler, and J. Biersack, "SRIM – The stopping and range of ions in matter (2010)," *Nuclear Instruments and Methods in Physics Research Section B: Beam Interactions with Materials and Atoms*, vol. 268, no. 11-12, pp. 1818–1823, Jun. 2010, 19th International Conference on Ion Beam Analysis, ISSN: 0168-583X. DOI: 10.1016/j.nimb.2010.02.091.

[106] E. Lukosi, O. Chvala, and A. Stowe, "Response functions of semiconducting lithium indium diselenide," *Nuclear Instruments and Methods in Physics Research Section A: Accelerators, Spectrometers, Detectors and Associated Equipment*, vol. 822, pp. 9–14, Jun. 2016, ISSN: 0168-9002. DOI: 10.1016/j.nima.2016.03.080.

[107] E. Herrera, D. Hamm, A. Stowe, *et al.*, "Neutron imaging with Timepix coupled lithium indium diselenide," *Journal of Imaging*, vol. 4, no. 1, Dec. 2018. DOI: 10.3390/jimaging4010010.

[108] C. A. Klein, "Bandgap dependence and related features of radiation ionization energies in semiconductors," *Journal of Applied Physics*, vol. 39, no. 4, pp. 2029–2038, Mar. 1968. DOI: 10.1063/1.1656484. eprint: 10.1063/1.1656484.

[109] Z. He, "Review of the Shockley-Ramo theorem and its application in semiconductor gamma-ray detectors," *Nuclear Instruments and Methods in Physics Research Section A: Accelerators, Spectrometers, Detectors and Associated Equipment*, vol. 463, no. 1-2, pp. 250–267, May 2001, ISSN: 0168-9002. DOI: 10.1016/s0168-9002(01)00223-6.

[110] D. Kania, M. Landstrass, M. Plano, L. Pan, and S. Han, "Diamond radiation detectors," *Diamond and Related Materials*, vol. 2, no. 5, pp. 1012–1019, Apr. 1993, Diamond 1992, ISSN: 0925-9635. DOI: 10.1016/0925-9635(93)90266-5.

[111] T. Behnke, P. Hüntemeyer, A. Oh, *et al.*, "The charge collection properties of CVD diamond," *Nuclear Instruments and Methods in Physics Research Section A: Accelerators, Spectrometers, Detectors and Associated Equipment*, vol. 414, no. 2-3, pp. 340–356, Sep. 1998, ISSN: 0168-9002. DOI: 10.1016/s0168-9002(98)00696-2.

[112] H. Pernegger, S. Roe, P. Weilhammer, *et al.*, "Charge-carrier properties in synthetic single-crystal diamond measured with the transient-current technique," *Journal of Applied Physics*, vol. 97, no. 7, p. 073 704, Apr. 2005. DOI: 10.1063/1.1863417.

[113] M. Pomorski, E. Berdermann, A. Caragheorgheopol, *et al.*, "Development of single-crystal CVD-diamond detectors for spectroscopy and timing," *physica status solidi (a)*, vol. 203, no. 12, pp. 3152–3160, Sep. 2006, ISSN: 1862-6319. DOI: 10.1002/pssa.200671127.

[114] M. Pomorski, E. Berdermann, W. de Boer, *et al.*, "Charge transport properties of single crystal CVD-diamond particle detectors," *Diamond and Related Materials*, vol. 16, no. 4-7, pp. 1066–1069, Apr. 2007, ISSN: 0925-9635. DOI: 10.1016/j.diamond.2006.11.016.

[115] R. S. Wallny, "Status of diamond detectors and their high energy physics application," *Nuclear Instruments and Methods in Physics Research Section A: Accelerators, Spectrometers, Detectors and Associated Equipment*, vol. 582, no. 3, pp. 824–828, Dec. 2007. DOI: 10.1016/j.nima.2007.07.104.

[116] A. Galbiati, S. Lynn, K. Oliver, *et al.*, "Performance of monocrystalline diamond radiation detectors fabricated using TiW, Cr/Au and a novel ohmic DLC/Pt/Au electrical contact," *IEEE Transactions on Nuclear Science*, vol. 56, no. 4, pp. 1863–1874, Aug. 2009. DOI: 10.1109/tns.2009.2020428.

[117] M. Pillon, M. Angelone, A. Krása, *et al.*, "Experimental response functions of a single-crystal diamond detector for 5-20.5MeV neutrons," *Nuclear Instruments and Methods in Physics Research Section A: Accelerators, Spectrometers, Detectors and Associated Equipment*, vol. 640, no. 1, pp. 185–191, Jun. 2011, ISSN: 0168-9002. DOI: 10.1016/j.nima.2011.03.005.

[118] M. Angelone, M. Pillon, G. Prestopino, *et al.*, "Thermal and fast neutron dosimetry using artificial single crystal diamond detectors," *Radiation Measurements*, vol. 46, no. 12, pp. 1686–1689, Dec. 2011, ISSN: 1350-4487. DOI: 10.1016/j.radmeas.2011.06.041.

[119] T. Wulz, B. K. Canfield, L. M. Davis, S. Spanier, and E. Lukosi, "Pulsed femtosecond-laser machining and deep reactive ion etching of diamond," *Diamond and Related Materials*, vol. 74, pp. 108–113, Apr. 2017. DOI: 10.1016/j.diamond.2017.02.018.

[120] T. G. Wulz, "Advanced radiation detection devices: 3D diamond detectors and KSr_2I_5:Eu scintillating crystals," PhD thesis, University of Tennessee, Knoxville, Aug. 2017.

[121] Y. Kumashiro, K. Kudo, K. Matsumoto, Y. Okada, and T. Koshiro, "Thermal neutron irradiation experiments on ^{10}BP single-crystal wafers," *Journal of the Less Common Metals*, vol. 143, no. 1, pp. 71–75, 1988, ISSN: 0022-5088. DOI: 10.1016/0022-5088(88)90031-8.

[122] Y. A. Bykovskii, K. Zatsev, P. Kervalishvili, *et al.*, "Neutron fluence probe on the base of boron carbide," *Technical Physics Letters*, vol. 19, pp. 57–59, 14 1993, ISSN: 0320-0116.

[123] B. W. Robertson, S. Adenwalla, A. Harken, *et al.*, "A class of boron-rich solid-state neutron detectors," *Applied physics letters*, vol. 80, no. 19, pp. 3644–3646, 2002, ISSN: 0003-6951. DOI: 10.1063/1.1477942.

[124] D. Emin and T. L. Aselage, "A proposed boron-carbide-based solid-state neutron detector," *Journal of Applied Physics*, vol. 97, no. 1, p. 013 529, Jan. 2005. DOI: 10.1063/1.1823579. eprint: 10.1063/1.1823579.

[125] A. Caruso, P. Dowben, S. Balkir, *et al.*, "The all boron carbide diode neutron detector: Comparison with theory," *Materials Science and Engineering: B*, vol. 135, no. 2, pp. 129–133, Nov. 2006, ISSN: 0921-5107. DOI: 10.1016/j.mseb.2006.08.049.

[126] J. Li, R. Dahal, S. Majety, J. Lin, and H. Jiang, "Hexagonal boron nitride epitaxial layers as neutron detector materials," *Nuclear Instruments and Methods in Physics Research Section A: Accelerators, Spectrometers, Detectors and Associated Equipment*, vol. 654, no. 1, pp. 417–420, Oct. 2011, ISSN: 0168-9002. DOI: 10.1016/j.nima.2011.07.040.

[127] T. Doan, S. Majety, S. Grenadier, *et al.*, "Hexagonal boron nitride thin film thermal neutron detectors with high energy resolution of the reaction products," *Nuclear Instruments and Methods in Physics Research Section A: Accelerators, Spectrometers, Detectors and Associated Equipment*, vol. 783, pp. 121–127, May 2015, ISSN: 0168-9002. DOI: 10.1016/j.nima.2015.02.045.

[128] T. Kamijoh, T. Nozaki, and K. Kuriyama, "Dielectric constant and its temperature dependence of $LiInSe_2$," S3, vol. 19, Japan Society of Applied Physics, Jan. 1980, p. 395. DOI: 10.7567/jjaps.19s3.395.

[129] T. Kamijoh and K. Kuriyama, "Annealing effects on electrical properties of $LiInSe_2$," *Journal of Applied Physics*, vol. 52, no. 2, pp. 1102–1103, Feb. 1981. DOI: 10.1063/1.328812.

[130] ——, "Single crystal growth of $LiInS_2$," *Journal of Crystal Growth*, vol. 46, no. 6, pp. 801–803, Jun. 1979, ISSN: 0022-0248. DOI: 10.1016/0022-0248(79)90230-6.

[131] ——, "Single crystal growth and characterization of $LiInSe_2$," *Journal of Crystal Growth*, vol. 51, no. 1, pp. 6–10, Jan. 1981, ISSN: 0022-0248. DOI: 10.1016/0022-0248(81)90003-8.

[132] K. Kuriyama and T. Nozaki, "Single-crystal growth and characterization of $LiGaSe_2$," *Journal of Applied Physics*, vol. 52, no. 10, pp. 6441–6443, Oct. 1981. DOI: 10.1063/1.328553. eprint: 10.1063/1.328553.

[133] V. Petrov, J. Zondy, O. Bidault, *et al.*, "Optical, thermal, electrical, damage, and phase-matching properties of lithium selenoindate," *Journal of the Optical Society of America B*, vol. 27, no. 9, p. 1902, Aug. 2010. DOI: 10.1364/josab.27.001902.

[134] P. Vijayakumar, M. Magesh, A. Arunkumar, *et al.*, "Investigations on synthesis, growth, electrical and defect studies of lithium selenoindate single crystals," *Journal of Crystal Growth*, vol. 388, no. 0, pp. 17–21, Feb. 2014, ISSN: 0022-0248. DOI: 10.1016/j.jcrysgro.2013.11.027.

[135] T. Kamijoh, T. Nozaki, and K. Kuriyama, "Dielectric constants and bond parameters of $LiInSe_2$ and $LiGaSe_2$," *Journal of Applied Physics*, vol. 53, no. 1, pp. 761–763, Jan. 1982. DOI: 10.1063/1.329946.

[136] Z. W. Bell and A. Burger, "Semiconductor radiation detector," U.S. Patent 7 687 780, Mar. 30, 2010.

[137] A. Stowe, J. Woodward, E. Tupitsyn, *et al.*, "Crystal growth in $LiGaSe_2$ for semiconductor radiation detection applications," *Journal of Crystal Growth*, vol. 379, no. 0, pp. 111–114, Sep. 2013, ISSN: 0022-0248. DOI: 10.1016/j.jcrysgro.2013.01.015.

[138] A. C. Stowe, J. Cochran, P. Bhattacharya, *et al.*, "Lithium-containing semiconductor crystals for radiation detection," in *MRS Online Proceedings Library Archive*, Materials Research Society, 2013. DOI: 10.1557/opl.2013.1145.

[139] A. C. Stowe, J. Morrell, P. Battacharya, E. Tupitsyn, and A. Burger, "Synthesis of a potential semiconductor neutron detector crystal $LiGa(Se/Te)_2$: Materials purity and compatibility effects," in *Hard X-Ray, Gamma-Ray, and Neutron Detector Physics XIII*, L. A. Franks, R. B. James, and A. Burger, Eds., SPIE, Sep. 2011. DOI: 10.1117/12.894968.

[140] B. Wiggins, E. Batista, A. Burger, K. Stassun, and A. Stowe, "Density functional theory investigation of the $LiIn_{1-x}Ga_xSe_2$ solid solution," *physica status solidi (b)*, vol. 253, no. 8, pp. 1465–1471, Jun. 2016. DOI: 10.1002/pssb.201600273.

[141] L. I. Isaenko, A. P. Yelisseyev, J.-J. Zondy, *et al.*, "Growth and characterisation of single crystals of ternary chalcogenides for laser applications," *Opto-electronics Review*, vol. 9, no. 2, A. Rogalski, K. Adamiec, and P. Madejczyk, Eds., pp. 135–141, Aug. 2001. DOI: 10.1117/12.435857.

[142] S. Wang, X. Zhang, X. Zhang, *et al.*, "Modified bridgman growth and properties of mid-infrared $LiInSe_2$ crystal," *Journal of Crystal Growth*, vol. 401, pp. 150–155, Sep. 2014, ISSN: 0022-0248. DOI: 10.1016/j.jcrysgro.2014.02.043.

[143] C.-G. Ma and M. Brik, "First principles studies of the structural, electronic and optical properties of $LiInSe_2$ and $LiInTe_2$ chalcopyrite crystals," *Solid State Communications*, vol. 203, pp. 69–74, Feb. 2015, ISSN: 0038-1098. DOI: 10.1016/j.ssc.2014.11.021.

[144] L. Isaenko, A. Yelisseyev, S. Lobanov, *et al.*, "$LiInSe_2$: A biaxial ternary chalcogenide crystal for nonlinear optical applications in the midinfrared," *Journal of Applied Physics*, vol. 91, no. 12, p. 9475, 2002. DOI: 10.1063/1.1478139.

[145] E. Herrera, D. Hamm, B. Wiggins, *et al.*, "LISe pixel detector for neutron imaging," *Nuclear Instruments and Methods in Physics Research Section A: Accelerators, Spectrometers, Detectors and Associated Equipment*, vol. 833, pp. 142–148, Oct. 2016. DOI: 10.1016/j.nima.2016.07.035.

[146] B. Wiggins, E. Tupitsyn, P. Bhattacharya, *et al.*, "Investigation of non-uniformity and inclusions in $^6LiInSe_2$ utilizing laser induced breakdown spectroscopy (LIBS)," in *Hard X-Ray, Gamma-Ray, and Neutron Detector Physics XV*, M. Fiederle, A. Burger, L. Franks, and R. B. James, Eds., SPIE, Sep. 2013. DOI: 10.1117/12.2024125.

[147] T. Ma, C. Yang, Y. Xie, *et al.*, "Electronic and optical properties of orthorhombic $LiInS_2$ and $LiInSe_2$: A density functional theory investigation," *Computational Materials Science*, vol. 47, no. 1, pp. 99–105, Nov. 2009, ISSN: 0927-0256. DOI: 10.1016/j.commatsci.2009.06.021.

[148] H. J. Beister, S. Ves, W. Hönle, K. Syassen, and G. Kühn, "Structural phase transitions and optical absorption of $LiInSe_2$ under pressure," *Phys. Rev. B*, vol. 43, no. 12, pp. 9635–9642, 12 Apr. 1991. DOI: 10.1103/PhysRevB.43.9635.

[149] A. Eifler, V. Riede, J. Brückner, *et al.*, "Band gap energies and lattice vibrations of the lithium ternary compounds $LiInSe_2$, $LiInS_2$, $LiGaSe_2$ and $LiGaS_2$," *Japanese Journal of Applied Physics*, vol. 39, no. S1, p. 279, 2000.

[150] Y. Cui, P. Bhattacharya, V. Buliga, *et al.*, "Defects in 6LiInSe2 neutron detector investigated by photo-induced current transient spectroscopy and photoluminescence," *Applied Physics Letters*, vol. 103, no. 9, p. 092 104, Aug. 2013. DOI: 10.1063/1.4819733.

[151] S. Weise, E. Nowak, A. Lenz, B. Schumann, and V. Krämer, "Investigations of the system $LiInSe_2$–$CuInSe_2$," *Journal of Crystal Growth*, vol. 166, no. 1-4, pp. 718–721, Sep. 1996, ISSN: 0022-0248. DOI: 10.1016/0022-0248(96)00141-8.

[152] L. Isaenko, I. Vasilyeva, A. Merkulov, A. Yelisseyev, and S. Lobanov, "Growth of new nonlinear crystals $LiMX_2$ (M = Al, In, Ga; X = S, Se, Te) for the mid-IR optics," *Journal of Crystal Growth*, vol. 275, no. 1-2, pp. 217–223, Feb. 2005, ISSN: 0022-0248. DOI: 10.1016/j.jcrysgro.2004.10.089.

[153] S. Weise and V. Krämer, "Phase study of the system Li_2Se-In_2Se_3," *Journal of Thermal Analysis and Calorimetry*, vol. 71, no. 3, pp. 1035–1038, Mar. 1, 2003, ISSN: 1572-8943. DOI: 10.1023/a:1023363218026.

[154] D. S. Hamm, M. Rust, E. H. Herrera, *et al.*, "Semiconducting lithium indium diselenide: Charge-carrier properties and the impacts of high flux thermal neutron irradiation," *Nuclear Instruments and Methods in Physics Research Section A: Accelerators, Spectrometers, Detectors and Associated Equipment*, 2018, forthcoming.

[155] L. Isaenko, A. Yelisseyev, S. Lobanov, *et al.*, "Ternary chalcogenides $LiBC_2$ (B = In, Ga; C = S, Se, Te) for mid-IR nonlinear optics," *Journal of Non-Crystalline Solids*, vol. 352, no. 23-25, pp. 2439–2443, Jul. 2006, ISSN: 0022-3093. DOI: 10.1016/j.jnoncrysol.2006.03.045.

[156] V. Badikov, V. Chizhikov, V. Efimenko, *et al.*, "Optical properties of lithium indium selenide," *Optical Materials*, vol. 23, no. 3-4, pp. 575–581, Sep. 2003, ISSN: 0925-3467. DOI: 10.1016/s0925-3467(03)00024-7.

[157] A. P. Yelisseyev, V. A. Drebushchak, A. S. Titov, *et al.*, "Thermal properties of the midinfrared nonlinear crystal $LiInSe_2$," *Journal of Applied Physics*, vol. 96, no. 7, pp. 3659–3665, Oct. 2004, ISSN: 0021-8979. DOI: 10.1063/1.1784616.

[158] Z. W. Bell, A. Burger, L. Matei, *et al.*, "Neutron detection in $LiInSe_2$," Jan. 2015.

[159] E. G. Seebauer and M. C. Kratzer, *Charged Semiconductor Defects, Structure, Thermodynamics and Diffusion*, 1st ed., ser. Engineering Materials and Processes. Springer Science & Business Media, Dec. 1, 2008, 308 pp., ISBN: 9781848820586. DOI: 10.1007/978-1-84882-059-3.

[160] A. C. Stowe, B. Wiggins, P. Bhattacharya, *et al.*, "Improving neutron detection in semiconducting $^6LiInSe_2$," in *Hard X-Ray, Gamma-Ray, and Neutron Detector Physics XVI*, A. Burger, L. Franks, R. B. James, and M. Fiederle, Eds., SPIE, Sep. 2014. DOI: 10.1117/12.2062139.

[161] E. Garmire, "Nonlinear optics in daily life," *Opt. Express*, vol. 21, no. 25, p. 30 532, Dec. 2013. DOI: 10.1364/oe.21.030532.

[162] L. Isaenko and I. Vasilyeva, "Nonlinear $LiB^{III}C_2^{YI}$ crystals for mid-IR and far-IR: Novel aspects in crystal growth," *Journal of Crystal Growth*, vol. 310, no. 7-9, pp. 1954–1960, Apr. 2008, ISSN: 0022-0248. DOI: 10.1016/j.jcrysgro.2007.11.201.

[163] D. C. Giltnane, "Thermal characteristics of lithium indium diselenide and lithium indium gallium diselenide neutron detection crystals," Master's thesis, University of Tennessee, May 2016.

[164] G. Kühn, E. Pirl, H. Neumann, and E. Nowak, "Heat capacity of $LiInS_2$, $LiInSe_2$ and $LiInTe_2$ between 200 and 550K," *Crystal Research and Technology*, vol. 22, no. 2, pp. 265–269, Feb. 1987, ISSN: 1521-4079. DOI: 10.1002/crat.2170220221.

[165] E. Gmelin and W. Hönle, "Anomalous lattice specific heat of $LiInSe_2$ at low temperatures," *Thermochimica Acta*, vol. 269-270, pp. 575–590, Dec. 1995, ISSN: 0040-6031. DOI: 10.1016/0040-6031(95)02569-3.

[166] J. Jakubek, T. Holy, E. Lehmann, *et al.*, "Properties of neutron pixel detector based on Medipix-2 device," in *IEEE Symposium Conference Record Nuclear Science 2004.*, IEEE, Oct. 26, 2004. DOI: 10.1109/nssmic.2004.1462363.

[167] X. Llopart and M. Campbell, "First test measurements of a 64k pixel readout chip working in single photon counting mode," *Nuclear Instruments and Methods in Physics Research Section A: Accelerators, Spectrometers, Detectors and Associated Equipment*, vol. 509, no. 1-3, pp. 157–163, Aug. 2003, ISSN: 0168-9002. DOI: 10.1016/s0168-9002(03)01565-1.

[168] J. Uher, T. Holý, J. Jakůbek, *et al.*, "Performance of a pixel detector suited for slow neutrons," *Nuclear Instruments and Methods in Physics Research Section A: Accelerators, Spectrometers, Detectors and Associated Equipment*, vol. 542, no. 1-3, pp. 283–287, Apr. 2005, ISSN: 0168-9002. DOI: 10.1016/j.nima.2005.01.149.

[169] J. Jakubek, T. Holy, E. Lehmann, *et al.*, "Spatial resolution of Medipix-2 device as neutron pixel detector," *Nuclear Instruments and Methods in Physics Research Section A: Accelerators, Spectrometers, Detectors and Associated Equipment*, vol. 546, no. 1-2, pp. 164–169, Jul. 2005, ISSN: 0168-9002. DOI: 10.1016/j.nima.2005.03.112.

[170] ——, "Neutron imaging with Medipix-2 chip and a coated sensor," *Nuclear Instruments and Methods in Physics Research Section A: Accelerators, Spectrometers, Detectors and Associated Equipment*, vol. 560, no. 1, pp. 143–147, May 2006, ISSN: 0168-9002. DOI: 10.1016/j.nima.2005.11.243.

[171] J. Jakubek, "Data processing and image reconstruction methods for pixel detectors," *Nuclear Instruments and Methods in Physics Research Section A: Accelerators, Spectrometers, Detectors and Associated Equipment*, vol. 576, no. 1, pp. 223–234, Jun. 2007, ISSN: 0168-9002. DOI: 10.1016/j.nima.2007.01.157.

[172] J. Uher and J. Jakubek, "Monte-Carlo simulation of fast neutron detection with Timepix," in *2009 IEEE Nuclear Science Symposium Conference Record (NSS/MIC)*, IEEE, Oct. 2009. DOI: 10.1109/nssmic.2009.5402355.

[173] ——, "Detection of fast neutrons with particle tracking detector Timepix combined with plastic scintillator," *Radiation Measurements*, vol. 46, no. 12, pp. 1624–1627, Dec. 2011, ISSN: 1350-4487. DOI: 10.1016/j.radmeas.2011.05.054.

[174] F. Krejci, J. Zemlicka, J. Jakubek, *et al.*, "Development and characterization of high-resolution neutron pixel detectors based on Timepix read-out chips," *Journal of Instrumentation*, vol. 11, no. 12, pp. C12026–C12026, Dec. 2016. DOI: 10.1088/1748-0221/11/12/c12026.

[175] A. S. Tremsin, W. B. Feller, and R. G. Downing, "Efficiency optimization of microchannel plate (MCP) neutron imaging detectors. I. square channels with ^{10}B doping," *Nuclear Instruments and Methods in Physics Research Section A: Accelerators, Spectrometers, Detectors and Associated Equipment*, vol. 539, no. 1, pp. 278–311, Feb. 2005, ISSN: 0168-9002. DOI: 10.1016/j.nima.2004.09.028.

[176] A. Tremsin, J. Vallerga, J. McPhate, *et al.*, "On the possibility to image thermal and cold neutron with sub-15μm spatial resolution," *Nuclear Instruments and Methods in Physics Research Section A: Accelerators, Spectrometers, Detectors and Associated Equipment*, vol. 592, no. 3, pp. 374–384, Jul. 2008, ISSN: 0168-9002. DOI: 10.1016/j.nima.2008.03.116.

[177] J. Vallerga, J. McPhate, A. Tremsin, and O. Siegmund, "High-resolution UV, alpha and neutron imaging with the Timepix CMOS readout," *Nuclear Instruments and Methods in Physics Research Section A: Accelerators, Spectrometers, Detectors and Associated Equipment*, vol. 591, no. 1, pp. 151–154, Jun. 2008, ISSN: 0168-9002. DOI: 10.1016/j.nima.2008.03.046.

[178] A. Tremsin, J. McPhate, J. Vallerga, *et al.*, "Detection efficiency, spatial and timing resolution of thermal and cold neutron counting MCP detectors," *Nuclear Instruments and Methods in Physics Research Section A: Accelerators, Spectrometers, Detectors and Associated Equipment*, vol. 604, no. 1-2, pp. 140–143, Jun. 2009, ISSN: 0168-9002. DOI: 10.1016/j.nima.2009.01.041.

[179] ——, "High-resolution neutron radiography with microchannel plates: Proof-of-principle experiments at PSI," *Nuclear Instruments and Methods in Physics Research Section A: Accelerators, Spectrometers, Detectors and Associated Equipment*, vol. 605, no. 1-2, pp. 103–106, Jun. 2009, ISSN: 0168-9002. DOI: 10.1016/j.nima.2009.01.137.

[180] A. Tremsin, J. McPhate, J. Vallerga, *et al.*, "Improved efficiency of high resolution thermal and cold neutron imaging," *Nuclear Instruments and Methods in Physics Research Section A: Accelerators, Spectrometers, Detectors and Associated Equipment*, vol. 628, no. 1, pp. 415–418, Feb. 2011, ISSN: 0168-9002. DOI: 10.1016/j.nima.2010.07.014.

[181] A. Tremsin, J. McPhate, J. Vallerga, *et al.*, "High-resolution neutron microtomography with noiseless neutron counting detector," *Nuclear Instruments and Methods in Physics Research Section A: Accelerators, Spectrometers, Detectors and Associated Equipment*, vol. 652, no. 1, pp. 400–403, Oct. 2011, ISSN: 0168-9002. DOI: 10.1016/j.nima.2010.08.009.

[182] A. Tremsin, M. Morgano, T. Panzner, *et al.*, "High resolution neutron imaging capabilities at BOA beamline at Paul Scherrer Institut," *Nuclear Instruments and Methods in Physics Research Section A: Accelerators, Spectrometers, Detectors and Associated Equipment*, vol. 784, pp. 486–493, Jun. 2015, ISSN: 0168-9002. DOI: 10.1016/j.nima.2014.09.026.

[183] D. S. Hussey, H. Wen, H. Wu, *et al.*, "Demonstration of focusing wolter mirrors for neutron phase and magnetic imaging," *Journal of Imaging*, vol. 4, no. 3, 2018, ISSN: 2313-433X. DOI: 10.3390/jimaging4030050.

[184] P. Trtik, J. Hovind, C. Grünzweig, *et al.*, "Improving the spatial resolution of neutron imaging at Paul Scherrer Institut – The Neutron Microscope Project ☆," *Physics Procedia*, vol. 69, pp. 169–176, 2015, ISSN: 1875-3892. DOI: 10.1016/j.phpro.2015.07.024.

[185] P. Trtik and E. H. Lehmann, "Progress in high-resolution neutron imaging at the Paul Scherrer Institut – The Neutron Microscope Project," *Journal of Physics: Conference Series*, vol. 746, no. 1, p. 012 004, Sep. 2016. DOI: 10.1088/1742-6596/746/1/012004.

[186] D. S. Hussey, J. M. LaManna, E. Baltic, and D. L. Jacobson, "Neutron imaging detector with 2μm spatial resolution based on event reconstruction of neutron capture in gadolinium oxysulfide scintillators," *Nuclear Instruments and Methods in Physics Research Section A: Accelerators, Spectrometers, Detectors and Associated Equipment*, vol. 866, no. Supplement C, pp. 9–12, Sep. 2017, ISSN: 0168-9002. DOI: 10.1016/j.nima.2017.05.035.

[187] D. S. Hamm, E. D. Lukosi, M. R. Rust, *et al.*, "Characterization of lithium indium diselenide," in *2015 IEEE Nuclear Science Symposium and Medical Imaging Conference (NSS/MIC)*, IEEE, Oct. 2015. DOI: 10.1109/nssmic.2015.7582284.

[188] X. Llopart, R. Ballabriga, M. Campbell, L. Tlustos, and W. Wong, "Timepix, a 65k programmable pixel readout chip for arrival time, energy and/or photon counting measurements," *Nuclear Instruments and Methods in Physics Research Section A: Accelerators, Spectrometers, Detectors and Associated Equipment*, vol. 581, no. 1-2, pp. 485–494, Oct. 2007, ISSN: 0168-9002. DOI: 10.1016/j.nima.2007.08.079.

[189] Oak Ridge National Laboratory. (2018). High Flux Isotope Reactor, U.S. Department of Energy, [Online]. Available: https://neutrons.ornl.gov/hfir.

[190] L. Crow, L. Robertson, H. Bilheux, *et al.*, "The CG1 instrument development test station at the high flux isotope reactor," *Nuclear Instruments and Methods in Physics Research Section A: Accelerators, Spectrometers, Detectors and Associated Equipment*, vol. 634, no. 1, S71–S74, Apr. 2011, ISSN: 0168-9002. DOI: 10.1016/j.nima.2010.06.213.

[191] H. Z. Bilheux, J.-C. Bilheux, W. B. Bailey, *et al.*, "Neutron imaging at the Oak Ridge National Laboratory: Application to biological research," in *Proceedings of the 2014 Biomedical Sciences and Engineering Conference*, IEEE, May 2014. DOI: 10.1109/bsec.2014.6867751.

[192] "Standard guide for thermal neutron radiography of materials," American Society for Testing and Materials, Standard ASTM E748-16, Feb. 15, 2016. DOI: 10.1520/e0748-16.

[193] Andor Technology. (2018), [Online]. Available: http://www.andor.com.

[194] C. Grünzweig, G. Frei, E. Lehmann, G. Kühne, and C. David, "Highly absorbing gadolinium test device to characterize the performance of neutron imaging detector systems," *Review of Scientific Instruments*, vol. 78, no. 5, p. 053 708, May 2007, ISSN: 0034-6748. DOI: 10.1063/1.2736892.

[195] M. K. Thompson, G. Moroni, T. Vaneker, *et al.*, "Design for additive manufacturing: Trends, opportunities, considerations, and constraints," *CIRP Annals - Manufacturing Technology*, vol. 65, no. 2, pp. 737–760, 2016, ISSN: 0007-8506. DOI: 10.1016/j.cirp.2016.05.004.

[196] H. Z. Bilheux, G. Song, K. An, *et al.*, "Advances in neutron radiography: Application to additive manufacturing Inconel 718," *Advanced Materials and Processes*, Jan. 2016, ISSN: 0882-7958 AW.

[197] Ultimaker, B.V. (2018), [Online]. Available: https://ultimaker.com.

[198] J. R. Jones and P. L. Lambdin, "New county and state records for Tennessee of an exotic pest, Halyomorpha halys (Hemiptera: Pentatomidae), with potential economic and ecological implications," *Florida Entomologist*, vol. 92, no. 1, pp. 177–178, Mar. 2009. DOI: 10.1653/024.092.0132.

[199] E. H. Weber, *E.H. Weber On The Tactile Senses*. Psychology Press, 1996, ISBN: 978-0863774218.

[200] A. A. Michelson, *Studies in Optics*, ser. The Univ. of Chicago Science Series. University of Chicago Press, 1927, ISBN: 9780226523880.

[201] F. Y. Shih, *Image Processing and Pattern Recognition, Fundamentals and Techniques*. Wiley-IEEE Press, May 11, 2010, 537 pp., ISBN: 9780470404614.

[202] E. Peli, "Contrast in complex images," *Journal of the Optical Society of America*, vol. 7, no. 10, p. 2032, Oct. 1990, ISSN: 1084-7529. DOI: 10.1364/josaa.7.002032.

[203] Ondrej Chvala. (2014). UTK Nuclear Engineering Department Cluster, The University of Tennessee, [Online]. Available: https://necluster.engr.utk.edu.

[204] Oak Ridge National Laboratory. (2016). Neutron Sciences, U.S. Department of Energy, [Online]. Available: https://neutrons.ornl.gov.

[205] A. C. Kak, M. Slaney, and G. Wang, *Principles of Computerized Tomographic Imaging*, 1. American Association of Physicists in Medicine, 2002, vol. 29, pp. 107–107, ISBN: 089871494X. DOI: 10.1118/1.1455742.

[206] Z. Zakaria, N. H. Jaafar, N. A. M. Yazid, *et al.*, "Sinogram concept approach in image reconstruction algorithm of a computed tomography system using MATLAB," in *2010 International Conference on Computer Applications and Industrial Electronics*, IEEE, Dec. 2010, pp. 500–505. DOI: 10.1109/iccaie.2010.5735132.

[207] J. Blachot, "Nuclear data sheets for A = 114," *Nuclear Data Sheets*, vol. 113, no. 2, pp. 515–714, 2012, ISSN: 0090-3752. DOI: https://doi.org/10.1016/j.nds.2012.02.002.

[208] ——, "Nuclear data sheets for A = 116," *Nuclear Data Sheets*, vol. 111, no. 3, pp. 717–895, 2010, ISSN: 0090-3752. DOI: https://doi.org/10.1016/j.nds.2010.03.002.

[209] G. McBeth, J. Lutkin, and R. Winyard, "A simple zero crossing pulse shape discrimination system," *Nuclear Instruments and Methods*, vol. 93, no. 1, pp. 99–102, May 1971, ISSN: 0029-554X. DOI: 10.1016/0029-554x(71)90144-3.

[210] T. Szczesmak, M. Grodzicka, M. Moszyński, *et al.*, "Digital neutron-gamma discrimination methods: Charge comparison versus zero-crossing," in *2014 IEEE Nuclear Science Symposium and Medical Imaging Conference (NSS/MIC)*, Nov. 2014, pp. 1–4. DOI: 10.1109/NSSMIC.2014.7431222.

[211] L. Rossi, P. Fischer, T. Rohe, and N. Wermes, *Pixel Detectors, From Fundamentals to Applications*. Springer Berlin Heidelberg, Jul. 8, 2006, ISBN: 9783540283331. DOI: 10.1007/3-540-28333-1.

[212] R. A. A. Campbell, R. W. Eifert, and G. C. Turner, "Openstage: A low-cost motorized microscope stage with sub-micron positioning accuracy," in *PloS one*, N. K. Haass, Ed., vol. 9, Public Library of Science (PLoS), Feb. 2014, e88977. DOI: 10.1371/journal.pone.0088977.

[213] D. Turecek, L. Pinsky, J. Jakubek, *et al.*, "Small dosimeter based on Timepix device for International Space Station," *Journal of Instrumentation*, vol. 6, no. 12, pp. C12037–C12037, Dec. 2011. DOI: 10.1088/1748-0221/6/12/c12037.

[214] T. Baca, M. Platkevic, J. Jakubek, *et al.*, "Miniaturized X-ray telescope for VZLUSAT-1 nanosatellite with Timepix detector," *Journal of Instrumentation*, vol. 11, no. 10, pp. C10007–C10007, Oct. 2016. DOI: 10.1088/1748-0221/11/10/c10007.

[215] J. C. Egner, M. Groza, A. Burger, *et al.*, "Integration of a ^{6}LiInSe$_2$ thermal neutron detector into a CubeSat instrument," *Journal of Astronomical Telescopes, Instruments, and Systems*, vol. 2, no. 4, p. 046 001, Nov. 2016. DOI: 10.1117/1.jatis.2.4.046001.

[216] J. Jakubek, M. Jakubek, M. Platkevic, *et al.*, "Large area pixel detector WIDEPIX with full area sensitivity composed of 100 Timepix assemblies with edgeless sensors," *Journal of Instrumentation*, vol. 9, no. 04, pp. C04018–C04018, Apr. 2014, ISSN: 1748-0221. DOI: 10.1088/1748-0221/9/04/c04018.

[217] P. Luke, "Unipolar charge sensing with coplanar electrodes – Application to semiconductor detectors," *Nuclear Science, IEEE Transactions on*, vol. 42, no. 4, pp. 207–213, Nov. 1994, ISSN: 0018-9499. DOI: 10.2172/34411.

[218] Z. He, G. Knoll, D. Wehe, and Y. Du, "Coplanar grid patterns and their effect on energy resolution of CdZnTe detectors," *Nuclear Instruments and Methods in Physics Research Section A: Accelerators, Spectrometers, Detectors and Associated Equipment*, vol. 411, no. 1, pp. 107–113, Jul. 1998, ISSN: 0168-9002. DOI: 10.1016/s0168-9002(98)00285-x.

[219] Z. He and B. W. Sturm, "Characteristics of depth-sensing coplanar grid CdZnTe detectors," *Nuclear Instruments and Methods in Physics Research Section A: Accelerators, Spectrometers, Detectors and Associated Equipment*, vol. 554, no. 1-3, pp. 291–299, Dec. 2005. DOI: 10.1016/j.nima.2005.06.064.

[220] D. S. Hamm, "Characterization and development of lithium indium diselenide for neutron detection and imaging applications," PhD thesis, University of Tennessee, Knoxville, May 2018.

[221] J. R. D. Copley and T. J. Udovic, "Neutron time-of-flight spectroscopy," *Journal of Research of the National Institute of Standards and Technology*, vol. 98, no. 1, p. 71, Jan. 1992, ISSN: 2165-7254. DOI: 10.6028/jres.098.006.

[222] H. Bilheux, K. Herwig, S. Keener, and L. Davis, "Overview of the conceptual design of the future VENUS neutron imaging beam line at the Spallation Neutron Source," *Physics Procedia*, vol. 69, pp. 55–59, 2015, Proceedings of the 10th World Conference on Neutron Radiography (WCNR-10) Grindelwald, Switzerland October 5–10, 2014, ISSN: 1875-3892. DOI: 10.1016/j.phpro.2015.07.007.

[223] A. Causier, I. Gérard, M. Bouttemy, P. Tran-Van, and A. Etcheberry, "Fundamentals of III-V semiconductor electrochemistry and wet etching processes: Br$_2$ etching properties onto InP," *ECS Transactions*, vol. 35, no. 8, pp. 61–66, 2011. DOI: 10.1149/1.3567737.

[224] J. Shen, X. Liu, Y. Zhao, *et al.*, "The influence of post treatment on physical properties of polycrystalline CuInS$_2$ thin films," *Materials Science in Semiconductor Processing*, vol. 50, no. Supplement C, pp. 49–54, Aug. 2016, ISSN: 1369-8001. DOI: 10.1016/j.mssp.2016.04.006.

[225] A. Rouse, C. Szeles, J. Ndap, *et al.*, "Interfacial chemistry and the performance of bromine-etched CdZnTe radiation detector devices," *IEEE Transactions on Nuclear Science*, vol. 49, no. 4, pp. 2005–2009, Aug. 2002, ISSN: 0018-9499. DOI: 10.1109/tns.2002.801705.

[226] D. E. Aspnes and A. A. Studna, "Chemical etching and cleaning procedures for Si, Ge, and some III-V compound semiconductors," *Applied Physics Letters*, vol. 39, no. 4, pp. 316–318, Aug. 1981, ISSN: 0003-6951. DOI: 10.1063/1.92705.

[227] P. T. Bowman, E. I. Ko, and P. J. Sides, "A potential hazard in preparing bromine-methanol solutions," *Journal of The Electrochemical Society*, vol. 137, no. 4, pp. 1309–1311, 1990. DOI: 10.1149/1.2086655.

[228] M. Ohring, *Material Science of Thin Films, Deposition and Structure*, 2nd. San Diego, CA: Academic Press, 2001, ISBN: 9780125249751.

[229] J. F. O'Hanlon, *A User's Guide to Vacuum Technology*, 3rd. John Wiley & Sons, 2005, 536 pp., ISBN: 9780471270522.

[230] A. C. Fischer, J. G. Korvink, N. Roxhed, *et al.*, "Unconventional applications of wire bonding create opportunities for microsystem integration," *Journal of Micromechanics and Microengineering*, vol. 23, no. 8, p. 083 001, Jun. 2013, ISSN: 0960-1317. DOI: 10.1088/0960-1317/23/8/083001.

[231] G. Alimonti, A. Andreazza, A. Bulgheroni, *et al.*, "Analysis of the production of ATLAS indium bonded pixel modules," *Nuclear Instruments and Methods in Physics Research Section A: Accelerators, Spectrometers, Detectors and Associated Equipment*, vol. 565, no. 1, pp. 296–302, Sep. 2006, Proceedings of the International Workshop on Semiconductor Pixel Detectors for Particles and Imaging, ISSN: 0168-9002. DOI: 10.1016/j.nima.2006.05.048.

[232] G. Alimonti, A. Andreazza, G. Corda, *et al.*, "Development of indium bump bonding for the ATLAS Insertable B-Layer (IBL)," *Journal of Instrumentation*, vol. 8, no. 01, P01024–P01024, Jan. 2013. DOI: 10.1088/1748-0221/8/01/p01024.

[233] W. Adam, C. Bauer, E. Berdermann, *et al.*, "The first bump-bonded pixel detectors on CVD diamond," *Nuclear Instruments and Methods in Physics Research Section A: Accelerators, Spectrometers, Detectors and Associated Equipment*, vol. 436, no. 3, pp. 326–335, Nov. 1999, ISSN: 0168-9002. DOI: 10.1016/s0168-9002(99)00548-3.

[234] C. Broennimann, F. Glaus, J. Gobrecht, *et al.*, "Development of an indium bump bond process for silicon pixel detectors at PSI," *Nuclear Instruments and Methods in Physics Research Section A: Accelerators, Spectrometers, Detectors and Associated Equipment*, vol. 565, no. 1, pp. 303–308, Sep. 2006, ISSN: 0168-9002. DOI: 10.1016/j.nima.2006.05.011.

[235] R. C. Gonzalez and R. E. Woods, *Digital Image Processing*. Pearson, Jul. 11, 2007, 954 pp., ISBN: 9780131687288.

[236] J. Canny, "A computational approach to edge detection," *IEEE transactions on pattern analysis and machine intelligence.*, vol. PAMI-8, no. 6, pp. 679–698, Nov. 1986, ISSN: 0162-8828. DOI: 10.1109/tpami.1986.4767851.

[237] R. O. Duda and P. E. Hart, "Use of the Hough transformation to detect lines and curves in pictures," *Communications of the ACM*, vol. 15, no. 1, pp. 11–15, Jan. 1972. DOI: 10.1145/361237.361242.

[238] P. Hart, "How the Hough transform was invented [DSP history]," *IEEE signal processing magazine*, vol. 26, no. 6, pp. 18–22, Nov. 2009, ISSN: 1053-5888. DOI: 10.1109/msp.2009.934181.

[239] J. J. Duderstadt and L. J. Hamilton, *Nuclear Reactor Analysis*. John Wiley & Sons, Inc., Jan. 2, 1976, pp. 1–670, 672 pp., ISBN: 0471223638.

[240] E. E. Lewis, *Fundamentals of Nuclear Reactor Physics*. Elsevier Science Publishing Co Inc, Jan. 18, 2008, pp. 1–269, 280 pp., ISBN: 9780123706317.

[241] ADVACAM. (2018), [Online]. Available: http://advacam.com.

[242] AJA International, Inc. (2018), [Online]. Available: http://www.ajaint.com.

[243] Amptek. (2018), [Online]. Available: http://amptek.com.

[244] Heinz Maier-Leibnitz Zentrum. (2018). ANTARES, Cold neutron radiography and tomography facility, [Online]. Available: https://mlz-garching.de/antares.

[245] Atominstitut. (2018), Technische Universität Wien, [Online]. Available: https://ati.tuwien.ac.at/startpage/EN/.

[246] Autodesk, Inc. (2018). AutoCAD, CAD software for anyone, anywhere, anytime, [Online]. Available: https://www.autodesk.com/products/autocad/overview.

[247] ——, (2018), [Online]. Available: https://www.autodesk.com.

[248] CAEN, S.p.A. (2018), [Online]. Available: http://www.caen.it.

[249] Oak Ridge National Laboratory. (2018). The CG1 instrument development beam line, U.S. Department of Energy, [Online]. Available: https://neutrons.ornl.gov/cg1.

[250] ——, (2018). The CG-1D neutron imaging facility, U.S. Department of Energy, [Online]. Available: https://neutrons.ornl.gov/imaging.

[251] Cremat, Inc. (2018), [Online]. Available: http://www.cremat.com.

[252] U.S. Department of Homeland Security. (2018), U.S. Government, [Online]. Available: https://www.dhs.gov.

[253] U.S. Department of Energy. (2018), U.S. Government, [Online]. Available: https://www.energy.gov.

[254] Autodesk, Inc. (2018). EAGLE, PCB design made easy, [Online]. Available: https://www.autodesk.com/products/eagle/overview.

[255] CERN. (2018), European Organization for Nuclear Research, [Online]. Available: https://home.cern.

[256] Federal Communications Commission. (2018), U.S. Government, [Online]. Available: https://www.fcc.gov.

[257] Fisk University. (2018), [Online]. Available: https://www.fisk.edu.

[258] Formlabs, Inc. (2018), [Online]. Available: https://formlabs.com.

[259] Futurrex, Inc. (2018), [Online]. Available: http://futurrex.com/en.

[260] General Atomics. (2018), [Online]. Available: http://www.ga.com.

[261] Hammond Manufacturing, Ltd. (2018), [Online]. Available: https://www.hammfg.com.

[262] National Institutes of Health. (2018). Imagej: Image processing and analysis in Java, [Online]. Available: https://imagej.nih.gov/ij/index.html.

[263] Jožef Stefan Institute. (2018), [Online]. Available: https://www.ijs.si/ijsw/IJS.

[264] Keysight Technologies. (2018), [Online]. Available: https://www.keysight.com/us/en/home.html.

[265] Kulicke & Soffa Industries, Inc. (2018), [Online]. Available: https://www.kns.com.

[266] National Instruments. (2018). LabVIEW, [Online]. Available: http://www.ni.com/en-us/shop/labview.html.

[267] CERN. (2018). The Large Hadron Collider, European Organization for Nuclear Research, [Online]. Available: https://home.cern/topics/large-hadron-collider.

[268] LEMO. (2018), [Online]. Available: https://www.lemo.com/en.

[269] The MathWorks, Inc. (2018), [Online]. Available: https://www.mathworks.com.

[270] ——, (2018). MATLAB, [Online]. Available: https://www.mathworks.com/products/matlab.html.

[271] CERN. (2017). Medipix colaboration, European Organization for Nuclear Research, [Online]. Available: http://medipix.web.cern.ch/medipix/index.php.

[272] E. Lukosi. (2017). JIAM Micro-Processing and Research Facility, The University of Tennessee, [Online]. Available: http://jiam.utk.edu/facilities/mprf/index.php.

[273] Los Alamos National Laboratory. (2018). A general Monte Carlo N-Particle (MCNP) transport code, [Online]. Available: https://mcnp.lanl.gov.

[274] MTI Corporation. (2018), [Online]. Available: http://www.mtixtl.com.

[275] National Instruments. (2018), [Online]. Available: http://www.ni.com/en-us.html.

[276] National Institutes of Health. (2018), U.S. Department of Health and Human Services, [Online]. Available: https://www.nih.gov.

[277] Oak Ridge National Laboratory. (2018), U.S. Department of Energy, [Online]. Available: https://ornl.gov.

[278] Octopus Imaging Software. (2018), [Online]. Available: https://octopusimaging.eu.

[279] AMETEK, Inc. (2017). ORTEC, [Online]. Available: https://www.ortec-online.com.

[280] Helmholtz Zentrum Berlin für Materialien und Energie. (2018), [Online]. Available: https://www.helmholtz-berlin.de/index_en.html.

[281] Python Software Foundation. (2018). Python, [Online]. Available: https://www.python.org.

[282] Radiation Monitoring Devices, Inc. (2018), [Online]. Available: http://rmdinc.com.

[283] Oak Ridge National Laboratory. (2018). Spallation Neutron Source, U.S. Department of Energy, [Online]. Available: https://neutrons.ornl.gov/sns.

[284] Specialty Coating Systems, Inc. (2018), [Online]. Available: https://scscoatings.com.

[285] Structure Probe, Inc. (2018). SPI Supplies, [Online]. Available: https://www.2spi.com.

[286] J. F. Ziegler. (2018). SRIM - The Stopping and Range of Ions in Matter, [Online]. Available: http://www.srim.org.

[287] Suss MicroTec, SE. (2018), [Online]. Available: https://www.suss.com/en.

[288] University of Tennessee, Knoxville. (2018), [Online]. Available: https://www.utk.edu.

[289] The University of Texas at Austin. (2018), [Online]. Available: https://www.utexas.edu.

[290] National Institute of Standards and Technology. (2018), U.S. Department of Commerce, [Online]. Available: https://www.nist.gov.

[291] Vanderbilt University. (2018), [Online]. Available: https://www.vanderbilt.edu.

[292] Oak Ridge National Laboratory. (2018). Versatile Neutron Imaging Instrument, U.S. Department of Energy, [Online]. Available: https://neutrons.ornl.gov/venus.

[293] Y-12 National Security Complex. (2018), U.S. Department of Energy, [Online]. Available: https://www.y12.doe.gov.

[294] E. Lukosi, E. Herrera, A. C. Stowe, *et al.*, "Investigation of a lithium indium diselenide detector for neutron transmission imaging," in *Hard X-Ray, Gamma-Ray, and Neutron Detector Physics XVI*, A. Burger, L. Franks, R. B. James, and M. Fiederle, Eds., SPIE, Sep. 2014. DOI: 10.1117/12.2063039.

[295] F. Mittelbach, M. Goossens, J. Braams, D. Carlisle, and C. Rowley, *The LaTeX companion*. Addison-Wesley Professional, 2004.

Appendix

Appendix A

General Chemistry

Chemical processes are used in the preparation and fabrication of radiation detectors. To prepare the sensor surfaces for subsequent thin film processing they are polished and etched. Furthermore, prototyping PCBs requires the use if wet chemical etching to remove copper from the substrate, leaving circuit traces behind.

A.1 Sensor Etching

The raw sensor is cut and shaped from the larger, cylindrical crystal boule after growth. The individual radiation sensor is extracted from the bulk using a diamond wire saw, with wire diameters ranging from 100 µm to 500 µm. While the saw gives excellent shape control, creating cuboid sensors from the cylindrical boule, the edges are rough and leave the crystal surface in a stressed state. This creates defect sites which create problems for metal adhesion, as well as offer recombination centers for charge trapping, negatively effecting the electrical performance. To return the crystal surface to a pristine, optically smooth state, the sensor is first treated with a mechanical polish and subsequent chemical etch.

Depending on the sensor chemical composition, aqueous etching may be accomplished using a variety of solutions including: HF, HCl, NH_4OH, and Br_2. Halogen molecules, in particular the Br_2, have been used for a range of materials including I-III-VI semiconductors [223, 224]. It was shown for CdZnTe radiation detectors, a 5.0 % BrMeOH solution successfully removed the surface oxides introduced during sawing and handling [225]. In removing the oxides with the acidic etchant, the surface was left Te-rich. The 20 Å Te-rich surface was removed *in situ* via Ar sputtering before metalization, revealing a stoichiometric surface.

After opting to use the BrMeOH etchant, establishing a material specific procedure was required. Typically, bromine concentrations of 1.0 % to 5.0 % by volume, are used for primary etching, followed by weaker 0.05 % wet etch or chemical polish [226]. The use of dilute etchant with low abrasion polishing pads protects the pad material while offering a finer polish with minimal residue. For softer materials, such as LISe, the chemical polish is removed from the sequence, using a milder wet etching series. The required chemicals

Table A.1. Sensor BrMeOH etching chemicals.

Name	Formula	Concentration	Usage
Acid waste	-	acid solution	waste
Bromine/methanol	$Br_2(CH_3)OH$	5% Br	etching solution
Bromine	Br_2	pure liquid	halogen for etching
Deionized water	DI H_2O	pure liquid	cleaning / dilution
Methanol	CH_3OH	pure liquid	solvent

for the general etching process are listed in Table A.1. Because the BrMeOH etch is frequently applied in semiconductor processing, the fundamental chemical reactions and imposed safety concerns are often overlooked. To better understand the etching mechanism, the following reactions have been listed (eq. 45 - 48) as discussed by Bowman *et al.* [227].

$$2Br_2(l) + CH_3OH(l) \rightarrow 4HBr(g) + CO(g) \tag{45}$$

$$\Delta H = -8.8\,\text{kJ/mol Br}_2 \qquad \Delta G = -92.5\,\text{kJ/mol Br}_2$$

$$HBr(g) + CH_3OH(l) \rightarrow CH_3Br(g) + H_2O(l) \tag{46}$$

$$\Delta H = -46.0\,\text{kJ/mol} \qquad \Delta G = -43.1\,\text{kJ/mol}$$

$$Br_2(l) + CH_3OH(l) \rightarrow H_2CO(g) + 2HBr(g) \tag{47}$$

$$\Delta H = 48.5\,\text{kJ/mol} \qquad \Delta G = -53.6\,\text{kJ/mol}$$

$$2Br_2(l) + 2CH_3OH(l) \rightarrow HCOOCH_3(g) + 4HBr(g) \tag{48}$$

$$\Delta H = -92.0\,\text{kJ/mol Br}_2 \qquad \Delta G = -89.1\,\text{kJ/mol Br}_2$$

The study investigated the reaction dynamics of concentrated BrMeOH solutions ranging from 10.0 % to 25.0 %. While all of these reactions may not be present in the dilute 1.0 % concentration solution, they should be anticipated. Any contaminants, an inherent consequence of impurities produced by polishing the sensor material, may present themselves as inhibitors or catalysts, unpredictably altering the reaction rate. The general sensor etching process has been summarized in Table A.2. The etching sequence utilizes 3 separate Pyrex beakers to effectively etch the sensor while avoiding surface staining. While the first beaker holds the primary etchant (deep red color), the second beaker will become contaminated with bromine and dissolved sensor material, turning a light yellow color. The second beaker will halt the etching process,

Table A.2. LISe sensor BrMeOH etching process.

Step	Action
1	*Prepare etching station*
(*a*)	Rinse 3 Pyrex glass beakers, 150 mL volume or larger, with MeOH.
(*b*)	Dispose of rinse solution in etchant waste.
(*c*)	Fill each beaker with 50 mL of MeOH.
2	*Mix etching solution*
(*a*)	Measure 1.0 mL of bromine liquid in Pyrex graduated cylinder.
(*b*)	Pour bromine from graduated cylinder into one of the Pyrex beakers containing MeOH.
(*c*)	Thoroughly rinse graduated cylinder with MeOH, and empty into etchant waste.
3	*Etch sensor*
(*a*)	Using ceramic tweezers, submerge sensor into the BrMeOH etching solution.
(*b*)	Carefully agitate the sensor, etching for 30 s.
(*c*)	Dip sensor into the second beaker of MeOH, rinsing sensor for 30 s.
(*d*)	Dip sensor into the third beaker of MeOH, for a 5 s final clean.
4	*Inspect sensor surface*
(*a*)	Observe sensor underneath optical microscope to assess surface change.
(*b*)	If surface finish still shows large defects, repolish sensor.
(*c*)	If surface finish still shows small defects, repeat **Step 3**.
5	After sensor shows desired optical surface finish, package to avoid oxidation and immediately follow with photolithography.



Figure A.1. Aqueous PCB etching station in fume hood.

diluting the remaining bromine adsorbed on the sensor surface. The third beaker serves as a final rinse removing any remaining surface contamination, permitting safe handling of the sensor.

Because the LISe sensors are relatively soft, the polishing and etching process should be implemented gradually. It was discovered from experimentation, excessive polishing would create a bowed surface, non-ideal for bump bonding. Consecutively cycling between polishing and etching helped to approach an ideal surface for contact patterning.

A.2 PCB Etching

PCBs are essential components used in all semiconducting detection systems, and more generally computer based data acquisition electronics. A simple, one-sided PCB consists of an insulating material, such as FR-4 fiber laminates, clad with a thin layer of conducting material. Common applications utilize copper cladding deposited by electroplating or laminating, with film thicknesses ranging from $0.5\,\mathrm{oz/ft^2}$ to $2.0\,\mathrm{oz/ft^2}$ ($18\,\mu\mathrm{m}$ to $70\,\mu\mathrm{m}$). The copper etching process outlined in this section will follow successful patterning with the photolithography techniques described in Appendix B.3. The etching process can be highly exothermic and should be conducted in a fume hood with the sash closed or at wrist level as shown in Figure A.1. The correct personal protective equipment (PPE) should be used at all times and can be found in the Safety Data Sheets (SDS) for the chemicals listed in Table A.3. The etching solution created in this method can be recovered and reused if fabricating a large number of PCBs. During prototyping, boards were either etched by themselves or as a pair and the solution was safely disposed as acid waste.

An industry standard, cupric chloride etching provides a straightforward method for fabricating PCBs in

Table A.3. PCB wet etching chemicals.

Name	Formula	Concentration	Usage
Acid waste	-	acid solution	waste
Baking soda	$NaHCO_3$	pure powder	acid neutralization
Copper	Cu	metallic strip	ion source / rate test
Deionized water	DI H_2O	pure liquid	cleaning / dilution
Hydrochloric acid	HCl	37 %	chlorine source
Hydrogen peroxide	H_2O_2	3 % and 35 %	oxygen source

the laboratory environment. Cupric chloride offers the following benefits over the alternative, ferric chloride: it does not contaminate the solution with iron, it creates a transparent solution for monitoring etch rate, the solution can be regenerated, and etch rate can be adjusted relatively easy. While there are only four elements in this solution (H, O, Cl, Cu), the etch rate can be dramatically altered by the cupric chloride and cuprous chloride concentrations.

The metallic copper is dissolved by aqueous copper(II) via the reduction-oxidation (redox) reaction, yielding copper(I) (eq. (49)).

$$\mathrm{Cu^0_{\{s\}} + Cu^{2+}_{\{aq\}} \longrightarrow 2\,Cu^{+}_{\{aq\}}} \tag{49}$$

In a hydrochloric acid solution, cupric chloride will oxidize metallic copper (eq. (50)), dissolving the cladding into solution as cuprous chloride.

$$\mathrm{CuCl_2 + Cu \longrightarrow 2\,CuCl} \tag{50}$$

The etchant recharge mechanism relies on the oxidation of $Cu_1{}^+$ back to the usable $Cu_2{}^+$ form. Illustrated in the partial reaction (eq. (51)), this depends on free Cl^- ion concentration in the solution.

$$\mathrm{2\,CuCl + 2\,Cl^- \longrightarrow 2\,CuCl_2 + 2\,e^-} \tag{51}$$

To initially charge the solution with cupric chloride, concentrated hydrogen peroxide is introduced to a piece of pure copper foil. Under normal conditions, hydrogen peroxide will decompose on its own (eq. (52a)) releasing oxygen gas.

$$\mathrm{2\,H_2O_{2\{aq\}} \longrightarrow 2\,H_2O_{\{l\}} + O_{2\{g\}}} \tag{52a}$$

The presence of free Cl^- will catalyze the chain decomposition of H_2O_2 (eq. (52b)) while leaving the Cl^- in free solution, accelerating the release of oxygen (eq. (52c)).

$$\mathrm{H_2O_{2\{aq\}} + Cl^-_{\{aq\}} \longrightarrow OCl^-_{\{aq\}} + H_2O_{\{l\}}} \tag{52b}$$

$$H_2O_{2\{aq\}} + OCl^-_{\{aq\}} \longrightarrow H_2O_{\{l\}} + O_{2\{g\}} + Cl^-_{\{aq\}} \tag{52c}$$

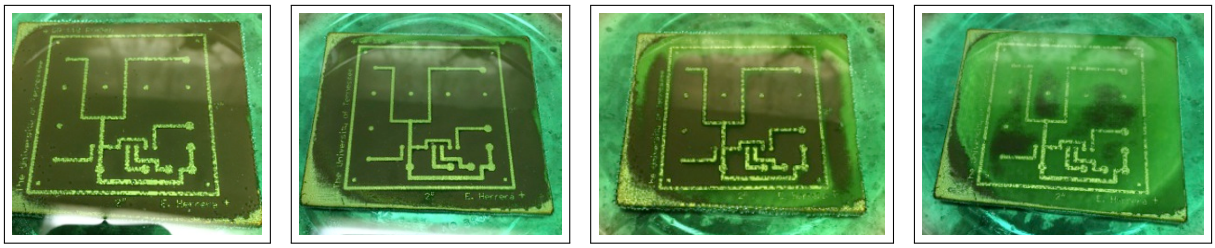
Introducing oxygen to the solution will oxidize metallic copper to cupric oxide (eq. (53)).

$$2\,Cu + O_2 \longrightarrow 2\,CuO \tag{53}$$

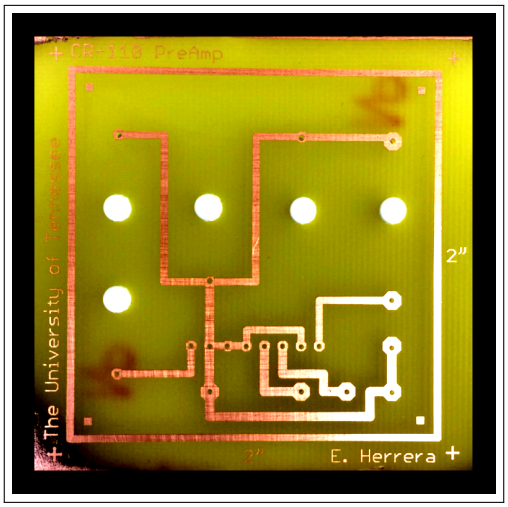
Cupric oxide, in the presence of HCl, will yield cupric chloride (eq. (54)).

$$CuO + 2\,HCl \longrightarrow CuCl_2 + H_2O \tag{54}$$

Experimenting with the concentrated (>30 %) hydrogen peroxide, it was possible to readily pre-charge the solution with cupric chloride ions. The initial piece of copper foil was sacrificially added to the solution with drops of concentrated H_2O_2. Initially, oxygen gas quickly releases from H_2O_2 breakdown, accelerated by the free HCl. The oxygen will serve as the initial oxidizing agent, removing copper ions from the foil surface and converting them to the desirable cupric chloride. As the free oxygen is consumed during copper oxidation, the freshly generated cupric chloride in the solution will take over as the primary etching agent. Adding copper strips, and promoting dissolution with concentrated H_2O_2 charges the etching solution over a period of minutes, instead of days as seen with dilute H_2O_2. Given the amount of copper on the single sided pre-amp PCB, the board successfully etched, in a matter of minutes as shown in Figure A.2. Immediately after submersing the PCB in the etching solution, the acid begins to attack the raw metal (Figure A.2a.). Small gas bubbles form along favorable nucleation sites, such as crevices formed at the edges of the resist and the exposed copper. After the first minute, broad regions of copper along the periphery have begun to dissolve as seen in Figure A.2b. The outer trim ring begins to separate from the surrounding metal after about two and a half minutes, shown in Figure A.2c. Approaching the five minute mark (Figure A.2d), the only remaining copper are the resist coated circuit traces and labels. The copper etching process, as tested, has been summarized in Table A.4. The technique has been shown to successfully prototype custom circuit designs, in-house, using the positive photolithography process in the Micro-Processing Research Facility (MPRF).



(a) $\Delta t = 3\,s$ (b) $\Delta t = 55\,s$ (c) $\Delta t = 163\,s$ (d) $\Delta t = 271\,s$



Final etched printed circuit board

Figure A.2. Pre-amp PCB manufacturing: time lapsed aqueous copper etching process using cupric chloride etchant.

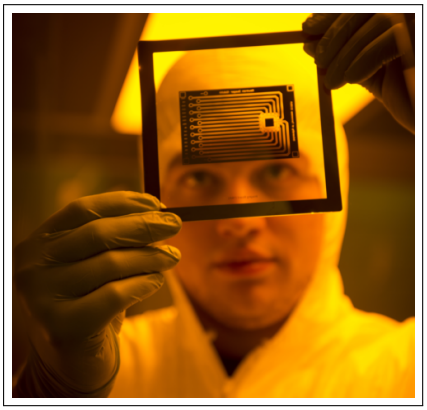
Table A.4. PCB wet etching process.

Step	Action
1	*Add solution*
(*a*)	Measure 40 mL of 3 % hydrogen peroxide in graduated cylinder.
(*b*)	Pour contents of graduated cylinder into large Pyrex dish.
(*c*)	Rinse graduated cylinder with DI water and dispose in acid waste.
2	*Add acid*
(*a*)	Measure 20 mL of 37 % hydrochloric acid in graduated cylinder.
(*b*)	Pour contents of graduated cylinder into large Pyrex dish.
(*c*)	Rinse graduated cylinder with DI water and dispose rinse solution in acid waste.
3	*Charge solution*
(*a*)	Prepare a section of thin Cu foil of roughly 1.0 cm^2 area.
(*b*)	Add Cu test strip to solution to charge etchant with Cu ions.
(*c*)	Monitor the dissolution rate and add 35 % hydrogen peroxide with dropper to adjust rate.
4	Repeat **Step 3** until the dissolution rate is controllable.
5	Dip PCB in solution using ceramic tweezers.
6	Lightly agitate board until edge of traces are clearly distinguished.
7	Rinse PCB with DI water until board is clean and etching has stopped.
8	Dispose of etching solution in acid waste bottle. (Alternatively, etching solution may be stored in clean, labeled bottle for later use.)

Appendix B

Thin Film Processing

The science of thin film processing opened new avenues in the miniaturization of modern electronics [228]. Semiconductor electronics depend on precision fabrication processes, ranging from the millimeter down to the nanometer scale. To achieve the quality required for such devices, processing equipment must be operated in a clean room, protecting sensitive surfaces from dust, oils and particulate contamination. In this controlled environment, even the spectrum of lighting is manipulated based on operational requirements, as shown in Figure B.1. The raw LISe crystal becomes a radiation sensor through photolithography and subsequent plasma sputtering. The delicate metallization process adheres high purity, thin film contacts to the sensor, without disrupting the material composition or crystalline structure. Packaging the sensor using wire-bonding or flip chip bump bonding creates fine pitch electrical signal channels, collecting data from each pixel. The resulting semiconductor device maintains radiation and electronic performance required for a semiconductor neutron detector.



(a) example of 5 in quartz lithography photomask (alumina sensor PCB)



(b) photolithography in MPRF clean-room on the MA-6 (left) with the AJA sputterer in the background (right)

Figure B.1. MPRF clean room used for patterning semiconducting neutron detectors.

B.1 Plasma Sputtering

Plasma sputtering captures the process of energetically impinging a pure material target with an ionized gas, ejecting atoms or molecules. The emitted target atoms or molecules are deposited on the substrate and surrounding chamber. This process is particularly effective at producing high quality thin films necessary for semiconductor radiation detectors [228, 229].

Direct Current Plasmas

DC plasmas are typically used to sputter pure metal targets, or metallic alloys, where the material resistivity is roughly $10^6\,\Omega \cdot \mathrm{cm}$ or less. Higher values of resistivity for the target material will require exceedingly larger values of bias voltage to produce an equivalent current density. Voltages exceeding a few kilovolts are difficult to reach and impractical to sustain in a standard laboratory environment. Furthermore, DC plasmas impart significant energy to the sputtering gas ions as well as the sputtered metal atoms, potentially damaging sensitive surfaces.

Alternating Current (Radio Frequency) Plasmas

To overcome the limitations of using DC plasma sputtering, AC bias permits sputtering high resistivity materials. Typical RF plasma processing follows the U.S. Federal Communications Commission (FCC) designated frequency of 13.56 MHz, however systems are designed across a range of 5 MHz to 30 MHz. At higher frequencies, the coupling capacitor may charge and discharge continuously, allowing significant current to flow through the target material. Using an AC system, insulating materials such as quartz and other oxides may be deposited, along with precious metals such as gold or platinum. At lower frequencies, below 1 MHz, the AC system performs similar to the DC conditions, except the cathode and anode are cyclically swapped. When frequencies are increased above the 1 MHz point, the electrons gain enough energy to ionize sputtering gas atoms, sustaining the plasma.

The rapidly oscillating electrons trapped between the electrodes will continue to ionize atoms not requiring the secondary source of electrons from the cathode. Furthermore, at frequencies above 100 kHz, the lighter electrons will acquire a larger fraction of the applied power, resulting in less energetic positive ions. Reducing the energy of the plasma gas ions lowers the energy imparted to the sputtered particles along with their impact damage on the sensor surface. Energetic sputtered atoms will create a peened topography on the surface, leaving the thin film in a state of compressive stress. At low energies, the sputtered ions will coalesce with the thin film and create a more homogeneous topography in tensile stress. Using the AC sputtering method assists adhesion while simultaneously protecting the surface of delicate radiation detectors.

Plasma Ignition

At room temperature and pressure, the sputtering gas will not interact with enough energy to produce ionized particles, or sputter the target material. Thus, the plasma ignition process begins with vacuuming down the process chamber, reducing the chamber pressure along with the MFP of internal ions and charged particles. First, the mechanical roughing pump is used to bring the chamber to medium vacuum, evacuating the atmospheric air and contamination gases from the system. A light, inert gas such as nitrogen may be injected into the system to help back fill the chamber, purging other contaminants.

Once the pressure reaches between 10 mTorr to 100 mTorr, the turbo pump spools up, reducing the pressure to high vacuum levels so the plasma may be ignited. The system is pumped to around 1 µTorr to ensure deadsorption of moisture from the internal surfaces. Once the chamber has been thoroughly purged, the sputtering gas (Ar) is introduced, increasing the pressure to around 1 mTorr. The selected target gun is switched on at a low power (10 W to 25 W) and begins the plasma ignition process. In the plasma, free electrons have a higher mobility than the more massive gas atoms, so they attain high kinetic energies in the presence of an applied field. Electrons will continue to bombard the cations, losing little energy in elastic collisions, until an inelastic collision causes the ionization of the molecule. After the electrons have been accelerated to high enough potentials, they ionize the process gas, stripping off electrons. A shutter sits on top of the chimney surrounding the target, and along with the use of magnetrons, confines the charged particles and sputtered atoms near the surface of the gun. The glow is caused by photon emission during the recombination of a cation and electron, and will be characteristic of the process gas. As the power is gradually increased, the density of the charge carriers in the chimney increases, consequently drawing more current through the plasma. Eventually, the ions present in the chimney will avalanche and create enough secondary ionization events to self stabilize the plasma. After the plasma has been successfully ignited, the shutter is opened and process pressure may be lowered to sub-ignition values.

As the plasma carries a current, the initial startup barriers in the physical system have been overcome and lowering pressure helps to increase the sputtered atom MFP. The low pressure ensures the sputtered atom reaches the substrate without interacting with a process gas ion. Maintaining a high-voltage bias is sufficient to continue the production of ionized species for sputtering. The bias voltage and pressure are regulated based on the sputtering target material for optimum sputtering rates and deposited film quality.

B.2 Negative Photolithography

Photolithography with NR9-1000PY (negative photoresist) is used to create thin film metal contacts on semiconductor grade radiation sensors. Negative photoresist describes a photopolymer which hardens, becoming insoluble to developing chemicals, after exposure to a prescribed spectra of light. The hardened resist creates a film coating used to selective apply thin film material coatings to a semiconductor surface. In particular, the method is used to fabricate the pixelated LISe imagers. The photolithography chemicals

Table B.1. Photolithography negative process chemicals.

Chemical	**Formula**	**Description / Usage**
Acetone	$(CH_3)_2CO$	solvent / resist removal
Deionized water	DI H_2O	solvent / rinsing
Ethanol	C_2H_5OH	solvent / cleaning
Isopropyl alcohol	C_3H_8O	solvent / cleaning
Methanol	CH_3OH	solvent / surface preparation
Negative photoresist	NR9-1000PY	photopolymer / masking
Photoresist developer	RD6	selective resist removal during development
Photoresist remover	RR41	final resist removal
Toluene	C_7H_8	solvent / wax removal
Apiezon wax	Apiezon Wax W	bonding and masking

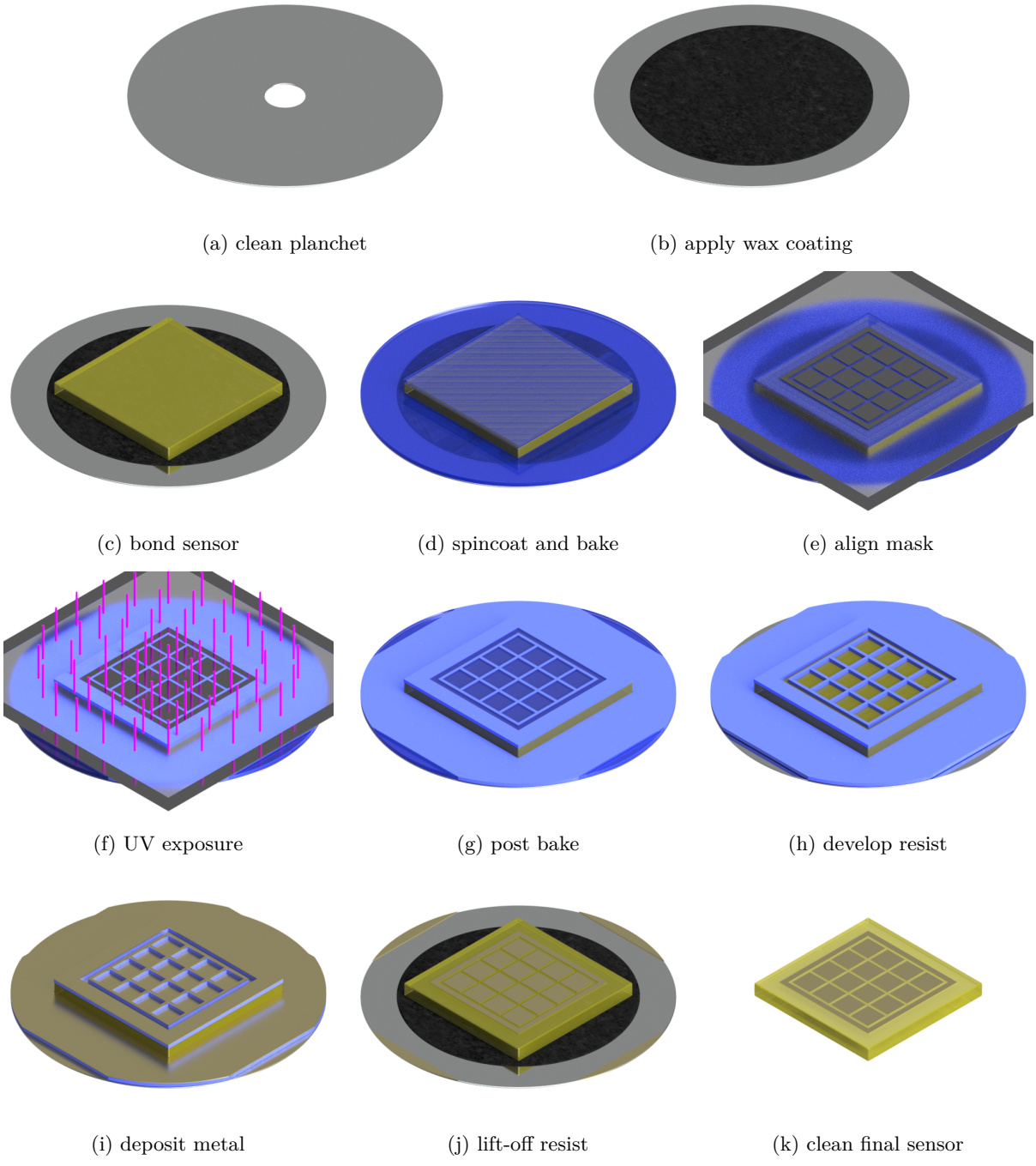
for the negative photoresist process are listed in Table B.1. The negative photolithography process, Figure B.2, shows the sequential stages used to fabricate the pixel detectors.

Step (a) begins with a clean stainless steel planchet, serving as the wafer. The thin metal wafer is used in place of a standard silicon wafer to adapt to the spin coater and mask aligner chuck. A small hole is drilled in the center of the planchet to allow solvent to reach the Apiezon wax underneath the sensor. The planchet is lightly polished and cleaned with solvents to remove residual Apiezon wax and material contamination between solvents.

Step (b) shows the planchet pre-coated with Apiezon wax. The hole in the plancet is cover with a piece of kapton on the back side. The Apiezon wax is shaved down and small flakes are placed in the center of the planchet. On a hot plate, the Apiezon wax is melted down at 90 °C, using drops of toluene to dilute the Apiezon wax and disperse it to the edges of the planchet.

Step (c) illustrates the LISe sensor after bonding to the Apiezon wax coated planchet. Bringing the temperature up to 100°, the sensor should be allowed to sink into the Apiezon wax so that the top surface is the only exposed area. The bonding process serves to protect the sensor's back surface, which may already be metallized, as well as the sidewalls from further metal deposition. If the sidewalls are coated in metal, there is potential for voltage breakdown, allowing charge to travel along the outside of the sensor instead of through the sensor bulk. This step also serves as a dehydration bake, drying the surface of the sensor and removing water that may reduce metal adhesion. Once bonded, the wafer should be placed on the workbench to slowly cool back to room temperature, preventing thermal shock in the sensor.

Step (d) follows the application of negative photoresist. The negative photoresist is stored in a chilled refrigerator to prolong the chemical life, protecting the photosensitive compound. For dispensing, a small



(a) clean planchet (b) apply wax coating

(c) bond sensor (d) spincoat and bake (e) align mask

(f) UV exposure (g) post bake (h) develop resist

(i) deposit metal (j) lift-off resist (k) clean final sensor

Figure B.2. Photolithography process using negative resist for pixelated LISe semiconductor sensor fabrication [107]. The LISe PD has been shown as an example to capture all the sensor features.

Table B.2. Spin coater negative resist recipe.

Step	T_{ramp}	T_{dwell}	**Description**
S00	0 s	0 s	Sequence startup, defines wafer as 2 in outer diameter.
S01	10 s	2 s	Initial ramp to 500 RPM. This step allows the wafer to auto-center on the chuck.
S02	15 s	25 s	Ramp to full spin coating speed of 3,000 RPM. This step planarizes coating.
S03	25 s	10 s	Ramp down to 1,000 RPM to slow wafer and continue evaporating solvent.
S04	5 s	2 s	Final ramp down to stationary. Sample is ready once it has come to rest.

quantity is stored at room temperature in a tinted dropper bottle, lowering the viscosity for spin coating. The resist is applied via eye dropper to the surface of the LISe sensor, dispensing roughly 50 µL of resist per drop. Immediately after applying the photoresist, the layer is spread thin by the 6800 Series Spin Coater (spin coater) to a nominal 1 µm thickness as described in Table B.2. Following spin coating, the wafer is removed using wafer tweezers and set on the hot plate for a 60 s pre-bake at 150 °C. The pre-bake helps to dry the resist, eliminating any residual moisture and allowing a slight anneal of the resist to homogenize thickness. The wafer is set to cool on the table to slowly remove heat from the sample.

Step (e) shows the pattern transfer process, conducted in the MA-6/BA-6 Mask and Bond Aligner (MA--6). The specific device mask is loaded into the contact printer and the wafer is aligned, positioning the pattern over the sensor area. This is the step where the use of a substrate wafer is crucial. Typically, the contact printer is used with a standard 3 in to 4 in silicon wafer. The entire mask pattern is transferred to the wafer, with extraneous features being removed along with the Apiezon wax.

Step (f) shows the resist exposure process. The photoresist on the crystal is exposed for 15 seconds using the I-line (365 nm) UV radiation from the pressurized mercury vapor lamp. The UV light chemically reacts with the photoresist, causing the exposed regions to harden through cross-linking of the polymeric bonds.

Step (g) captures the post-exposure bake, assisting the polymer cross-linking by applying 100 °C via hot plate for 60 s. This bake helps to remove the nitrogen component of the photo-compound which would be otherwise detrimental in the sputtering process due to off gassing. The bake also facilitates the breakdown of unexposed regions for pattern development.

Step (h) follows the pattern development using photoresist developer for 8 s to 10 s. The developer dissolves the soluble, unexposed regions, carrying away the polymer and leaving an exposed region mimicking the desired pattern. Depending on the development time, some undercutting will occur where the developed photoresist leaves a slight negative grade sidewall profile. This effectively creates a small (1 µm to 5 µm) gap between the open channels and the edge of the resist. Without this gap, lift-off can become either difficult or impossible.

Step (i) shows the metallized sensor. Once the sample has been patterned, the crystal is inspected using

an optical microscope. This is the first point the pattern can be inspected without exposing the resist using the white light from the microscope. After pattern inspection, the substrate wafer is loaded on the AJA sputterer chuck and vacuumed down to 1.0 µTorr or less. Reaching high-vacuum first helps to evacuate residual nitrogen along with moisture that has been adsorbed to the various surfaces. One advantage of the Apiezon wax is its ability to getter impurities in a high vacuum system. After the system is evacuated, the pressure is adjusted to roughly 4.0 mTorr for plasma sputtering. A high-purity metallic target is the source of atoms for the uniform thin film deposited on the photoresist and exposed regions of the crystal.

Step (j) depicts the lift-off stage conducted in a solvent bath. A glass petri dish containing photoresist remover is heated on the hot plate to 80 °C. Before placing the metallized wafer in the petri dish, scratches are made along the non-sensor areas using the ceramic tweezers, exposing the Apiezon wax underneath. The scratches allow the resist remover to penetrate underneath the metal thin film, attacking the resist beneath. Depending on the pattern complexity and coverage area, the development times will differ. Introducing small amounts of acetone into the solution will speed the dissolution process, however, too much acetone can cause the loose metal film to re-adhere to the surface, shorting contacts. Once the excess metal has been removed, exposing the final pattern, toluene should be added to the solution to begin dissolving the Apiezon wax. As the petri dish holds a limited volume and the solvents are highly volatile, the solution will continuously evaporate and additional toluene must be introduced. Typically, the solution will saturate, turning opaque black, requiring a fresh petri dish of pure toluene. Repeating this process will eliminate the Apiezon wax, now in solution, along with lifted metal that my contaminate the sensor surface.

Step (k) shows the finalized sensor, free from the planchet. The metallized crystal should be removed from the toluene and rinsed in isopropyl alcohol (IPA) then MeOH to remove residual contaminants, providing a final clean before air drying with nitrogen. All devices require inspection using the optical microscope before integration with other electronics to characterize pixel size and metal film quality. If the sensor has only been metallized on one side, these steps are repeated with the opposite side of the sensor exposed to the patterning process.

The steps conducted in the negative photolithography process have been summarized in Table B.3. As a preliminary validation test, a silicon wafer is patterned with aluminum metal, shown in Figure B.3. Because the systems are designed for silicon wafers, the process parameters may be dialed in without the complications of the planchet carrier or fragile crystalline sensor. The test wafer also serves to characterize the quality of new photomasks, ensuring the design and pattern scaling meets the requirements of the detector. After the process sequence has been reviewed, the semiconductor grade sensors are patterned on both sides, taking great care to minimize stress on the sensor as well as material waste.

Table B.3. Photolithography with negative photoresist for sensor fabrication.

Step	Action
a	Prepare cleaned planchet.
b	Apply Apiezon wax to planchet at 90 °C.
c	Bond sensor to coated planchet at 100 °C.
d	Generously apply negative photoresist across substrate and run negative spin coating recipe (see Table B.2). Follow with soft bake on hotplate at 150 °C for 60 s.
e	Install photomask in MA-6. Load sensor wafer and align photomask.
f	Expose resist for 15 s using distance contact on MA-6.
g	Hard bake on hotplate at 100 °C for 60 s.
h	Dispense photoresist developer across surface of sensor for 8 s to 10 s. Immediately rinse the surface with DI water to halt the development process. Dry patterned surface using compressed nitrogen gun, driving all fluid from center outward.
i	Inspect resist pattern to ensure quality of development and appropriate sidewall taper. Run metal deposition in the AJA sputterer.
j	Soak patterned substrate in photoresist remover at 80 °C. Acetone may be added sparingly to facilitate metal lift-off. Add toluene to remove the Apiezon wax.
k	If acetone was used, a light IPA pre-rinse will help to remove acetone streaking. Perform final rinse with MeOH. Dry with compressed nitrogen gun.

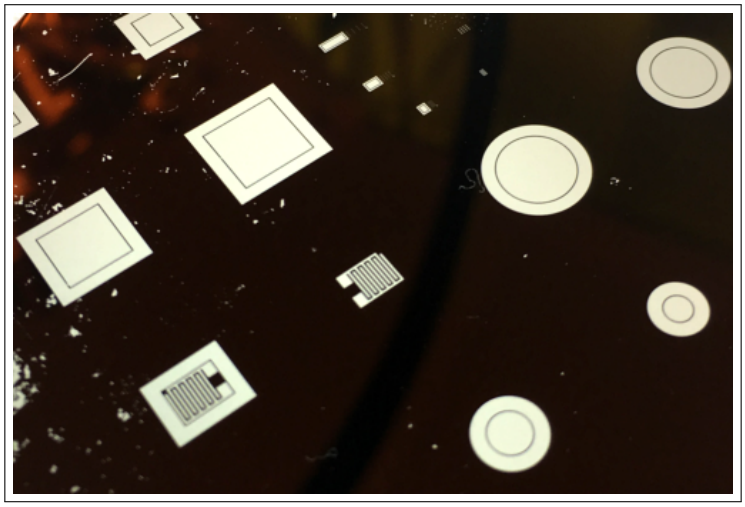


Figure B.3. Silicon test wafer patterned with coplanar, circular, and rectangular broadface contacts.

Table B.4. Photolithography positive process chemicals.

Chemical	**Formula**	**Description / Usage**
Acetone	$(CH_3)_2CO$	solvent / resist removal
Deionized water	DI H_2O	solvent / rinsing
Ethanol	C_2H_5OH	solvent / cleaning
Isopropyl alcohol	C_3H_8O	solvent / cleaning
Methanol	CH_3OH	solvent / surface preparation
Positive photoresist	PR1-1000A	photopolymer / masking
Photoresist developer	RD6	selective resist removal during development

B.3 Positive Photolithography

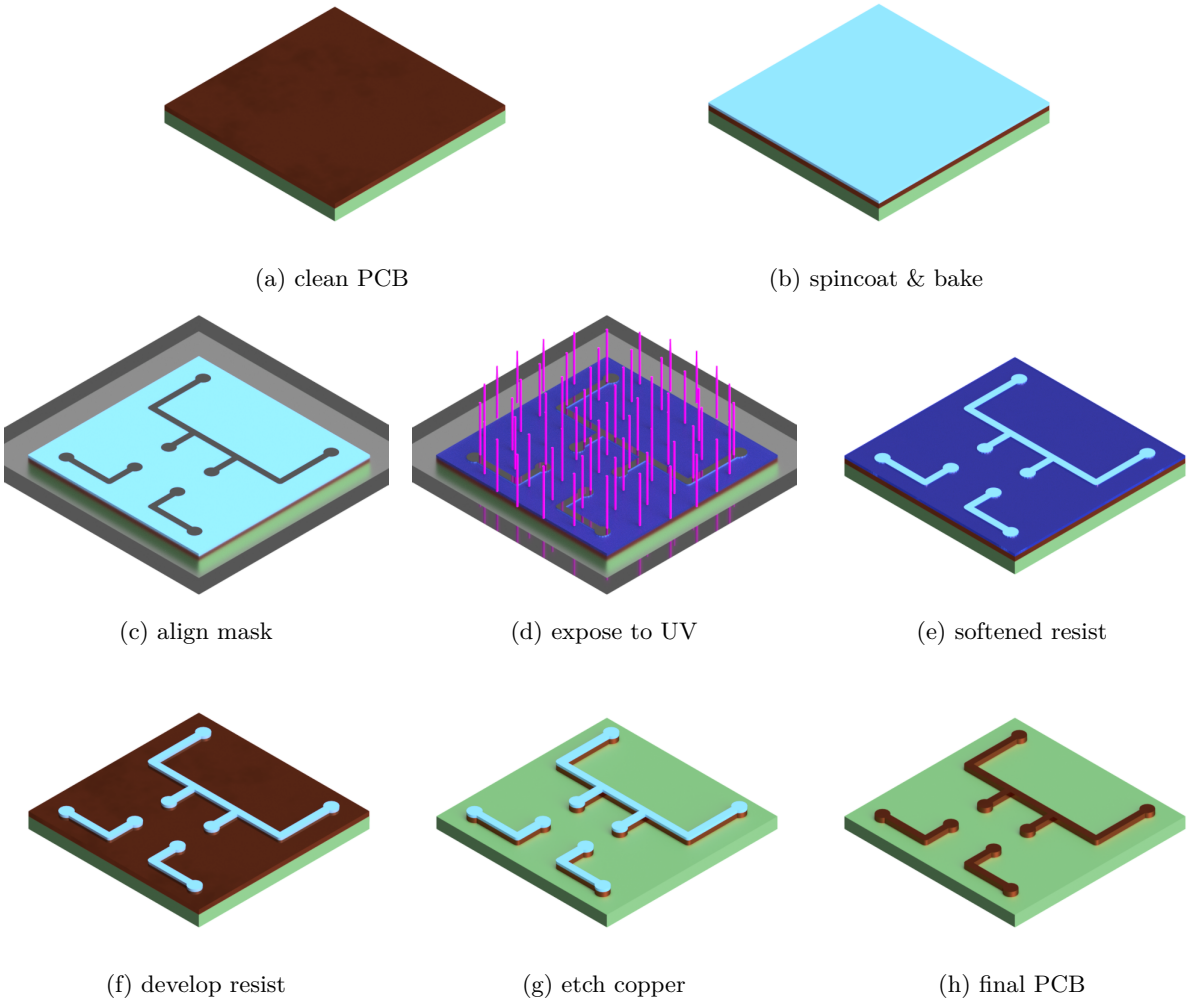
Photolithography using PR1-1000A (positive photoresist) finds use in masking substrates for etching, both aqueous and ion based. Positive photoresist is a photopolymer which softens, becoming soluble in developer, when exposed to photon emissions. This particular process will be described as it applies to PCBs for copper trace wet etching. The photolithography chemicals for the positive photoresist process are listed in Table B.4. The positive photolithography process, Figure B.4, shows the sequential stages used to fabricate general PCBs.

Step (a) begins with a clean PCB substrate of desired size to accommodate the circuit design. The board should be large enough to minimize the signal traces proximity to the edge of the PCB, generally using a trim ring to outline the board. Most commercial grade PCB substrates come pre-coated with a protective layer to inhibit surface oxidation and ensure nominal cladding thickness. This protective layer is removed using a scouring pad and acetone to scrub the surface, dissolving the plastic and priming the metal surface to bond with the photoresist. A final rinse with IPA then MeOH leaves a dry, clean surface, free of streaking and contaminants.

Step (b) involves spin coating the PCB with positive photoresist. The process also uses the spin coater, however disposable pipettes deliver the larger volume of resist required to coat the entire PCB surface. The spin coating recipe also varies with the size of the board, requiring slower speeds for larger boards to adequately spread the resist across the surface. The overall spin cycle follows a similar profile as with the negative process recipe. Once coated, the PCB is heated to 120 °C for 120 s on the hot plate.

Step (c) follows a more traditional sequence using the MA-6. The photomask is installed and the PCB centered in the chuck. The alignment process benefits from the larger scale pattern, typically having fiducial markers at each corner to guide the edge. Furthermore, the photomasks for PCB fabrication typically only have a single design across the quartz plate.

Step (d) exposes the photoresist to the same 365 nm UV radiation. Here, the hard contact setting is



(a) clean PCB (b) spincoat & bake

(c) align mask (d) expose to UV (e) softened resist

(f) develop resist (g) etch copper (h) final PCB

Figure B.4. Photolithography process using positive resist for PCB manufacturing.

used, with only a 4 s exposure time. The shorter time minimizes the sidewall angle and undercut, producing the thickest mask possible to protect the surface during wet etching.

Step (e) shows the softened photoresist after exposure. Because the pattern is generally much larger, the features are visible by the naked eye. The pattern should be inspected near the edges to ensure the resist was fully spread across the surface, and the pattern transferred to all regions where metal should be covered. If the PCB is pre-drilled for through hole components, the area around the holes should also be reviewed. The metallization near holes is crucial for component electrical conductivity and establishing an appropriate surface for soldering.

Step (f) exposes the bare copper with the desired trace pattern protected by the insoluble resist. The positive photoresist is less sensitive to over development so the photoresist developer resist remover is liberally applied to the surface until the pattern is clearly developed. All excess resist must be removed, otherwise spots of metal may remain across the board, shorting traces or leading to signal breakdown. After development, the PCB is rinsed with DI water and dried with compressed nitrogen. An optional anneal may be conducted on the hot plate at 145° for 5 min to further dry the resist and enhance adhesion for wet etching.

Step (g) shows the PCB etching process detailed in Appendix A.2. For more exotic PCBs that use other cladding materials, the process will be similar, using an etchant that reacts with the specific cladding metal and not the photoresist. After the etching process is complete, the PCB will still have a thin layer of resist covering the copper traces. This layer is dissolved using acetone, followed by a clean with IPA and MeOH to remove and surface films and remaining contamination.

Step (h) illustrates the final, one-sided, PCB. Once the PCB has be cleaned and dried, the pattern is inspected under a low power LM to determine if any shorts or breaks exist in the trace pattern. As the bare copper layer will begin to oxidize, the PCB components should be immediately soldered to the board. Furthermore, a protective insulating coating, such as Konform, should be applied to the surface to encapsulate the bare metal. The steps conducted in the positive photolithography process have been summarized in Table B.5.

B.4 Wire Bonding

An analog to soldering wires on PCBs, wire bonding describes a process of electronically coupling micron-scale electronics. The K&S wire bonder implements a wedge bond technique to connect 0.5 mil to 3.0 mil diameter wire between device contacts. The standard process for wedge bonding follows the sequence described by Fischer *et al.* in Figure B.5 [230]. In Step (a), the wire is threaded through the bonding wedge tip. Care is taken when passing the wire through the wedge orifice to avoid bending the wire, introducing kinks that reduce the mechanical stability of the wire bond. The wire clamp closes on the bonding wire to ensure the ultra-light wire remains in position and does not retract on the spool. Step (b) makes the first bond on the sensor, by depressing the wire bonder head into the contact surface with a specified compressive force

Table B.5. Photolithography with positive photoresist for PCB manufacturing.

Step	Action
a	Clean PCB surface and remove and protective layer with solvents as necessary.
b	Generously apply positive photoresist across PCB and run positive spin coating recipe. Follow with soft bake on hotplate at 120 °C for 120 s.
c	Install photomask in MA-6. Load PCB and align photomask.
d	Expose resist for 4 s using hard contact setting on MA-6.
e	Visually inspect pattern for full exposure at edges of PCB and through holes.
f	Dispense photoresist developer across surface of PCB until transferred pattern is well defined. Rinse surface with DI water to clean remaining photoresist developer. Dry patterned surface using compressed nitrogen gun, driving all fluid from center outward. Optional bake at 145 °C for 5 min to anneal resist.
g	Etch copper layer as described in Appendix A.2.
h	Dissolve remaining resist using acetone to expose the patterned metal layer. Remove surface residue with IPA.

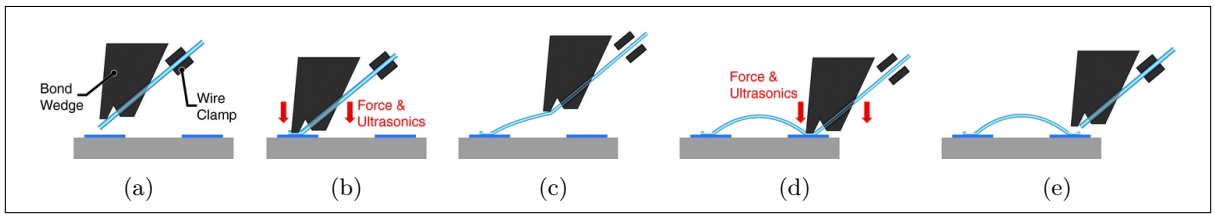


Figure B.5. Process flow of standard ultra-sonic (US) wedge-wedge bonding (diamgram courtesy Fischer *et al.* (2013) [230]).

Table B.6. Calibrated base settings for the K&S wire bonder.

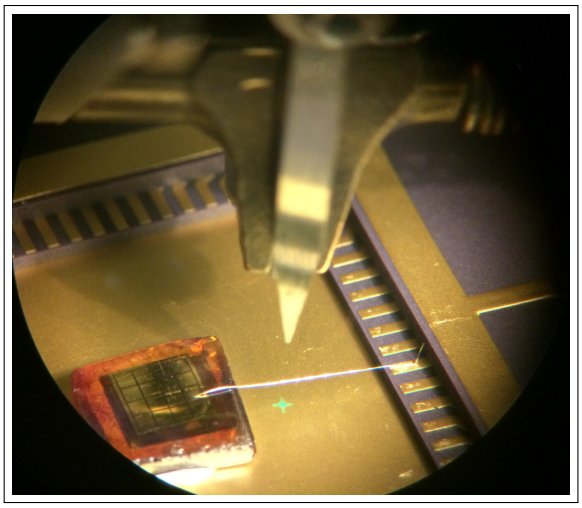
Page 1		**Page 2**		**Page 3**		**Page 4**	
Search 1*:	5.99	Step:	0.00	Search 2*:	5.99	Mode:	STND
Power 1:	1.76	Kink:	2.50	Power 2:	2.15	Time:	LONG
Time 1:	4.00	Reverse:	2.50	Tail:	LONG	Time 2:	5.00
Force 1:	1.80	Y-Speed:	2.00	Force 2:	1.90	Auto:	OFF
		Loop:	8.50	Tail:	5.00		
				Tear:	5.00		

* search height must be adjusted for stage height

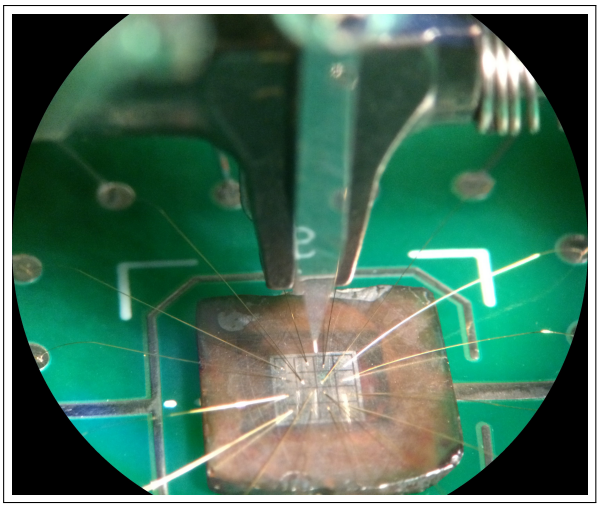
ranging from 10 g to 160 g. The established settings for the K&S wire bonder are presented in Table B.6. The bonding head utilizes a 60 kHz US transducer to vibrate the wedge, creating the metallic weld between the bond wire and contact pad. In Step (c), the wire clamp opens and the wedge bonding tool is lifted to a prescribed height while moving in the direction of the next bond. Step (d) shows the wedge tool descending on the second bond, smoothly arching the wire, creating a permanent bend to suspend the wire over other electronics. Again, the wedge is compressed into the bonding pad with US agitation to establish the second bond. Finally in Step (e), the wire is pinched by the wire clamp and the wedge tool jerks backwards, breaking the wire and leaving the finished bond.

All bonds fabricated in this research utilized 99.99 % Au wire of 1.0 mil diameter bonded with a 45° wedge. The heated bonding stage was also set to a temperature of 100 °C to promote the Au wire to Au bonding pad adhesion. Common practice finds ASIC devices housed in a chip carrier. This type of packaging bonds an ASIC substrate to the center well of a multi-channel readout chip, with wire bonds extending from the top of the ASIC to the readout pads, as shown in Figure B.6a. Each channel is insulated, connecting to a pin extending from the back of the chip, allowing the chip carrier to mate with a matched socket. Chip carriers may be directly attached, or mounted via chip socket to a PCB containing peripheral electronics and connections. This configuration offers a small form factor, with a replaceable package in the event of ASIC failure. For radiation detectors, this type of packaging permits the testing of multiple sensors without having to alter the electrical connections to readout electronics.

Alternatively, the sensor may be directly mated to a device specific PCB as seen in Figure B.6. Wire bonding pads are included on the surface of the PCB, routed directly to through hole soldering vias. The traces from the sensor PCB are connected with a smaller jumper wire to the input traces of the pre-amp module. This configuration offers a nearly direct connection between the radiation sensor and readout electronics.



(a) LISe PD mounted to 64-ch ASIC chip carrier with test wirebond



(b) LISe bonded to readout PCB

Figure B.6. LISe PDs under Kulicke and Soffa 4500 Digital Series Manual Wire Bonder.

B.5 Bump Bonding

As the channel density increases in a pixelated imaging device, the previously described wire bonding techniques are no longer viable. Flip chip bump bonding offers a method of directly coupling the pixelated sensor to an identically pixelated readout ASIC. Instead of bonding micron-thick wires from the detector pixels to the readout bonding pad, the pixels are electrically coupled to the associated ASIC pixel via bump bonds [231, 232]. The bump ball diameters for this technology range from 20 µm to 40 µm, resulting in a bond height of 10 µm to 15 µm [233]. The applicable pixel pitches span from 20 µm to 50 µm, suitable for the 55 µm Timepix system, common in high-resolution radiation detection. The process has been illustrated below (Figure B.7) courtesy Rossi *et al.* (2006), describing the original processing methodology detailed by Broennimann *et al.* (2006) [211, 234]. The flip chip bump bond facility used to process the LISePix system applied the larger indium bump bonds to the Timepix, slightly altering the following process to accommodate LISe processing temperature limits. Step (a) illustrates the chip coated with a capping layer such as SiO_2, to insulate the underlying ASIC circuitry. This capping layer exposes only the bonding pad for each pixel, precisely covering the edges of the contact to minimize current leakage. In Step (b), the chip is coated in photoresist, and a thin base layer (Au) is sputtered into the bonding well, creating a cradle for the bump bond up to the capping layer. Step (c) follows a similar process as Step (b), depositing a roughly 5 µm thick layer of indium, with a 50 µm diameter, to form the bump bond (described for a 100 µm pixel pitch design) [211]. After wet lift off, Step (d) shows the ASIC prepared with the bonding metals.

A similar sequence, following Steps (a-d), is applied to the LISe sensor using a smaller thickness of 2 µm and diameter of 20 µm for the indium deposit. Step (e) shows the effects of the 180 °C reflow process, providing the activation energy for the indium to reform into a spherical bead. The reflow is only applied to

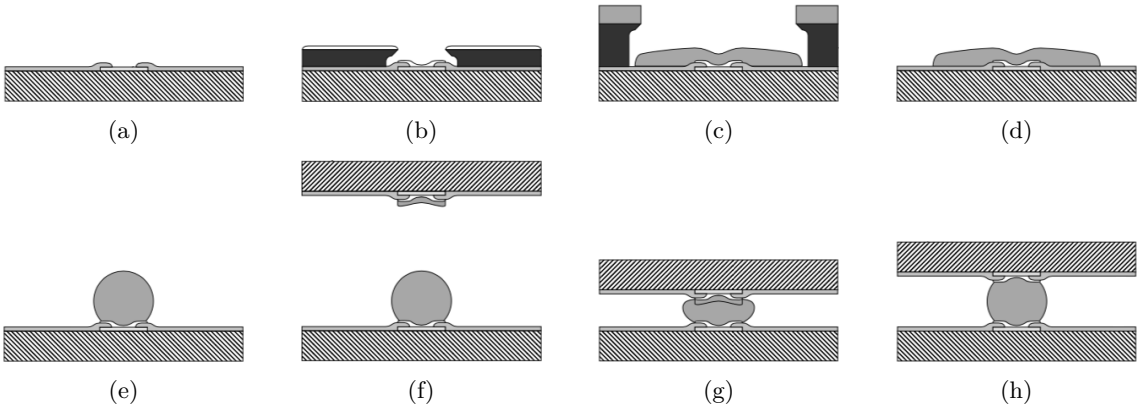


Figure B.7. Sketch of the indium bump deposition processes followed by reflow and flip chip operation (courtesy Rossi *et al.* (2006) [211, 234]).

the ASIC side and not the thinner indium on the sensor side. This prevents thermal shock in the LISe crystal along with lithium off-gassing which can negatively effective the device sensitivity. In Step (f) the bumped ASIC chip and the sensor are brought into alignment. As the sensor may be opaque and has metallized contacts, this process is performed blind, relying the on precision positioning stage to approximate the alignment. During the bonding process, Step (g), the two substrates are compressed, roughly 1.0 g per bump, and reflowed again, this time at a lower temperature of 100 °C. The indium coat on the sensor side helps the bump bond to wet the contact, self-aligning each pixel to position the chip. Step (h) shows the final bump bond, with the indium creating a spherical interconnect between the two contacts.

Appendix C

Image Processing

This appendix describes analytical techniques utilized in the evaluation of neutron imaging data [192]. Images were created by placing a neutron absorbing material in front of a neutron beam, and capturing the transmitted neutrons on a multi-channel detection system. While the primary application of these methods focuses on neutron radiography, image processing extends to the broader spectrum of radiographic imaging.

C.1 Neutron Image Pre-Processing

Typically, neutron images start with 3 sets of data: the dark field, the open beam or white field, and the object image. Each data set is composed of multiple frames, captured using identical settings, to create an average image.

Digital Imaging

The pre-processing sequence is used to accumulate the individual, raw acquisition files into a compiled image, representative of the data set. This processing may be completed using a range of image analysis tools, however the size and number of images are best accommodated by a well planned processing algorithm. A standard tool in the digital image community, ImageJ features a wide range of prepackaged functions and algorithms. For larger jobs, or multiple experimental setups, the practical approach incorporates matrix based computing environments such as MATLAB or open source scripting languages such as Python™. The specific Python code to process the LISePix binary data files has been included in File S7.

Using the programmatic software approach can render a set of final images from hundreds or thousands of input frames without the need for manual user intervention. This strategy helps to minimize user input, code authoring redundancy and user error in large data set analysis. A digital image is defined by an $M \times N$

Supplement 7. "Timepix-image-preprocessor.zip" : Archive file contains Python class file and processing script to handle large data directories produced from LISePix neutron imaging experiments. The preprocessor extracts binary information and compiles the data into user ready averaged images. (*available online*)

array of intensity values, given in eq. (55) [235].

$$f(x,y) = \begin{bmatrix} f(1,1) & f(1,2) & \dots & f(1,N) \\ f(2,1) & f(2,2) & \dots & f(2,N) \\ \vdots & \vdots & \ddots & \vdots \\ f(M,1) & f(M,2) & \dots & f(M,N) \end{bmatrix} \tag{55}$$

The functional representation, $f(x,y)$, describes the intensity at each pixel location given by the indices, (x,y). The traditional matrix form may also be used and serves as an equivalent representation. Using the definition, $a_{ij} = f(x=i, y=j) = f(i,j)$, the matrix takes the form given in eq. (56) [235].

$$\mathbf{A} = \begin{bmatrix} a_{1,1} & a_{1,2} & \dots & a_{1,N} \\ a_{2,1} & a_{2,2} & \dots & a_{2,N} \\ \vdots & \vdots & \ddots & \vdots \\ a_{M,1} & a_{M,2} & \dots & a_{M,N} \end{bmatrix} \tag{56}$$

Dark Field

The dark field image captures the system response, fully powered and biased, without the radiation source or beam. This measurement will capture the electronic baseline, defined by the leakage current, also known as the dark current, along with any dead (non-responsive) or hot (fully saturated) channels. The dark field also serves as the initial operational check, ensuring the cabling, and readout electronics have been properly installed at the experiment site. If the device was damage, a cable is shorted, or the operational temperatures of the system are outside the normal parameters, the dark field measurement will show a non-radiation based response, indicating system malfunction.

Open Beam

The open beam image, also referred to as the white field, shows the characteristic response of the imaging system to a given radiation field. The name white field describes the image produced from capturing an unobstructed radiation source, returning a value approaching the saturation limit for all functioning pixels. Depending on the intensity of the radiation source, the acquisition is tailored to collect data that spans a significant portion of the dynamic system intensity range without over saturating the sensor. The open beam image is a convolution of the non-uniformities in the radiation beam and each sensor channel. As a neutron beam is moderated, redirected and filtered to a desired energy range, periodic banding will occur perpendicular to the beam. Furthermore, the output in a given channel to a detection event may vary across channels as a result of minor inhomogeneities during manufacturing. The subsequent acquisitions for the object image should ideally be repeated using identical operational settings, counting time, and averaging

frames.

Object Image

The object image is the last data set to be collected. The imaging target object should be a radiation absorber, removing a significant portion of the radiation flux to create a discernible change from the open beam response (*i.e.* contrast). While the object may be any article under investigation, it helps if the material has a uniform composition, or posses constituents with significantly varying levels of attenuation to enhance image contrast.

Process

The first pre-processing step averages each frame in a sequence into a single raw image file. For the most basic imaging experiment with a fixed acquisition time (or temporally normalized frames), this process reduces $K_{exp} = K_{DF} + K_{OB} + K_I$ frames into 3 mean images corresponding to the dark field, open beam, and object image. Each mean image, $\bar{f}(x, y)$, is created following eq. (57) from K frames in the set.

$$\bar{f}(x,y) = \frac{1}{K}\sum_{i=1}^{K} f_i(x,y)$$

$$\bar{f}(x,y) = \frac{1}{K}\sum_{i=1}^{K} \begin{bmatrix} f_i(1,1) & f_i(1,2) & \dots & f_i(1,N) \\ f_i(2,1) & f_i(2,2) & \dots & f_i(2,N) \\ \vdots & \vdots & \ddots & \vdots \\ f_i(M,1) & f_i(M,2) & \dots & f_i(M,N) \end{bmatrix} \tag{57}$$

The dark field typically requires only a few frames, K_{DF}, to capture the radiation independent electronic signal. The number of open beam frames, K_{OB}, will depend on the radiation source strength as well as the sensitivity of the detection system to the given radiation spectrum. As the experimental variable, the object image will generally require the largest number of frames, K_I, to ensure sufficient contrast between the open beam and attenuated signal from the object.

After averaging, the dark field is subtracted from both the open beam and the object images. This effectively reduces the image baseline intensity to zero, facilitating the normalization process. In most cases, the dark field will respond as a uniform gray value, however, dead and hot pixels will be resolved by this subtractive procedure. The baseline corrected object image is divided by the baseline corrected open beam image to produce the normalized experimental image. The resultant image is scaled between zero and one, with zero indicating non-beam areas and one corresponding to full beam view. By normalizing the object image to the open beam, any inconsistencies in the neutron flux should be removed from the final image.

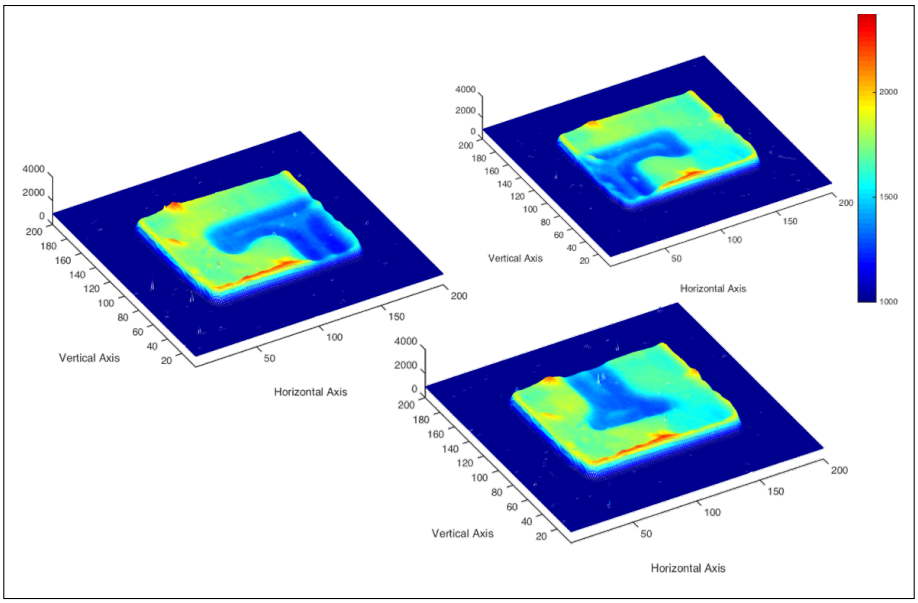


Figure C.1. Example of mosaic stitching technique using LISe scintillator with 3 positions [96].

C.2 Mosaic Stitching

When prototyping a new crystalline imaging material, the availability of sensor samples may be limited by growth experimentation. With each trial, the electronic quality of the single crystals improves, along with stochiometric refinement. However, in early sensor design, the available imaging area is limited, representing only a fraction of the boule cross-sectional area. This section details the mosaic stitching methodology applied to increase the effective area for smaller sensors, using multiple frames as seen in Figure C.1. As a scintillator, the LISe sensor was only able to capture a portion of the *Power-T* imaging target. Using, $K = 3$, different object positions, the full image is visible across the sensor active area, with a degree of overlap. It should also be noted that each of the K images are already cleaned and averaged from the raw acquisition, as described in Appendix C.1. First, eq. (58) determines the expanded matrix of size, $M^* \times N^*$, to span the increased image dimensions introduced by the largest image position shifts, Δx and Δy.

$$M^* = M + \max(\Delta x) \qquad N^* = N + \max(\Delta y) \tag{58}$$

In this example, the top left image sees a vertical shift, $\Delta y > 0$, the bottom center sees a horizontal shift, $\Delta x > 0$, and the top right requires both, $\Delta x > 0$ and $\Delta y > 0$. The expanded image, $f_i^*(x, y)$, is preallocated with a zero matrix to boost processing speed and ensure any unmapped values do not affect the final result. These image shifts are applied in eq. (59) where the pixel map incorporates a pixel sized shift across the image.

$$f_i^*(x, y) = f_i(x + \Delta x_i, y + \Delta y_i)$$

$$f_i^*(x,y) = \begin{bmatrix} f_i(1+\Delta x_i, 1+\Delta y_i) & f_i(1+\Delta x_i, 2+\Delta y_i) & \dots & f_i(1+\Delta x_i, N+\Delta y_i) \\ f_i(2+\Delta x_i, 1+\Delta y_i) & f_i(2+\Delta x_i, 2+\Delta y_i) & \dots & f_i(2+\Delta x_i, N+\Delta y_i) \\ \vdots & \vdots & \ddots & \vdots \\ f_i(M+\Delta x_i, 1+\Delta y_i) & f_i(M+\Delta x_i, 2+\Delta y_i) & \dots & f_i(M+\Delta x_i, N+\Delta y_i) \end{bmatrix} \tag{59}$$

Because the stitching process is based on an averaging function, the number of images used to average a pixel will range span $[1, K]$. While the images are being remapped to the expanded matrix, $f_i^*(x,y)$, an equivalent sized binary matrix, $g_i^*(x,y)$, is created to tally the locations containing active pixel data, as in eq. (60).

$$g_i^*(x,y) = \begin{bmatrix} \begin{cases} 0, & f_i^* = 0 \\ 1, & f_i^* > 0 \end{cases} & \dots & \begin{cases} 0, & f_i^* = 0 \\ 1, & f_i^* > 0 \end{cases} \\ \vdots & \ddots & \vdots \\ \begin{cases} 0, & f_i^* = 0 \\ 1, & f_i^* > 0 \end{cases} & \dots & \begin{cases} 0, & f_i^* = 0 \\ 1, & f_i^* > 0 \end{cases} \end{bmatrix} \tag{60}$$

The finalized stitched mosaic image, $h(x,y)$, is formed from dividing the summed expanded image, $F^*(x,y)$, by the summed counting matrix, $G^*(x,y)$, as seen in eq. (61).

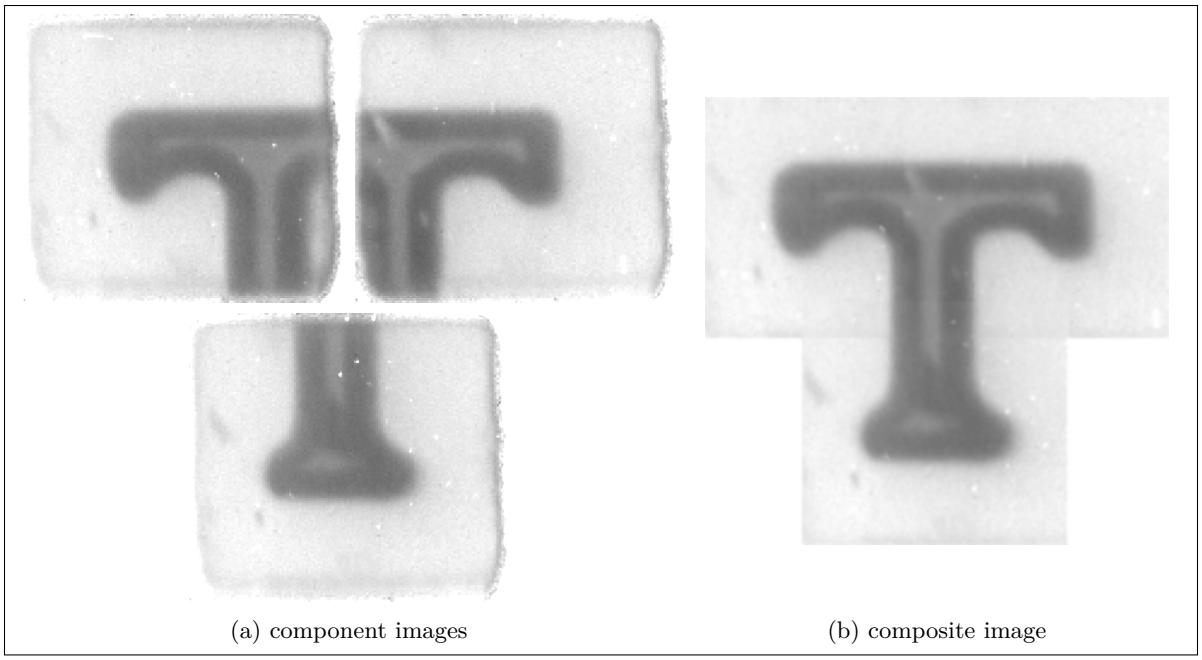
$$h(x,y) = F^*(x,y) \cdot [G^*(x,y)]^{-1}$$

$$h(x,y) = \sum_{i=1}^{K} f_i^*(x,y) \cdot \left[\sum_{i=1}^{K} g_i^*(x,y) \right]^{-1} \tag{61}$$

This process is visually demonstrated in Figure C.2. The end result is an image spanning an area larger than the original sensor, while maintaining feature contrast and spatial resolution across overlapping regions. It should also be noted the edges of sensor area were cropped to produce a perfect rectangular area, before stitching. Leaving the as-cut sensor outline created artifacts due to inconsistent averaging across those pixels. These edge pixels have varying response due to multiple factors: large surface roughness at the edge interface, scattering at sharp crystal edges, inconsistent material thickness, light escaping from the side of the sensor, etc. The cropping was conducted iteratively, removing only enough rows and columns to eliminate the sporadic averaging.

C.3 Super-Sampling

Radiographic image super-sampling outlines a technique to provide enhanced image resolution in a few channel pixel detector, or a pixel pitch limited device. In the early LISe semiconductor systems, the device



(a) component images (b) composite image

Figure C.2. Normalized component neutron images used to create the composite *Power-T* neutron image (LISe scintillator) [96] (see Figure 4.2b).

functioned as a counter (single channel) or a 16-channel pixel detector. With such few channels, any decrease in pixel size to enhance resolution would result in a subsequent decrease in pixel active area.

To overcome this limitation, larger pixels of pitch, $P_x \times P_y$, were used to maximize coverage area and conform to the dimensional requirements for wirebonding. In the experimental setup, the imaging target was translated in both directions perpendicular to the beam axis, sweeping across the sensor active area. By sub-stepping the target at intervals smaller than the pixel pitch, $P_u \times P_v$, each pixel captures a averaged response corresponding to the region of the target in front of the pixel. Plotting the response for each channel, shown in Figure C.3, demonstrates the ability of a single physical pixel to resolve an image using precise target manipulation. For a single acquisition position, the sensor will capture data for the physical $M_0 \times N_0$ pixels, producing the base image, $f(x, y)$, given by eq. (62).

$$f(x,y) = \begin{bmatrix} f(1,1) & f(1,2) & \dots & f(1,N_0) \\ f(2,1) & f(2,2) & \dots & f(2,N_0) \\ \vdots & \vdots & \ddots & \vdots \\ f(M_0,1) & f(M_0,2) & \dots & f(M_0,N_0) \end{bmatrix} \tag{62}$$

The matrix is also shown as a series of indexed pixels, each channel, f_i, assigned an integer value spanning

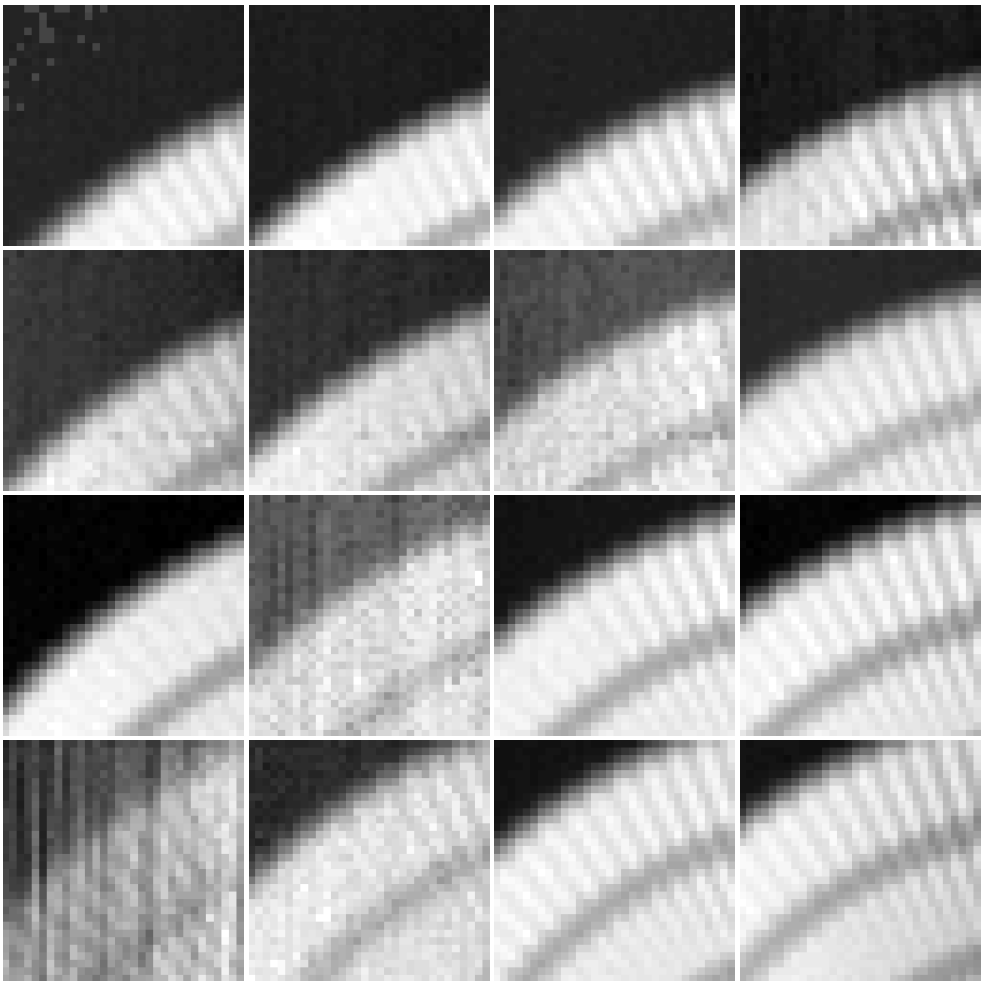


Figure C.3. Mosaic of individual pixel images after super-sampling LISe PD. Images used to generate composite image of the Siemens Star [145].

$[1, M_0 N_0]$ in eq. (63).

$$f(x,y) = \begin{bmatrix} f_1 & f_2 & \cdots & f_{N_0} \\ f_{N_0+1} & f_{N_0+2} & \cdots & f_{2N_0} \\ \vdots & \vdots & \ddots & \vdots \\ f_{(M_0-1)\cdot N_0+1} & f_{(M_0-1)\cdot N_0+2} & \cdots & f_{M_0 N_0} \end{bmatrix} \tag{63}$$

As previously mentioned, the few channel image suffers from poor resolution as a result of maximizing the pixel pitch. Instead, the intensity value, f_i, from each physical pixel will be recorded as a single virtual pixel, $f_i(u,v)$, of size, $P_u \times P_v$, spanning the $M \times N$ sub-steps, shown in eq. (64).

$$f_i(u,v) = \begin{bmatrix} f_i(1,1) & f_i(1,2) & \cdots & f_i(1,N) \\ f_i(2,1) & f_i(2,2) & \cdots & f_i(2,N) \\ \vdots & \vdots & \ddots & \vdots \\ f_i(M,1) & f_i(M,2) & \cdots & f_i(M,N) \end{bmatrix} \tag{64}$$

Each virtual image will be offset, Δu and Δv, along the respective direction for the stitching process, shown in eq. (65a).

$$\Delta u = \frac{P_x}{P_u} \cdot (x-1) \qquad \Delta v = \frac{P_y}{P_v} \cdot (y-1) \tag{65a}$$

$$\Delta u = \frac{P_x}{p_u} \cdot (x-1) \cdot C \qquad \Delta v = \frac{P_y}{p_v} \cdot (y-1) \cdot C \tag{65b}$$

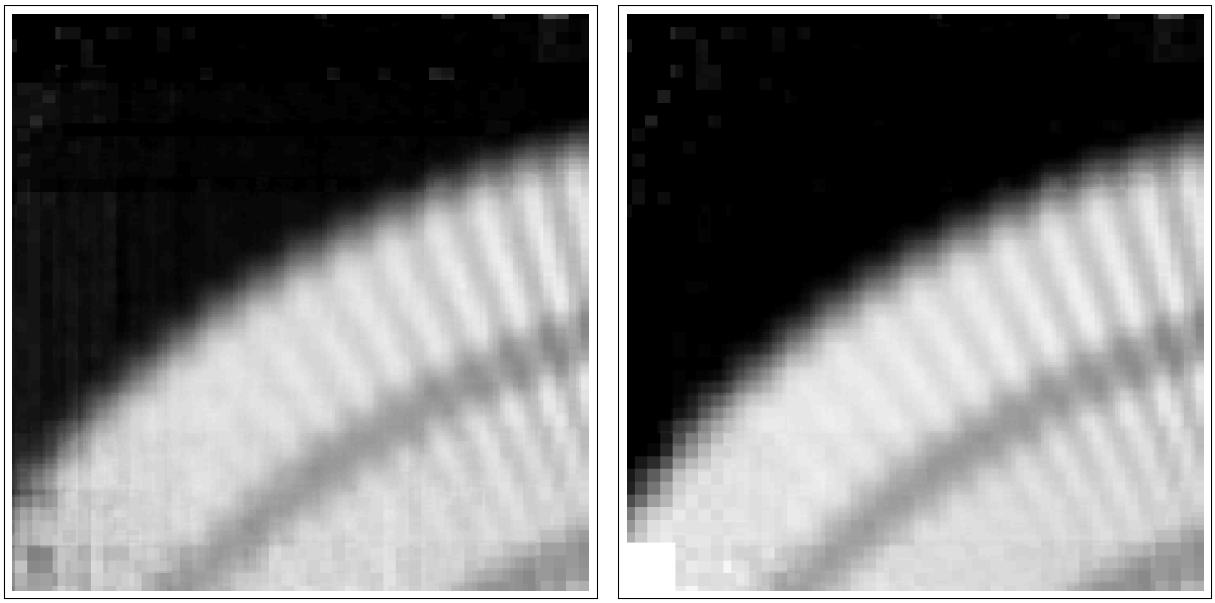
If the fractions, P_x/P_u or P_y/P_v, do produce integer quotients, a constant value, C, is introduced in eq. (65b), further sub-dividing each virtual pixel into sub-pixels of size, $P_u/C \times P_v/C$. The expanded matrix size, $M^* \times N^*$, takes a similar form as eq. (58), shown here as eq. (66a) and eq. (66b), depending on the sub-division of the virtual pixels.

$$M^* = M + \max(\Delta u) \qquad N^* = N + \max(\Delta v)$$

$$M^* = M + \frac{P_x}{P_u} \cdot (M_0 - 1) \qquad N^* = N + \frac{P_y}{P_v} \cdot (N_0 - 1) \tag{66a}$$

$$M^* = M + \frac{P_x}{P_u} \cdot (M_0 - 1) \cdot C \qquad N^* = N + \frac{P_y}{P_v} \cdot (N_0 - 1) \cdot C \tag{66b}$$

The virtual images from each physical pixel are mapped to the larger composite image space. The remapping



(a) (b)

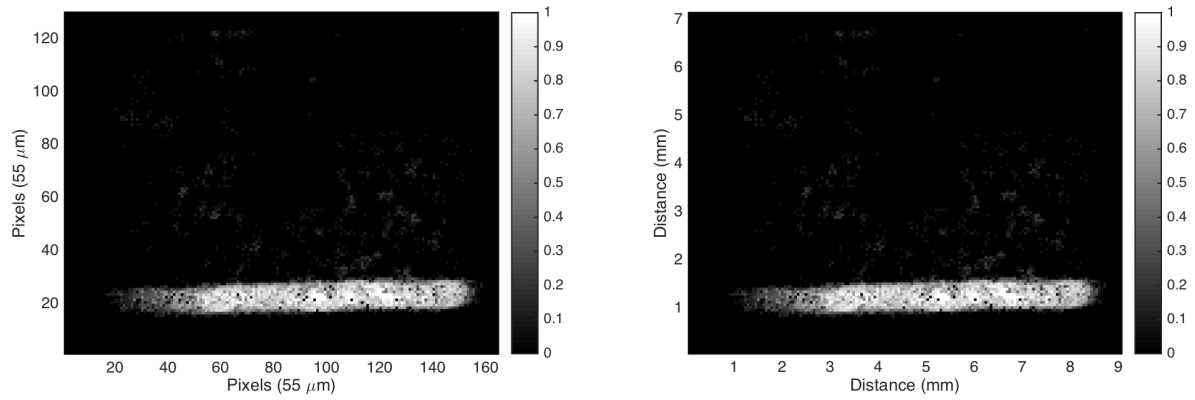
Figure C.4. Composite image of Siemens Star using super-sampling technique (see Figure 4.13).

image function is given by, $f_i^*(u,v)$, as seen in eq. (67).

$$f_i^*(u,v) = f_i(u + \Delta u_i, v + \Delta v_i)$$

$$f_i^*(u,v) = \begin{bmatrix} f_i(1+\Delta u_i, 1+\Delta v_i) & f_i(1+\Delta u_i, 2+\Delta v_i) & \dots & f_i(1+\Delta u_i, N+\Delta v_i) \\ f_i(2+\Delta u_i, 1+\Delta v_i) & f_i(2+\Delta u_i, 2+\Delta v_i) & \dots & f_i(2+\Delta u_i, N+\Delta v_i) \\ \vdots & \vdots & \ddots & \vdots \\ f_i(M+\Delta u_i, 1+\Delta v_i) & f_i(M+\Delta u_i, 2+\Delta v_i) & \dots & f_i(M+\Delta u_i, N+\Delta v_i) \end{bmatrix} \tag{67}$$

Using this image function, the final composite image is produced following eq. (60) and eq. (61). The response from each channel noticeably varies, attributed to inconsistencies in electronic coupling at the contact-wirebond interface. If the wirebond disrupts the thin film metal contact on the sensor surface, subsequently the electrical field through that cross-section of the sensor will also be distorted. This affects both the charge transport properties as well as the signal formation on the contact surface for the affected pixel. The composite image may be formed from all, or a subset of available channels to enhance the final image, as shown in Figure C.4. Numbering the channels from left to right and top to bottom, channels 7, 10, and 12 were omitted to generate Figure C.4b. This comparison shows the minor improvement obtained by eliminating poor performing channels. The lower left region more clearly resolves the last couple of line pairs, however a pixel sized blank space exists having removed the edge pixel. Both images show nearly



(a) index scaling (55 µm pixels) (b) metric scaling

Figure C.5. Raw image after dark field subtraction and open beam normalization.

identical right halves, resolving the same line pair resolution based on visual inspection.

C.4 Modulation Transfer Function

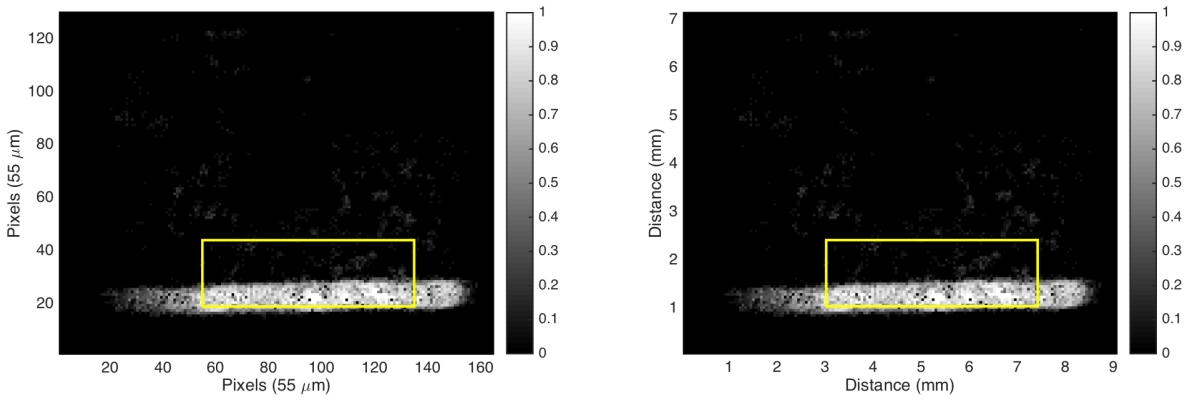
The MTF calculation provides an analytical technique for evaluating spatial resolution of imaging systems. As applies to radiography, a detector captures a sharp edge of radiation absorbing material. The sudden shift from open beam radiation to heavily attenuated radiation provides a means of characterizing the sharpness of the system. Furthermore, the analysis accounts for resolution limits imposed by the pixel size of the sensor. The general applicability across a range of sensor materials and operating modes allows direct comparison of ultimate system performance when testing prototype detectors.

C.4.1 Analytical Methods

This section will cover the numerical analysis implemented using MATLAB. The calculation methodology has been designed as an automated program, minimizing user inputs and harnessing built in MATLAB scripts where possible. The resulting algorithm produced the computed resolution value and the series of output images documenting the analysis.

Base Image

The base image served as the input matrix, $(M \times N)$, for the MTF calculator after pre-processing, as described in Appendix C.1. Along with the pixel size, S_{pix}, and selected region of interest, the calculation process is automated to generate reliable, repeatable results. The first processing step comprises plotting the raw intensity data in both pixel and distance axes to ensure proper pre-processing. The pixel size is used to scale the input data (Figure C.5), providing a usable output value from the MTF curve. If the edge



(a) index scaling (55 µm pixels)

(b) metric scaling

Figure C.6. Raw image with ROI overlay shown by yellow outline ($x = [55, 135]$, $y = [19, 44]$).

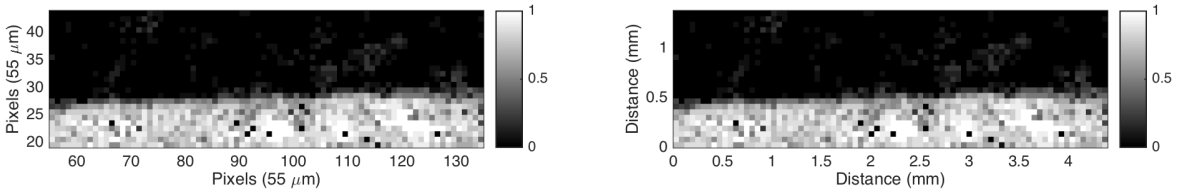
profile is aligned parallel to the horizontal pixel rows, the calculated resolution value would be lower limited by the pixel size. For this reason, a slight angle is introduced during the experiment to create an edge profile spanning multiple pixel rows.

Region of Interest

The user specified ROI captures an area that roughly splits the edge profile between open beam and attenuated sections. To preserve the fidelity of the calculation, this region should be exclusive of image artifacts or sensor dead zones (Figure C.6). The ROI is cropped to the specified area ($m \times n$), reducing the data size and accelerating the calculation processing time. The smaller image area (Figure C.7) more clearly depicts the edge profile angle. Increasing the data index, perpendicular to the edge profile, benefits the analytical process without contaminating the data. As a smoothing algorithm, interpolation prevents artificial edge sharpening as seen in the 10× gain image ($m \times n^*$) shown in Figure C.7c and Figure C.7d. The increased sampling rate benefits the subsequent alignment and differentiation steps. Furthermore, the extra data points will not change the overall shape of the final MTF curve but will provide more points to accurately estimate the 10 % threshold.

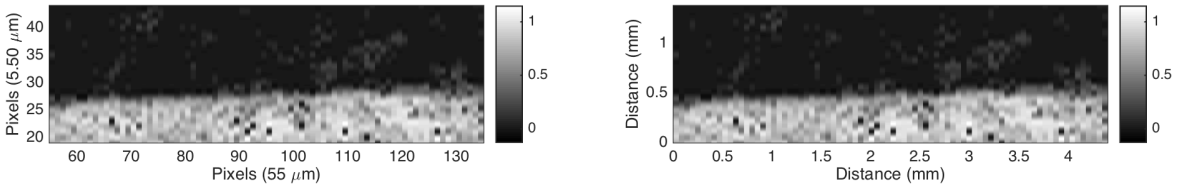
Edge Detection

The first step in the edge detection process applies the Canny edge detector to the cropped ROI [236], generating the binary image shown in Figure C.8. The Canny edge detection algorithm is automated as a MATLAB function, but may be generalized to 4 individual steps common among software packages. Step (1) reduces the image noise by preprocessing with a Gaussian filter, typically 5×5 in size. In step (2), a Sobel kernel is applied along both directions to evaluate the intensity gradients and associated angle for each pixel [201]. Step (3), suppresses all non-maximum pixels, effectively determining if a pixel falls along



(a) index scaling with 55 µm pixels

(b) metric scaling



(c) index scaling with 10× oversampling

(d) metric scaling with 10× oversampling

Figure C.7. ROI image crop and oversampling perpendicular to edge.

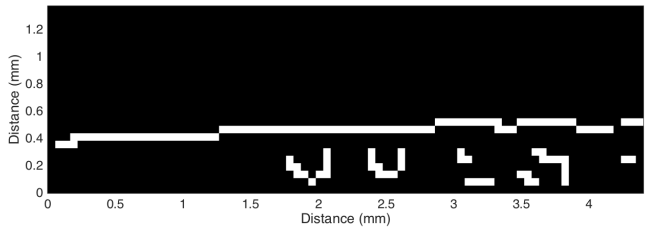


Figure C.8. Canny edge detector applied to the interpolated ROI image, creating a binary image displaying the shallow angle edge profile.

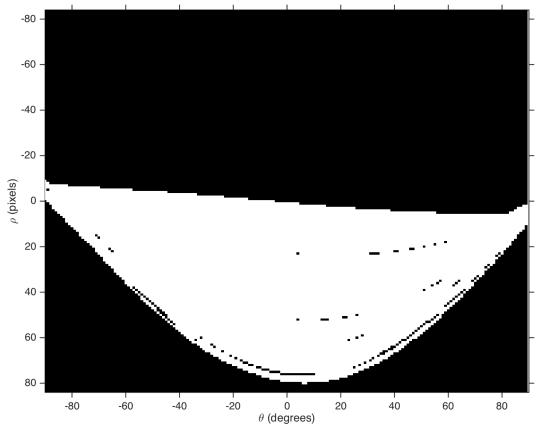


Figure C.9. Hough transform applied to binary edge profile to extract line angle.

the edge based on its gradient direction and magnitude compared to neighboring pixels. The final step (4) applies thresholding hysteresis to extend pixels that fall along an edge, effectively creating a binary image of only the pixels forming edge lines.

The Hough transform has been implemented in a vast range of image processing methods to detect lines or edges in image data [237, 238]. To evaluate colinear points in a sample image, the location of each Cartesian point can be represented by the Hesse normal form eq. (68).

$$\rho_i = x\cos(\theta_i) + y\sin(\theta_i) \tag{68}$$

The length, ρ_i, of the line from the origin to the perpendicular intersection at point position, (x, y), depends on the angle, θ_i, between the line and the x-axis. The image is sampled across the range, $-90° \leq \theta_i < 90°$, and non-zero entries are calculated and tallied, shown in Figure C.9. The Hough transform function returns a simple data set in this instance, because the input is a binary, few line image. The transform data is evaluated to find the data peak, indicating the primary edge angle used in the alignment process.

Edge Spread Function

After interpolation, the region of interest is flattened by plotting the edge profile, perpendicular to the edge axis, as a function of distance. Shown in Figure C.10, the edge profile demonstrates varying intensity in both white field and dark field regions. Furthermore, the edge profile has a distinguishable width due to the edge angle imparted by the experimental setup. Some vertical banding can be seen as an artifact of the finite interpolation gain. For each interpolated edge profile, i, the edge angle, θ, can be removed by offsetting the distance vector, d_i, using the calculated value from the Hough transform and the total distance along the edge axis, x_i (eq. (69)).

$$d(i) = y_0(i) - y_{offset}(i)$$

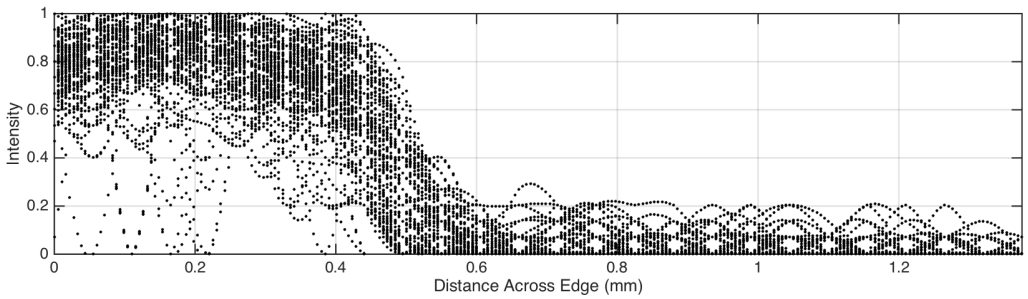


Figure C.10. ESF for each vector showing raw position.

$$d(i) = y_0(i) - x(i)\tan(\theta) \tag{69}$$

The resulting edge profile, Figure C.11, shows a narrower edge transition and no longer has clear banding from the interpolation process. The aligned ESF still exhibits varying intensity in the dark field and more prominently in the white field regions, due to varying pixel performance and inconsistencies in the open beam. The distance vectors no longer correspond to the original binning after the alignment process. Thus, the ESF curves are rebinned using the sampling rate in the raw ESF profile, generating the averaged ESF profile shown in Figure C.12. The averaged ESF exhibits a significantly smoother white field as well as the dark field region. The edge transition region also follows a smoother slope, benefiting the differentiation process. After calculating the LSF, the edge inflection point was determined and the centered ESF plotted in Figure C.13.

Line Spread Function

The ESF is differentiated using a MATLAB function implementing a first order numerical approximation. Increasing the sampling rate by interpolating the raw ESF profiles helps to smooth the differentiation approximation. The value for the LSF at each index, L_i, is calculated from the difference between the corresponding ESF element, E_i, and the following value, E_{i+1}, as in eq. (70).

$$L_i = E_{i+1} - E_i \quad for \quad 1 \leq i \leq n-1 \tag{70}$$

For an ESF curve containing n points, the resulting LSF curve will have a length of $n-1$. A simple correction can be made by appending the final value, E_n, to the original vector, extending the length of the LSF without affecting the final result. The resultant, raw LSF curve is shown in Figure C.14. The raw LSF is normalized to the peak maximum, scaling the data to the intensity range $y = [0, 1]$. A Gaussian fit calculates the peak position as shown in Figure C.15. The peak position is measured from the origin, giving the approximate offset required to center the LSF. This value results in the centered LSF as shown in Figure C.16, along with the previous Figure C.13. For the MTF calculation, ideally the LSF tails should approach zero, indicating a

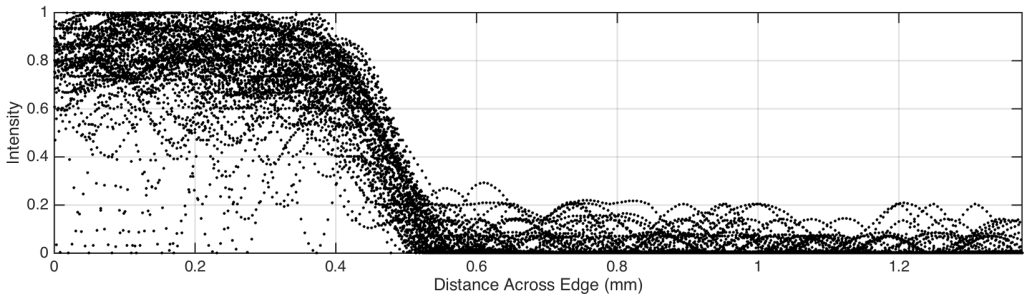


Figure C.11. ESF after edge angle correction using value calculated with Hough transform.

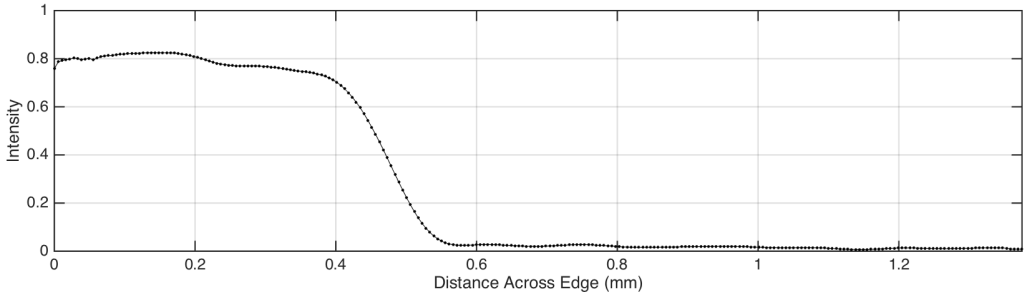


Figure C.12. Averaged ESF.

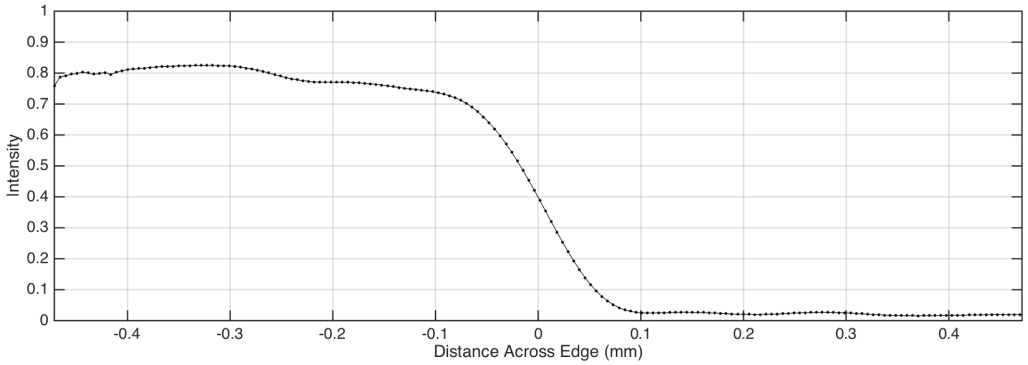


Figure C.13. ESF centered about inflection point.

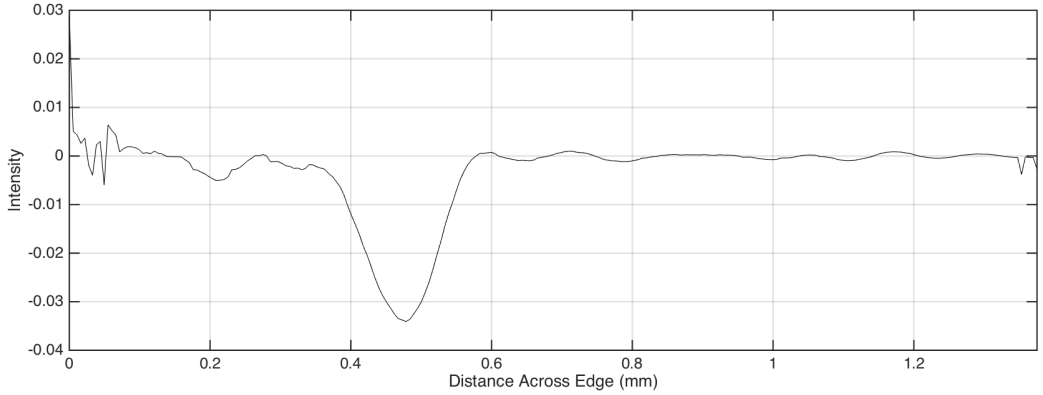


Figure C.14. Raw LSF after numerical differentiation of the ESF.

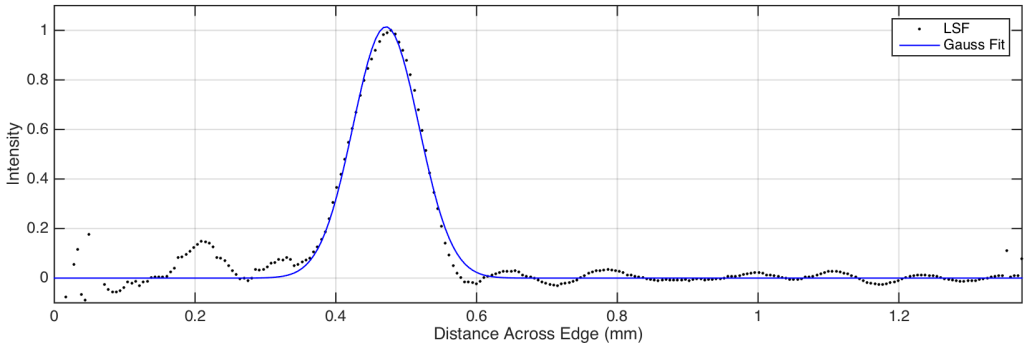


Figure C.15. LSF normalized to edge spread peak with location found from Gaussian fit.

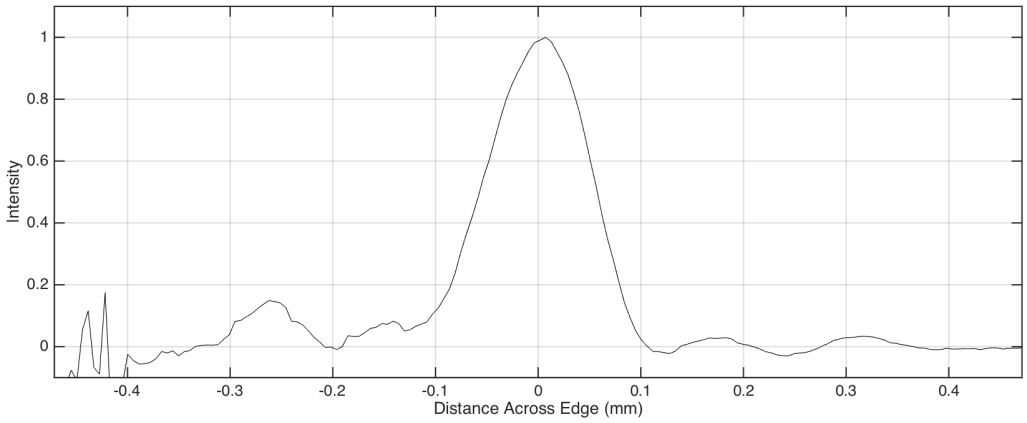


Figure C.16. LSF centered about inflection point.

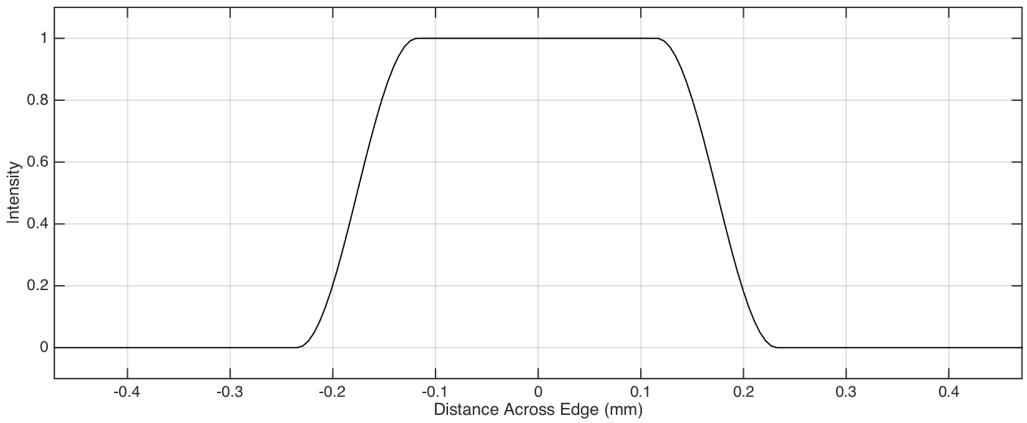


Figure C.17. Tukey window with $\alpha = 0.5$ and $N = 0.5N_{LSF}$.

uniform white or dark field region. The extraneous intensity fluctuations near the tails will contaminate the MTF curve once converted to frequency space. Applying a window function is useful in preserving the LSF peak data, while minimizing the tail information. For a given window size of N points, the most generic function is the rectangular window, given by eq. (71).

$$w(n) = 1 \quad for \quad 0 \leq n \leq N-1 \tag{71}$$

Effectively passing data within this window preserves the value, while points outside the window are zeroed. Another type of window uses a cosine shape to reduce the function value to zero at the edge of the tails. The basic form of the Hann window is given in eq. (72), producing a single lobe of a raised cosine function.

$$w(n) = \frac{1}{2}\left[1 - \cos\left(\frac{2\pi n}{N-1}\right)\right] = \sin^2\left(\frac{\pi n}{N-1}\right) \quad for \quad 0 \leq n \leq N-1 \tag{72}$$

The Tukey window provides a modified version of the Hann window by combining it with the standard rectangular function. The window shape depends on the parameter, α, indicating the percentage of the window width corresponding to the cosine component as in eq. (73).

$$w(n) = \begin{cases} \frac{1}{2}\left[1 + \cos\left(\frac{2\pi n}{\alpha(N-1)} - \pi\right)\right] & 0 \leq n < \frac{\alpha(N-1)}{2} \\ 1 & \frac{\alpha(N-1)}{2} \leq n \leq (N-1)(1-\frac{\alpha}{2}) \\ \frac{1}{2}\left[1 + \cos\left(\frac{2\pi n}{\alpha(N-1)} - \frac{2\pi}{\alpha} + \pi\right)\right] & (N-1)(1-\frac{\alpha}{2}) < n \leq (N-1) \end{cases} \tag{73}$$

For the MTF calculator, the Tukey window maintains $\alpha = 0.5$, splitting the cosine and rectangular regions equally. The length of the window is defined as half the length of the LSF as shown in Figure C.17. Multiplying the centered LSF by the modified Tukey window provides a cleaned input for the MTF process.

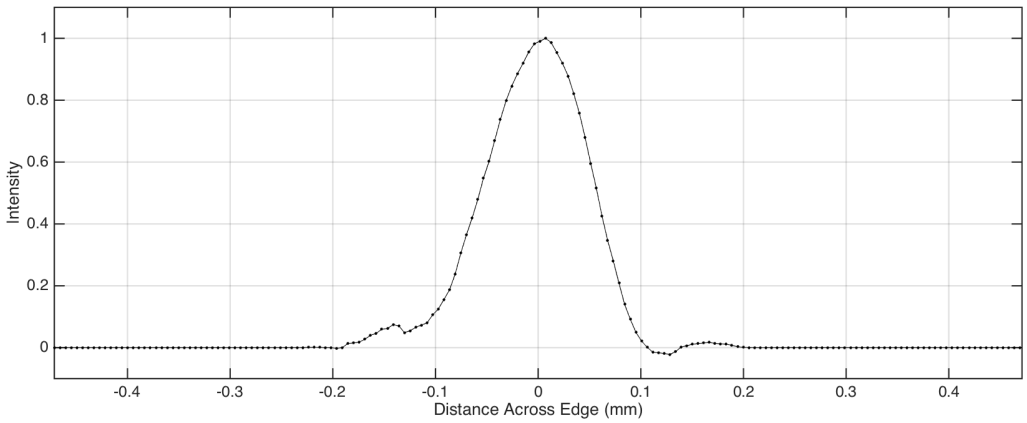


Figure C.18. LSF after applying Tukey window.

The tails have been significantly tapered while maintaining an unchanged differentiated edge peak as shown in Figure C.18. At this point, the LSF is fully processed, providing a smooth edge profile with a Gaussian shape. The curve represents sensor data in the spatial domain and needs to be converted to the frequency domain to assess the spatial resolution limit.

Modulation Transfer Function

The continuous Fourier transform (CFT), $F(\omega)$, follows the integral shown in eq. (74) for a continuous spatial function, $f(x)$.

$$F(\omega) = \int_{-\infty}^{\infty} f(x) e^{-j\omega x} dx \tag{74}$$

The forward discrete Fourier transform (DFT), $f[k]$, assumes the continuous spatial function is sampled across N data points, spaced X apart as seen in eq. (75).

$$F(\omega) = \sum_{k=0}^{N-1} f[k] e^{-j\omega kX} \tag{75}$$

In the physical experiment, data is assumed periodic, evaluated at the frequency, ω, and its harmonics given by eq. (76).

$$\omega = 0, \frac{1}{NX}, \frac{2}{NX}, \ldots, \frac{n}{NX}, \ldots, \frac{(N-1)}{NX} \tag{76}$$

The sampling spacing, X, is defined by the interpolation gain, G, and the pixel size, S_{pix}, to yield meaningful results as in, eq. (77).

$$X = \frac{2G}{S_{pix}} \tag{77}$$

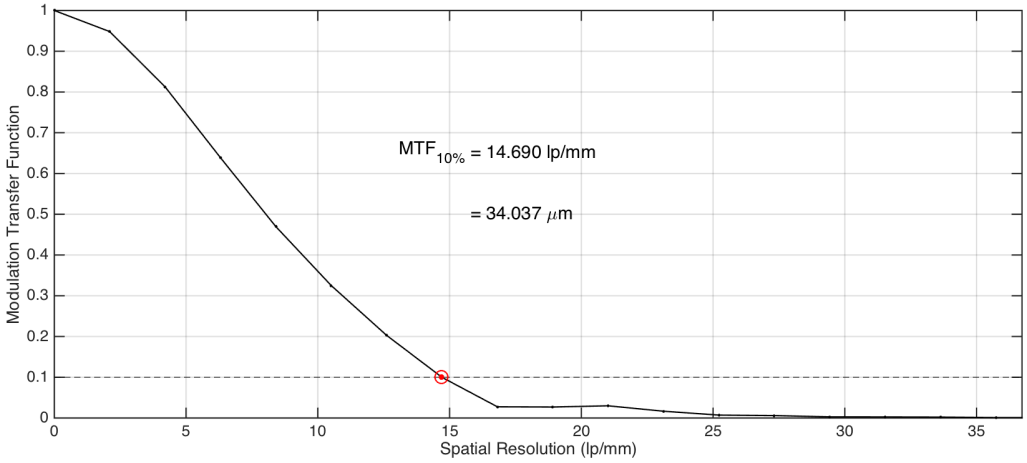


Figure C.19. MTF curve with evaluated resolution marked by 10% cutoff limit.

Substituting into eq. (75) yields the form used for the MTF process, eq. (78), which is properly scaled to units of line pairs per millimeter (lp/mm).

$$F[n] = \sum_{x=0}^{N-1} f[k] e^{-j(n/NX)k} \tag{78}$$

The MTF is normalized to the maximum value, typically the value at the zero frequency, spanning a range of $y = [0, 1]$. The resolution parameter is evaluated by fitting a spline to the MTF curve and evaluating the abscissa for a 10 % MTF cut-off value, shown in Figure C.19. The MTF calculator script plots the final curve with the spatial resolution displayed in values of line pairs per millimeter as well as the converted micron resolution value for the edge.

C.4.2 MTF Calculator

The MTF calculator program (see File S8) comprises a series of MATLAB scripts to process an image file, evaluating the edge resolution parameter. The main script file is run from the root directory. Function source files are stored in the "/functions" subdirectory. The raw images, saved in tagged image file format (TIFF) file format, are stored in the "/inputs" subdirectory. The individual raw images are pre-processed in an external image software such as ImageJ. All figure files generated from the script are saved in the "/outputs" subdirectory, in portable network graphic (PNG) format.

Supplement 8. "MTF-calculator.zip" : Archive file contains directory structure for MATLAB based MTF calculator script. The program includes numerical assessment and plotting functionality. (*available online*)

main.m

This script serves as the user defined input file and the active run. The calculator requires 3 input variables: the file name to select the image, the device pixel size for scaling the output plots, and the region of interest to crop the raw image.

```
%% Startup
clc;
clear;
format shortg;

%% Set Image Parameters
file_name = 'slit_750um.tif';% input image
pixel_size = 0.055;% mm
region_of_interest = [55,135,19,44];% pixel

%% Process MTF
calculate_mtf( file_name, pixel_size, region_of_interest, false );
```

calculate_mtf.m

This script is the primary function controlling the calculation. The manipulated data exists in the scope of this function, with subfunctions being called to perform specific operations on the data. After processing the data, all figures are sequentially generated at the end of the function. The individual subfunctions have been included in File S8, with their methods detailed in the previous Appendix C.4.1.

```
function calculate_mtf( arg_file, arg_size, arg_roi, arg_vertical )

%% Input Arguments
if nargin < 4
    arg_vertical = true;
end

%% Setup File Structure
FOLDER = get_FOLDER();
INPUT = get_INPUT( arg_file, FOLDER );
OUTPUT = get_OUTPUT( FOLDER, INPUT );

%% Process Data
IMG = get_IMG( INPUT );
IMG = set_scale( IMG, arg_size );
IMG = set_roi( IMG, arg_roi );
```

```
17 IMG = crop_IMG( IMG );
18 IMG = interpolate_IMG( IMG, arg_vertical );
19
20 IMG = find_edge( IMG );
21 IMG = get_ESF( IMG );
22 IMG = sort_ESF( IMG );
23 IMG = get_LSF( IMG );
24 IMG = center_LSF( IMG );
25 IMG = apply_window( IMG );
26
27 IMG = get_MTF( IMG );
28
29 %% Generate Output Figures
30 for i = [1:22]
31     plot_figure(i,IMG,OUTPUT);% GOT NEUTRONS?
32 end
33
34 end
```

Appendix D

Nuclear Cross Sections

This appendix includes neutron cross section plots for reference. The individual isotopes use the microscopic cross sections following the Evaluated Nuclear Data File (ENDF) library [45]. The cross sections for LISe and its constituent elements have also been included, calculated from the ENDF data for individual isotopes [239, 240].

D.1 Neutron Sensitive Isotopes for Detection and Imaging

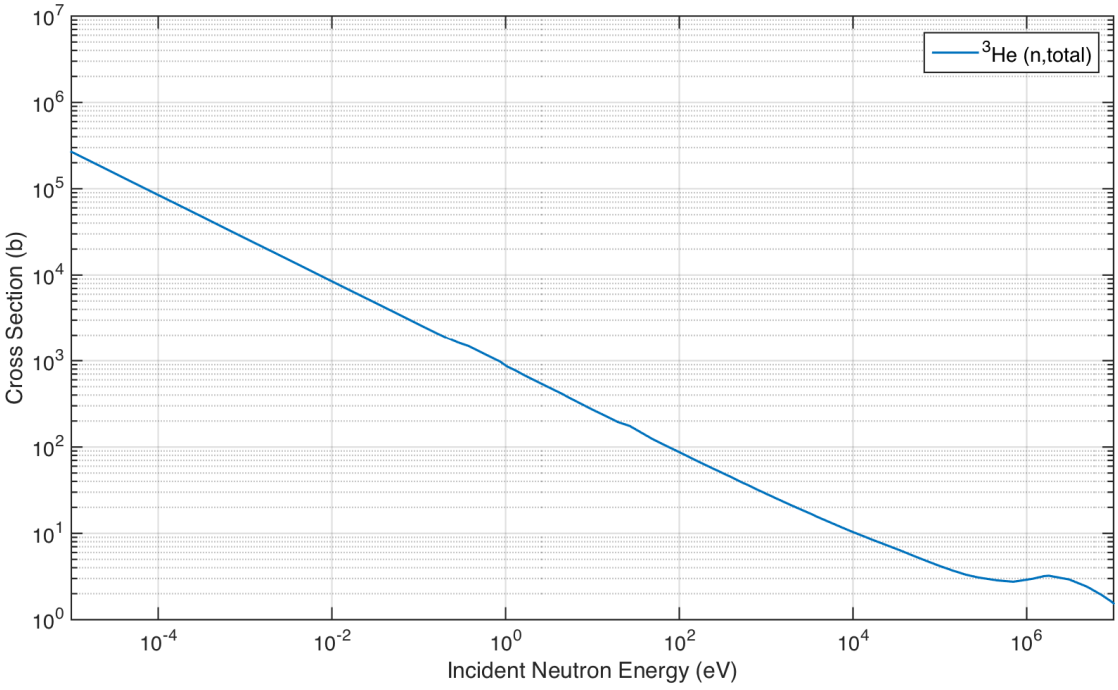


Figure D.1. Total neutron cross section for ^{3}He ($a/o = 0.000134\,\%$).

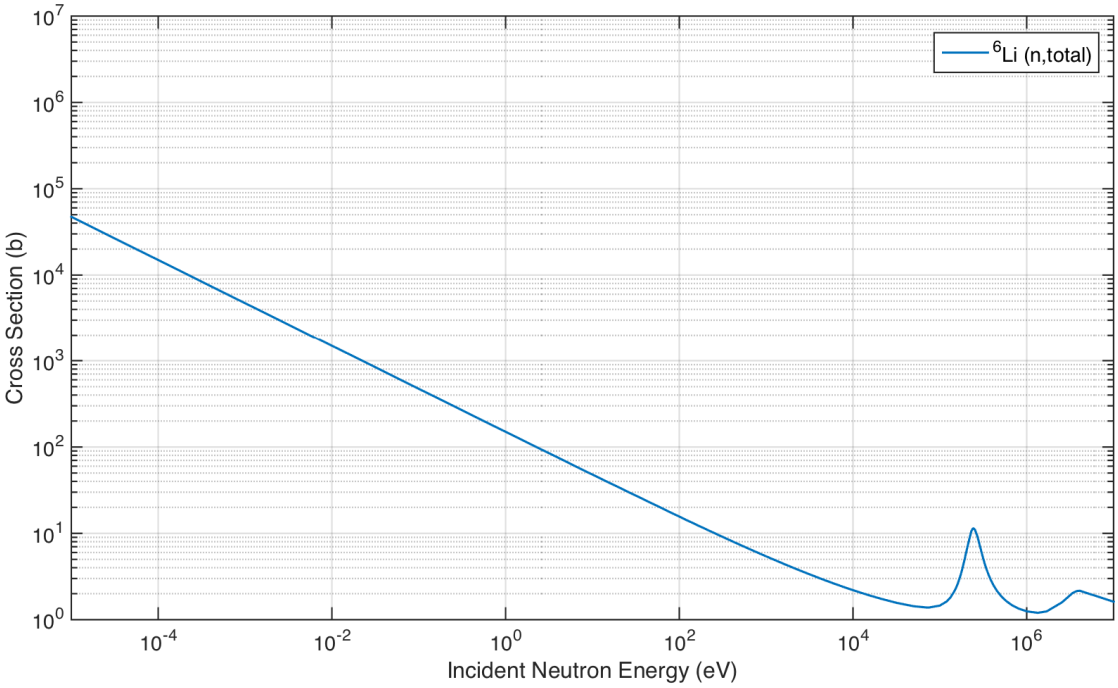


Figure D.2. Total neutron cross section for ^{6}Li ($a/o = 7.59\,\%$).

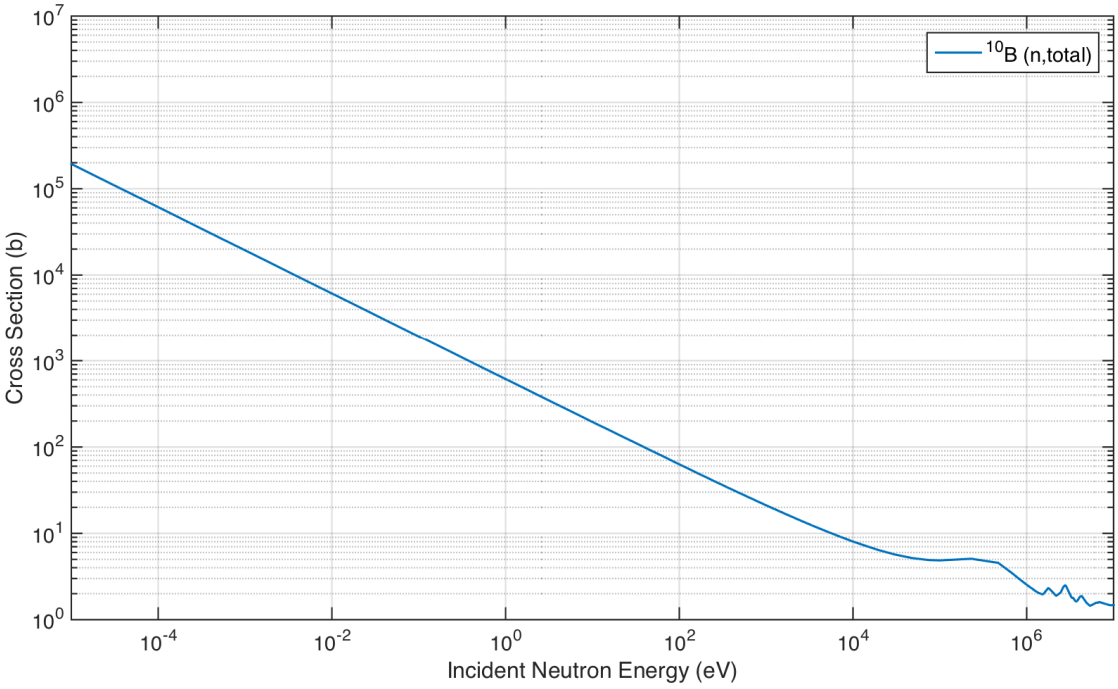


Figure D.3. Total neutron cross section for ^{10}B ($a/o = 19.9\,\%$).

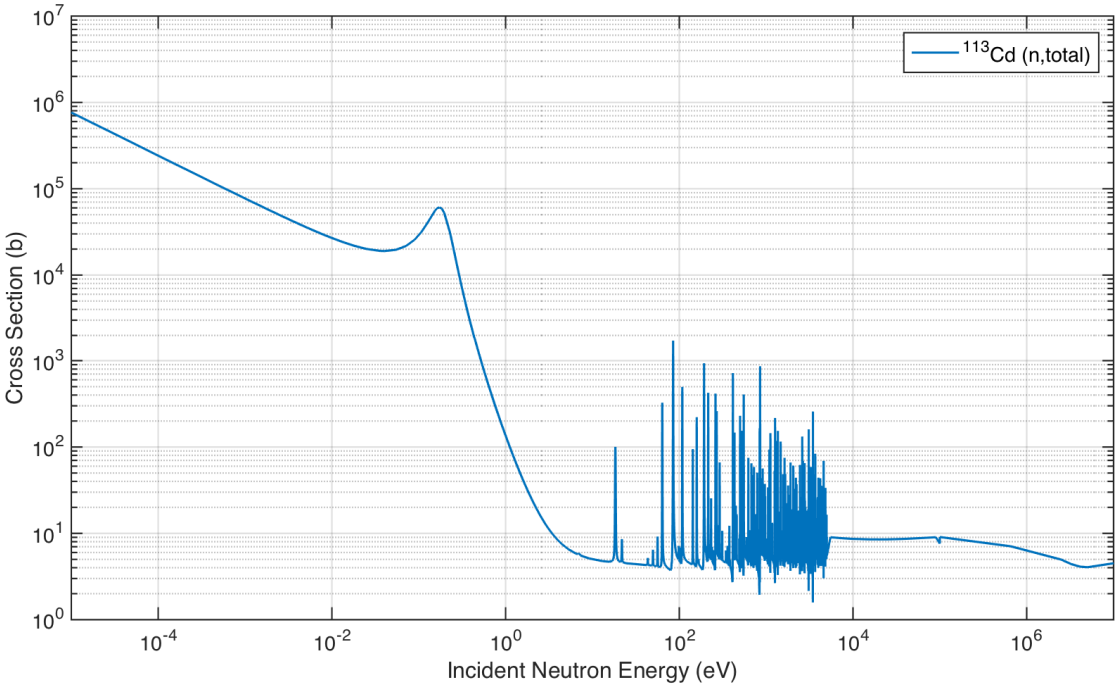


Figure D.4. Total neutron cross section for ^{113}Cd ($a/o = 12.22\,\%$).

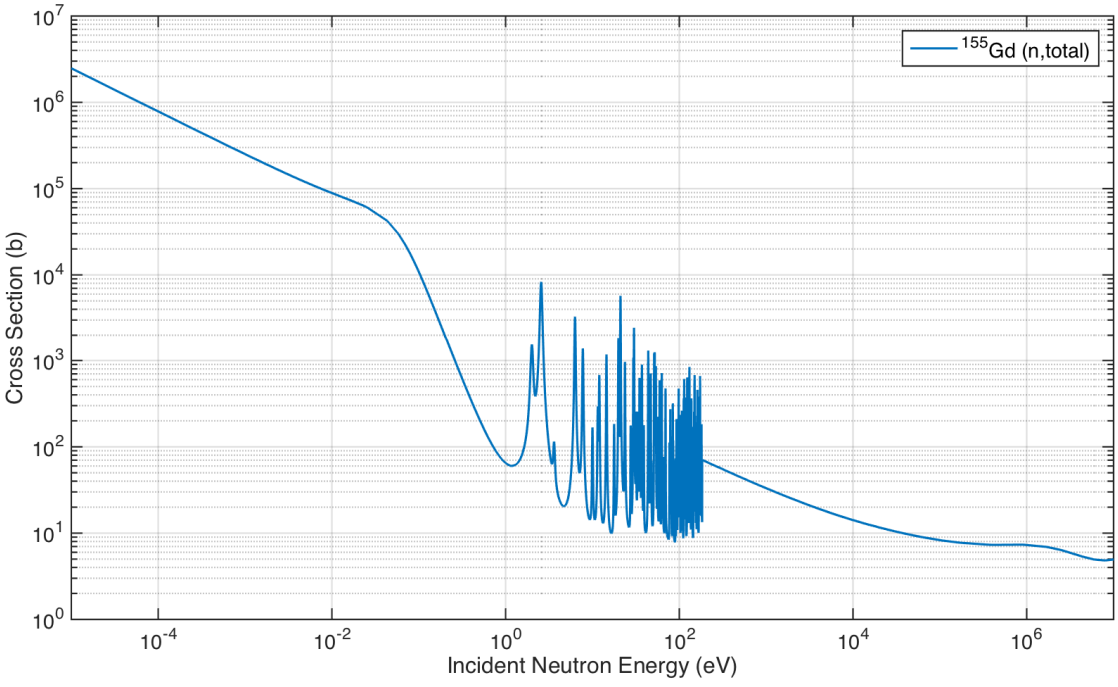


Figure D.5. Total neutron cross section for ^{155}Gd ($a/o = 14.80\,\%$).

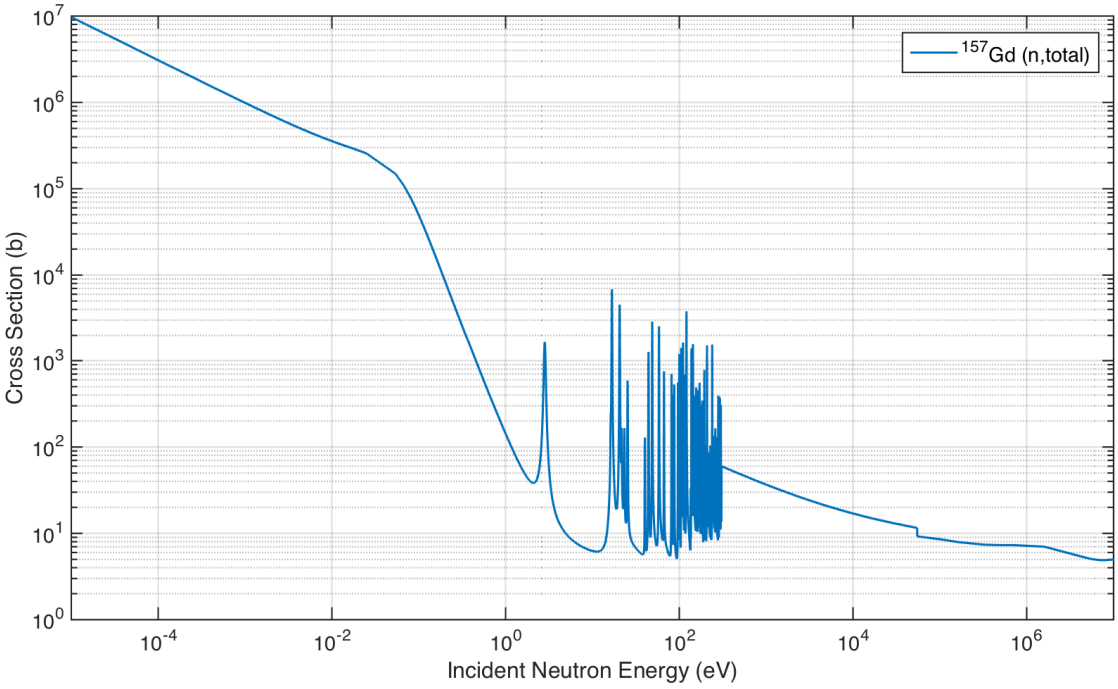


Figure D.6. Total neutron cross section for ^{157}Gd ($a/o = 15.65\,\%$).

D.2 Lithium Indium Diselenide

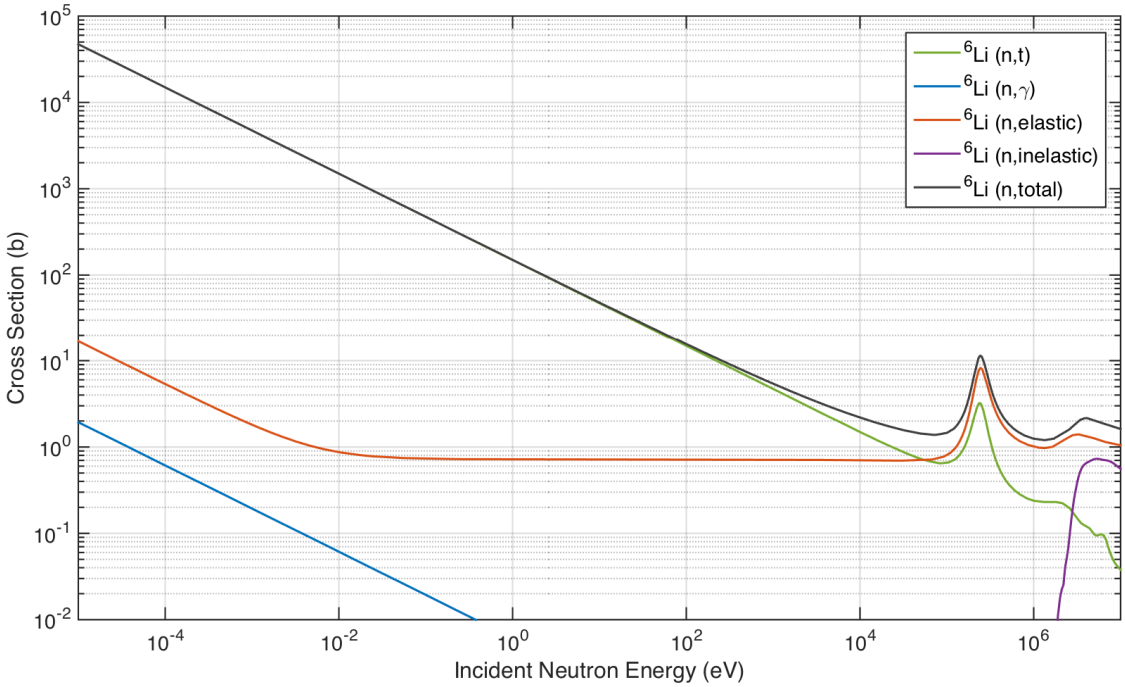


Figure D.7. Selected neutron cross sections for ^{6}Li ($a/o = 7.59\,\%$).

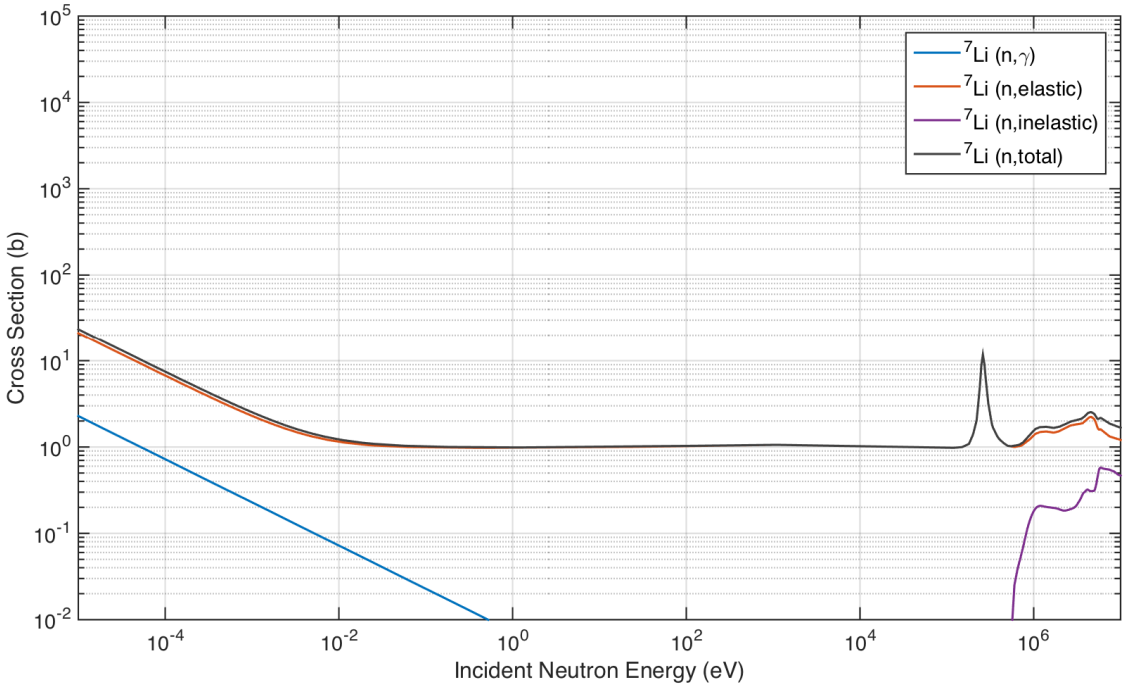


Figure D.8. Selected neutron cross sections for ^{7}Li ($a/o = 92.41\,\%$).

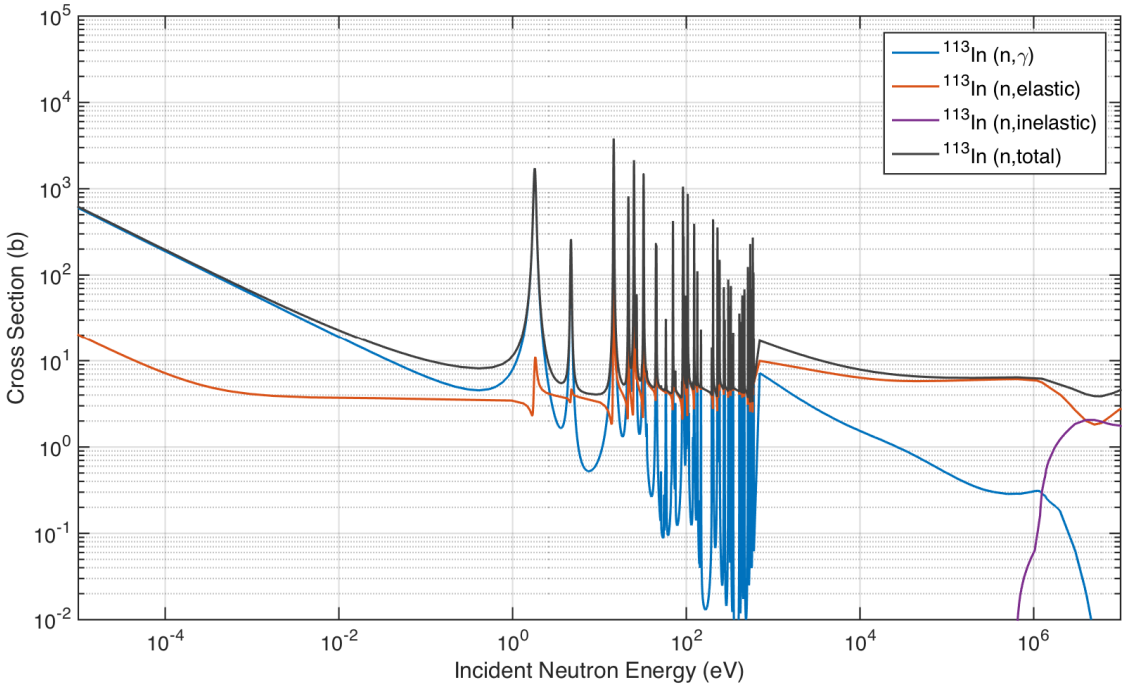


Figure D.9. Selected neutron cross sections for ^{113}In ($a/o = 4.28\,\%$).

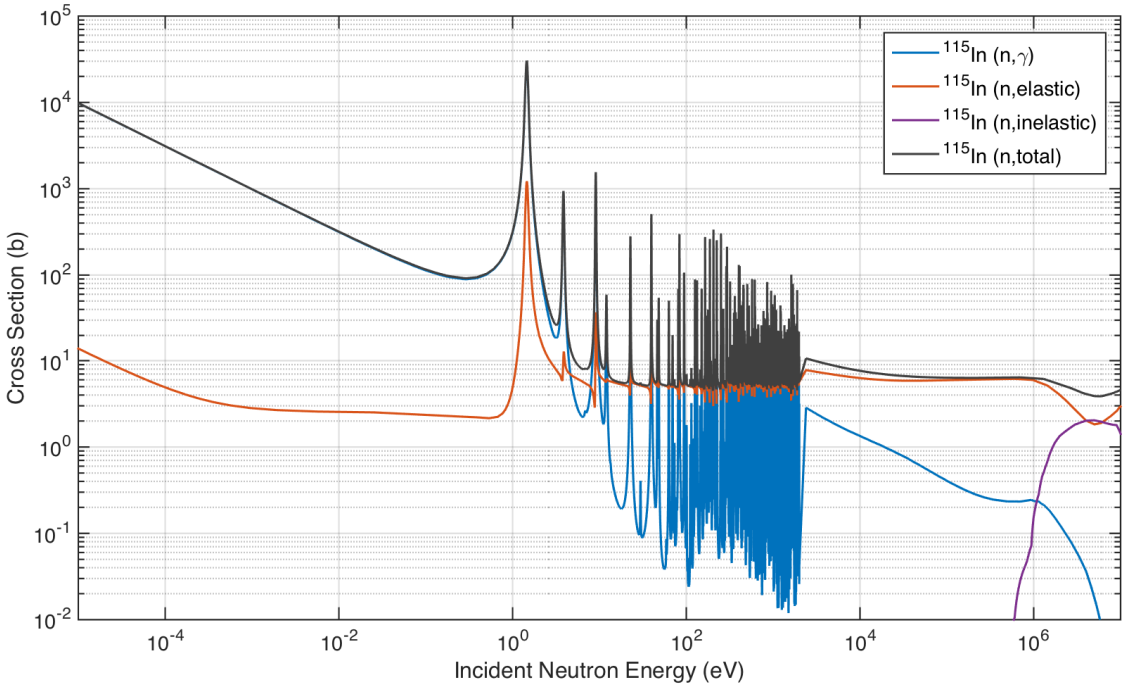


Figure D.10. Selected neutron cross sections for ^{115}In ($a/o = 95.71\,\%$).

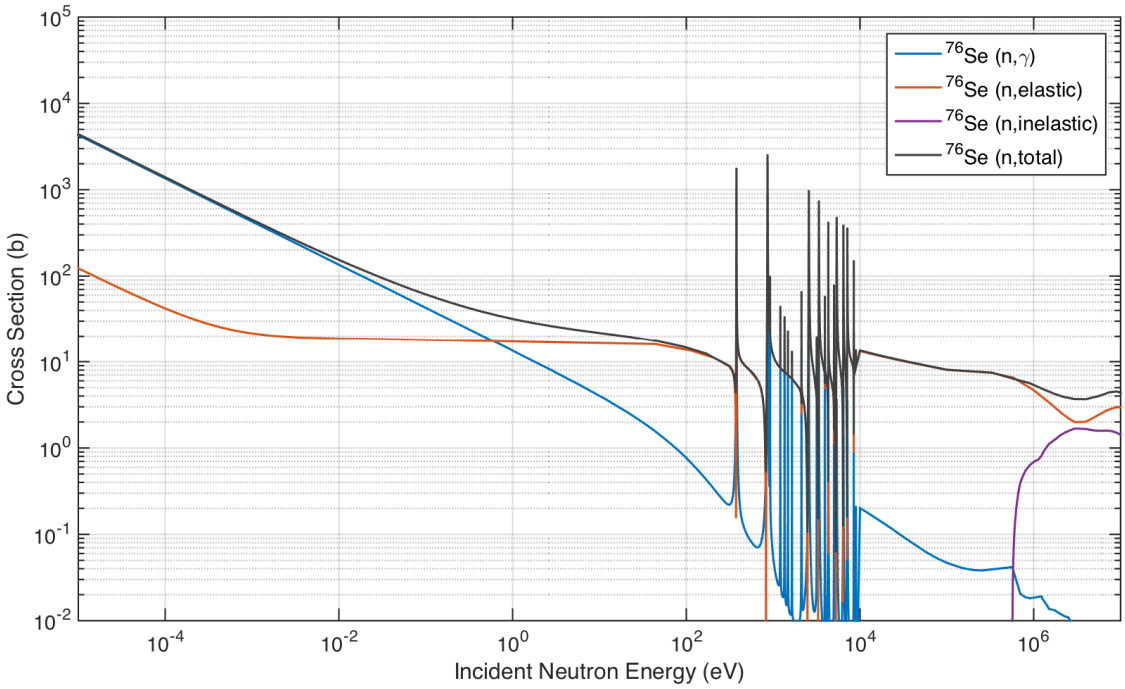


Figure D.11. Selected neutron cross sections for ^{76}Se ($a/o = 9.36\,\%$).

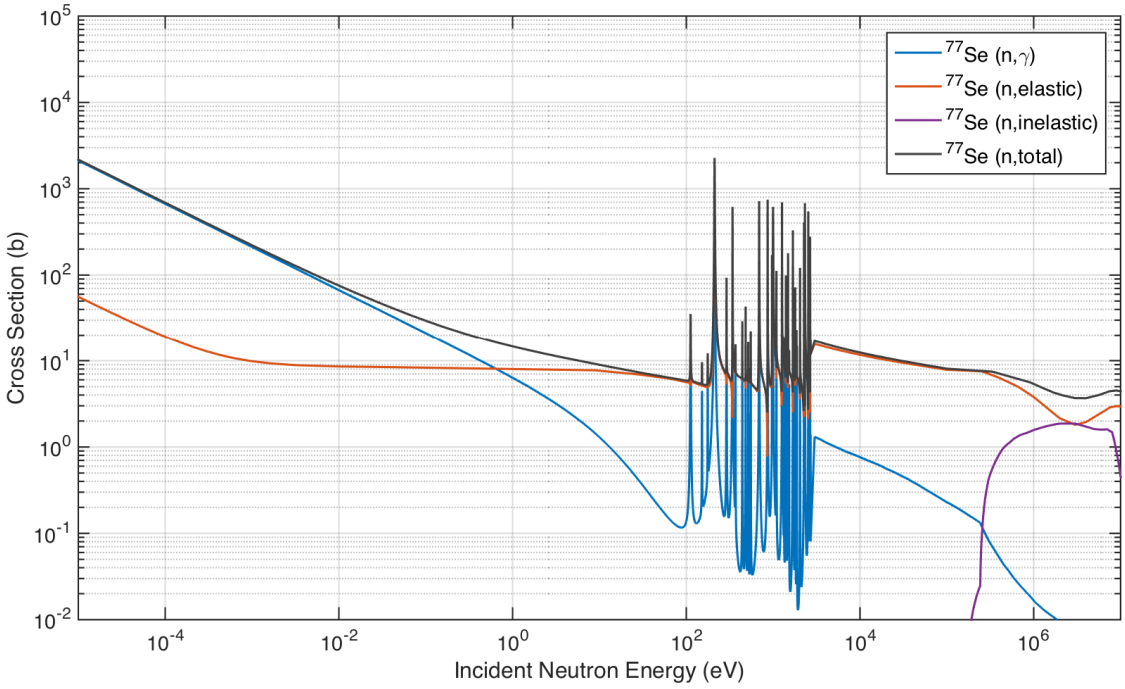


Figure D.12. Selected neutron cross sections for ^{77}Se ($a/o = 7.63\,\%$).

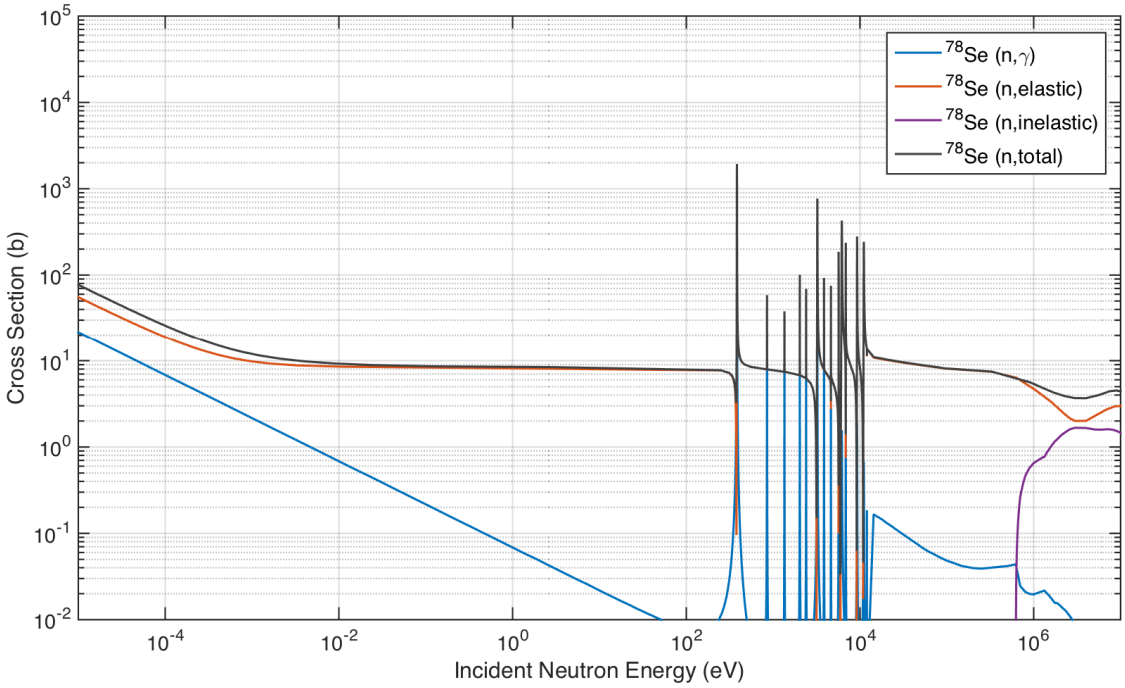


Figure D.13. Selected neutron cross sections for ^{78}Se ($a/o = 23.78\,\%$).

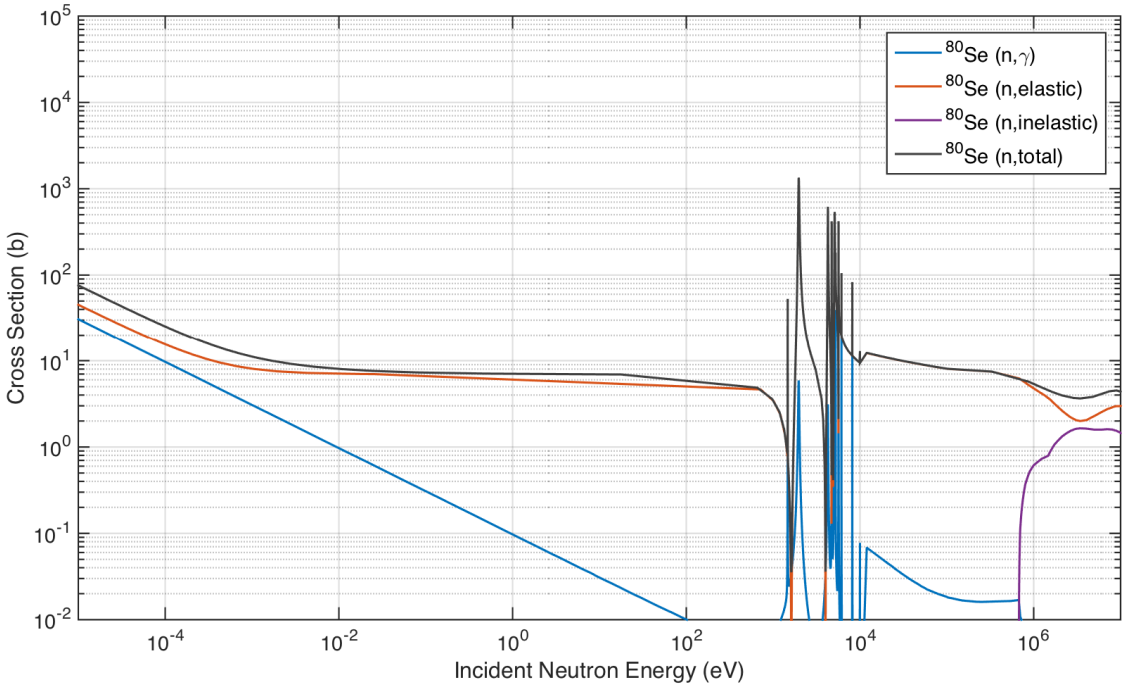


Figure D.14. Selected neutron cross sections for ^{80}Se ($a/o = 49.61\,\%$).

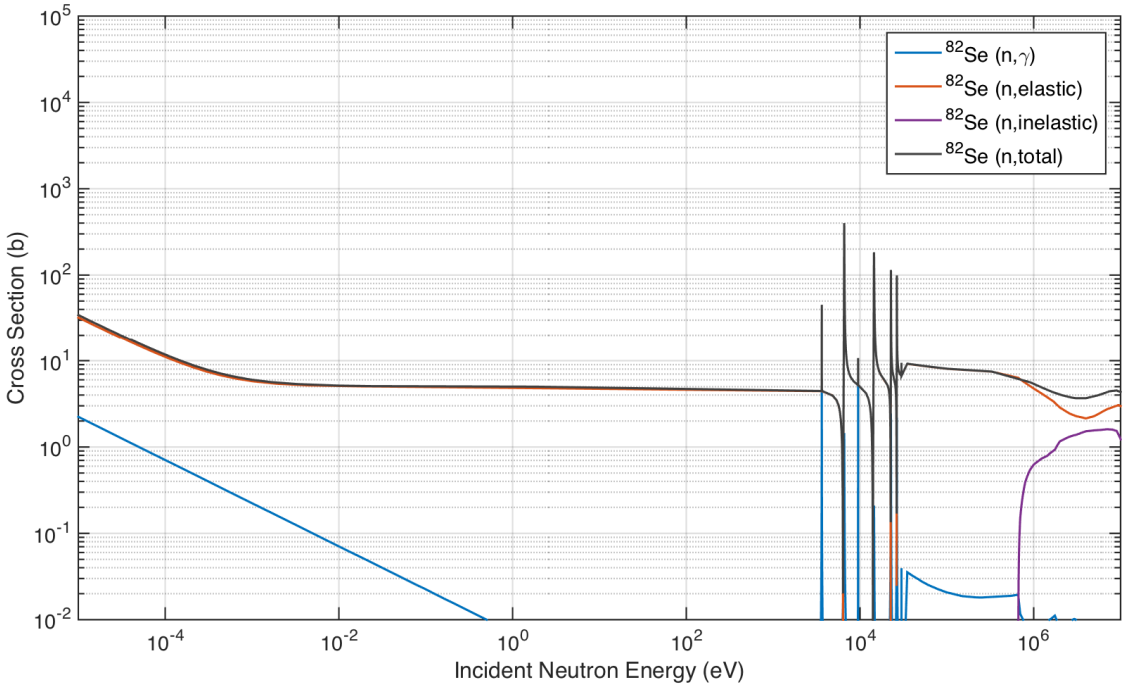


Figure D.15. Selected neutron cross sections for ^{82}Se ($a/o = 8.73\,\%$).

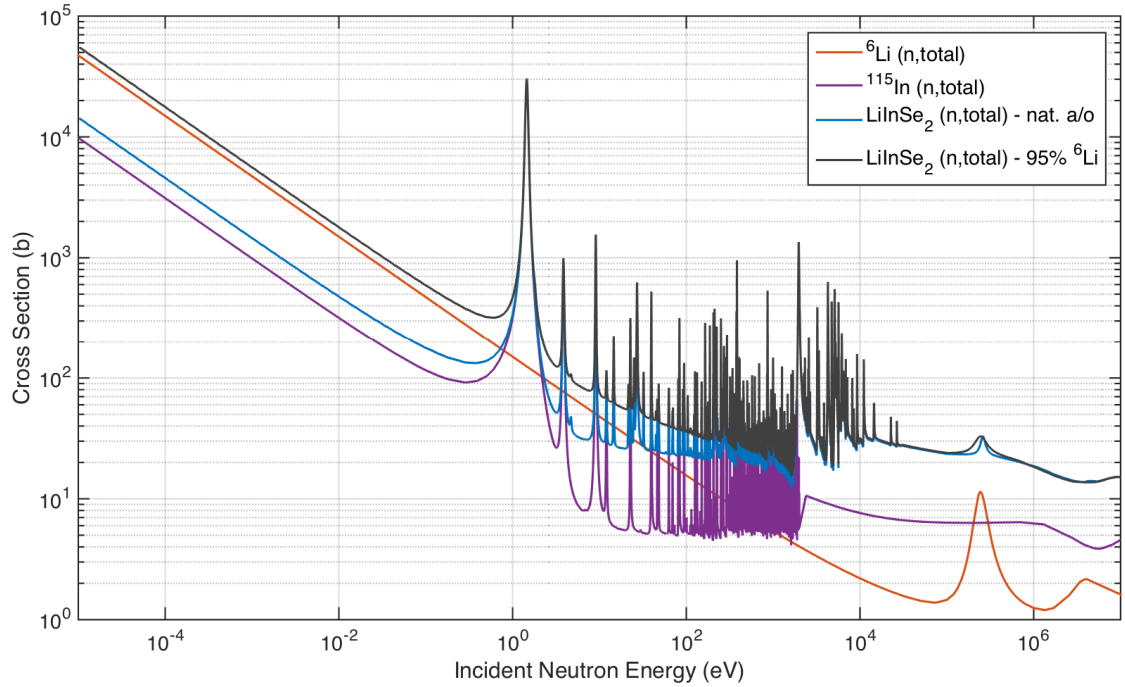


Figure D.16. Selected neutron cross sections for LISe compound.

D.3 Engineering Materials

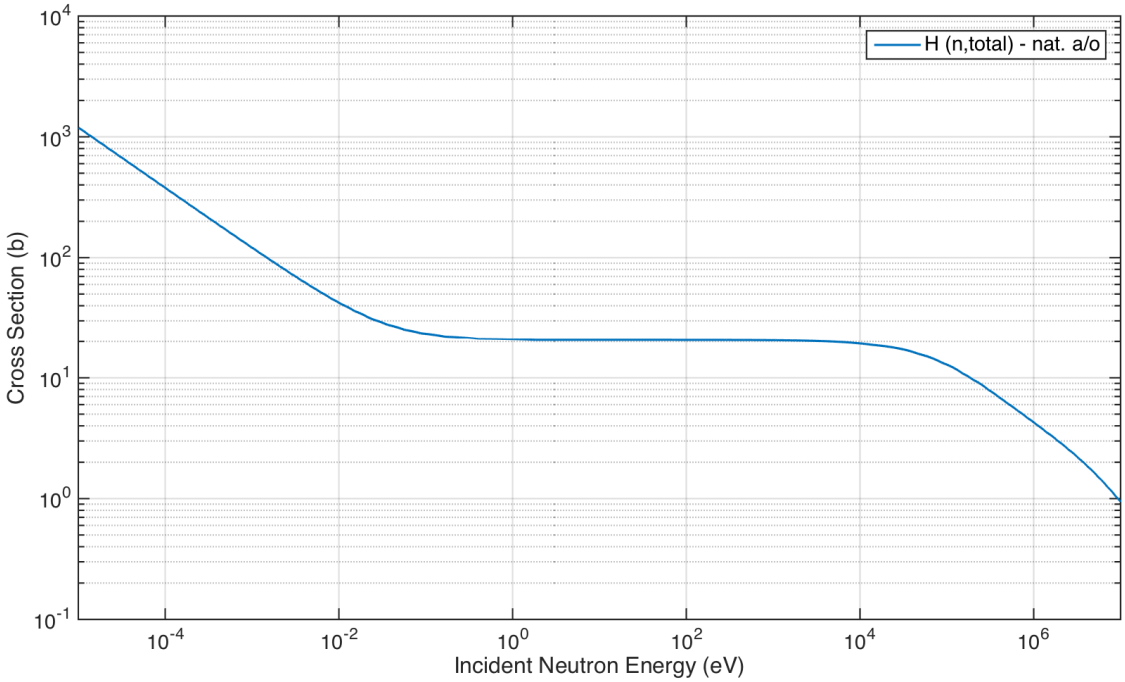


Figure D.17. Total neutron cross section for elemental hydrogen.

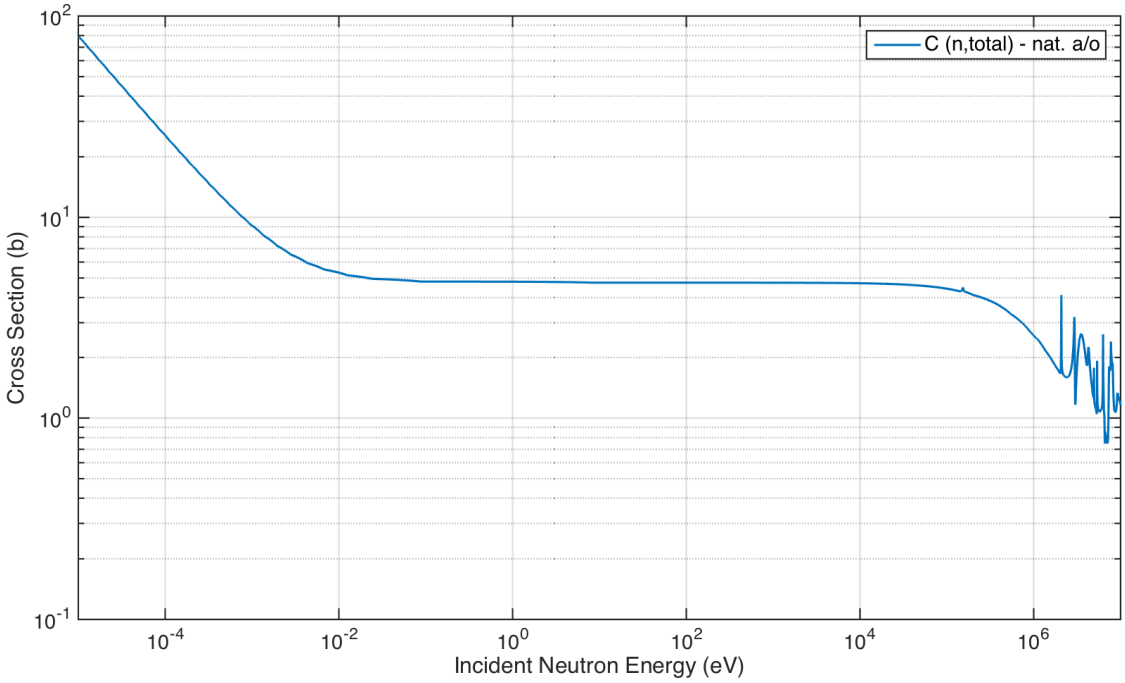


Figure D.18. Total neutron cross section for elemental carbon.

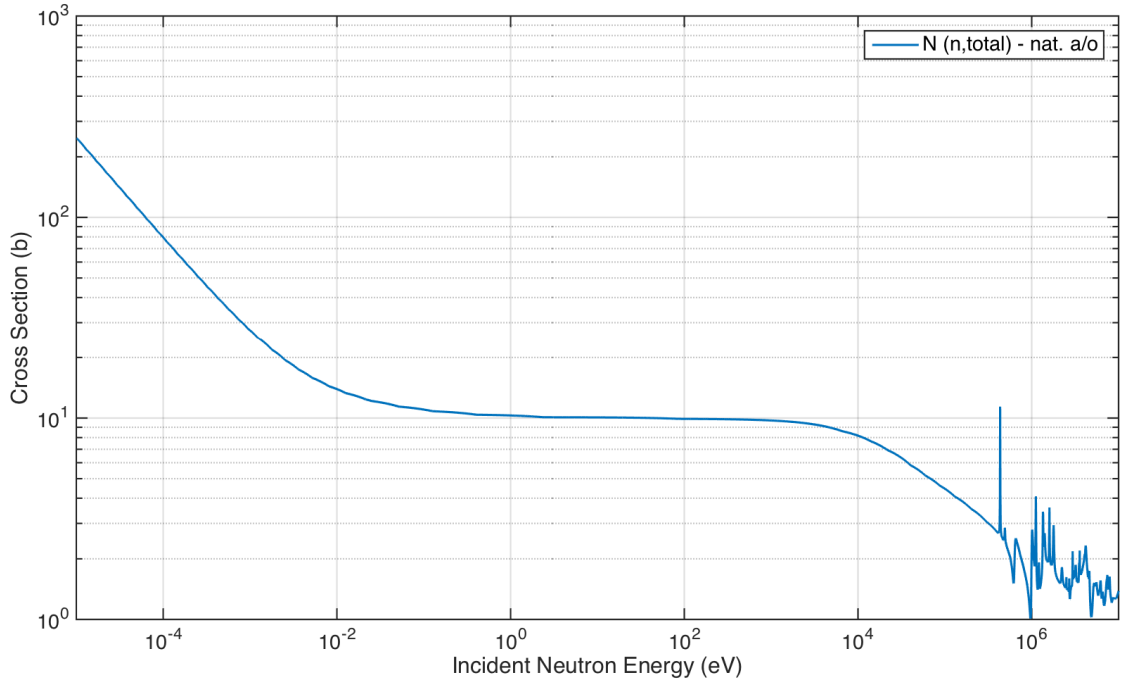


Figure D.19. Total neutron cross section for elemental nitrogen.

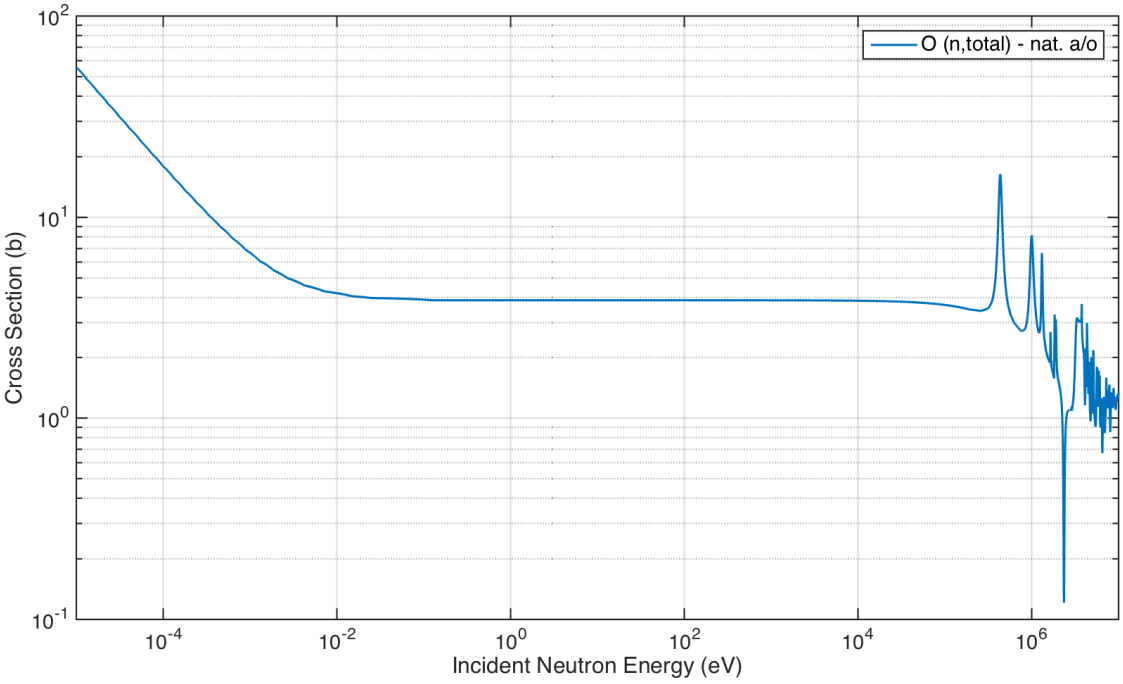


Figure D.20. Total neutron cross section for elemental oxygen.

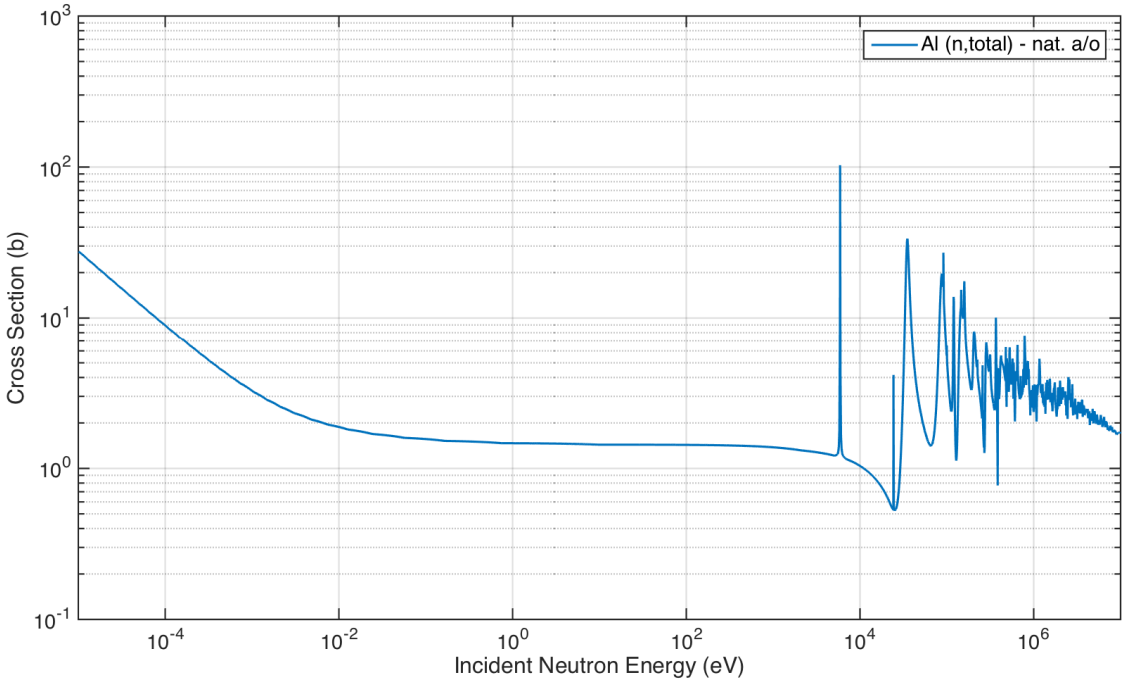


Figure D.21. Total neutron cross section for elemental aluminum.

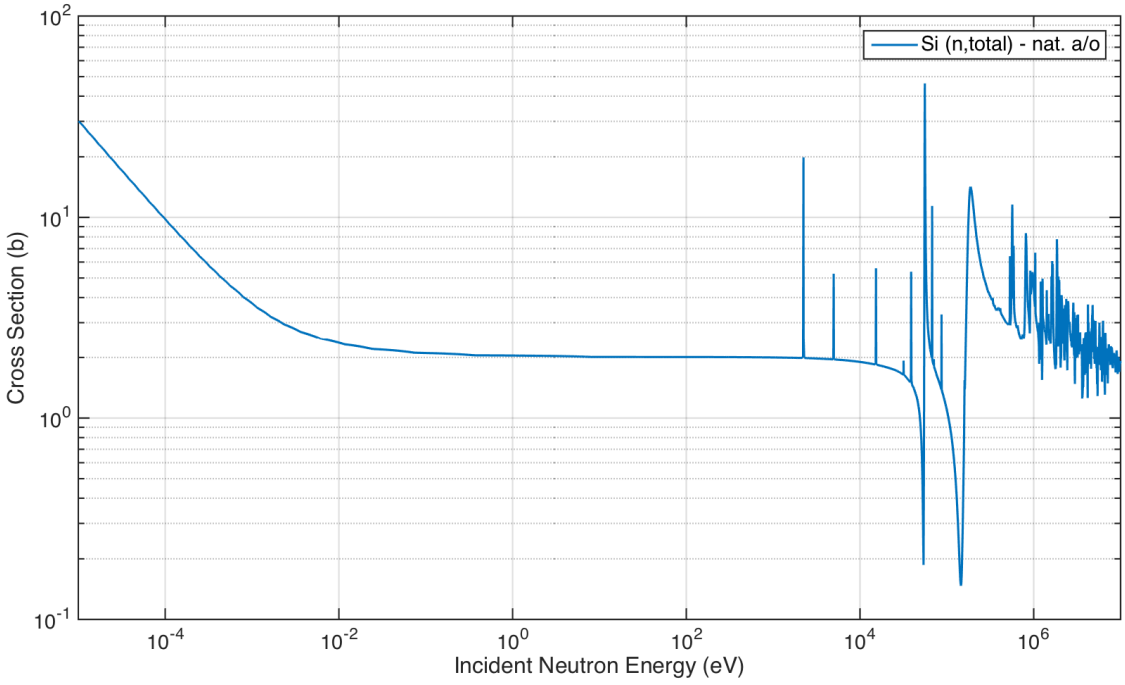


Figure D.22. Total neutron cross section for elemental silicon.

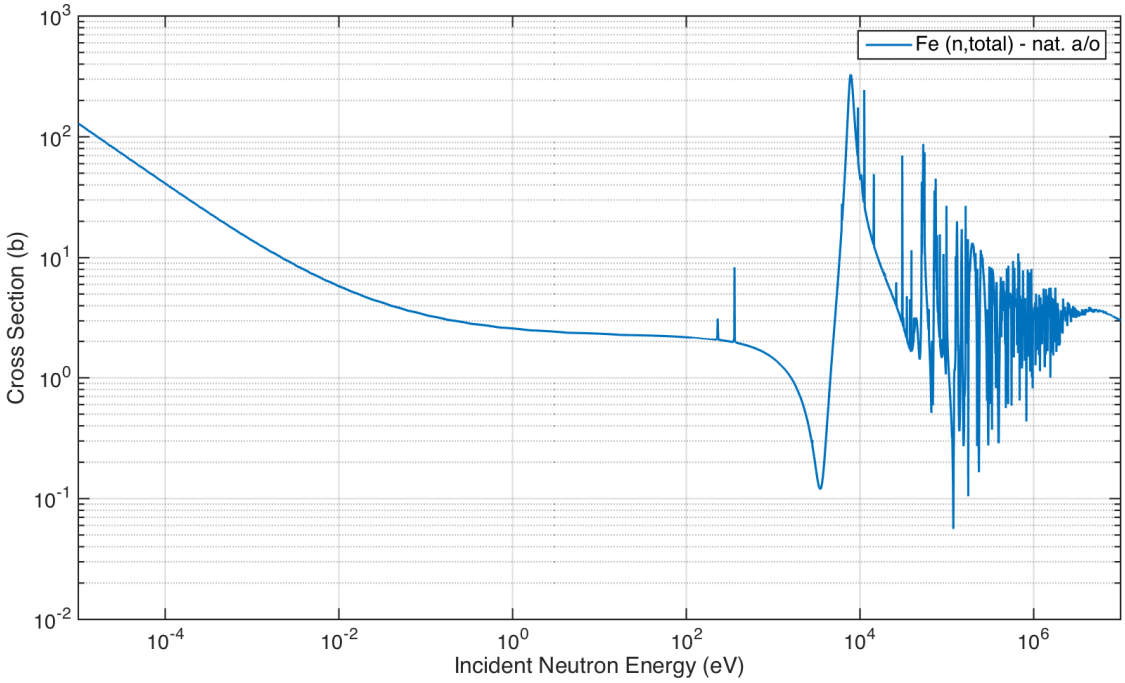


Figure D.23. Total neutron cross section for elemental iron.

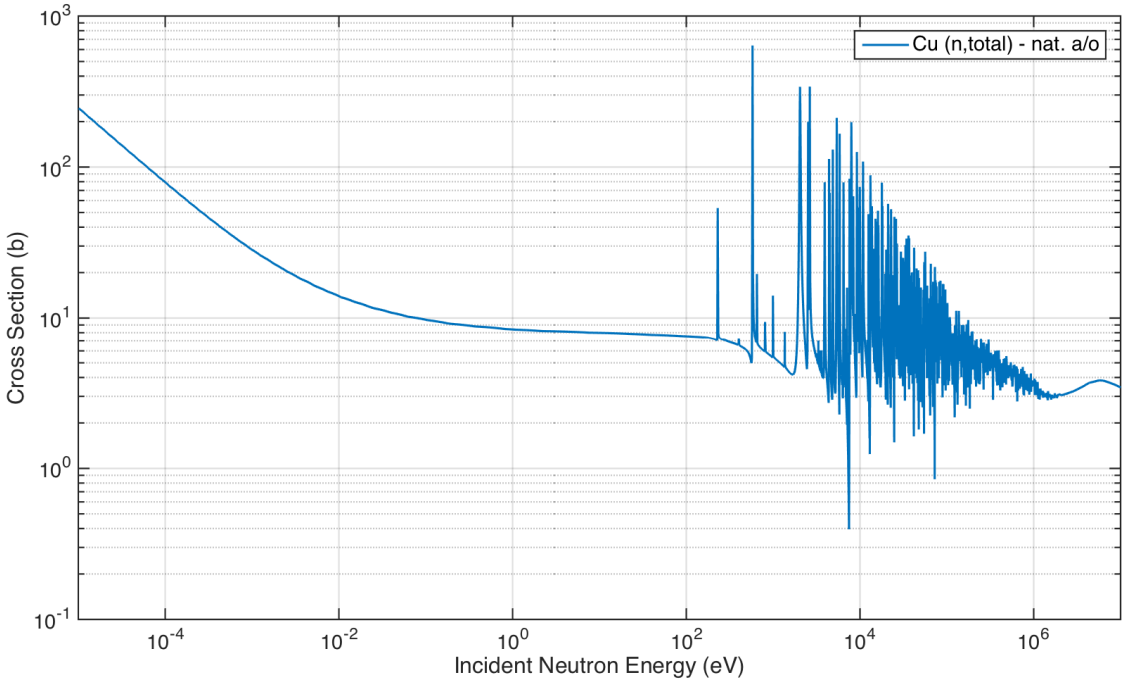


Figure D.24. Total neutron cross section for elemental copper.

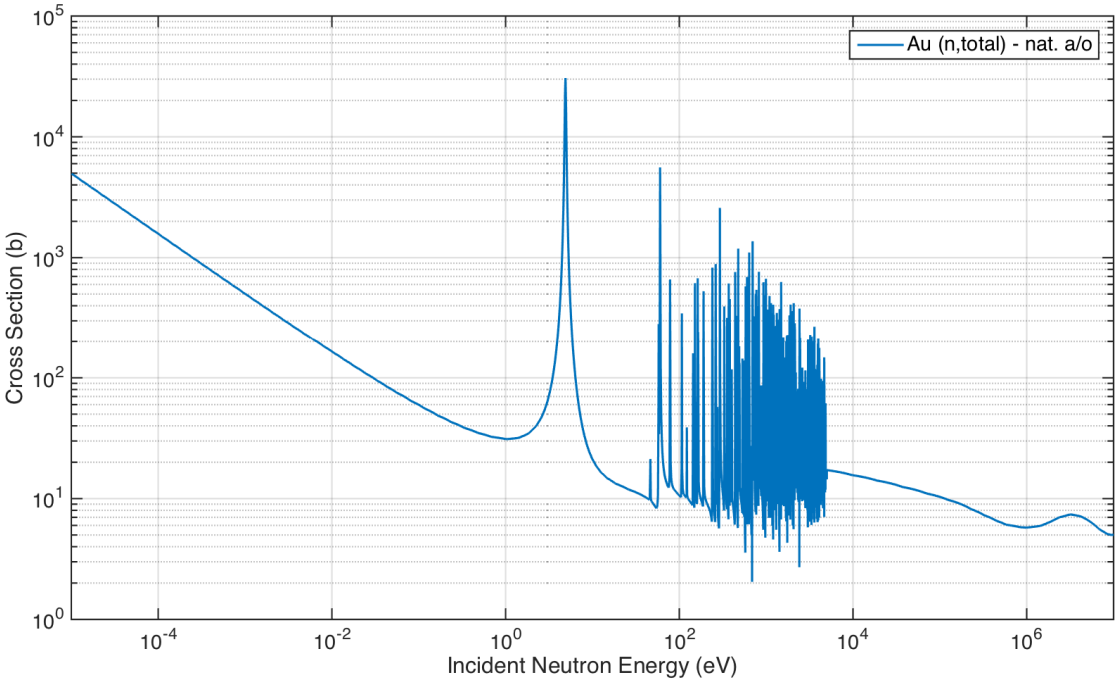


Figure D.25. Total neutron cross section for elemental gold.

Appendix E

Glossary

A

acetone [*formula:* $(CH_3)_2CO$] The simplest ketone solvent. 49

acrylonitrile butadiene styrene (ABS) [*formula:* $(C_8H_8)_x \cdot (C_4H_6)_y \cdot (C_3H_3N)_z$] A thermopolymer used in 3D printing, typically available as spooled filament of varying diameter. 74

ADVACAM USA [Grand Forks, ND] A company specializing in semiconductor sensor manufacturing, micro packaging, radiation imaging cameras and development of imaging solutions for industrial and academic needs, along with commercializing the Medipix technology that is under development at CERN [241]. 114

AJA International, Inc. [N. Scituate, MA] A manufacturer of thin film deposition systems including: magnetron sputtering, e-beam evaporation, thermal evaporation, and ion milling systems [242]. 190

alumina (*also*: aluminum oxide) [*formula:* Al_2O_3] A naturally occurring mineral from the oxidized state of aluminum. 58

AMPTEK©, Inc. [Bedford, MA] A high technology company and a recognized world leader in the design and manufacture of state-of-the-art nuclear instrumentation for the satellite, X-ray and γ-ray detection, laboratory, analytical, and portable instrumentation industries [243]. 51

Andor Technology Ltd [Belfast, Northern Ireland] A developer and manufacturer of high performance digital cameras [193]. 193

ANTARES [Garching, Germany] A neutron imaging facility designed to deliver radiographs and CT of samples, similar to an X-ray machine [244]. 4

Apiezon wax [*formula:* Apiezon Wax W] A vacuum sealing, mounting and etching wax from the Apiezon© product line. 143

ATC-Orion 5 UHV Plasma Sputtering System [*Mfr.*: AJA] An ultra-high vacuum (UHV) physical vapor deposition tool accommodating up to (5) 2 in sputtering sources including: metals, alloys and some ceramics, used in semiconductor device fabrication. 49

Atominstitut (ATI) [Vienna, Austria] An inter-university institute feature a TRIGA Mark II research reactor broad range of research and education ranging from very fundamental questions about symmetries and interactions in nuclear and particle physics to neutron, atomic, quantum-physics and quantum optics to radiation and reactor physics to applied tasks such as environmental monitoring, radiation protection or for example the radiation resistance of modern materials [245]. 4

A Toroidal LHC ApparatuS (ATLAS) [Geneva, Switzerland] One of the seven particle detector experiments constructed at the LHC. 33

AutoCAD© [*Dev.*: Autodesk] A commercial CAD and drafting software application [246]. 60

Autodesk, Inc. [San Rafael, CA] A software company specializing in architecture, engineering, construction, manufacturing, media, and entertainment industries [247]. 190

B

beamline A collimated radiation beam formed by directing a radiation source, typically isotropic, into a homogenized beam of particles or photons. xiv

bismuth germanate (BGO) [*formula:* $Bi_4Ge_3O_{12}$] An inorganic crystalline scintillator used for photon detection, in particular high energy γ-rays. 24

bismuth pivalate [*formula:* $C_{15}H_{27}BiO_6$] A polymer used for scintillator detectors. 22

bis(pinacolato)diboron (B_2Pin_2) [*formula:* $[(CH_3)_4C_2O_2B]_2$] A covalent compound containing two boron atoms and two pinacolato ligands. 23

boric acid (*also*: sassolite) [*formula:* H_3BO_3] A weak, monobasic Lewis acid of boron, which is often used as an antiseptic, insecticide, flame retardant, neutron absorber, or precursor to other chemical compounds. 23

boron-10 (n,a) reaction [*RX:* $^{10}B(n,\alpha)^7Li$] The primary reaction between boron-10 and thermal neutrons. 16

bromine/methanol (BrMeOH) [*formula:* $Br_2(CH_3)OH$] An etching solution consisting of 5% Br in MeOH. *See also:* bromine, methanol. 49

C

cadmium-113 (n,g) reaction [*RX:* $^{113}Cd(n,\gamma)^{114}Cd$] The primary reaction between cadmium-113 and thermal neutrons. 17

CAEN S.p.A. [Staten Island, NY] A company providing a complete range of high-voltage and low-voltage systems, and front-end data acquisition (DAQ) modules which meet IEEE standards for nuclear and particle physics [248]. 51

carbon-12 (n,a) reaction [*RX:* $^{12}C(n,\alpha)^9Be$] The primary reaction between carbon-12 and thermal neutrons. 35

***m*-carborane** [*formula:* $C_2H_{12}B_{10}$] A cluster composed of boron, carbon and hydrogen atoms, of polyhedra shape, used as a source of boron loading. 23

chemical vapor deposition (CVD) A chemical process used to produce high quality, high-performance, solid materials. 33

- **plasma-enhanced CVD (PECVD)** A chemical vapor deposition process used to deposit thin films from a gas state to a solid state on a substrate using a plasma to facilitate chemical reactions. 194

chlorine-35 (n,p) reaction [*RX:* $^{35}Cl(n,p)^{35}S$] The primary reaction between chlorine-35 and fast neutrons. 24

CLYC [*formula:* Cs_2LiYCl_6:Cl] An inorganic crystalline scintillator developed by RMD that uses PSD for simultaneous γ-ray and neutron detection. 24

CLYC-6 [*formula:* $Cs_2(^6Li)YCl_6$:Cl] CLYC enriched to 95 % lithium-6 isotopic concentration. *See also:* CLYC. 24

CLYC-7 [*formula:* $Cs_2(^7Li)YCl_6$:Cl] CLYC enriched to 99 % lithium-7 isotopic concentration. *See also:* CLYC. 24

Cold Guide 1 Beamline (CG-1) [Oak Ridge, TN] The largest of the four guides housed in the Cold Guide Hall at HFIR, split into four separate beams [249]. 67

Cold Guide 1A Instrument (CG-1A) [Oak Ridge, TN] One of the beamline instruments stemming from CG-1 at HFIR. 67

Cold Guide 1D Instrument (CG-1D) [Oak Ridge, TN] A polychromatic neutron beamline in the cold range conducting neutron radiography and CT for applications in AM, materials science, geoscience, biology, energy, and transportation. Part of CG-1 at HFIR [250]. xiv

complementary metal-oxide semiconductor (CMOS) A technology for constructing integrated circuits. 191

- **scientific complementary metal-oxide semiconductor (sCMOS)** A scientific grade complementary metal-oxide semiconductor (CMOS) device used for high-resolution imaging. 46

computed tomography (CT) A technique using computer-processed combinations of many radiograph measurements taken from different angles to produce cross-sectional (tomographic) images. 3

- **electron computed tomography (eCT)** 83
- **micro computed tomography (μCT)** 83
- **neutron computed tomography (nCT)** vii, 83

computer-aided design (CAD) A computer based approach to engineering, CAD programs are widely used for part modeling and design. 53

connectors

- **Bayonet Neill-Concelmann (BNC)** A quick release RF connector used with coaxial cabling, typically (50 Ω), common in nuclear engineering applications. 51
- **LEMO 00 coaxial connector (LEMO 00)** A miniature push-pull (50 Ω) coaxial connector, created by LEMO, used as front panel connectors in NIM systems as a smaller alternative to BNCs. 58
- **micro coaxial connector (MCX)** A snap-on coaxial RF connector, typically available in 50 Ω impedance. 72
- **safe high-voltage connector (SHV)** A coaxial RF connector similar to BNC connectors, with a protruding insulator rated at a 5 kV operational limit. 51

CNS-Y12 A neutron imaging target 3D printed to reflect the Y-12 company logo. 74

Cremat, Inc. [West Newton, MA] A company dedicated to manufacturing and selling CSPs and their accessories, as well as producing custom circuitry for customers needing specialized equipment. They also perform contract research in the fields of radiation detectors and low noise electronics [251]. 51

CR-150 Preamplifier PCB [*Mfr.*: Cremat] A an evaluation board for any of the CR-11X CSP modules with provisions to be powered either by a wall-mounted power supply or by the user's ±12 V power supply. 53

CR-110 Preamplifier Module [*Mfr.*: Cremat] A CSP used to read out pulse signals from radiation detectors as diverse as semiconductor radiation detectors (*e.g.* CdTe, CZT), scintillator-photodiode detectors, gas-based detectors such as ionization chambers and proportional counters, and PMTs. 51

crystal bonding wax [*formula:* EQ-WaxB-1] A high quality paraffin based wax for holding samples during cutting crystals, ceramics, wafers, and all brittle materials, manufactured and sold by MTI. 49

D

E3630A 35W Triple Output DC Power Supply [*Mfr.*: Keysight] A triple output DC power supply offering 35 W of power running at up to ±20 V and up to 0.5 A. 72

U.S. Department of Homeland Security (DHS) A cabinet department of the United States federal government with responsibilities in public security, roughly comparable to the interior or home ministries of other countries [252]. 5

U.S. Department of Energy (DOE) A cabinet-level department of the United States Government concerned with the United States' policies regarding energy and safety in handling nuclear material [253]. 5

V1724 8-channel Digitizer [*Mfr.*: CAEN] A 1-unit wide VME 6 U module housing an 8-Channel 14 bit 100 MS/s Flash analog-to-digital converter (ADC) Waveform Digitizer and featuring 2.25 Vpp single ended input dynamics. 72

DMDPA (*also*: 1,4-dimethyl-9,10-diphenylanthracene) [*formula:* $C_{28}H_{22}$] A plastic scintillator additive used to boost LY. 24

E

EAGLE [*Dev.*: Autodesk] A scriptable electronic design automation (EDA) application with schematic capture, PCB layout, auto-router and computer-aided manufacturing (CAM) features [254]. 53

European Organization for Nuclear Research (CERN) [Geneva, Switzerland] A European research organization that operates the largest particle physics laboratory in the world [255]. 114

Evaluated Nuclear Data File (ENDF) A standard file format used globally to encode nuclear data evaluations for use in research and nuclear technology (release ENDF/B-VII.1 used in this research). 176

F

U.S. Federal Communications Commission (FCC) An independent agency of the United States government created to regulate interstate communications by radio, television, wire, satellite, and cable [256]. 141

file formats A standard way that information is encoded for storage in a computer file.

- **portable network graphic (PNG)** A raster graphics file format that supports lossless data compression. 173
- **tagged image file format (TIFF)** A flexible, adaptable file format for handling images and data within a single file, by including the header tags. 173

Fisk [Nashville, TN] A private historically black university founded in 1866 [257]. 37

Flame Retardant 4 (FR-4) A fire classification given to laminates formed from woven fiberglass cloth impregnated with an epoxy resin, used in the manufacture of PCBs. 55

Form-2 3D printer [*Mfr.*: Formlabs] An industrial quality SLA 3D printer featuring high-resolution desktop printing using a variety of photoresins, easily installed and swapped via resin tanks. 74

Ultimaker 2^+ 3D printer [*Mfr.*: Ultimkaer] An industrial quality FDM 3D printer and successor to the Ultimaker Original, using spooled filament feed stock, swappable nozzles, and a heated build plate. 74

Formlabs, Inc. [Somerville, MA] A designer and manufacturer of 3D printers, specializing in SLA systems available for desktop application [258]. 74

Fourier transforms A linear operation that decomposes a signal function into the frequencies that make it up.

- **continuous Fourier transform (CFT)** A version of the transform defining completely and exactly the frequency domain, where the frequency domain is continuous and range unlimited. 172
- **discrete Fourier transform (DFT)** A form of Fourier analysis that is applicable to the uniformly-spaced samples of a continuous function. 172
- **fast Fourier transform (FFT)** An algorithm that samples a signal over a period of time (or space) and divides it into its frequency components, yielding the DFT. 108

Futurrex, Inc. [Franklin, NJ] A global manufacturer of high-purity specialty chemicals and novel processing solutions for the global microelectronics, photonics and other high growth technology markets [259]. 194

G

gadolinium-155 (n,g) reaction [*RX:* $^{155}\mathrm{Gd}(n,\gamma)^{156}\mathrm{Gd}$] The primary reaction between gadolinium-155 and thermal neutrons. 18

gadolinium-157 (n,g) reaction [*RX:* $^{157}\mathrm{Gd}(n,\gamma)^{158}\mathrm{Gd}$] The primary reaction between gadolinum-157 and thermal neutrons. 18

gadolinium oxysulfide (Gadox) [*formula:* Gd_2O_2S] A neutron sensitive scintillating compound exhibiting large beam attenuation when applied as a thin film. 26

Geiger-Müller (G-M) A G-M tube is a gas filled element of the Geiger counter, a sensing instrument for detecting ionizing radiation. 15

General Atomics (GA) [San Diego, CA] A defense contractor specializing in nuclear physics including nuclear fission and nuclear fusion [260]. 197

H

Hammond Manufacturing, Ltd. [Guelph, Canada] A manufacturer of diverse products including: electrical and electronic enclosures, power outlet strips, electronic transformers, as well as equipment rack and cabinet solutions for audio-visual, pro-audio and data/comm applications [261]. 66

helium-3 (n,p) reaction [*RX:* $^3He(n,p)^3H$] The primary reaction between helium-3 and thermal neutrons. 15

High-Flux Isotope Reactor (HFIR) [Oak Ridge, TN] The highest flux reactor-based source of neutrons for research in the United States, providing one of the highest steady-state neutron fluxes of any research reactor in the world [189]. 46

NHQ 203M High-Voltage Power Supply A compact two channel high-voltage power supply in a single NIM module chassis providing up to 3 kV bias. 72

I

ANDOR iKon-L DW936 CCD camera [*Mfr.*: Andor] A high dynamic range (HDR) CCD camera offering outstanding resolution, FOV ($27.6 \times 27.6\,mm^2$), sensitivity and dynamic range performance, featuring a 2,048 × 2,048 array of 13.5 µm pixels. 69

ImageJ [*Dev.*: U.S. National Institute of Health (NIH)] A public domain Java image processing program inspired by NIH Image for the Macintosh, running either as an online applet or as a downloadable application, on any computer with a Java 1.4 or later virtual machine [262]. 105

infra-red (IR) A portion of the electromagnetic radiation spectrum between 700 nm and 1 mm, often corresponding to thermal radiation from materials near room temperature.

mid infra-red (mid-IR) mid infra-red region of the visible spectrum. 26

isopropyl alcohol (*also*: isopropanol) (IPA) [*formula:* C_3H_8O] A secondary alcohol solvent used for cleaning surfaces. 146

J

Jožef Stefan Institute (JSI) [Ljublijana, Slovenia] The largest research institute in Slovenia with research areas in physics, chemistry, molecular biology, biotechnology, information technologies, reactor physics, energy and environment [263]. 4

K

kapton A polymide film used as tape backing in UHV and cryogenic applications, maintaining a low outgassing rate. 143

Keysight Technologies, Inc. [Santa Rosa, CA] A company that manufactures electronics test and measurement equipment and software (spun off from Agilent Technologies, Inc. a former division of HP, Inc.) [264]. 72

knife-edge An experiment used with the MTF technique to measure the resolvable contrast across an abrupt transition. 108

Kulicke and Soffa Industries, Inc. (K&S) [Santa Ana, CA] A provider of semiconductor packaging and electronic assembly solutions supporting the global automotive, consumer, communications, computing and industrial segments [265]. 60

L

LabVIEW [*Dev.*: National Instruments (NI)] A systems engineering software for applications that require test, measurement, and control with rapid access to hardware and data insights [266]. 72

Large Hadron Collider (LHC) [Geneva, Switzerland] The world's largest and most powerful particle collider, the most complex experimental facility ever built, and the largest single machine in the world [267]. 33

LaTeX An open source, high-quality typesetting system, LaTeX includes features designed for the production of technical and scientific documentation [31]. 198

LEMO® [Écublens, Switzerland] An electronic and fibre optic connector manufacturer [268]. 191

light-tight enclosure A sealed enclosure used to isolate optically sensitive devices from external sources of light. 69

Li-ion battery (LIB) A type of rechargeable battery in which lithium ions move from the negative electrode to the positive electrode during discharge and back when charging. 3

lithium-6 (n,a) reaction [*RX:* $^6Li(n,\alpha)^3H$] The primary reaction between lithium-6 and thermal neutrons. 16

^{6}LiF/ZnS:(Cu) (1:2) scintillator screen (LiF/ZnS screen) [*Mfr.*: RC TRITEC] A neutron sensitive scintillator screen mixture consisting of ^{6}LiF/ZnS:(Cu) at a (1:2) ratio an an aluminum backing plate (0.4 mm), with an emission peak at 530 nm (green) resulting from the copper activator. 26

lithium-6 fluoride (^{6}LiF) [*formula:* ^{6}LiF] A neutron sensitive scintillating compound. 25

lithium fluoride, zinc sulfide (LiF/ZnS) [*formula:* ^{6}LiF/ZnS] A lithium-6 enriched scintillator mixture with integrated absorber and fluorescent pigment. *See also:* lithium-6 fluoride. 3

lithium indium diselenide (LISe) [*formula:* $LiInSe_2$] The topic material of this dissertation. vii

lithium-6 indium diselenide (^{6}LISe) [*formula:* $^6LiInSe_2$] Lithium indium diselenide (LISe) enriched to 95% lithium-6 isotopic concentration. *See also:* lithium indium diselenide. 100

LISe 16-channel pixel detector (LISe PD) [*Mfr.*: UTK] A prototype 16-channel pixel detector fabricated at UTK, used for low to medium resolution thermal neutron imaging. 48

LISe scintillator A LISe sample optically polished for scintillator operation. 26

LISe-1 A scintillator sample from boule #092613. 87

LISe-6.1 A scintillator sample from boule #010515. 92

LISe-6.3 A scintillator sample from boule #010515. 92

Timepix coupled LISe imager (LISePix) [*Mfr.*: UTK] A high-resolution semiconductor neutron imaging system based on coupling the neutron sensitive compound LISe to a Timepix readout. vii

lithium methacrylate (LiME) [*formula:* $C_4H_5LiO_2$] A lithium based polymer used for scintillator neutron detectors. 22

lithium phenylsalicylate (LiPSA) [*formula:*] A lithium based polymer used for scintillator neutron detectors. 23

lithium pivalate [*formula:* $C_5H_9LiO_2$] A lithium based polymer used for scintillator neutron detectors. 22

lithium salicylate (LiSal) [*formula:* $C_7H_5LiO_3$] A lithium based polymer used for scintillator neutron detectors. 23

M

MA-6/BA-6 Mask and Bond Aligner [*Mfr.*: Süss MicroTec (Karl Süss)] A mask and bond aligner designed for up to a 150 mm wafer size, used for microelectromechanical systems (MEMS) applications, production of optical components and compound semiconductors. 145

The MathWorks®, Inc. [Natick, MA] A company specializing in mathematical computing software [269]. 194

MATLAB™ [*Dev.*: MathWorks] A proprietary programming language, MATLAB allows matrix manipulations, plotting of functions and data, implementation of algorithms, creation of user interfaces, and interfacing with programs written in other languages, including C, C++, C#, Java, Fortran and Python [270]. 82

Medipix A family of read-out chips, including the Timepix, for particle imaging and detection developed by the Medipix Collaborations at CERN [271]. 42

Medipix1 chip [*Mfr.*: CERN] The Medipix1 chip was the first large area single photon counting CMOS imaging chip., comprising a matrix of 64×64 identical pixels each measuring $170 \times 170\,\mu m^2$. 45

Medipix2 ASIC [*Mfr.*: CERN] The Medipix2 ASIC, the successor of the Medipix1 chip, is a high spatial, high contrast resolving CMOS pixel read-out chip working in single photon counting mode. 45

methanol (*also*: methyl alcohol) (MeOH) [*formula:* CH_3OH] A simple solvent used for cleaning surfaces. 49

Micro-Processing Research Facility (MPRF) [Knoxville, TN] A Class 100 cleanroom facility at UTK offering services including: optical lithography, thin film deposition, reactive ion etching (RIE) and plasma-enhanced CVD (PECVD) [272]. 137

microscope An instrument used to see objects that are too small to be seen by the naked eye.

light microscope (LM) The traditional form of microscopy using visible light, also known as an optical microscope. 64

monoborylated benzene (*also*: 4,4,5,5-tetramethyl-2-phenyl-1,3,2-dioxaborolane) (MBB) [*formula:* $C_{12}H_{17}BO_2$] An additive used for boron-loaded plastic scintillators. 23

Monte Carlo N-Particle Transport Code, revision 6 A general-purpose Monte Carlo N-Particle code that can be used for neutron, photon, electron, or coupled neutron/photon/electron transport [273]. 24

MTI Corporation [Richmond, CA] The leading manufacturer of oxide crystals, substrates and lab equipment for material research, providing high-quality and low-cost precision machines for material research and research and development (R&D) Labs, including: low-speed cutting saws, wire diamond saws, automatic polishing machines, high-temperature ovens, tube furnaces, and a complete set of equipment for research of rechargeable battery materials [274]. 192

N

National Instruments™ Corporation (NI) [Austin, TX] A producer of automated test equipment and virtual instrumentation (VI) software. Common applications include data acquisition, instrument control and machine vision [275]. 193

U.S. National Institute of Health (NIH) The primary agency of the United States government responsible for biomedical and public health research [276]. 193

4001C NIM Bin [*Mfr.*: ORTEC] A general type of NIM electronics and support infrastructure used for trigger electronics and data acquisition in radiation detection. 72

NR9-1000PY (negative photoresist) [*formula:* NR9-1000PY] A negative photoresist from Futurrex for 1 µm resist thickness. 142

U.S. Nuclear Regulatory Commission (NRC) An independent agency of the United States government tasked with protecting public health and safety related to nuclear energy [32]. 8

O

Oak Ridge National Lab (ORNL) [Oak Ridge, TN] The largest DOE science and energy laboratory, conducting basic and applied research to deliver transformative solutions to compelling problems in energy and security [277]. 67

Octopus Imaging Software A set of intuitive programs that help with the reconstruction of 2D projection data to 3D volumes, the analysis, and the visualization of that 3D volume [278]. 77

ORTEC© [Oak Ridge, TN] A company specializing in design and manufacture of precision detectors, nuclear instrumentation, analysis software, and systems for industry, academia, and government agencies [279]. 72

P

Paul Scherrer Institute (PSI) [Villigen, Switzerland] The largest research institute for natural and engineering sciences in Switzerland, conducting cutting-edge research in three main fields: matter and materials, energy and environment and human health [57]. 2

Helmholtz-Zentrum Berlin (HZB) [Villigen, Switzerland] An institute studying the structure and dynamics of materials and investigating solar cell technology. Several large scale facilities are available, the most important of which are the 10 MW BER-II nuclear research reactor at the Lise Meitner campus [280]. 3

A3818 PCIe CONET2 Controller [*Mfr.*: CAEN] A peripheral component interconnect express (PCIe) x8 card that can plug into both ×8 and ×16 PC PCIe slots (V1.1 or 2.0), which allows the control of up to 4 CONET2 independent networks. 72

peripheral component interconnect (PCI) A local computer bus for attaching hardware devices in a computer. 195

peripheral component interconnect express (PCIe) A high-speed serial computer expansion bus standard, designed to replace the older peripheral component interconnect (PCI) standard. 195

photoresist remover [*formula:* RR41] A photoresist cleaning solvent from Futurrex for positive and negative photoresists. 146

photoresist developer [*formula:* RD6] A photoresist developer solvent from Futurrex for positive and negative photoresists. 145

plutonium/beryllium (Pu/Be) [*formula:* ^{239}PuBe] A material commonly used as a neutron source consisting of plutonium-239 surrounded by beryllium encased in stainless steel. 35

poly(*p*-phenylene oxide) (PPO) [*formula:* varies] A high-temperature thermoplastic used for structural parts, electronics, household and automotive items that depend on high heat resistance, dimensional stability and accuracy. 22

poly(methyl methacrylate) (PMMA) [*formula:* $(C_5O_2H_8)_n$] A transparent thermoplastic often used in sheet form as a lightweight or shatter-resistant alternative to glass, and may also be used as a casting resin in inks and coatings. 22

polyethylene (PE) [*formula:* $(C_2H_4)_n$] The most common plastic used globally. 105

polylactic acid (PLA) [*formula:* variable] A thermopolymer used in 3D printing, typically available as spooled filament of varying diameter. 74

polymer electrolytic fuel cell (PEFC) An electrochemical cell that converts the chemical energy from a fuel into electricity through an electrochemical reaction of hydrogen fuel with oxygen or another oxidising agent. 2

polypropylene (PP) [*formula:* $(C_3H_6)_n$] The second most common plastic used globally, this plastic is white, rugged and chemically resistant. 26

polystyrene (PS) [*formula:* $(C_8H_8)_n$] A synthetic aromatic thermoplastic polymer that is clear, hard, and brittle. 22

polyvinyl toluene (PVT) [*formula:* $[CH_2CH(C_6H_4CH_3)]_n$] A synthetic aromatic thermoplastic polymer, that is clear, hard and brittle. 22

Power-T A neutron imaging target 3D printed to reflect a UTK school logo. xv

PR1-1000A (positive photoresist) [*formula:* PR1-1000A] A positive photoresist from Futurrex for 1 µm resist thickness. 146

printed circuit board (PCB) A structure consisting of a flat sheet of insulating material, such as FR-4 board, and a layer of copper foil, laminated to the substrate, providing a physical structure supporting and electrically connecting circuit components. 50

pyrolitic boron nitride (PBN) [*formula:* BN] A heat and chemically resistant refractory compound, traditionally used as parts of high-temperature equipment. 37

Python™ An easy to learn, powerful programming language, with efficient high-level data structures and a simple but effective approach to object-oriented programming [281]. 155

Q

***Q*-value** The amount of energy released by a given nuclear reaction. 12

R

radiation Energy given off by matter in the form of rays or high-speed particles. 1
- **alpha particle (α)** A form of charged particle radiation consisting of a ^{3}He nucleus. vii
- **beta particle (β)** A form of charged particle radiation with the rest mass of an electron. 9
  - **beta plus particle (β^+)** A positively charged β consisting of a high-energy positron. 28
  - **beta minus particle (β^-)** A negatively charged β consisting of a high-energy electron. 15
- **delta-ray (δ-ray)** A secondary electron with enough energy to escape a significant distance away from the primary radiation beam and produce further ionization, sometimes used to describe any recoil particle caused by secondary ionization. 28
- **electromagnetic radiation** Radiation consisting of individual packets, or photons, of light.
  - **gamma-ray (γ-ray)** Electromagnetic radiation originating from atomic nuclei with energies from 0.1 MeV to 10 MeV. 5
  - **X-ray** Electromagnetic radiation originating from orbital electrons with energies from 0.1 keV to 100 keV. 2
- **epsilon-ray (ε-ray)** A form of particle radiation consisting of tertiary electrons produced by secondary radiation. 28
- **neutron** An ionizing radiation particle with a neutral charge.
  - **cold neutron** A neutron possessing an energy less than 25 meV. vii
  - **fast neutron** A neutron possessing an energy between 1.0 MeV to 20.0 MeV. 9
  - **thermal neutron** A neutron possessing an energy between 0.025 eV to 1.0 eV. 9
  - **ultra-cold neutron (UCN)** A neutron possessing an energy less than ∼300 neV. 21
- **triton (*T*)** A form of charged particle radiation consisting of a tritium nucleus. 16

Radiation Monitoring Devices, Inc. (RMD) [Watertown, MA] A world leader in providing innovative solutions across a broad range of security, medical and industrial applications, including radiation imaging and detection, nuclear instrumentation and non-destructive test equipment [282]. 24

Radon transform The integral transform which takes a function f defined on the plane to a function R_f defined on the (two-dimensional) space of lines in the plane, whose value at a particular line is equal to the line integral of the function over that line. 84
- **inverse Radon transform** The inversion function for image reconstruction. 85

RC TRITEC Ltd. [Teufen, Switzerland] A Swiss small/medium scale company with more than 80 years tradition in manufacturing new and safer types of luminous materials, from the strongest afterglow pigments to labelled compounds in medical research [90]. 26

response functions
- **edge spread function (ESF)** 80
- **line spread function (LSF)** 45
- **modulation transfer function (MTF)** vii, 79

S

PSI Siemens star imaging mask [*Mfr.*: PSI] A neutron imaging resolution test mask featuring a Siemens star, fabricated from a quartz substrate coated in a Gd thin film. 46, 74

silicon photomultiplier (SiPM) A solid-state single photon sensitive electronic device constructed from an avalanche photodiode, offering a silicon analog to the traditional PMT. 26

silver paste [*formula:* Ag (70%)] A conductive mounting paste manufactured by SPI Supplies, sold under the product name Silver Paste Plus™. 60

Spallation Neutron Source (SNS) [Oak Ridge, TN] A one-of-a-kind research facility at ORNL that provides the most intense pulsed neutron beams in the world for scientific research and industrial development [283]. 197

Specialty Coating Systems™, Inc. (SCS) [Indianapolis, IN] A world leader in Parylene conformal coating services and technologies for the medical device, electronics, automotive and military industries [284]. 196

SPI Supplies® [West Chester, PA] A leading manufacturer and distributor of sample preparation equipment and consumable supply items for the routine operation of the typical SEM, TEM, LM, SPM and surface analysis laboratory [285]. 196

6800 Series Spin Coater [*Mfr.*: Specialty Coating Systems (SCS)] A programmable spin coater used for applying thin film photoresists to semiconductor substrates. 143

Stopping and Range of Ions in Matter A collection of software packages which calculate many features of the transport of ions in matter [286]. 29

Süss MicroTec, Se. (Karl Süss) [Garching, Germany] A supplier of equipment and process solutions for the semiconductor industry and related markets. The high precision microstructuring systems like photolithography tools are used for manufacturing of processors, memory chips, MEMS, LED and other micro system devices [287]. 194

T

University of Tennessee (UTK) [Knoxville, TN] A public sun- and land-grant university founded in 1794, and the publishing university for this dissertation [288]. 100

The University of Texas at Austin (UT) [Austin, TX] A public research university and the flagship institution of the University of Texas System, founded in 1881 [289]. 198

National Institute of Standards and Technology (NIST) [Gaithersburg, MD] A measurement standards laboratory, and a non-regulatory agency of the United States Department of Commerce with a mission to promote innovation and industrial competitiveness [290]. 47

Timepix v2 ASIC [*Mfr.*: CERN] The Timepix chip evolved from the Medipix2 development. The pixels have identical size to those of Medipix2 but the functionality within each pixel has been changed. In Timepix each pixel can be programmed to count hits like Medipix2, or to record Time-Over-Threshold (providing rough analog information), or to measure arrival time of the first particle to impinge on the pixel. 6

toluene [*formula:* C_7H_8] An aromatic hydrocarbon used as a solvent. 143

TRIGA nuclear reactor [*Mfr.*: General Atomics (GA)] A pool-type nuclear reactor operating at low-power ($\sim$ 1 MWth), used for education and scientific research at academic institutions (named after **T**eaching, **R**easearch, and **I**sotope production **G**eneral **A**tomics). 4

U

Ultimaker, B.V. [Somerville, MA] A 3D printer manufacturing company specializing in FDM printers and supporting software [197]. 192

V

Vanderbilt [Nashville, TN] A private research university founded in 1873 [291]. 37

Versatile Neutron Imaging Instrument (VENUS) [Oak Ridge, TN] A neutron beam line designed to be as versatile as possible to encompass the largest range of applications, while being fully optimized to benefit from the unique capabilities of the Spallation Neutron Source (SNS) [292]. 115

virtual instrument (VI) An instrument consisting of an industry-standard computer or workstation equipped with powerful application software, cost-effective hardware such as plug-in boards, and driver software, which together perform the functions of traditional instruments. 72

V2718 VME-PCIe Optical Link Bridge [*Mfr.*: CAEN] A VME to PCI Optical Link Bridge, housed in a 1-unit wide VME 6 U module, serving as a VME Master module and can be controlled by a standard PC equipped with PCI or PCIe CAEN Controller cards. 72

VME 8010 Crate [*Mfr.*: CAEN] A VME crate featuring 21 slots for 6 U modules with internal power supply (470 W) and ventilation. 72

VPPO (*also*: 2-phenyl-5-(4-vinyl-phenyl)-oxazole) [*formula:* $C_{17}H_{13}NO$] An plastic scintillator mixture integrating the base matrix, neutron sensitive isotope, and fluor on a single polymer chain. 23

W

wavelength-shifting (WLS) A property of some photofluorescent materials, absorbing a single, higher frequency photon and emitting multiple, lower frequency photons. 22

WidePIX [*Mfr.*: ADVACAM] The WidePIX 10x10 is currently the world's largest photon counting imaging camera with 6.5 MP, consisting of 10×10 Timepix devices tiled in an edgeless configuration. 45

4500 Digital Series Manual Wire Bonder [*Mfr.*: K&S] An automatic step back wirebonder used with aluminum or gold wire to connect micro circuitry using a range of application specific wedge tips. 60

X

X-Ray Imatek, S.L. [Barcelona, Spain] A company aimed in researching, developing, marketing and manufacturing detector technology for digital X-ray imaging. 66

Y

CNS Y-12 (Y-12) [Oak Ridge, TN] A DOE facility tasked with maintaining the U.S. nuclear stockpile, reducing global threats, and fueling the U.S. Nuclear Navy [293]. 37

Vita

Elan Hunter Herrera is an engineer from Dallas, Texas. In 2007 he earned his high school diploma from Edward S. Marcus High School in Flower Mound, TX. While in high school he also worked with the robot team and was employed at Fry's Electronics as a Mobile Electronics Certified Technician. He attended The University of Texas at Austin (UT) where he studied Mechanical Engineering. During his studies, he trained as a Reactor Operator at the department managed TRIGA Mk II nuclear research reactor. He completed his Bachelors of Science degree in 2013 with a specialization in Nuclear Engineering.



Later, he relocated to Knoxville, Tennessee, in pursuit of a Ph.D. in Nuclear Engineering. There, he studied under Dr. Eric Lukosi, researching a novel semiconducting neutron detector, LISe [96, 97, 107, 145, 154, 160, 187, 294] obtaining his Masters of Science degree in 2015. He went on to write this dissertation, using LaTeX [295], in completion of the degree of Doctor of Philosophy in Nuclear Engineering.